



THE UNIVERSITY  
*of* ADELAIDE

# STRUCTURAL EVOLUTION OF DEFORMATION BANDS

DREW CHRISTOPHER LUBINIECKI

Department of Earth Sciences  
School of Physical Sciences  
University of Adelaide

This thesis is submitted in fulfilment of the  
requirements for the degree of Doctor of  
Philosophy

September 2019

---

## Table of Contents

---

Abstract	5
Declaration	6
Acknowledgements	7
<b>Chapter 1 – Introduction</b>	
Project overview and background geology	8
Thesis outlines	15
References	18
<b>Chapter 2 – Cenozoic structural evolution of the Mount Lofty and Flinders ranges, South Australia</b>	
Introduction	24
Geological setting of the Adelaide fold and thrust belt	26
Methods	32
Structural data from the St. Vincent Basin and Frome Embayment	30
Palaeostress evolution of the St. Vincent and Lake Eyre basins	38
Discussion: The structural evolution of siliciclastic- and carbonate-hosted deformation bands in formations adjacent to Mount Lofty and Flinders Ranges bounding faults	43
Conclusions	49
References	50
<b>Chapter 3 – Structural evolution of carbonate-hosted deformation bands adjacent to a major neotectonic fault, Sellicks Beach, South Australia</b>	
Introduction	57
Geological setting of the Willunga Embayment	60
Methods	65
Structural data from the Port Willunga Formation	65
Palaeostress evolution of the St. Vincent Basin and Lake Eyre Basin	67

---

## Table of Contents

---

Discussion: The structural evolution of carbonate-hosted deformation bands within the Port Willunga Formation	73
Conclusions	79
References	
<b>Chapter 4 – Cenozoic evolution of the Mount Lofty and Flinders ranges, South Australia</b>	
Introduction	88
Geological setting of the Dead Tree section	89
Methods	91
Structural Data from the Dead Tree section	91
Discussion: Structural evolution of dilation bands at the Dead Tree section	96
Conclusion	101
References	102
<b>Chapter 5 – Structural evolution of deformation bands within the Manitou Falls Formation, Athabasca Basin, Canada.</b>	
Introduction	108
Geological history of the Athabasca Basin	112
Methods	113
Structural analysis of Fox Lake and Wide Lake deformation bands	126
Discussion: Faults within the Manitou Falls Group and their relationships to local uranium deposits	130
Conclusions	130
References	131
<b>Chapter 6 – Cataclastic-dilation deformation bands: A new type of cataclastic deformation band in the Athabasca Basin, Canada.</b>	
Introduction	139
Geological history of the Athabasca Basin	141
Methods	144

---

## Table of Contents

---

Microstructural analysis of Fox Lake and Wide Lake deformation bands	145
Discussion: Growth and temporal evolution of Manitou Falls Group deformation bands	150
Conclusions	155
References	156

### **Chapter 6 – Conclusions**

Implications to understanding the nature of deformation bands and their structural evolution in sedimentary sequences	161
---	-----

### **Supplementary Data**

Appendix A	168
Appendix B	241
Appendix C	247
Appendix D	250
Appendix E	257

---

## Abstract

---

Deformation bands are the most common strain features observed in deformed upper crustal sections of porous sedimentary rocks, like sandstone and carbonate grainstone. A deformation band is a tabular zone of localised strain that forms as a result of compaction due to sediment loading and high deviatoric stress. These bands of strain exhibit considerable variation in structural kinematic styles (compaction band, shear band, dilation band, and hybrids) and formation mechanics (disaggregation band, cataclastic band, phyllosilicate band, and cement/dissolution band). The variations may enhance or retard subsurface fluid flow and create permeability anisotropy, especially surrounding fault zones. Uranium is mobilised easily by fluids in sedimentary basins, thus this project explores practical uses for sedimentary-hosted mineral exploration, specifically targeting faulting. Fault-induced deformation bands reflect the stress state at the time of formation, creating a foundation for palaeostress reconstructions using deformation bands as indicators of discrete changes to the local and far-field stress. Despite considerable research to siliciclastic-hosted bands, research bias has contributed to a lack of understanding of carbonate-hosted cataclastic bands and dilation bands. This study presents an investigation of the structural styles that govern the formation mechanisms of newly described deformation bands observed at Marion Bay, Stenhouse Bay, Port Vincent, Port Willunga, and Sellicks Beach in the southern Mount Lofty Ranges; the Dead Tree section and Paralana Hill in the northern Flinders Ranges in South Australia; and the Athabasca Basin in northern Saskatchewan, Canada.

Detailed face mapping and structural analysis of 737 deformation bands and 397 fractures observed near the Port Vincent Fault, Marion Bay Fault, Stenhouse Bay Fault, Willunga Fault, and Paralana Fault infers the structural evolution of the Mount Lofty Ranges is remarkably similar to the palaeostress evolution of the northern Flinders Ranges. These results define a five stage evolution sequence for the region: Stage 1) NW–SE extension (early Palaeocene–early Eocene); Stage 2) N–S extension (middle Eocene–middle Miocene); Stage 3) N–S compression (late Miocene); Stage 4) NW – SE compression (Pliocene–middle Pleistocene); Stage 5) E–W compression (late Pleistocene–Present-day). Detailed face mapping, permeameter, and transmitted light microscopy results confirms 286 dilation bands are hosted within the Eyre Formation at the Dead Tree section in the northern Flinders Ranges. Integration of this data with our palaeostress model and Paralana Fault geometry reveals the region underwent transtension during Stages 2 and 4 of our palaeostress model, resulting in the formation of dilation bands observed at the Dead Tree section. I suggest these events enhanced localised effective permeability between the Mount Painter uranium source and Four Mile uranium deposit. Detailed face mapping, permeameter, and transmitted light microscopy results confirms 221 cataclastic bands with differing intensities of cataclasis, pressure solution, disaggregation, and cementation are hosted within the Port Willunga Formation at Sellicks Beach. To standardize the nomenclature, I suggest the fault rock classification scheme of cataclasis intensity for carbonate-hosted deformation bands. In the Athabasca Basin, I mapped 1713 deformation bands in detail within the Manitou Falls Formation. Six stage palaeostress model is inferred for the Manitou Falls Formation: Stage 1) NW–SE extension; Stage 2) E–W extension; Stage 3) NE–SW extension (1.3 Ga); Stage 4) NW–SE transpression; Stage 5) N–S compression; Stage 6) E–W compression. Scanning electron microscopy indicates cataclasis, dissolution, dilation, and fracture control formation mechanics in the Manitou Falls Formation. For the first time ever, I document the occurrence of reactivated cataclastic bands. This study confirms deformation bands are excellent indicators of discrete changes to the local and far-field stress regime, enhance our understanding of the evolution of Earth's crust, and present a useful tool to understand fault history and fluid flow, especially for sedimentary hosted uranium exploration.

---

## Declaration

---

I, Drew Christopher Lubiniecki, certify that this work contains no material which has been accepted for the award of any other degree or diploma in my name, in any university or other tertiary institution and, to the best of my knowledge and belief, contains no material previously published or written by another person, except where due reference has been made in the text. In addition, I certify that no part of this work will, in the future, be used in a submission in my name, for any other degree or diploma in any university or other tertiary institution without the prior approval of the University of Adelaide and where applicable, any partner institution responsible for the joint-award of this degree.

I acknowledge that copyright of published works contained within this thesis resides with the copyright holder(s) of those works.

I also give permission for the digital version of my thesis to be made available on the web, via the University's digital research repository, the Library Search and also through web search engines, unless permission has been granted by the University to restrict access for a period of time.

\_\_\_\_\_  
Drew Christopher Lubiniecki

30/07/2019  
Date

---

## Acknowledgements

---

I want to start off by saying this Ph.D. experience has been invaluable towards my personal and professional growth, and I surprisingly really enjoyed the journey. This awesome roller coaster ride would not have been possible without the academic support of my brilliant supervisors Rosalind King, Simon Holford, and Mark Bunch. This dream team academic panel has provided me with encouragement, motivation, and confidence, further enhancing my skillsets (particularly scientific communication and critical thinking) needed for pursuit of this Ph.D. challenge.

The Geological Survey of South Australia and the Saskatchewan Geological Survey have been fundamentally supportive to my Ph.D., organized through a memorandum of understanding, aimed at enhancing innovation and research between the two states. A huge thank you goes out to Steve Hill, Stephen Hore, and crew at the Geological Survey of South Australia, in addition to Gary Delaney, Colin Card, and crew at the Saskatchewan Geological Survey for their helpful insights, discussions, and everything in-between. This collaboration has involved many generous businesses and organisations, and I would like to acknowledge their contributions towards this project. Thank you Dave Thomas and crew at Cameco for their cooperation and expertise in the Athabasca Basin, northern Saskatchewan; Doug and Margaret Sprigg for their warm support and access to their Arkaroola property in the northern Flinders Ranges; Ruth Williams, Ben Wade, and Dave Kelsey for their direction around at Adelaide Microscopy.

One of the biggest lessons that I learned during this Ph.D. experience is that I can do anything that I want, as long I am willing to work hard and persevere. I want to thank my beautiful bunch of friends and fellow Ph.D. students that have been here to celebrate the highs and pull me through the lows. In no specific order, these people are my Klemzig family/ Mardi Gras Crew, Morgan, Kam, Dingo Jack, Rowan, Jack, Gilby, Briony, Romana, Renee, Dinner Guy, Pineapple Pants, Sandy, Goatie, Mitch, Kiara, Brandon, Dicko, Georgie, James, Cooper, Fin, and Furph. This crew has kept me entertained inside and out of the Mawson Laboratories, including various university field trips throughout the Mount Lofty and Flinders ranges and holidays throughout Australia and Europe.

Travel has always been an inspiration to me, and I have been very lucky throughout my Ph.D. to do my fair share of domestic and international travel to attend conferences, field-work, and study. To that effect, I thank the Eric Rudd Scholarship and the International Geoscience Congress Travel Grant Scheme for their contributions to my project, which supported travel to Canada, UK, Austria, and Japan. My quality research group S<sup>3</sup> has been around for many of these educational trips in the Adelaide region, shenanigans at certain late-night establishments in London, the Dragon House in Somerset, and the writing retreat to the Central Coast.

Last but not least, I would like to thank my family, including my biggest supporter and ultimate fan, my darling mother Brenda.

# CHAPTER 1

### What is a deformation band?

The most common strain feature found in rigid upper crustal porous sedimentary rocks are deformation bands (Fossen et al., 2007). In porous sedimentary rocks, strain is initially accommodated by pore space collapse, forming highly localised tabular zones of continuous inelastic strain, commonly known as deformation bands (Aydin and Johnson, 1978, Fossen et al., 2007). A deformation band is tabular in shape and forms a continuous zone of localised strain resulting from sediment loading-induced compaction or high deviatoric stresses (Fossen et al.,

2007). A single deformation band trace is usually planar; but in some cases, it may be wavy or anastomose (normal to the direction of shear) and rarely cross other bands (Aydin and Johnson, 1983). Weathering preferentially exposes deformation band material owing to colour variations between deformation bands and their host rock, and differing induration between the high-density, usually cemented, deformation band material and relatively low-density host rock. Deformation bands thus are revealed as high relief features standing out from adjacent undeformed host rocks, superficially resembling quartz veins. This resemblance

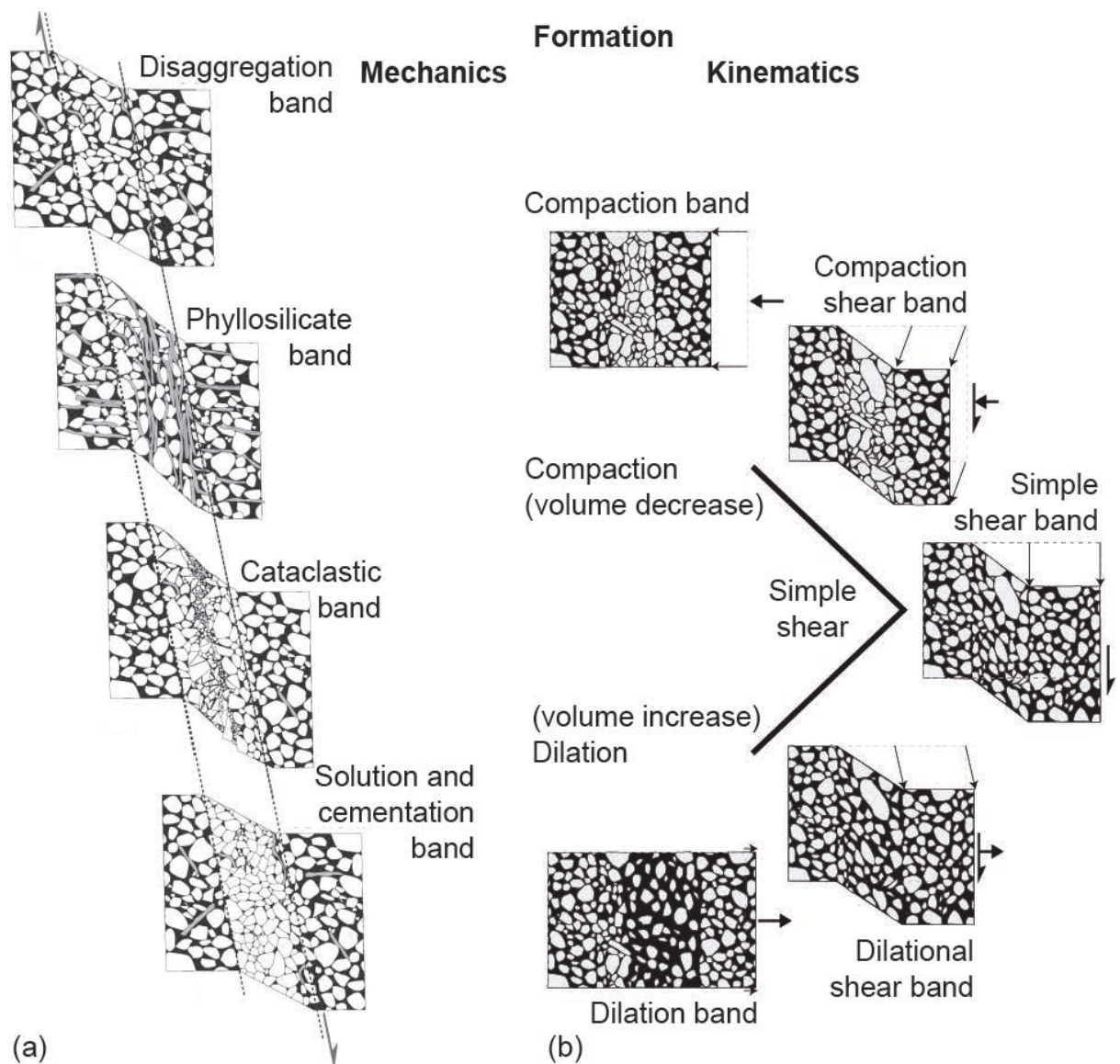


**Figure 1.** Kinematic classification of deformation bands after Fossen et al. 2007.

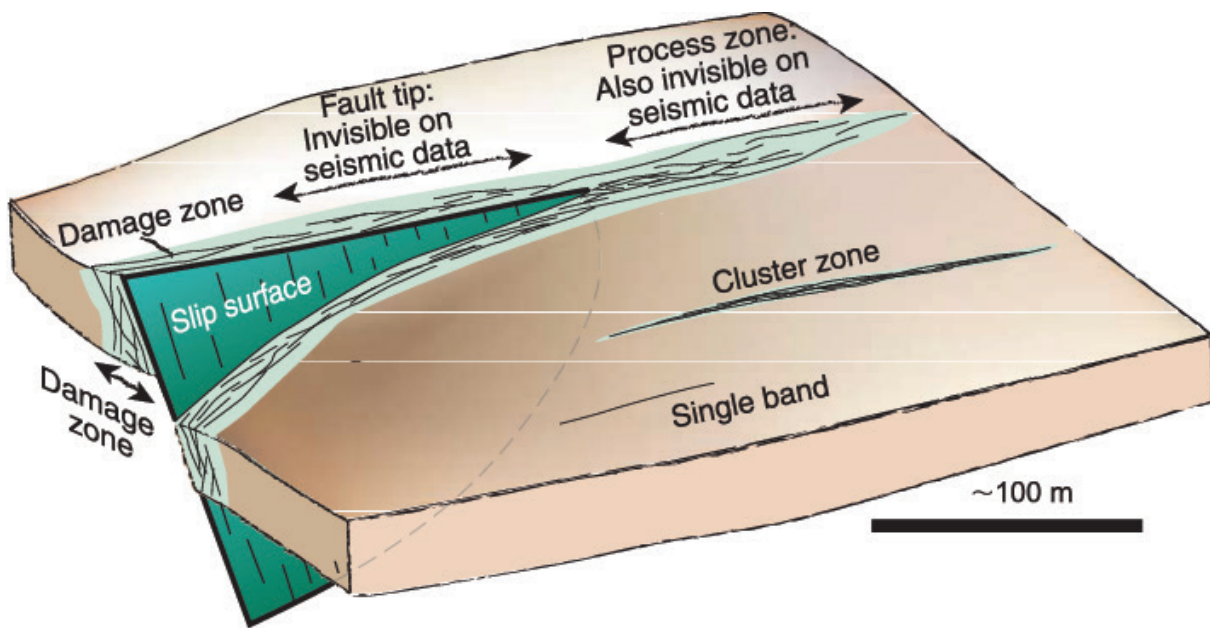


**Figure 2.** Schematic diagram of a fault tip in porous sandstone, depicting the formation of deformation bands after Fossen et al. 2007.

resulted in misinterpretation up until the mid-1990's when Antonellini and Aydin (1994) first recognised their importance to permeability in the subsurface.

Deformation bands were first documented by Aydin and Johnson (1978) in the Entrada and Navajo Sandstones of the San Rafael Desert, Utah. Here, deformation bands were observed forming a hierarchy of styles and characteristics highlighting a progressive sequence, evolving from a single band, to a cluster, and eventually forming a slip surface (i.e. fault) (Fig. 1) (Aydin and Johnson, 1983). Single deformation bands generally range in thickness between 1–2 mm and can be up to tens of metres in length (Aydin and Johnson, 1983, Antonellini et al., 1994). Deformation bands represent low-displacement zones, offsetting bedding planes and other deformation bands by millimetres, with an upper range limit of a few centimetres (Antonellini et al., 1994). Deformation band clusters zones form next in sequence and are made up of many parallel juxtaposed deformation bands, commonly reaching much greater

offsets of centimetre or decimetre scale (Aydin and Johnson, 1983). Slip surfaces are the last in sequence to form, making up a distinct zone of deformation bands with a discontinuous fractured surface accommodating displacement of metre scale or more (Aydin and Johnson, 1983).

Deformation bands occur in upper-crustal tectonic and non-tectonic settings, and are associated with fault zones, vertical uplifts, monocline or drape folds, growth and collapse of salt structures, growth of shale diapirs, and slumping (e.g. Jamison and Stearns, 1982, Antonellini et al., 1994, Hesthammer and Fossen, 1999, Cashman and Cashman, 2000, Fisher and Knipe, 2001, Fossen et al., 2007). Deformation bands form as a result of the strain hardening process (Aydin and Johnson, 1978, Aydin and Johnson, 1983). Strain initiates around imperfections, such as exceptionally large or oddly shaped pore spaces; causing pore space to collapse, reducing pore volume and increasing grain contact points. The increased grain contact points create

enhanced friction between grains that promotes strong grain interlocking and reduction in continued strain until it ceases. This progression is a strain hardening pathway typical of most deformation bands. Progressive evolution by shear failure is initiated by micro-fractures in the zones parallel to the initial band caused by initial elastic loading, forming a cluster or deformation band zone (Aydin and Johnson, 1983, Mair et al., 2000). Strain hardening thus promotes development of another deformation band within susceptible weak zones of adjacent host rock (Mair et al., 2000).

### Deformation band classifications, characteristics, and properties

Deformation bands can be classified

based on their formation kinematics as compaction bands, dilation bands, shear bands, or hybrid shear bands (Fig. 2) (e.g. Aydin et al., 2006). Compaction bands and dilation bands involve volumetric strain only that is induced by pure shear, resulting in either decreased or increased pore space, respectively. Where simple shear is dominant shear bands develop, creating small offsets of host rock. Hybrid shear bands are a result of compaction or dilatant volumetric strain (Aydin et al., 2006). Factors underpinning the formation, geometry, and kinematic configuration of deformation bands are confining pressure, deviatoric stress, and pore fluid pressure (Fossen et al., 2007). The geometry of deformation bands adhere to Anderson's Faulting

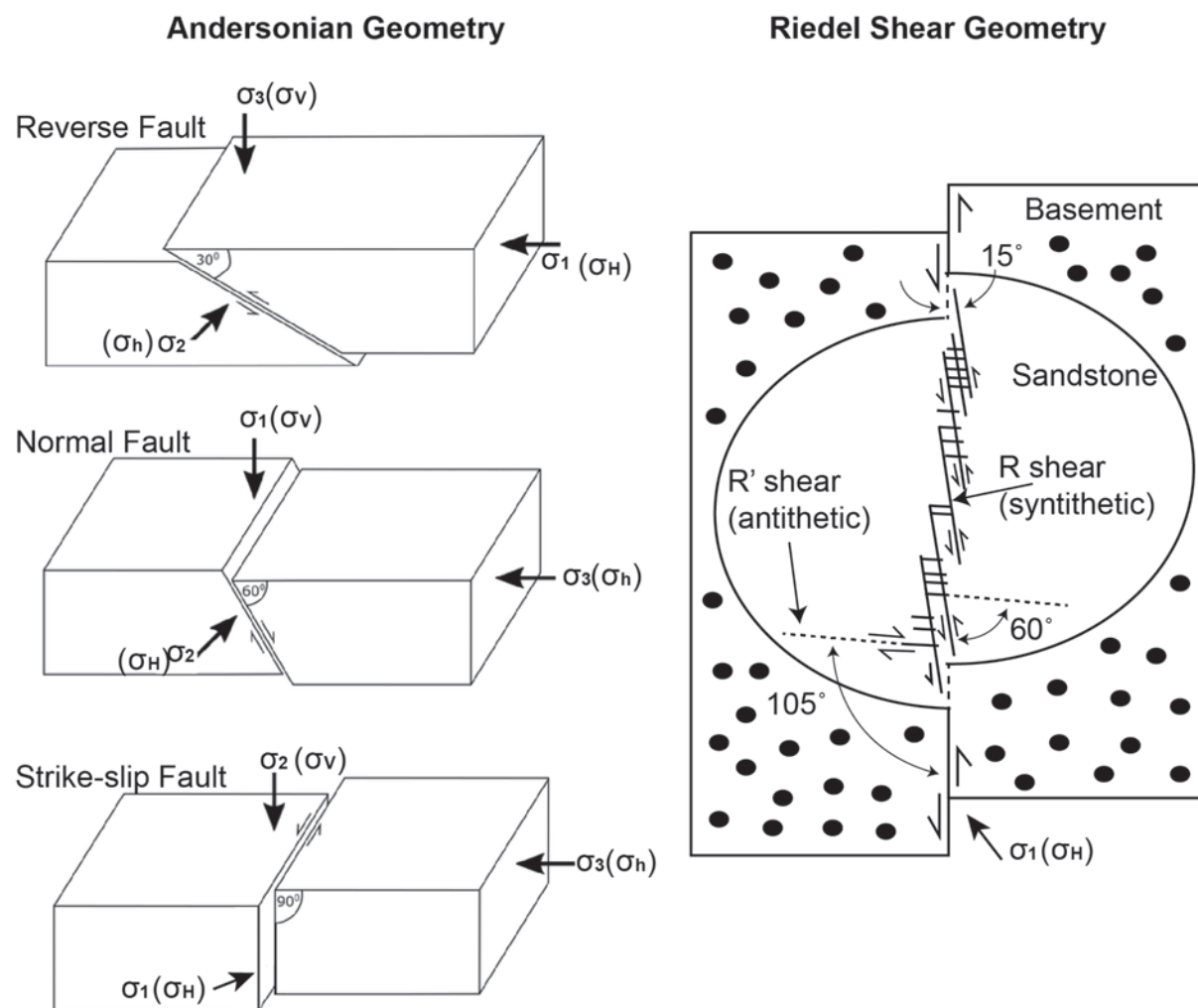


**Figure 3.** Schematic diagram of the Andersonian fault systems and Riedel shear systems.

Theory and Riedel Shear systems (e.g. Davis et al., 2000, Fossen et al., 2011). Rocks generally have an angle of internal friction of approximately  $30^\circ$ , which is the angle between the normal force and resultant force when failure occurs in response to shear stress (Anderson, 1951). Anderson's Faulting Theory hypothesizes the maximum stress ( $\sigma_1$ ) will bisect the acute angle of conjugate faults by  $30^\circ$  (Fig. 3). Therefore, reverse faults should form dip angles of  $30^\circ$ , normal faults should form dip angles of  $60^\circ$ , and strike-slip faults should form dip angles of  $90^\circ$ . In the case of simple shear, high deviatoric stress forms conjugate shear-enhanced compaction bands to accommodate strain. In the case of pure shear, low deviatoric stress promotes the geometric formation of a singular deformation band normal to the maximum stress; resulting in formation of a pure compaction band.

Deformation bands can also be classified based on their formation mechanics (Fig. 2). Rock properties controlling the formation mechanics of deformation bands are: 1) degree of lithification; 2) mineralogy; 3) grain size; 4) grain sorting and; 5) grain shape (Fossen et al., 2007). For example, deformation band thickness is proportional to the mean grain size of the host rock (Antonellini et al., 1994, Fossen et al., 2007). Generally, there are four categories of deformation bands described by this classification: (1) disaggregation band; (2) cataclastic band; (3) phyllosilicate band; (4) dissolution and cementation bands (Fossen et al., 2007).

The formation of disaggregation bands involves significant granular flow, a product of grain rotation, grain translation, and breaking grain-bonding cement (Fossen et al., 2007). Grain translation induces grain boundary sliding, resulting in a distinct fabric and alignment of elongated grains with the orientation of

the disaggregation band, making them easily distinguishable in the field (Fig. 2) (Antonellini et al., 1994). Disaggregation bands are generally the first to form in a burial sequence prior to lithification when confining pressure and burial depth are low (Antonellini et al., 1994, Fossen et al., 2007). As porosity decreases with increasing burial depth and diagenesis, the formation of pure compaction bands will shift to shear compaction bands and disaggregation will shift to cataclasis (Fossen et al., 2011).

Cataclastic bands form with increasing burial depth and lithification, typically at depths between 1–3 km (Ballas et al., 2015). Although, cataclastic bands have been described in poorly consolidated sandstones less than 1 km in depth (Cashman and Cashman, 2000). Cataclasis intensity increases with increasing burial depth, highlighting a progressive sequence of strain intensity (Antonellini et al., 1994). The major mechanisms involved during cataclastic band formation are grain grinding, grain fracture and grain comminution or grain crushing (Fig. 2) (e.g. Aydin, 1978, Aydin and Johnson, 1978, Antonellini et al., 1994, Aydin and Johnson, 1983, Tondi et al., 2006). The grain size distribution of a cataclastic band exhibits two distinct zones: an inner zone and an outer zone. The inner zone is composed mainly of low porosity, highly fractured and crushed grain matrix; while the thin outer zone exhibits an intermediate level of porosity and grain crushing relative to the highly porous non-fractured parent material (Aydin, 1978). The fault rock classification scheme by Sibson (1977) is used to define cataclasis intensity for siliciclastic deformation bands by Ballas et al. (2012); however, carbonate-hosted deformation bands lack a similar documented relationship and classification.

Phyllosilicate bands are not depth depen-

dent and only form when phyllosilicate content exceeds 15% (Fig. 2); these bands form by phyllosilicate smearing, a product of alignment and mixing of platy minerals (Fossen et al., 2007). Dissolution bands are composed of tightly packed corrugated or sutured grain boundaries, showing no signs of cataclasis (Fig. 2) (Gibson, 1998). Cementation bands form as a result of displaced dissolution or abrasive grain boundary sliding and cataclasis, which creates highly reactive surfaces promoting cement precipitation (Fig. 2) (Fisher and Knipe, 2001). Precipitation and dissolution of quartz is promoted when temperatures exceed 90°C (Walderhaug, 1996).

### **Significance of deformation bands in aquifers, petroleum, and mineral systems**

Deformation bands can act as conduits for fluid flow through porous sedimentary rocks during their early growth stages, but they can become baffles to fluid flow leading to reservoir compartmentalization in their later stages of development (Fossen and Bale, 2007). Geometry, band connectivity, and permeability contrast between band and host rock are the most important characteristics controlling effective permeability of deformation bands (Rotevatn et al., 2013). Maximum permeability will occur parallel to compaction bands, while the minimum permeability effect will occur perpendicular to band, resulting in permeability anisotropy (Fossen et al., 2011, Farrell et al., 2014). Deformation bands have proven to be important in petroleum geomechanical and petrophysical studies because they influence the flow pattern during injection or recovery of fluids (Fossen and Bale, 2007). Geomechanical studies have driven deformation band research because the petrophysical implications of their development are expected to con-

fer negative effects on sweep efficiency of petroleum reservoirs; in other words, deformation bands may prevent fluids from sweeping highly permeable layers (Fossen et al., 2011).

Historically, research has focused mainly on the permeability reducing properties of siliciclastic compaction bands and as a result deformation bands have become best-known for their permeability retarding effects (e.g. Manzocchi et al., 1998, Gibson, 1998, Fossen and Bale, 2007, Sallet and Wibberley, 2013). This has resulted in major research gaps surrounding our understanding of the geomechanics, nomenclature, and petrophysical properties of carbonate-hosted cataclastic bands (e.g. Tondi et al., 2006, Cilona et al., 2012, Rotevatn et al., 2016) and dilation bands (e.g. Antonellini and Aydin, 1994, Bésuelle, 2001, Du Bernard et al., 2002, Borja and Aydin, 2004, Okubo and Shultz, 2005). Differential stresses modulates structural permeability; it is important to understand how they have changed throughout time. For example, fault-related hydrothermal veins generally form by episodic rupturing of faults resulting from dynamic stress cycling (Sibson, 1994). Although sandstone and grainstone faults generally reduce permeability, fluid flow may still be enhanced in the basement, thereby creating a dynamic fluid system at the basement-basin contact. In the Athabasca Basin, this contact is where the basin unconformity-related high-grade uranium deposits are located. This has created an opportunity to study, define, and explore the potential of deformation bands to benefit exploration and mineral geoscience by exploring their influence on mineralisation in sedimentary rocks of the brittle upper crust. Deformation bands hosted within the

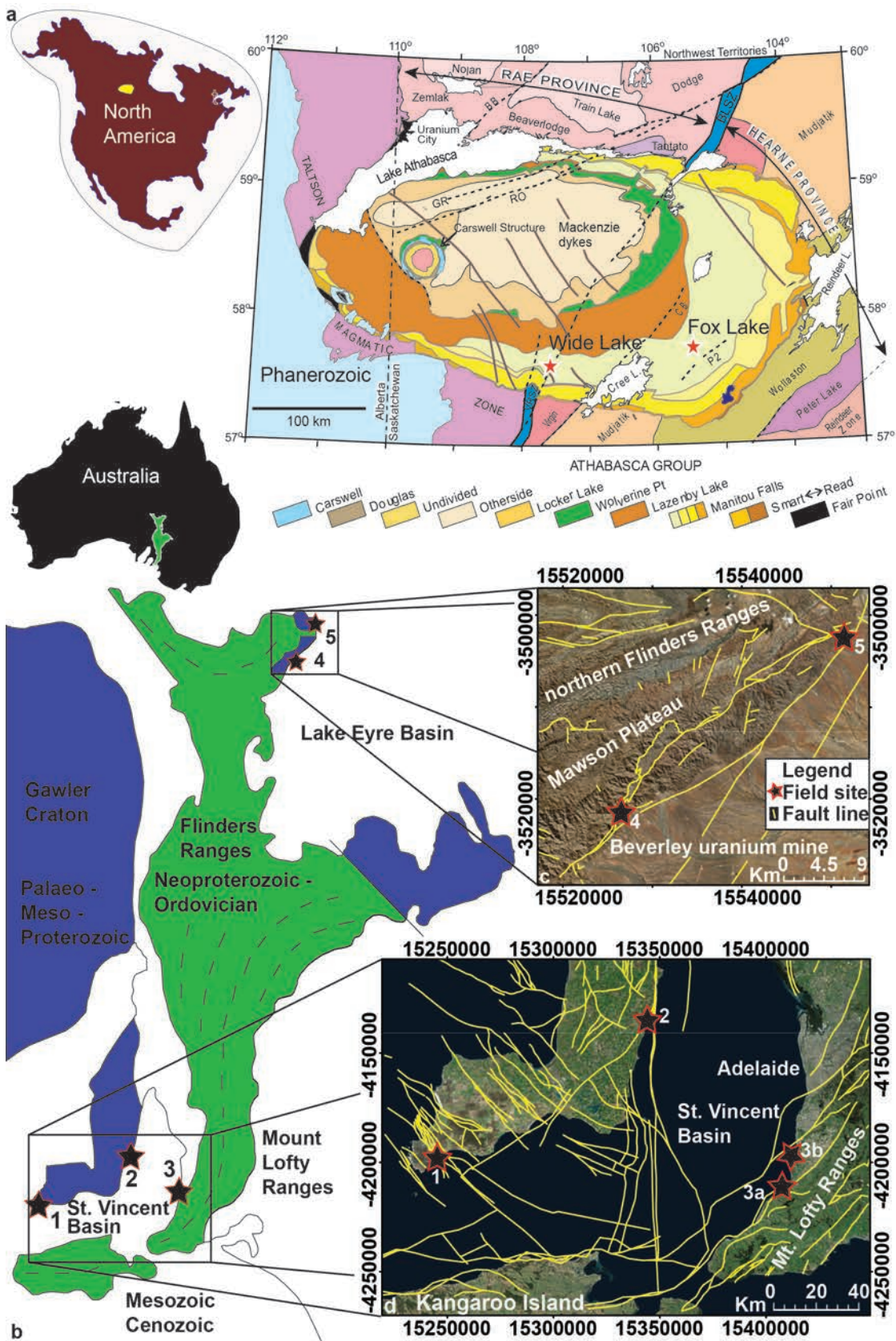


**Figure 4.** Schematic geological maps and satellite images of the project study areas: **a)** Athabasca Basin; **b)** Adelaide fold and thrust belt; **c)** northern Flinders Ranges and Eyre Basin and; **d)** Mount Lofty Ranges and St. Vincent Basin.

Mesoproterozoic Manitou Falls Formation of the Athabasca Basin are investigated to this end.

The state of stress and fault geometries influence the way fluids move through the subsurface and may cause localized areas of extension within rock subject to compression (i.e. dilatant jog); these areas may show enhanced fluid flow (Zhang et al., 2008). Thus, to understand how and where fluids may have been channeled through faults in the past, it is important to define the evolution of palaeostress. Current methods for determining a palaeostress pathway lack fundamental structural evidence and neglect due consideration of rock-fault heterogeneities and basement geology characteristics (e.g. Müller et al., 2012). Deformation bands conform to Andersonian and Riedel shear geometries (e.g. Antonellini and Aydin, 1994, Davis et al., 2000); their cross-cutting relationships can therefore be used to document discrete changes in the palaeostress regime over geological time. Time constraints are challenging, and calcite cement dating can be easily reset (Arboit et al., 2015). Thus, this project requires a new method for dating palaeostress.

## Thesis Outline

This project documents deformation band abundances, deformation band formation mechanisms, local fault histories, influences of deformation bands on local and regional fluid flow, and the role of deformation bands in localizing economic mineral deposits. I investigate: i) a new workflow for modelling palaeostress through a structural chronostratigraphic study of deformation bands hosted within the Pleistocene Bridgewater Formation, Pliocene Hallet Cove Sandstone, Oligo-

cene-Miocene Port Willunga Formation, Eocene Eyre Formation, Cretaceous Parabarana Sandstone, and Cambrian Heatherdale Shale of the St Vincent Basin and Northern Flinders Ranges (Chapter 2); ii) universal classification for carbonate grainstone hosted cataclastic bands within the Oligocene-Miocene Port Willunga Formation, cropping out at Sellicks Beach and Port Willunga, South Australia (Chapter 3); iii) impacts of dilation bands on the adjacent Four Mile uranium deposit hosted within the Eocene Eyre Formation in the northern Flinders Ranges, South Australia (Chapter 4); iv) the role deformation bands play in defining sandstone faults of the Athabasca Basin, proximal Fox Lake, McArthur River, and Centennial uranium deposits in northern Saskatchewan, Canada (Chapter 5).

## Chapter 2

The Cenozoic tectonic evolution of the Mt Lofty Ranges and Flinders Ranges—Figure 4b—is poorly constrained. Attempts to model the Australian palaeostress fields by Müller et al. (2012) use tectonic-scale fault reactivations simulations, which are based only on computer generated plate reconstruction and lack underpinning by the available structural evidence. Thermochronological investigations lack critical localised information, such as stress state and principal stress orientation (e.g. Foster et al., 1994, Mitchell et al., 2002). In this chapter I investigate the Cenozoic tectonic events that occurred in the Mt Lofty Ranges and Flinders Ranges area by combining a series of structural datasets. We have developed a workflow to temporally reconstruct palaeostress using deformation bands and fundamental structural concepts. Deformation bands are cohesive and form a geometric relationship (Andersonian) to the regional principal stress, providing evidence for the regional palaeostresses at the time of their formation (Fig. 3). Additionally,

crosscutting relationships can be used to infer relative ages of deformation band sets and therefore, changes in palaeostress conditions through time. To relate the stress state to a space in time, datasets from rocks of varying ages were used to temporally constrain the palaeostress boundaries. The palaeostress models from the Mount Lofty Ranges and Flinders Ranges correspond, revealing step changes temporally bound by the age of the sedimentary rock.

### Chapter 3

The geomechanical processes of carbonate-hosted deformation bands are significantly understudied and cataclastic nomenclature undefined (e.g. Tondi, 2007, Rath et al., 2011, Ciona et al., 2012, Antonellini et al., 2014, Rotevatn et al., 2016). This chapter investigates the microstructural characteristics of carbonate grainstone-hosted cataclastic bands observed within wavecut platforms and cliffs at Sellicks Beach and Port Willunga, South Australia (Fig. 4b). This is the first documented case study of deformed carbonate grainstone in Australia. The exceptionally well exposed Port Willunga Formation adjacent to the Willunga Fault makes this site a natural laboratory for a type-section account of carbonate-hosted cataclastic band investigations. We provide a series of detailed cross-section face maps of cliff sections and wave cut platforms depicting the cataclastic band exposures of the present-day footwall of the Willunga Fault, demonstrating a detailed account of intraplate strain accommodation. I provide a fault rock model by Sibson (1977), applied to siliciclastic deformation bands by Ballas et al. (2012) to defined cataclasis intensity within the Port Willunga Formation carbonate grainstone deformation bands.

### Chapter 4

This chapter builds on descriptions and petrophysical properties of dilation bands, while investigating their formation mechanisms and explicit influence on the adjacent Four Mile uranium deposit, northern Flinders Ranges, South Australia (Fig. 4b). This study has identified dilational deformation bands within the Eyre Formation, cropping out at the Dead Tree section adjacent to the Paralana Fault and Four Mile Fault. The Eyre Formation is a kaolinized sandstone that hosts the Four Mile uranium deposit, inadvertently discovered by drilling in sedimentary rocks not previously thought prosperous due to their close proximity to the northern Flinders Ranges (Hore and Hill, 2009). Current models describing the genesis of mineralisation oversimplify and fail to recognise impacts of neotectonic faulting (e.g. Skirrow et al., 2009, Wilson, 2015). Detailed structural analysis of the observed dilation bands constrains the recent structural evolution of the Paralana Fault and Four Mile Fault. This implies a transtensional fault jog – connecting the Paralana Fault and Four Mile Fault – has enhanced localised trans-tension in a region undergoing compression, resulting in the formation of dilation bands in at the Dead Tree section (Fig. 4b). The dilation bands have increased the effective permeability of the Eyre Formation at the Dead Tree section, which is situated intermediately between the Four Mile uranium deposit in the Lake Eyre Basin, and the Mt. Painter Inlier uranium source. I suggest these dilation bands must not only control volume and direction of fluid flow, but also control the location the Four Mile deposit and quite possibly the locations of other deposits not yet discovered.

## *Chapter 5*

The structural evolution of the Athabasca Basin – host to the world’s largest source of high grade uranium – is poorly understood (Reid et al., 2014). The Athabasca Basin is well mapped (Fig. 4a), demonstrating an extensive fault network that is related to the high grade uranium deposits associated with the basin unconformity (e.g. Hoeve and Sibbald, 1978, Hoeve et al., 1980, Jefferson et al., 2007, Zenghua et al., 2017, Li et al., 2015). While most structural investigations focus on the pre-sedimentary basin structural metamorphic evolution of the regional rocks, this chapter aims to enhance our understanding of the post-basin deposition brittle structural evolution of the Athabasca Group. This chapter builds on the relationships and characteristics observed in Chapters 2 and Chapter 4 and applies them to the structural evolution of the Athabasca Basin Manitou Falls Formation of northern Canada. I combine two structural datasets observed by surficial grid mapping of outcrop and drill core from the southern and eastern Athabasca Basin at Fox Lake and Wide Lake to illustrate structural evolution of major faults from opposing sides of the basin. Microstructural investigations infer reactivation of cataclastic deformation bands by localised dilation. This implies localised permeability enhancement at the Fox Lake uranium deposit by the uranium mineralisation event.

## References

- ANDERSON, E. M. 1951. *The dynamics of faulting and dyke formation with applications to Britain*, Hafner Pub. Co.
- ANTONELLINI, M. & AYDIN, A. 1994. Effect of faulting on fluid flow in porous sandstones: petrophysical properties. *AAPG bulletin*, 78, 355-377.
- ANTONELLINI, M., PETRACCHINI, L., BILLI, A. & SCROCCA, D. 2014. First reported occurrence of deformation bands in a platform limestone, the Jurassic Calcare Massiccio Fm., northern Apennines, Italy. *Tectonophysics*, 628, 85-104.
- ANTONELLINI, M. A., AYDIN, A. & POLLARD, D. D. 1994. Microstructure of deformation bands in porous sandstones at Arches National Park, Utah. *Journal of Structural Geology*, 16, 941-959.
- ARBOIT, F., AMROUCH, K., COLLINS, A. S., KING, R. & MORLEY, C. 2015. Determination of the tectonic evolution from fractures, faults, and calcite twins on the southwestern margin of the Indochina Block. *Tectonics*, 34, 1576-1599.
- AYDIN, A. 1978. Small faults formed as deformation bands in sandstone. *Pure and Applied Geophysics*, 116, 913-930.
- AYDIN, A., BORJA, R. I. & EICHHUBL, P. 2006. Geological and mathematical framework for failure modes in granular rock. *Journal of Structural Geology*, 28, 83-98.
- AYDIN, A. & JOHNSON, A. 1978. Development of faults as zones of deformation bands and as slip surfaces in sandstone. *Pure and Applied Geophysics*, 116, 931-942.
- AYDIN, A. & JOHNSON, A. M. 1983. Analysis of faulting in porous sandstones. *Journal of Structural Geology*, 5, 19-31.
- BALLAS, G., FOSSEN, H. & SOLIVA, R. 2015. Factors controlling permeability of cataclastic deformation bands and faults in porous sandstone reservoirs. *Journal of Structural Geology*, 76, 1-21.
- BALLAS, G., SOLIVA, R., SIZUN, J.-P., BENEDICTO, A., CAVAILHES, T. & RAYNAUD, S. 2012. The importance of the degree of cataclasis in shear bands for fluid flow in porous sandstone, Provence, France. *AAPG bulletin*, 96, 2167-2186.
- BÉSUELLE, P. 2001. Compacting and dilating shear bands in porous rock: Theoretical and experimental conditions. *Journal of Geophysical Research*, 106, 13435-13442.
- BORJA, R. I. & AYDIN, A. 2004. Computational modeling of deformation bands in granular media. I. Geological and mathematical framework. *Computer Methods in Applied Mechanics and Engineering*, 193, 2667-2698.
- CASHMAN, S. & CASHMAN, K. 2000. Cataclasis and deformation-band formation in unconsolidated marine terrace sand, Humboldt County, California. *Geology*, 28, 111-114.
- CILONA, A., BAUD, P., TONDI, E., AGOSTA, F., VINCIGUERRA, S., RUSTICHELLI, A. & SPIERS, C. J. 2012. Deformation bands in porous carbonate grainstones: Field and laboratory observations. *Journal of Structural Geology*, 45, 137-157.
- DAVIS, G. H., BUMP, A. P., GARCÍA, P. E. & AHLGREN, S. G. 2000. Conjugate Riedel deformation band shear zones. *Journal of Structural Geology*, 22, 169-190.
- DU BERNARD, X., EICHHUBL, P. & AYDIN, A. 2002. Dilation bands: A new form of localized failure in granular media. *Geophysical Research Letters*, 29, 2176-2180.
- FARRELL, N. J. C., HEALY, D. & TAYLOR, C. W. 2014. Anisotropy of permeability in faulted porous sandstones. *Journal of Structural Geology*, 63, 50-67.
- FISHER, Q. J. & KNIPE, R. J. 2001. The permeability of faults within siliciclastic petroleum reservoirs of the North Sea and Norwegian Continental Shelf. *Marine and Petroleum Geology*, 18, 1063-1081.
- FOSSEN, H. & BALE, A. 2007. Deformation bands

- and their influence on fluid flow. *AAPG Bulletin*, 91, 1685-1700.
- FOSSEN, H., SCHULTZ, R. A., SHIPTON, Z. K. & MAIR, K. 2007. Deformation bands in sandstone: a review. *Journal of the Geological Society of London*, 164, 755-769.
- FOSSEN, H., SCHULTZ, R. A. & TORABI, A. 2011. Conditions and implications for compaction band formation in the Navajo Sandstone, Utah. *Journal of Structural Geology*, 33, 1477-1490.
- FOSTER, D., MURPHY, J. & GLEADOW, A. 1994. Middle tertiary hydrothermal activity and uplift of the northern flinders ranges, South Australia: Insights from apatite fission-track thermochronology. *Australian Journal of Earth Sciences*, 41, 11-17.
- GIBSON, R. G. 1998. Physical character and fluid-flow properties of sandstone-derived fault zones. *Geological Society, London, Special Publications*, 127, 83-97.
- HESTHAMMER, J. & FOSSEN, H. 1999. Evolution and geometries of gravitational collapse structures with examples from the Statfjord Field, northern North Sea. *Marine and Petroleum Geology*, 16, 259-281.
- HOEVE, J. & SIBBALD, T. I. 1978. On the genesis of Rabbit Lake and other unconformity-type uranium deposits in northern Saskatchewan, Canada. *Economic Geology*, 73, 1450-1473.
- HOEVE, J., SIBBALD, T. I. I., RAMAEKERS, P. & LEWRY, J. F. 1980. *Athabasca basin unconformity-type uranium deposits A special class of sandstone-type deposits*, International Atomic Energy Agency (IAEA), IAEA.
- HORE, S. B. & HILL, S. M. 2009. Palaeoredox fronts: setting and associated alteration exposed within a key section for understanding uranium mineralisation at the Four Mile West deposit. *Mesa Journal*, 55, 34-39.
- JAMISON, W. R. & STEARNS, D. W. 1982. Tectonic deformation of Wingate Sandstone, Colorado National Monument. *The American Association of Petroleum Geologists Bulletin*, 66, 2584-2608.
- JEFFERSON, C., THOMAS, D., GANDHI, S., RAMAEKERS, P., DELANEY, G., BRISBIN, D., CUTTS, C., PORTELLA, P. & OLSON, R. 2007. Unconformity-associated uranium deposits of the Athabasca Basin, Saskatchewan and Alberta. *Bulletin-Geological Survey of Canada*, 588, 23.
- LI, Z., BETHUNE, K. M., CHI, G., BOSMAN, S. A. & CARD, C. D. 2015. Topographic features of the sub-Athabasca Group unconformity surface in the southeastern Athabasca Basin and their relationship to uranium ore deposits. *Canadian Journal of Earth Sciences*, 52, 903-920.
- MAIR, K., MAIN, I. & ELPHICK, S. 2000. Sequential growth of deformation bands in the laboratory. *Journal of Structural Geology*, 22, 25-42.
- MANZOCCHI, T., RINGROSE, P. S. & UNDERHILL, J. R. 1998. Flow through fault systems in high-porosity sandstones. *Geological Society, London, Special Publications*, 127, 65-82.
- MITCHELL, M. M., KOHN, B. P., O'SULLIVAN, P. B., HARTLEY, M. J. & FOSTER, D. A. 2002. Low-temperature thermochronology of the Mt Painter Province, South Australia. *Australian Journal of Earth Sciences*, 49, 551-563.
- MÜLLER, R. D., DYKSTERHUIS, S. & REY, P. 2012. Australian paleo-stress fields and tectonic reactivation over the past 100 Ma. *Australian Journal of Earth Sciences*, 59, 13-28.
- OKUBO, C. H. & SHULTZ, R. A. 2005. Evolution of damage zone geometry and intensity in porous sandstone: insight gained from strain energy density. *Journal of the Geological Society*, 162, 939-949.
- RATH, A., EXNER, U., TSCHEGG, C., GRASEMANN, B., LANER, R. & DRAGANITS, E. 2011. Diagenetic control of deformation mechanisms in deformation bands in a

- carbonate grainstone. *AAPG Bulletin*, 95, 1369-1381.
- REID, K. D., ANSDELL, K., JIRICKA, D., WITT, G. & CARD, C. 2014. Regional Setting, Geology, and Paragenesis of the Centennial Unconformity-Related Uranium Deposit, Athabasca Basin, Saskatchewan, Canada. *Economic Geology*, 109, 539-566.
- ROTEVATN, A., SANDVE, T. H., KEILEGAVLEN, E., KOLYUKHIN, D. & FOSSEN, H. 2013. Deformation bands and their impact on fluid flow in sandstone reservoirs: the role of natural thickness variations. *Geofluids*, 13, 359-371.
- ROTEVATN, A., THORSHEIM, E., BASTESSEN, E., FOSSMARK, H. S. S., TORABI, A. & SÆLEN, G. 2016. Sequential growth of deformation bands in carbonate grainstones in the hangingwall of an active growth fault: Implications for deformation mechanisms in different tectonic regimes. *Journal of Structural Geology*, 90, 27-47.
- SAILLET, E. & WIBBERLEY, C. 2013. Permeability and flow impact of faults and deformation bands in high-porosity sand reservoirs: Southeast Basin, France, analog. *AAPG Bull.*, 97, 437-464.
- SIBSON, R. H. 1977. Fault rocks and fault mechanisms. *Journal of the Geological Society*, 133, 191-213.
- SIBSON, R. H. 1994. Crustal stress, faulting and fluid flow. *Geological Society, London, Special Publications*, 78, 69-84.
- SKIRROW, R. G., JAIRETH, S., HUSTON, D., BAS-TRAKOV, E., SCHOFIELD, A., VAN DER WIELEN, S. & BARNICOAT, A. 2009. Uranium mineral systems: processes, exploration criteria and a new deposit framework. *Geoscience Australia Record*, 20, 44.
- TONDI, E. 2007. Nucleation, development and petrophysical properties of faults in carbonate grainstones: Evidence from the San Vito Lo Capo peninsula (Sicily, Italy). *Journal of Structural Geology*, 29, 614-628.
- TONDI, E., ANTONELLINI, M., AYDIN, A., MARCHEGIANI, L. & CELLO, G. 2006. The role of deformation bands, stylolites and sheared stylolites in fault development in carbonate grainstones of Majella Mountain, Italy. *Journal of Structural Geology*, 28, 376-391.
- WALDERHAUG, O. 1996. Kinetic modeling of quartz cementation and porosity loss in deeply buried sandstone reservoirs. *AAPG bulletin*, 80, 731-745.
- WILSON, T. 2015. Uranium and uranium mineral systems in South Australia - Third edition, Report Book 2015/00011. Department of State Development, South Australia, Adelaide
- ZENGHUA, L., GUOXIANG, C., BETHUNE, K. M., DAVID, T. & GERARD, Z. 2017. Structural Controls on Fluid Flow During Compressional Reactivation of Basement Faults: Insights from Numerical Modeling for the Formation of Unconformity-Related Uranium Deposits in the Athabasca Basin, Canada. *Economic Geology*, 112, 451-466.
- ZHANG, Y., SCHAUBS, P., ZHAO, C., ORD, A., HOBBS, B. & BARNICOAT, A. 2008. Fault-related dilation, permeability enhancement, fluid flow and mineral precipitation patterns: numerical models. *Geological Society, London, Special Publications*, 299, 239-255.

---

# CHAPTER 2

Lubiniecki, D. C., King R. C., Holford S. P., Bunch M. A., Hore S., Hill, S. M.  
*Cenozoic structural evolution of the Mount Lofty Ranges and Flinders Ranges, South Australia, constrained by analysis of deformation bands.* Accepted for publication July 10, 2019. Australian Journal of Earth Science Sp. Ed. Flinders Ranges.

---

# Statement of Authorship

Title of Paper	Cenozoic structural evolution of the Mount Lofty and Flinders ranges, South Australia, constrained by analysis of deformation bands		
Publication Status	<input type="checkbox"/> Published	<input checked="" type="checkbox"/> Accepted for Publication	<input type="checkbox"/> Unpublished and Unsubmitted work written in manuscript style
Publication Details	Lubiniecki, Drew Christopher, et al. "Cenozoic evolution of the Mount Lofty and Flinders ranges, South Australia, constrained by analysis of deformation bands." Australian Journal of Geoscience Special Edition: Flinders Ranges.		

## Principal Author

Name of Principal Author (Candidate)	Drew Lubiniecki		
Contribution to the Paper	Completed fieldwork, collected and interpreted data, collected and analysed samples, wrote and prepared manuscript, acted as corresponding author.		
Overall percentage (%)	75%		
Certification:	This paper reports on original research I conducted during the period of my Higher Degree by Research candidature and is not subject to any obligations or contractual agreements with a third party that would constrain its inclusion in this thesis. I am the primary author of this paper.		
Signature		Date	<b>24/9/2019</b>

## Co-Author Contributions

By signing the Statement of Authorship, each author certifies that:

- i. the candidate's stated contribution to the publication is accurate (as detailed above);
- ii. permission is granted for the candidate to include the publication in the thesis; and
- iii. the sum of all co-author contributions is equal to 100% less the candidate's stated contribution.

Name of Co-Author	Rosalind King		
Contribution to the Paper	Supervised fieldwork, aided in collection of data and samples, helped with data interpretation and manuscript revision.		
Signature		Date	<b>18/9/2019</b>

Name of Co-Author	Simon Holford		
Contribution to the Paper	Supervised fieldwork, aided in collection of data and samples, helped with data interpretation and manuscript revision.		
Signature		Date	<b>15/9/19</b>

Name of Co-Author	Mark Bunch		
Contribution to the Paper	Supervised fieldwork, aided in collection of data and samples, helped with data interpretation and manuscript revision.		
Signature		Date	<b>18/09/2019</b>

Name of Co-Author	Stephen Hore		
Contribution to the Paper	Financial support, government correspondent, field-site introduction to some key locations which aided in collection of data and samples and overall concept of thesis.		
Signature		Date	15/8/19.

Name of Co-Author	Steven Hill		
Contribution to the Paper	Financial support, government correspondent, and overall concept of thesis.		
Signature		Date	11/9/19

Please cut and paste additional co-author panels here as required.

---

## Cenozoic structural evolution of the Mount Lofty Ranges and Flinders Ranges, South Australia, constrained by analysis of deformation bands

---

### Abstract

The presence of deformation bands in Upper Cretaceous–Pleistocene sediments of the St Vincent and Lake Eyre basins, South Australia supports the occurrence of intraplate normal and reverse faulting in this region throughout the Cenozoic. Current tectonic models for the development of this region lack structural evidence and underestimate the role and influence of extensional tectonics in the Cenozoic tectonic evolution of the Mount Lofty Ranges and Flinders Ranges. This lack of understanding has resulted in poor structural and chronological constraints of the regions paleostress models. For the first time ever, we use detailed mapping and structural analysis of deformation bands across different chronostratigraphic units to identify variations in paleostress. Deformation bands are discrete, measurable strain features that develop readily in clastic sedimentary rocks in response to regional stress. We present a comprehensive structural analysis of five study sites across six chronostratigraphic units adjacent to the Mount Lofty Ranges and Flinders Ranges. Here, we have recorded 737 cataclastic and dilation bands and 397 fractures adjacent to reactivated Cenozoic faults, which reveal step changes in structural sets, identifying temporal constraints for our paleostress model. Our analysis supports the notion of a regional late Miocene shift in the paleostress regime from N–S extension to N–S compression, followed by a rotation of the maximum horizontal stress ( $\sigma_H$ ) from NW–SE to E–W. This coincides with a well-documented pulse of late Miocene–Pliocene compression and uplift observed throughout southeastern Australia. Our results indicate that deformation bands are a useful resource for constraining discrete changes in local stress regimes and enhances our understanding of dynamic intraplate strain accommodation within the Mount Lofty Ranges and Flinders Ranges, which has been proven useful for hydrocarbon and mineral exploration in neighbouring Otway Basin and Gippsland Basin.

**Keywords:** Willunga Fault, Paralana Fault, Sellicks Beach, deformation band, neotectonic, stress rotation

---

### Introduction

The Cenozoic tectonic evolution of the Mount Lofty Ranges and Flinders Ranges in South Australia has long been the subject of debate (e.g. Hillis et al., 2008; Holford et al., 2009; Preiss, 2019; Quigley et al., 2006; Sandiford, 2003; Sandiford et al., 2009; Tokarev et al., 1999). Historical seismic records indicate these ranges are arguably Australia's most seismically active intraplate regions (C  lerier et al., 2005); recent Quaternary topography and drainage patterns attest to this (Sandiford, 2003). The Mount

Lofty Ranges and Flinders Ranges initially formed as a fold and thrust belt during the Cambrian–Ordovician Delamarian Orogeny (Foden et al., 2006); the ranges subsequently reactivated and uplifted to their present state by Cenozoic crustal shortening driven intraplate strain accommodation (C  lerier et al., 2005; Hillis et al., 2008; Holford et al., 2011c; Sandiford, 2003). Studies of Quaternary reverse faulting in the region are common, mainly documenting Cambrian rocks thrust over Quaternary sediments (e.g. C  lerier et al., 2005; Quigley et al., 2007; Sandiford, 2003; Sprigg, 1946; Williams, 1973).

However, the transition from the prior regime of extension to compression is poorly understood, with extension related to the final breakup of eastern Gondwana beginning in the Jurassic, which formed a series of rift basins in southeastern Australia (e.g. Bight Basin, Otway Basin and Gippsland Basin) as Antarctica unzipped and pushed away from Australia (Flöttmann and Cockshell, 1996). The precise transition from extension to compression appears to vary throughout southeastern Australia, characterised as Eocene in the Gippsland Basin (Sandiford et al., 2004), and Late Cretaceous in the Otway Basin (Krassay et al., 2004). In contrast, the St Vincent Basin is unique, both younger than the Gippsland and Otway rift basins, and only characterised by late Miocene compressional tectonics. Overall the attempts to elucidate the temporal evolution of the Cenozoic paleostress record across the region of the Mount Lofty Ranges and Flinders Ranges is ambiguous and lacking structural evidence (e.g. Müller et al., 2012).

A deformation band is a discrete strain structure that forms as a result of pore space collapse or enlargement in granular porous granular rocks, commonly a direct result of faulting (Fossen et al., 2007). Deformation bands exhibit a cohesive shear-enhanced strain-hardening characteristic and thus, may provide an excellent tool to elucidate the structural evolution of faults and paleostress records (Aydin and Johnson, 1978). These characteristics make cross-cutting relationships and chronology easily identifiable. Linking structural and chronostratigraphic datasets allows for temporal constraints on the regional paleostress evolution in our study area, through the process of elimination of observed stress regimes in Cretaceous–Pleistocene sedimentary rocks within the St Vincent and Lake Eyre basins. This paper reconciles the uncertainties pertaining to the

poorly constrained Cenozoic paleostress evolution record in South Australia, supported by quantitative structural data and models. As a result, we suggest the Mount Lofty Ranges and Flinders Ranges have evolved under a unique paleostress pattern distinct from other parts of southeastern Australia. Interestingly, the results have important implications for improving our understanding of the tectonic forces driving intracratonic far-field stress accommodation and temporal constraints of brittle fault reactivation, which are essential for reducing the risk of mineral and petroleum exploration.

For the first time, we provide chronostratigraphic and structural evidence, supporting a Late Cretaceous–Present-day paleostress model of the Mount Lofty Ranges and Flinders Ranges, using deformation bands as specific indicators of discrete changes in the regional stress regime. We report the occurrence of siliciclastic- and carbonate-hosted deformation bands in the Upper Cretaceous Paraburra Sandstone, Eocene Eyre Formation, Oligocene–upper Miocene Port Willunga Formation, Pliocene Hallett Cove Sandstone, and Pleistocene Bridgewater Formation. Our results suggest that the onset of Cenozoic compression in the Mount Lofty Ranges and Flinders Ranges does not occur until the late Miocene and provides evidence of extensional tectonics until the late Miocene. We present evidence bearing on the timing of the onset of Cenozoic compression, indicating the maximum horizontal stress ( $\sigma_H$ ) rotated from NW–SE to E–W and occurred subsequent to the well-documented pulse of late Miocene compression (e.g. Holford et al., 2011b). This paper provides highly resolved evidence of Cenozoic structural evolution in the St Vincent and Lake Eyre basins, which has played an important role in determining hydrocarbon, geothermal, and mineral prospectivity across the Mount

Lofty Ranges and Flinders Ranges.

### Geological setting of the Adelaide fold and thrust belt

The north–south-trending Adelaide fold and thrust belt is divided into the Mount Lofty Ranges to the south and the Flinders Ranges to the north and is separated at the surface by lacustrine and fluvial cover sequences (Figure 1). The Mount Lofty Ranges border Adelaide to the east, stretching 300 km from the Cape Jervis to Peterborough. The

Flinders Ranges form the largest ranges in South Australia, stretching just over 400 km from Port Pirie to Lake Callabonna. The Mount Lofty Ranges and Flinders Ranges are a product of the Delamarian Orogeny, a Cambrian–Ordovician fold and thrust belt that formed during the final amalgamation of Gondwana (Foden *et al.*, 2006). Subduction-related contractional orogenesis initiated at  $514 \text{ Ma} \pm 3 \text{ Ma}$  in the Flinders Ranges and lasted until  $490 \pm 3 \text{ Ma}$  in the Mount Lofty Ranges (Foden *et al.*, 2006). The opening of

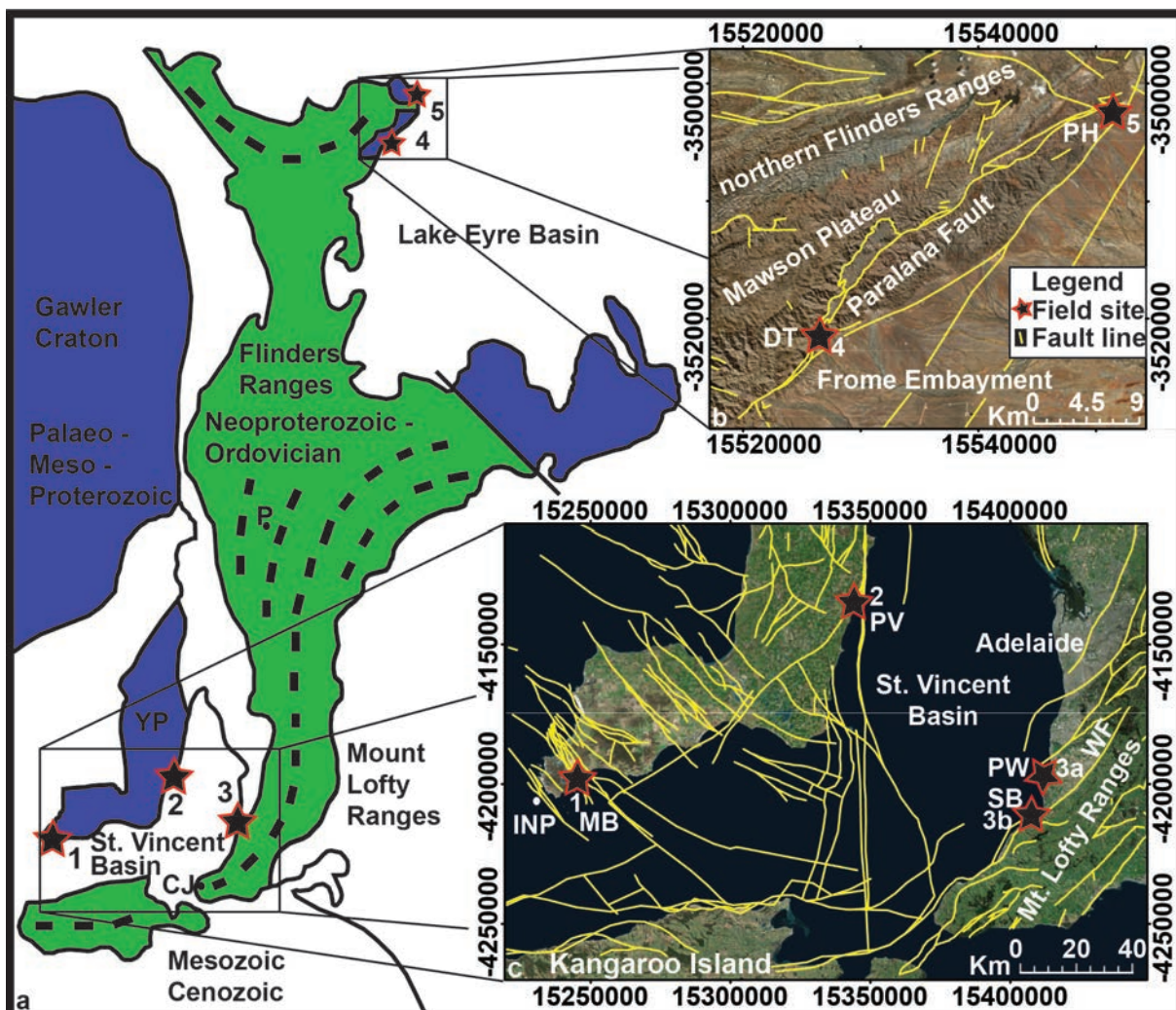


**Figure 1.** (a) Simplified geological map outline of the Mount Lofty Ranges and Flinders Ranges (dashed lines indicate structural form, colour indicates age, stars indicate field locations, WL indicates the Willunga Fault, YP indicates the Yorke Peninsula, CJ indicates Cape Jervis, P indicates Peterborough, PW indicates Port Willunga, PV indicates Port Vincent, MB indicates Marion Bay, PH indicates Parabarana Hill, DT indicates Dead Tree section, and SB indicates Sellicks Beach) modified from Celerier *et al.* (2005). Satellite image insets of: (b) the northern Flinders Ranges, and (c) the southern Mount Lofty Ranges.

the Tasman Sea in the Late Cretaceous saw reactivation of long-lived structures like the Paralana Fault and development of other major structures like the Willunga Fault (Figure 1). It has been suggested that the ranges were uplifted once again in the Cenozoic by crustal extension-related denudation and exhumation, then crustal shortening-related intracratonic uplift (e.g. Foster et al., 1994; Mitchell et al., 2002; Sandiford, 2003; Tokarev, 2005).

### **Cenozoic history of the St Vincent Basin**

The St Vincent Basin is a small, mostly offshore depocentre located between the Yorke Peninsula and the Mount Lofty Ranges. Basin opening commenced in the Eocene and formed as a result of rift-related extension associated with the opening of the Tasman Sea (Holford et al., 2011a). With regards to our field localities, Innes National Park and Port Vincent are situated on the basin's western edge, whereas Sellicks Beach and Port Willunga are located on-shore along the basin's eastern edge adjacent to the Willunga Fault (Figure 1).

The Willunga Fault is one of Australia's most prominent neotectonic structures and is associated with the occurrence of young topography, recent drainage patterns, and steep cliffs along the Sellicks Hill scarp face (Sandiford, 2003). This fault marks the boundary between Cenozoic sediments of the St Vincent Basin and upper Proterozoic–lower Paleozoic Adelaidean sediments that form the Mount Lofty Ranges and Flinders Ranges (Figure 2a). The Willunga Fault is one of many curvilinear faults that dominate the onshore sections of the St Vincent Basin bordering the western section of the Mount Lofty Ranges, maintaining a max elevation of 727 m at the Mount Lofty Peak. The Heatherdale Shale is

a lower Cambrian interbedded shale and siltstone that crops out immediately south of the Willunga Fault, forming the hanging wall (Figure 2b). Here, the intensely fractured formation beds dip near-vertically ( $\approx 80^\circ$ ) towards the north where bedding also approaches vertical, parallel to the Willunga Fault (Figure 2a). The Willunga Fault originally formed as part of a NNE–SSW-oriented half-graben associated with the final separation of Australia from Antarctica during the middle Eocene (Flöttmann and Cockshell, 1996; Holford et al., 2011a; Norvick and Smith, 2001). This resulted in extension and subsidence of the St Vincent Basin; increased accommodation space allowed marine transgression and deposition of the Port Willunga, Hallet Cove Sandstone, and Pooraka formations (Tokarev, 2005).

The Oligocene–Miocene Port Willunga Formation is a yellow carbonate grainstone with variable thickness, reaching 150 m at Sellicks Beach (Fairburn, 1998). Tokarev (2005) interpreted the variable thickness to be the result of differential normal fault displacement along the Willunga Fault, which dominated from the middle Eocene to the middle Miocene. However, structural evidence is limited, with only Quaternary reverse displacement observed and recorded along the Willunga Fault within Cactus Canyon at Sellicks Beach (Figure 2b) (Sandiford, 2003). Late Miocene–Pliocene regional tectonic compression triggered uplift and erosion Precambrian Adelaidean metasedimentary rocks (Tokarev, 2005), resulting in the formation of a low-angle unconformity within the St Vincent Basin separating the Port Willunga Formation from the overlying Hallet Cove Sandstone (Sandiford, 2003). At Sellicks Beach, the unconformity separates the Port Willunga Formation from overlying Quaternary alluvial fans sediments, known as the Pooraka Formation. How-

ever, on the Yorke Peninsula, the Hallett Cove Sandstone – a medium-grained yellow calcareous sandstone – uncon-

formably underlies the Bridgewater Formation, a yellow fossiliferous coarse-grained calcareous sandstone.

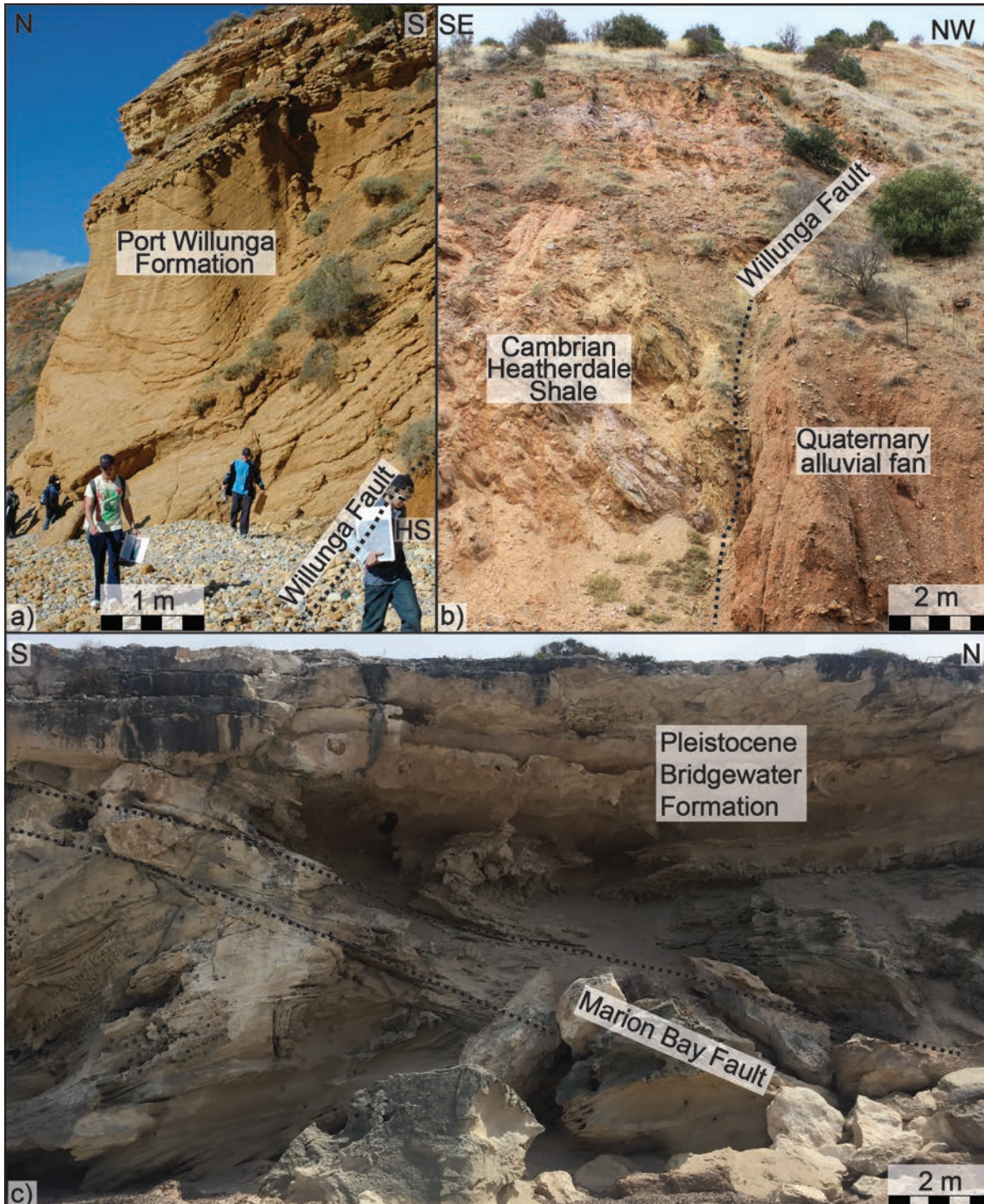


**Figure 2.** Photographs of major neotectonic faults in the Mount Lofty Ranges. (a) Willunga Fault contact between Heatherdale Shale and Port Willunga Formation at Sellicks Beach (field location 3); (b) Willunga Fault contact juxtaposing Quaternary alluvial fans to the Cambrian Heatherdale Shale at Cactus Canyon (field location 3); (c) Marion Bay Fault observed within the Pleistocene Bridgewater Formation at Marion Bay (field location 1).

Differential elevation of Port Willunga Limestone between the Willunga Fault hanging wall and footwall, suggests post-early Miocene vertical displacement of  $\approx 240$  m (Sandiford, 2003; Tokarev et al., 1999). Correlation of interglacial benches in the hanging wall and footwall of the Willunga Fault implies reverse-sense movement on the near-vertical Willunga Fault has resulted in time-averaged vertical displacement of 50 to 70 m per Myr (Sandiford, 2003). Uplift and increased erosion of Neoproterozoic and Cambrian rocks southeast of the Willunga Fault resulted in generation of the Quaternary alluvial fan sediments, which unconformably overlie the Port Willunga Formation at Sellicks Beach and Port Willunga (Figure 2b) (Cann et al., 2014).

### **Cenozoic history of the Frome Embayment**

The Lake Eyre Basin is a large intracratonic basin formed by subsidence (Alley, 1998), resulting from pull of the fossilised New Guinea slab subducting under eastern-central Australia (Schellart and Spakman, 2015). The Frome Embayment forms a small section of the Callabonna Sub-basin, which forms a section of the larger Lake Eyre Basin, one of the world's largest internal river drainage systems (Figure 1) (Drexel and Preiss, 1995). The Paralana Fault zone flanks the northern Flinders Ranges to the west, and the Frome Embayment to the east (Figure 1). Large-scale faults like the Paralana Fault in the northern Flinders Ranges have controlled deposition of cover successions since the Neoproterozoic (Paul et al., 1999). The Paralana Fault initially developed as an extensional fault during the middle Proterozoic, and has been intermittently active since (Preiss, 1990). The Paralana Fault inverted during the Cambrian–Ordovician Delamerian Orogeny, which caused intense

deformation of the Adelaidean cover sediments, including exhumation and denudation of the radiogenic Mount Painter and Mount Babbage inliers (Paul et al., 1999). Today, the Paralana Fault zone is a major range-bounding reverse-fault, marking the boundary between the early–late Proterozoic northern Flinders Ranges and Mesozoic–Cenozoic Lake Eyre Basin sedimentary units (Figure 1b). The Paralana Fault juxtaposes the northern Flinders Ranges to the Eyre Formation at the Dead Tree section and Parabarana Sandstone at Parabarana Hill. The Eyre Formation is an Eocene kaolinised quartz sandstone and the Parabarana Sandstone is a Cretaceous yellow quartz sandstone.

The Cenozoic tectonic evolution of the northern Flinders Ranges and adjacent Frome Embayment is ambiguous, considering the regions anomalously high geothermal gradient for thermochronology studies. Apatite fission track ages from Mount Painter and Mount Babbage inliers imply regional denudation occurred during the Paleocene–Eocene; however, a decrease in the geothermal gradient and minor erosion contributing to these results cannot be ruled out (Mitchell et al., 2002). The most recent period of major uplift – giving the Flinders Ranges their modern topographical appearance – was suggested to have occurred during the Miocene (Foster et al., 1994). Webb (1958) suggested tilted gravels in the northern Flinders Ranges indicate late or early Pliocene uplift. Uplift continued into the Quaternary where fault slip rates of the Willunga Fault have been estimated at 10–50 m per Myr (Figure 2) (Sandiford, 2008). Present-day principal stress orientations have been determined in the northern Flinders Ranges from earthquake focal mechanisms, borehole breakouts, drilling-induced tensile fractures and hydraulic fracture tests, all of which indicate a NW–SE  $\sigma_H$  (Den-

ham et al., 1979; Hillis and Reynolds, 2000, 2003; Hillis et al., 2008). Broad Cretaceous–Present day paleostress reconstruction models for the Australian continent have been computed by Müller *et al.* (2012) using time-dependent fault slip tendency analysis to determine the predicted variation in  $\sigma_H$  over time.

### Structural data from the St Vincent Basin and Frome Embayment

Here, we describe structural data from

737 deformation bands and 397 fractures mapped within the Bridgewater Formation at Marion Bay, Hallet Cove Sandstone at Port Vincent, Port Willunga Formation and Heatherdale Shale at Sellicks Beach, Eyre Formation at the Dead Tree section, and Parabarana Sandstone at Parabarana Hill indicated by the stars in Figure 1 (Table 1).

### Methods

To investigate the detailed structure of

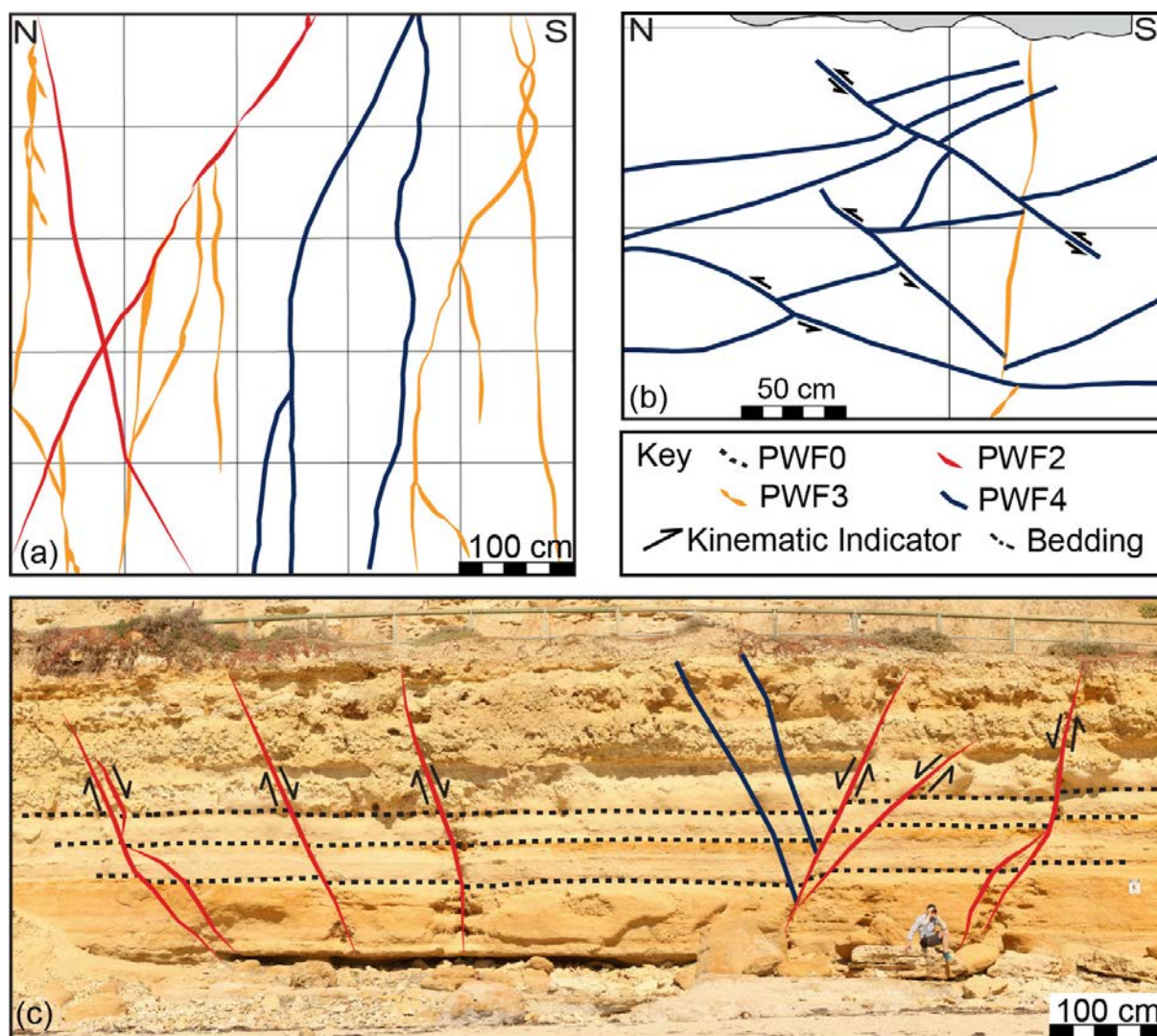


**Figure 3.** Mapped sections of the Port Willunga Formation illustrating cross-cutting and abutting relationships. **(a)** Grid map illustrating the spatial relationships between DBS 1, 2, 3, and 4 in plan-view (Face Map 2). **(b)** Face map illustrating the spatial relationships between Deformation Band Set 3 and 4 in cross-section view (Fig. 5-Face Map 5). **(c)** Photograph of a graben-like structure depicting Deformation Band Set 2 within the Port Willunga Formation at Port Willunga (Fig. 5-Face Map 7).

**Table 1.** Table of data collected from all formations.

Structural set	Set A			Set B			Dihedral angle
	Average strike	Dip direction	Average dip	Average strike	Dip direction	Average dip	
BF2b	NW–SE	–	80	NE–SW	–	79	74°
BF2a	N–S	–	90	–	–	–	–
BF1	E–W	N	29	NE–SW	SE	30	54°
HCS2	N–S	W	26	N–S	E	34	60°
HCS1	ENE– WSW	N	36	ENE– WSW	S	30	66°
PWF4	NW–SE	NE	33	NW–SE	SW	40	73°
PWF3	NW–SE	–	90	E–W	–	90	50°
PWF2	NW–SE	NE	35	NE–SW	SE	35	53°
PWF1	NW–SE	NE	53	E–W	S	53	62°
PWF0	NE–SW	NW	19	E–W	S	18	31° (fold)
EF4b	NE–SW	–	87	NW–SE	–	86	66°
EF4a	NW–SE	SW	42	N–S	E	27	60°
EF3	NE–SW	NW	17	NNE– SSW	E	45	60°
EF2b	NW–SE	–	85	NNE– SSW	–	82	68°
EF2a	NW–SE	NE	40	NE–SW	SE	51	54°
EF1	E–W	N	49	E–W	S	56	68°
PS3b	E–W	–	80	NE–SW	–	82	48°
PS3a	NW–SE	SW	46	NE–SW	SE	30	59°
PS2	NNE– SSW	NW	17	NNE– SSW	E	55	72°
PS1	E–W	S	69	E–W	N	45	66°
HS4	NW–SE	NE	28	NW–SE	SW	24	52°
HS3	N–S	W	24	NE–SW	SE	42	62°
HS2	E–W	N	16	E–W	S	34	50°
HS1	NNW– SSE	E	69	NW–SE	SW	64	51°

the aforementioned formations, we measured and recorded deformation bands observed in outcrop and created a series of grid maps and face maps (Figures 3 and 4). Field locations were chosen based on the location of Archean–Ordovician faults illustrated in the South Australian Resource Industry Gateway (SARIG); South Australia’s geo resource metadata archive. A series of stereonet diagrams using Stereonet9 software developed by Allmendinger et al. (2012) were produced and highlight Andersonian conjugate relationships used to define the structural sets. These structural sets highlight the structural strain history of the nearby faults and have been used to infer principal stress orientations. Within the St Vincent Basin, the Bridgewater Formation and Hallet Cove Sandstone are sub-horizontal in orientation; thus, we used the original data for analysis, as the bedding and structure within had not been tilted. The Port Willunga Formation grainstone was corrected by unfolding bedding to fold limbs ( $S_0$  30/177 and 08/098). The Heatherdale shale fractures were not corrected because folding of the nearly vertical-dipping beds occurred at greater depths than reached during Cenozoic deformation, likely during the Delamerian Orogeny. Within the Eyre Basin, the Eyre Formation was corrected by unfolding to tilted bedding ( $S_0$  28/118), and the Parabarana Sandstone was corrected by unfolding to one fold limb ( $S_0$  49/095).

### **Innes National Park, Yorke Peninsula**

#### *Observations from the Bridgewater Formation*

Seven cemented disaggregation bands from Marion Bay and Stenhouse Bay, which are assigned to the Bridgewater Formation Set 1 (BF1), form a conjugate relationship, striking E–W and dipping 29° N, and striking NE–SW and dipping 30° SE (Table 1). No indication of offset

was identified; however, their geometric relationship implies some form of shear enhancement due to their conjugate geometry in accordance with the Andersonian Theory of Faulting (Anderson, 1951). Thirteen N–S-striking deformation bands dipping vertically have no observable offset relationships and are assigned to the Bridgewater Formation Set 2a (BF2a; Table 1). Thirty-seven conjugate deformation bands, which strike NW–SE and NE–SW, and dip near vertical 80° towards the SW and 79° towards the NE, respectively (Table 1), are assigned to the Bridgewater Formation Set 2b (BF2b). Kinematic indicators such as plan-view bedding offsets are consistent with strike-slip displacement in BF2b.

Deformation bands are observed forming within folded beds at the Stenhouse Bay Fault, located 1.6 km NE of Stenhouse Bay (Figure 1c, location 1). The fold limbs strike N–S dipping 41° E, and strike E–W dipping 32° N, and the axial plane strikes E–W and dips 64° S (Table 1). Two thrust faults at the approximate location of a fault observed in SARIG are referred to here as the Marion Bay Fault, at the southern edge of Marion Bay (Figure 1c, location 1). The thrust faults strike E–W and dip 24° towards the north, matching the orientation of BF1 (Figure 2c). The Marion Bay Fault and Stenhouse Bay Fault strike NW–SE and are categorised within SARIG as having an Archean–early Mesoproterozoic origin.

#### *Chronological relationship of Bridgewater Formation deformation band sets*

No cross-cutting relationships within the Bridgewater Formation deformation bands were observed; thus their chronological order is based on the parallel structural analysis and interpreted paleostress evolution of the Hallet Cove

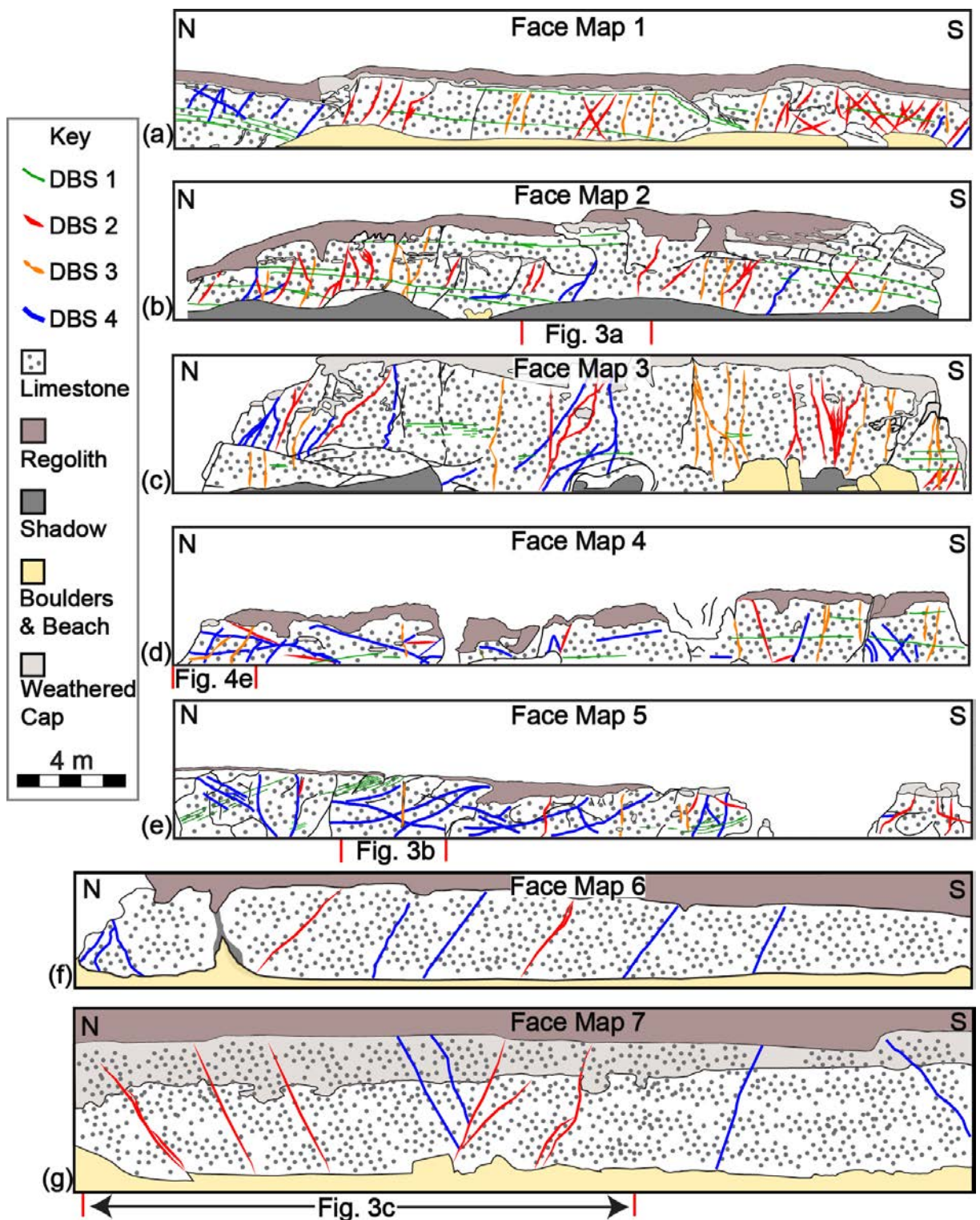


**Figure 4.** Face maps highlighting deformation band structures in the Port Willunga Formation. (a) Face Map 1 oriented north-south (location: Sellicks Beach). (b) Face Map 2 oriented north-south (location: Sellicks Beach). (c) Face Map 3 oriented north-south (location: Sellicks Beach). (d) Face Map 4 oriented north-south (location: Sellicks Beach). (e) Face Map 5 oriented north-south (Location: Sellicks Beach). (f) Face Map 6 oriented north-south (location: Port Willunga). (g) Face Map 7 oriented north-south (location: Port Willunga).

Sandstone.

### Port Vincent, Yorke Peninsula

#### *Observations from the Hallet Cove Sandstone*

Twenty-seven conjugate deformation bands at Port Vincent, which strike ENE–WSW, and dip  $36^\circ$  towards the N and  $36^\circ$  towards the S, are assigned to the Hallet Cove Sandstone Set 1 (HCS1; Table 1). Thirty-five conjugate deformation bands, which strike N–S, and dip  $34^\circ$  towards the E and  $26^\circ$  towards the W, are assigned to the Hallet Cove Sandstone Set 2 (HCS2; Table 1). Kinematic indicators are consistent with reverse-sense displacement for HCS1 and HCS2. All structures are located along the boundary of a N–S-striking Archean–early Mesoproterozoic fault, and approximately 550 m W of a N–S-striking Ordovician fault with an eastward dip (Figure 1c, location 2).

#### *Chronological order of Hallet Cove Sandstone deformation band sets*

The chronological order of HCS1 and HCS2 is based on mutually exclusive cross-cutting relationships. Deformation band set HCS2 cross-cuts HCS1 in multiple locations at Port Vincent. Therefore, HCS1 is interpreted to have formed prior to HCS2 (Table 2).

### Sellicks Beach and Port Willunga, Mount Lofty Ranges

One grid map (Figure 3), and seven face maps (Figure 4) were produced to illustrate the spatial and temporal relationships of deformation within the Willunga Fault footwall from Locality 3 (Figure 1). The steep SE-dipping Willunga Fault juxtaposes the Cambrian Heatherdale Shale next to Quaternary Pooraka Formation at Cactus Canyon (Figure 2b). Neotectonic fault trace structures in the hanging wall indicate reverse-sense displacement (Sandiford, 2003). The Willunga Fault

continues SW from Cactus Canyon towards Sellicks Beach (Figure 5) and 430 m SW, from where the Willunga Fault crops out at the beach, the Port Willunga Formation is juxtaposed to the Heatherdale Shale (Figure 2a).

#### *Observations from the Port Willunga Formation*

Port Willunga Formation Set 0 (PWF0) is bedding-parallel, showing no signs of shear displacement (Figure 4). Twenty-eight deformation bands at Sellicks Beach, which exhibit wavy characteristics with wavelengths of 5–10 mm, are assigned to PWF0. They appear as discrete structures 1–2 mm thick and in clusters spanning up to 15 cm. The Port Willunga Formation exhibits open fold geometry at Sellicks Beach with limbs dipping shallowly (i.e.  $15\text{--}20^\circ$ ) to the S and NW (Figure 6). However, PWF0 is planar and dips shallowly (i.e.  $10^\circ$ ) to the S at Port Willunga with bedding progressively steepened towards the S, dipping up to  $65^\circ$  N at the southern end of Sellicks Beach within 5 m of the Willunga Fault (Figure 2a).

One hundred conjugate deformation bands, which strike from ESE–WNW, and dip  $53^\circ$  towards the N and  $53^\circ$  towards the S, are assigned to the Port Willunga Formation Set 1 (PWF1; Table 1). Kinematic indicators are consistent with normal displacement offsetting PWF1, with up to 4 cm displacement. Slip-surfaces observed at Port Willunga form a mild graben-like structure, conforming to the characteristics that define PWF1 (Figure 3c) is observed in Face Map 7 at Port Willunga (Figure 4g).

Fifty-one conjugate deformation bands, which range from NE–SW dipping  $35^\circ$  towards the SE, and NW–SE and  $35^\circ$  towards the NE, are assigned to the Port Willunga Formation Set 2 (PWF2; Table 1). Kinematic indicators are consistent

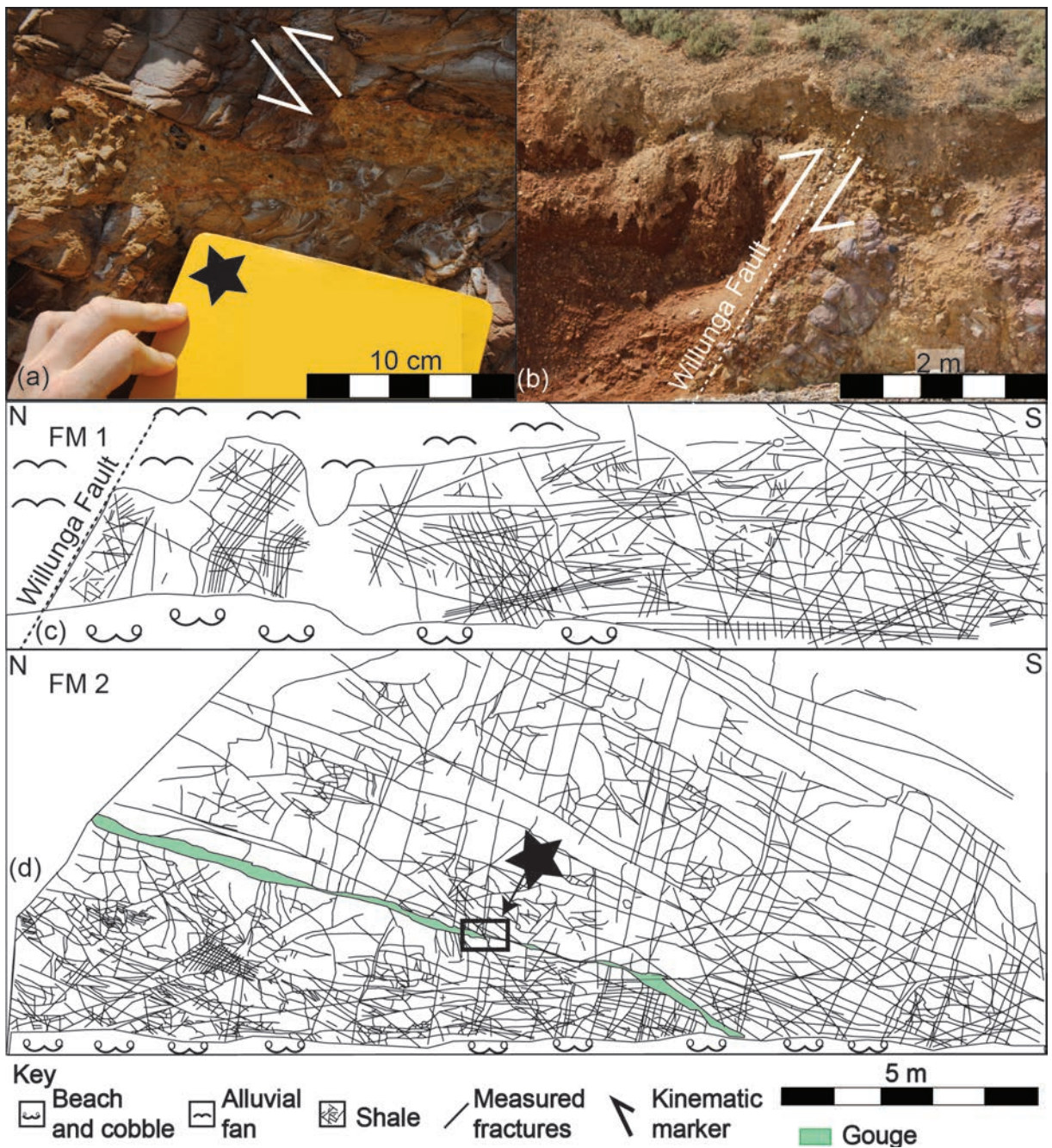


**Figure 5.** Photographs and face maps highlighting the damage zone of the Willunga Fault at Sellicks Beach. **(a)** Reverse fracture cross cutting thrust fault gouge zone. **(b)** Willunga Fault cropping out at Sellicks Beach, highlighting imbricated Heatherdale Shale block. **(c)&(d)** Face maps of fractured sections of the Willunga Fault damage zone within the Heatherdale Shale.

with reverse displacement, offsetting PWF0 with up to 4 cm displacement.

Seventy-one near-vertical deformation bands, which strike from WSW–ENE to N–SE, are assigned to the Port Willunga Formation Set 3 (PWF3; Table 1). These

deformation bands exhibit both planar and wavy geometry with wavelengths of 5–25 mm and form individual structures 2–5 mm thick, as well as anastomosing clusters 4–15 mm wide. There are no observable kinematic indicators defining shear displacement for PWF3 but PWF3

is observed abutting PWF1 and PWF2 (Figure 3a).

Nineteen conjugate deformation bands, which strike from NW–SE to N–S with an average dip of  $33^\circ$  towards the NE and  $40^\circ$  towards the SW, are assigned to the Port Willunga Formation Set 4 (PWF4; Table 1). Individual bands have planar geometry, with thicknesses of 1–2 mm whereas clusters of deformation bands have widths of up to 11 cm (Figure 4). Kinematic indicators are consistent with reverse-sense displacement of up to 10 cm (Figure 3).

#### *Chronological order of Port Willunga Formation deformation band sets*

The chronological order of development for individual deformation band sets was determined through observation of cross-cutting relationships. PWF4 cross-cuts all other sets, indicating that it is the youngest (Table 2). PWF3 is not observed to be cross-cut by PWF0–2, but PWF3 abuts PWF1 and PWF2, indicating PWF3 is younger than PWF1 and PWF2 (Figure 3a). All deformation band sets except PWF3 cross cut PWF0, indicating PWF0 is the oldest deformation band set. PWF1 formed under a normal fault stress regime and must have formed prior to PWF2, which formed under a reverse fault stress regime (Table 2).

#### *Observations made from the Heatherdale Shale*

The Heatherdale Shale crops out in steep cliffs south of the Willunga Fault at Sellicks Beach, where Fracture Maps 1 and 2 are located (Figure 5). Fracture Maps 1 and 2 contain 440 fractures, which based on the correspondence with a contemporary principal stress analysis of Cenozoic deformation bands in the adjacent Port Willunga Formation, 397 of these are associated with the Cenozoic evolution of the Willunga Fault. Detailed

structural analysis has highlighted four individual conjugate fracture sets (Table 1).

One hundred and twenty-three fractures at Sellicks Beach is a conjugate set, which strikes NW–SE, and dips  $\approx 69^\circ$  E and  $\approx 64^\circ$  SW, that are assigned to the Heatherdale Shale Set 1 (HS1; Table 1). HS1 was not observed to exhibit shear offset and due to lack of observed definitive relationships we have not defined the fracture mode for Fracture Set 1 but it must be either Mode II or Mode III as they form a conjugate set, eliminating Mode I as a possibility.

Forty-six fractures, which strikes E–W, and dips  $\approx 16^\circ$  N and  $\approx 34^\circ$  S, are assigned to the Heatherdale Shale Set 2 (HS2; Table 1). No shear offsets were observed for Fracture Sets 3 and as no definitive relationships were observed, we have not defined a fracture mode for Fracture Set 3; however, as they form a conjugate set this set is either opening Mode II or Mode III, eliminating Mode I as a possibility.

One hundred and forty-three conjugate fractures, which strike N–S and NE–SW, and dip  $\approx 24^\circ$  W and  $\approx 42^\circ$  SE, are assigned to the Heatherdale Shale Set 3 (HS3; Table 1). This set exhibits a series of kinematic markers, indicating reverse-sense displacement with up to 10.0 cm throw. A SE-dipping thrust fault distinguished by its orange (i.e. iron-oxide stain) weathered surface stands out against the pale pinkish-yellow outcrop of Heatherdale Shale (Figure 5a). This thrust fault zone ranges in thickness from 1–15 cm and is infilled with fault gouge (Figure 5d) and strikes NE–SW and dips a moderate  $50^\circ$  towards the SE, similar to HS3, and is temporally related to HS3. We suggest HS3 fractures may represent opening Mode II, based on the observed offsetting shear displacement, where

slip occurs parallel to the fracture plane creating small steps on the rock face. (Figure 5a).

Eighty-five fractures are a conjugate set, which strike NW–SE, and dip  $\approx 28^\circ$  NE and  $\approx 24^\circ$  SW, are assigned to the Heatherdale Shale Set 4 (HS4; Table 1). These fractures exhibit reverse displacement kinematic indicators with an upper limit total displacement of 2.5 cm (Figure 5c, d). We suggest HS4 fractures may represent opening Mode II, based on the observed offsetting shear relationships, where slip occurs parallel to the fracture plane creating small steps on the rock face. (Figure 5d).

#### *Chronological order of Heatherdale Shale fracture sets*

The chronological order of the individual conjugate fracture sets (Table 2) was determined through observed cross-cutting relationships and known sequential orientations of  $\sigma_H$  associated with PWF 1–4 hosted within the footwall of the Willunga Fault (Figure 5). HS1 does not cross cut any other fracture set; therefore, it must be older than HS 2–4. HS2  $\sigma_H$  aligns E-W parallel to the PWF1, indicating HS2 is younger than HS1, but older than HS3 (Figure 6). HS4 cross cuts HS3, indicating that HS4 must be younger.

#### **Dead Tree section, northern Flinders Ranges**

##### *Observations from the Eyre Formation*

Thirty-one conjugate deformation bands at the Dead Tree section, which strike E–W, and dip  $49^\circ$  towards the N and  $56^\circ$  towards the S, are assigned to the Eyre Formation Set 1 (EF1; Table 1). A 1.4 m dextrally offset slip-surfaces with similar strike and dip to EF1 was observed. Twenty-six conjugate deformation bands, which strike NW–SE and NE–SW, and dip  $40^\circ$  towards the NE and  $51^\circ$  towards the SE, are assigned to the Eyre Forma-

tion Set 2a (EF2a; Table 1). Seventy-four conjugate deformation bands, which strike NW–SE and NNE–SSW, and dip near vertical, are assigned to the Eyre Formation Set 2b (EF2b; Table 1). Thirty-four conjugate deformation bands, which strike NE–SW and NNW–SSE, and dip  $17^\circ$  towards the NW and  $45^\circ$  towards the E, are assigned to the Eyre Formation Set 3 (EF3; Table 1). Ninety-two conjugate deformation bands, which strike NW–SE and N–S, and dip  $42^\circ$  towards the SW and  $27^\circ$  towards the E, are assigned to the Eyre Formation Set 4a (EF4a; Table 1). Twenty-nine conjugate deformation bands that strike NW–SE and NE–SW and dip near vertical are assigned to the Eyre Formation Set 4b (EF4b; Table 1). Kinematic indicators for EF2a, EF3 and EF4a are consistent with reverse-sense displacement, whereas kinematic indicators for EF2b and EF4b are consistent with strike-slip sense displacement and EF1 with normal-sense displacement.

#### *Chronological order of Eyre Formation deformation band sets*

The chronological order of the individual Eyre Formation conjugate deformation band sets is shown in Table 2 and was determined through observed cross-cutting relationships. EF1, which is cross-cut by EF2b and EF4b (Table 2), is the only deformation band set that does not cross-cut any other deformation band sets, indicating it is the oldest deformation band set. EF2b is observed to be cross-cut by EF3 and EF4a, indicating that it is older than EF3 and EF4 (Table 2). EF4a cross-cuts EFS3, indicating EF3 is older (Table 2).

#### **Parabarana Hill, northern Flinders Ranges**

##### *Observations from the Parabarana Sandstone*

Twenty-four conjugate deformation bands

at Parabarana Hill, which strike E–W, and dip 69° towards the S and 45° towards the N, are assigned to the Parabarana Sandstone Set 1 (PS1; Table 1). No kinematic indicators were observed for PS1; however, their geometric relationship is consistent with a normal fault stress regime (Figure 6). Thirty-six conjugate deformation bands, which strike NNE–SSW and dip 17° towards the NW and 55° towards the SE, are assigned to the Parabarana Sandstone Set 2 (PS2; Table 1). Kinematic indicators are consistent with reverse-sense displacement. Nine conjugate deformation bands, which strike NW–SE and NE–SW, and dip 30° towards the SE and 46° towards the SW, are assigned to the Parabarana Sandstone Set 3a (PS3a; Table 1). Kinematic indicators are consistent with reverse-sense displacement. Twenty-four conjugate deformation bands, which strike NE–SW and E–W, dipping near vertical, are assigned to the Parabarana Sandstone Set 3b (PS3b; Table 1). Kinematic indicators were not observed in outcrop, but their geometric relationship is consistent with a strike-slip fault stress regime (Figure 6). However, it should be noted that the mapped outcrop was a vertical section of rock, an unsuitable rock-face orientation to view strike-slip displacement.

#### *Chronological order of Parabarana Sandstone deformation band sets*

The chronological order of the individual conjugate deformation band sets shown in Table 2 was determined through observed cross-cutting relationships. PS3b is observed to cross cut PS3a, indicating that PS3b is younger than PS3a (Table 2). PS3a cross cuts PS2, indicating that PS3a is younger than PS2 (Table 2). No cross-cutting features define PS1, indicating PS1 must be the oldest set.

### **Paleostress evolution of the St Vincent and Lake Eyre basins**

The regional structural synthesis demonstrates the intricate relationship of paleostress and deformed sedimentary packages adjacent to the Mount Lofty Ranges and Flinders Ranges. The interplay between Cenozoic intraplate tectonic reactivation of range-bounding faults (e.g. Willunga Fault and Paralana Fault) and the structural evolution of deformed juxtaposed sediments along with a new Cenozoic paleostress evolution model of the Mount Lofty Ranges and Flinders Ranges (Figure 6) is presented. This model supports the notion of late Miocene onset of compression, including late Miocene–Pliocene basin inversion, followed by a rotation of  $\sigma_H$  from NW–SE to E–W.

#### **Tectonic Stage 1**

Sellicks Beach, where the reactivated Willunga Fault juxtaposes Quaternary alluvial fans to Oligocene–Miocene carbonate grainstone and Cambrian shale is a key locality for this study. When identifying Cenozoic fractures in the Cambrian-age Heatherdale Shale, we must consider the presence of pre-existing fractures. The fracture density in the Heatherdale Shale increases towards the Willunga Fault (Figure 7) resulting from late Miocene–Quaternary tectonic activity (Holford et al., 2011a; Sandiford, 2003; Tokarev, 2005; Tokarev et al., 1999). Most (397 of 440) fractures measured in this area are likely to be associated with the Cenozoic activity of the Willunga Fault (Figure 6); the remaining 43 fractures (10%) have unknown origin but are interpreted to be unrelated to Cenozoic movement of the Willunga Fault.

In the Bridgewater Formation, based on similar NNW–SSE  $\sigma_H$  with HSC1, BF1 is inferred to form first, implying BF2a and BF2b formed next and are interpreted to have similar E–W  $\sigma_H$  with HSC2.

One hundred and twenty-three fractures that make up HS1 at Sellicks Beach are interpreted as Stage 1 in our paleostress model, forming under NE–SW extension (Figure 6) with the  $\sigma_h$  (minimum horizontal stress) orientation of HS1 (i.e. NE–SW) matching the orientation of Tasman Sea ocean-spreading ridge transform faults that strike NE–SW (Gaina *et al.*, 1998). Therefore, Stage 1 is defined as having a Late Cretaceous–early Eocene faulting genesis and is likely associated with the opening of the Tasman Sea from the Late Cretaceous to mid-Eocene

(Figure 6).

**Tectonic Stage 2**

Stage 2, which comprises 122 deformation bands observed in both the St Vincent and Lake Eyre basins, have an interpreted E–W  $\sigma_h$  orientation for PWF1, EF1, and PS1 and are associated with N–S extension in the St Vincent and Lake Eyre basins (Figure 6). Temporal and spatial relationships observed within the Port Willunga Formation, Eyre Formation, and Parabarana Sandstone formations suggest that PWF1, EF1, and

Formation name	Paleostress model	Extension		Compression		
		Stage 1	Stage 2	Stage 3	Stage 4	Stage 5
	Paleostress $\sigma_H$	Northwest–Southeast	East–West	North–South	Northwest–Southeast	East–West
Epoch		Early Paleocene–early Eocene	Middle Eocene–middle Miocene	Late Miocene–early Pleistocene	middle Pliocene–late Pleistocene	Late Pleistocene–Present-day
Bridgewater Formation Pleistocene						
Hallet Cove Sandstone Pliocene						
Port Willunga Formation Oligocene–late Miocene						
Eyre Formation Eocene						
Parabarana Sandstone Cretaceous						
Heatherdale Shale Cambrian						

**Figure 6.** Structural evolution model of the Mount Lofty Ranges and Flinders Ranges, highlighting the palaeostress evolution of juxtaposed sedimentary rocks within the St. Vincent Basin and Lake Eyre Basin. Black arrows represent the maximum horizontal stress.

**Table 2.** *Younging tables of deformation band sets.*

<b>Unit</b>	<b>Location of observations</b>				
Hallet Cove Sandstone	Deformation band cross-cutting relationships in cliff faces north of Port Vincent	HCS2	HCS1		
HCS2					
HCS1		λ			
Port Willunga Formation	Deformation band crosscutting relationships in cliff faces at Sellicks Beach and Port Willunga	PWF4	PWF3	PWF2	PWF1
PWF4					
PWF3		λ			
PWF2		λ			
PWF1		λ		λ	
Eyre Formation	Deformation band cross-cutting relationships in creek banks at the Dead Tree section	EF4b	EF3	EF2b	EF1
EF4b					
EF4a					
EF3		λ			
EF2b		λ	λ		
EF2a					
EF1		λ		λ	
Parabarana Sandstone	Deformation band cross-cutting relationships in cliff faces at Parabarana Hill	PS3a	PS2	PS1	
PS3a					
PS3b		λ			
PS2		λ			
PS1					
Heatherdale Shale	Deformation band cross-cutting relationships in cliff faces at Sellicks Beach	HS4	HS3	HS2	HS1
HS4					
HS3		λ			
HS2					
HS1					

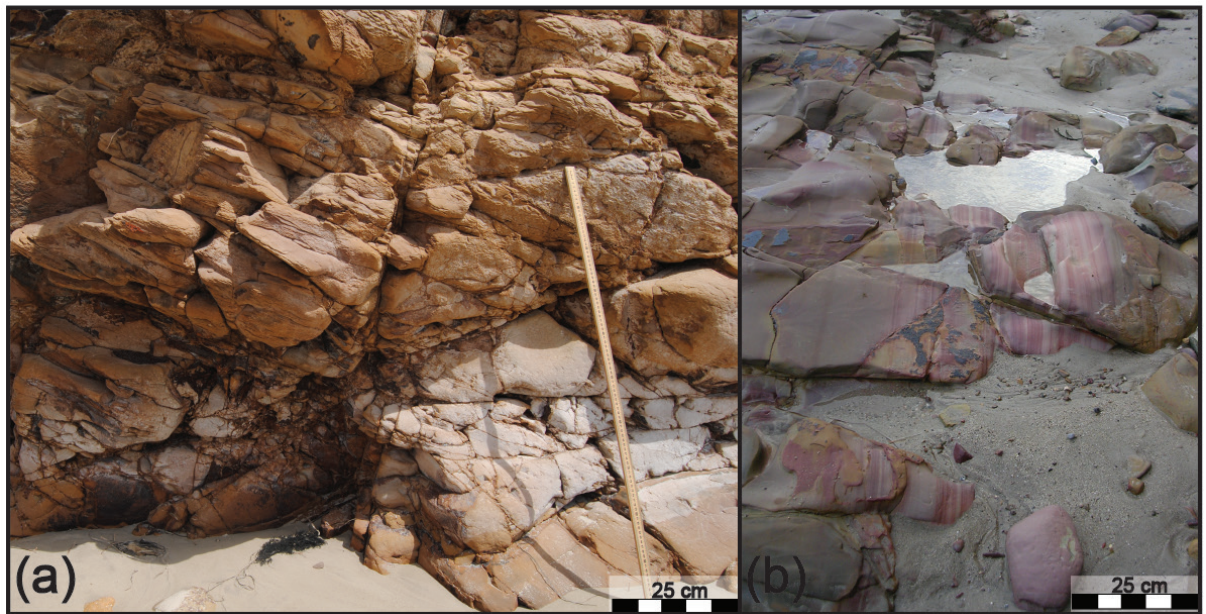


**Figure 7.** Photographs of the Willunga Fault damage zone Heatherdale Shale **(a)** located 10 m SE of the Willunga Fault the fault and; **(b)** located 50 m SE of the Willunga Fault.

PS1 were the first conjugate deformation band sets to form in each formation, respectively. Their similar stress field state and principal stress orientations supports the notion that they formed concurrently. Stage 2 of our paleostress model includes deformation in the Port Willunga Formation, Eyre Formation, and Parabarana Sandstone and implies that the oldest possible paleostress age is Late Cretaceous (Parabarana Sandstone), and the youngest possible age is late Miocene (Port Willunga Formation). Stage 2  $\sigma_h$  (i.e. N–S) matches with N–S-striking transform faults in the Southern Ocean spreading system; thus, Stage 2 is likely associated with crustal and lithospheric thinning related to the final separation of Antarctica and Australia during the mid-Eocene (Norvick and Smith, 2001). However, N–S extension must have continued until at least the late Miocene in order to deform the upper Miocene sedimentary rocks of the Port Willunga Formation at Sellicks Beach. N–S-dipping deformation bands observed within the Port Willunga Formation, Eyre Formation, and Parabarana Sandstone conform to

crustal extension-related Andersonian faulting (Figure 6).

### Tectonic Stage 3

Stage 3, which is composed of 219 deformation bands observed in both St Vincent and Lake Eyre basins, have an interpreted N–S  $\sigma_h$  for PWF2, EF2a, EF2b, and HS2, associated with N–S compression (Figure 6). EF2a is interpreted to have formed in a reverse fault stress regime whereas EF2b formed in a strike-slip fault stress regime (Figure 6); both deformation band sets likely formed at the same time based on similar N–S  $\sigma_h$  orientations and consecutive temporal relationships, as a result of reactivation of multiple Pararana Fault splays near the Dead Tree section during Stage 2 (i.e. NNW–SSE-striking fault splay and WSW–ESE-striking fault splay; Figure 1a).

The transition from N–S extension to N–S compression in the paleostress model resulted in the reactivation of the Willunga and Pararana faults and the onset of inversion of the St Vincent and

Lake Eyre basins associated with Stage 2 (Figure 6). The onset of inversion was likely due to tectonic changes at the most proximal plate boundary, specifically the formation of the Southern Alps in New Zealand between *ca* 12 and 6.4 Ma (Holford et al., 2011a; Sandiford et al., 2004). Temporal and spatial relationships observed within the Port Willunga Formation, Eyre Formation and Heatherdale Shale formations suggest that HS2, PWF2, EF2a, and EF2b were the second conjugate deformation band sets to form in each formation. respectively, supporting the notion that they formed concurrently. The age of these formations implies that the oldest possible paleostress age is younger than the youngest sedimentary rock, the Port Willunga Formation at Sellicks Beach so the oldest possible age for Stage 3 is late Miocene.

#### **Tectonic Stage 4**

Stage 4, which is composed of 289 deformation bands observed in both St Vincent and Lake Eyre basins, has similar interpreted stress states with NNW–SSE  $\sigma_H$  for HS3, PWF3, HCS1, and BF1 in the St Vincent Basin, with a slightly rotated orientation of WNW–ESE  $\sigma_H$  for EF3, and PS2 in the northern Flinders Ranges (Figure 6). Thus, Stage 4 is associated with NW–SE compression in the St Vincent and Lake Eyre basins (Figure 6). This grouping allows for some spatial variance in the principal stress orientations. Temporal and spatial relationships observed within the Heatherdale Shale, Parabarana Sandstone, Eyre Formation, Port Willunga Formation, Hallet Cove Sandstone, and Bridgewater Formation suggests that HS3, PS2, EF3, PWF3, HCS1, and BF1 were the second last deformation band sets to form in their respective formations, supporting concurrent formation. The age of these formations implies that the youngest possible paleostress age is late Pleisto-

cene (Bridgewater Formation) and the temporal evolution of Stage 4 spans the Pliocene–late Pleistocene (Figure 6).

Based on their near vertical dip and lack of shear offset PWF3 deformation bands could be interpreted as pure compaction bands but they are similar to discrete wavy structures only identifiable as pure compaction bands based on their lack of shear-offset, discussed by Fossen et al. (2011) in the Navajo Sandstone, Utah. The strike for PWF3 ranges from NE–SW to N–S (Figure 6) and offsets were not observed in cross-section view so we interpret PWF3 as shear-enhanced compaction bands that formed under a strike-slip fault stress regime, where  $\sigma_H$  is oriented NW–SE.

In the Port Willunga Formation, PWF0 – the oldest structures at Sellicks Beach – formed as a result early burial and diagenesis *sensu* Tondi et al. (2006). These bedding-parallel deformation bands exhibit an open fold structure with an axial plane that strikes NE–SW, inferring a NW–SE  $\sigma_H$  principal stress orientation (Figure 6). The Parabarana Sandstone and Bridgewater Formation also exhibit similar folds with NE–SW axial planes implying a NW–SE  $\sigma_H$  (Figure 6), which conforms to the principle stress orientation of Stage 4. Folded Pleistocene gravels of the Pooraka Formation in the nearby Sellicks region (Jayawardena (2013) were estimated to be no older than 125 Ka. Therefore, we infer the Pooraka Formation, Bridgewater Formation, Port Willunga Formation and Parabarana Sandstone folded concurrently during the late Pleistocene.

#### **Tectonic Stage 5**

Stage 5, which is composed of 381 deformation bands observed in both St Vincent and Lake Eyre basins, has an interpreted orientation of  $\sigma_H$  for HS4, PS3, EF4, PWF4, HCS2, and BF2 of between

ENE–WSW and E–W; thus, we associate these deformation band sets with Stage 5 ENE–WSW compression (Figure 6). Temporal and spatial relationships observed within the Heatherdale Shale, Parabarana Sandstone, Eyre Formation, Port Willunga Formation, Hallet Cove Sandstone, and Bridgewater Formation infers that HS4, PS3, EF4, PWF4, HCS2, and BF2 were the last set of structures to form in the St Vincent and Lake Eyre basins. We suggest they formed concurrently based on their similar geometry and orientation. The Bridgewater Formation is the youngest formation in this series of sediments (i.e. late Pleistocene), and infers the oldest possible age of Stage 5 is late Pleistocene. Therefore, the temporal evolution of Stage 5 spans the late Pleistocene (post 125 Ka) to the present-day and was subject to E–W compression (Hillis and Reynolds, 2003).

The transition from NW–SE compression to NE–SW compression (Paralana Fault), and E–W compression (St Vincent Basin) resulted in the formation of multiple deformation band sets with similar  $\sigma_H$  orientations at similar points in time. BF2a are purely compaction bands indicated by their lack of shear offset, and BF2b are shear-enhanced compaction bands based on their observable shear offsets and geometric relationship to strike-slip fault displacement. These deformation band sets formed concurrently under E–W compression. EF4a and PS3a conform to the geometric relationship of reverse fault stress regime, and EF4b and PS3b conform to the geometric relationship of a strike-slip fault stress regime. The temporal distribution of EF4 and PS3 indicates they may have formed consecutively. However, EF4a, EF4b PS3a, and PS3b all formed under the same ENE–WSW  $\sigma_H$ , indicating concurrent formation that was likely caused by the interaction of the NE–SW-striking Paralana Fault and neighbouring E–W-striking faults with

their failure resulting in strike-slip and reverse fault stress regimes under the same principal stress orientation (Figure 1b).

A synthesis of the evolution of paleostress inferred to have occurred in the St Vincent and Lake Frome basin regions is as follows:

- Stage 1: NE–SW extension (normal faulting)
- Stage 2: N–S extension (normal faulting)
- Stage 3: N–S compression (reverse faulting and strike-slip faulting)
- Stage 4: NW–SE compression (reverse faulting and folding)
- Stage 5: E–W compression (reverse faulting and strike-slip faulting)

## Discussion

The paleostress relationships between the deformation bands hosted within siliciclastic- and carbonate rocks of the St Vincent Basin and Frome Embayment are used to identify the Cenozoic structural evolution adjacent to the bounding faults of the Mount Lofty and Flinders ranges.

### Mount Lofty Ranges and Flinders Ranges paleostress model

The Cenozoic evolution of range-bounding faults juxtaposing the St Vincent Basin and Frome Embayment with the Mount Lofty Ranges and Flinders Ranges, respectively, has resulted in a coevolution of fault-induced deformation bands and fractures with a similar paleostress model for the Mount Lofty Ranges-bounding St Vincent Basin sediments and the Flinders Ranges-bounding Frome Embayment sediments (Figure 6). Structural analysis of these combined

datasets has resulted in one unified paleostress evolution pattern, stretching across South Australia's Mount Lofty Ranges and Flinders Ranges and illustrates the progressive development of Cenozoic structures (i.e. deformation bands and fractures) into five periods of recent tectonic deformation defined by a unique pattern of stress orientations and magnitudes (Figure 6):

- Stage 1 (early Paleocene–early Eocene): NW–SE extension
- Stage 2 (middle Eocene–middle Miocene): N–S extension
- Stage 3 (Late Miocene–early Pliocene): N–S compression
- Stage 4 (middle Pliocene–late Pleistocene): NW–SE compression
- Stage 5 (late Pleistocene–Present-day): E–W compression

*Stage 1: early Paleocene–early Eocene (NW–SE extension)*

Throughout the Late Cretaceous to Eocene, a dynamic Australian Plate stress state was associated with the breakup of Gondwana and the evolution of a spreading ridge along the SE plate boundary (Gaina *et al.*, 1998). Tectonic reconfiguration at 95 Ma initiated slow rifting between Australia and East Antarctica, with the opening of the Tasman Sea between 82 and 52 Ma (Gaina *et al.*, 1998). Reconstructions of the Tasman Sea opening by Gaina *et al.* (1998) illustrate the spreading ridge was dominated by NE–SW transform faults, with  $\sigma_h$  oriented NE–SW (i.e. direction of maximum extension), and demonstrates the Late Cretaceous–early Eocene was dominated by NE–SW extension, matching the Stage 1  $\sigma_h$  orientation recorded in the Heatherdale Shale (Figure 6). Additionally, reconstructed Southern Ocean seafloor spreading ridges modelled by Scheibner

(1999) infer that the spreading ridge was located approximately 200 km from the St Vincent Basin, which may indicate that these events are temporally and spatially similar, implying Stage 1 of our model depicts a state of intraplate rifting associated with the opening of the Tasman Sea facilitated opening of the St Vincent Basin. The oldest Southern Ocean isochron (middle Eocene) is situated 350 km S of the St Vincent Basin, adjacent to the youngest Tasman Sea floor spreading ridge isochron (early Paleocene–early Eocene; (Scheibner, 1999), further constraining the temporal evolution of Stage 1.

*Stage 2: middle Eocene–middle Miocene (N–S extension)*

The final stage of rifting between Antarctica and Australia occurred during the middle-Eocene, resulting in N–S extension (Norvick and Smith, 2001). North–south extension facilitated the opening of the St Vincent Basin by segmentation and subsidence and resulted in the formation of the NW-dipping Willunga Fault during the middle Eocene. Down-to-basin block movements towards the NW along the Willunga Fault enabled marine transgression and sedimentation within the St Vincent Basin (Tokarev, 2005).

The Parabarana Sandstone, Eyre Formation and Port Willunga Formation are the only stratigraphic units in this study that exhibit direct evidence of Stage 2 N–S extension. The Port Willunga Formation is the youngest of the three formations based on foraminiferal ages, with deposition determined to be early Miocene at Sellicks Beach (Drexel and Preiss, 1995). Therefore, the age of Stage 2 extended into at least the early Miocene (likely extending further into the middle Miocene) in order to deform the Port Willunga Formation and produce N–S extension structures (Figure 6). North–south-strik-

ing transform faults associated with the Southern Ocean Spreading Ridge modelled by Scheibner (1999) align parallel with  $\sigma_h$  interpreted in this study for Stage 2 implying these events are contemporaneous.

Holford et al. (2011a) suggest that a middle Eocene unconformity and inversion structures in the Gippsland Basin marks the initial transition from Cenozoic extension to compression. However, our models indicate that extension dominated the tectonic regime of the Mount Lofty Ranges and Flinders Ranges until the middle Miocene (Figure 6) and implies southeastern Australia was subject to a dynamic paleostress field, where the SE Australian continental margin (i.e. Gippsland Basin) was undergoing crustal shortening, while the intraplate state of South Australian was simultaneous undergoing crustal extension. The long-lived, deep-seated nature of the faults hosted within the Flinders and Mount Lofty Ranges provides relatively high-magnitude strain accommodation in response to far-field intraplate stresses, which may allow for the observed differential onset of Cenozoic compression.

### *Stage 3: late Miocene–early Pliocene (N–S compression)*

The late Miocene marked the transition from cool-water carbonate sedimentation to siliciclastic-rich sedimentation within the Port Willunga Formation at Sellicks Beach (Sandiford et al., 2004). Crustal segmentation and subsidence continued to produce new accommodation space until the late Miocene, when the St Vincent Basin experienced a shift in the stress regime from extension to compression and is marked by the transition of sedimentary depositional sequences from shallow detrital carbonates to siliciclastic reefs (Tokarev, 2005). Changes at the Indo-Australian Plate margin re-

sulted in intraplate strain accommodation that caused periods of enhanced basin-wide deformation. Such step changes (magnitudes and/or orientations) in the intraplate stress regime were also observed for the Otway Basin (e.g. Holford et al., 2014). This deformation pulse is recorded in the St Vincent Basin sequence by an angular unconformity separating the Oligocene–Miocene Port Willunga Formation from the Pliocene Hallett Cove Sandstone with ~100 m of uplift observed along the Willunga Fault (Sandiford et al., 2004).

The shift in stress regime resulted in epeirogenic tectonic movements (i.e. multiple episodes of upward and downward crustal block movements), reverse faulting, and accompanied uplift and erosion at Sellicks Beach (Tokarev, 2005). Both reverse and normal kinematic indicators observed in PWF2 indicate that the deformation bands formed by both N–S extension and N–S compression, implying a dynamic stress field (Figure 6). The late Miocene tectonic shift seems likely to have induced both N–S extensional and N–S compressional shear-enhanced compaction bands as a result of the epeirogenic tectonic movements described by Tokarev (2005), which suggests this period was dominated by alternating episode of downward and upward crustal movement caused by instability of the stress state during the transition from crustal thinning to crustal shortening. This type of tilting may have enhanced coastal inundation and erosion (Tokarev, 2005), later described by Sandiford (2007). Our paleostress analysis indicates normal kinematic indicators observed in PWF1 and EF1 due to a normal fault stress regime with  $\sigma_h$  oriented N–S, whereas reverse kinematic indicators observed in PWF2 and EF2 imply compression with  $\sigma_h$  oriented N–S (Figure 6). Therefore, our paleostress model supports the epeirogenic tectonic

movements described by Tokarev (2005), as the St Vincent and Lake Eyre basins transitioned from subsidence to inversion in the late Miocene. Inversion lasted through to the early Pliocene, marked by unconformities observed in all depocentres east of the St Vincent Basin (Holford et al., 2011a).

*Stage 4: middle Pliocene–late Pleistocene (NW–SE compression)*

Stage 4 of the paleostress model commenced in the middle Pliocene following the late Miocene pulse of compression, as a direct result of inversion of the St Vincent Basin and Frome Embayment along the range-bounding Paralana and Willunga faults (Figure 1). Similar to Otway Basin inversion, step changes in the St Vincent Basin and Frome Embayment reveal sudden changes in the stress regime (Figure 6) that are likely the result of basin sediment unloading, which reduced the vertical stress magnitude. Thus, basin inversion was responsible for reorganisation of the principal stress orientations, causing a rotation of  $\sigma_H$  as the stress regime transitioned from NW–SE  $\sigma_H$  to E–W  $\sigma_H$  along the Paralana Fault in the northern Flinders Ranges and E–W in the Mount Lofty Ranges (Figure 6). Results from the late Pleistocene Bridgewater Formation indicates the stress regime evolved from NW–SE compression (BF1) to E–W compression (BF2) (Figure 6). Therefore, in order to deform the Bridgewater Formation, NW–SE compression must have existed until at least the late Pleistocene and the rotation of  $\sigma_H$  from NW–SE to E–W must have been complete by the late Pleistocene.

Rotation of  $\sigma_H$  resulted from sedimentary unloading facilitated by major regional faults like the Willunga Fault and Paralana Fault (Figure 1). This rotation is the result of a shuffle and reorganisation of the principal stress magnitudes and

orientations (decreasing vertical stress) subsequent to the late Miocene uplift. Thus, the rotation of  $\sigma_H$  from NW–SE to E–W is supported by interpretations of structures observed within both Willunga Fault and Paralana Fault systems (e.g. HS3–4, PS 2–3, EF 3–4, PWF 3–4, HCS1–2, and BF1–2). These deformation band sets correlate with the paleostress rotation through approximately parallel  $\sigma_H$  orientations (Figure 6).

Folds observed in this study within the Parabarana, Port Willunga, and Bridgewater formations imply that  $\sigma_H$  was oriented NW–SE at the time each formation was folding (Figure 6). These results match the findings of Jayawardena (2013), who observed an open fold (fold axis oriented NW–SE) within the late Pleistocene Pooraka Formation – a poorly consolidated alluvial fan – near Sellicks Beach with a principal stress orientation ( $\sigma_H$  NW–SE) that matches  $\sigma_H$  of Stage 4, so is inferred as contemporaneous (Figure 6). The Pooraka Formation is the youngest folded sediment in the Mount Lofty and Flinders ranges, implying the folding event must have occurred post deposition of the Pooraka Formation (i.e. 125 ka). Jayawardena (2013) estimated the folding event to have occurred at the earliest *ca* 118 ka that would constrain the end of Stage 4 to the late Pleistocene.

*Stage 5: late Pleistocene–Present-day compression*

Thick Quaternary-aged alluvial fan sediments unconformably overlie the Port Willunga Formation, indicating a relatively rapid development of hinterland relief, thus substantial erosion must have occurred during uplift in the Quaternary along rivers and streams (Tokarev, 2005). The increase in potential energy is contemporaneous with uplift of the western Mount Lofty Ranges (Tokarev, 2005). The

late Pleistocene  $\sigma_H$  shift to E–W in the St Vincent Basin produced a series of disconnected reverse fault splays (Tokarev, 2005), which are well exposed in Cactus Canyon (Figure 2b) and some 950 m SW at the beach in Fracture Map 5a (Jayawardena, 2013; Sandiford, 2003; Tokarev, 2005). It is well accepted that the study area is currently undergoing E–W compression (e.g. Hillis et al., 2008), implying Stage 5 of our model commenced at the late Pleistocene and continues as E–W  $\sigma_H$  crustal shortening.

### Comparison with a computer-based paleostress model

The Mount Lofty Ranges and Flinders Ranges paleostress model presented here is compared with paleostress models of Müller *et al.* (2012), which used Matlab software to calculate the slip tendency of 8326 fault planes from the Australian continent, temporally comparing the likelihood of reactivation and inversion of steeply dipping faults to the stress state of the continent. A summary of their model interpretation of the paleostress history of the Mount Lofty Ranges and Flinders Ranges is summarised in Table 3. With any geological computer model, heterogeneity of rock composition and non-documented structure may significantly influence the outcome. These models also depend heavily on fault slip-tendencies of known faults ignoring the unsurmountable number of unknown faults within the Australian continent, many of which lie beneath cover sequences. Müller *et al.* (2012) uses the growth of inversion structures (i.e. folds) interpreted from seismic profiles to support their models. This evidence may support timing of compression for that region. However, this evidence offers no link to the stress state or principal stress orientation at the time of deformation and lack strong structural evidence such as physical bedding measurements.

There are similarities between our models (Table 3). Müller *et al.* (2012) noted substantial uncertainty for their Cretaceous model, relatively low magnitude  $\sigma_H$  for the Late Cretaceous–Eocene model, and suggested a period of quiescence during the early–middle Miocene. Our structural analysis and paleostress model demonstrate NE–SW extension was dominant from the early Paleocene to the early Eocene (Figure 6) and we suggest that the low  $\sigma_H$  magnitude and periods of quiescence indicated by Müller *et al.* (2012) may be interpreted as crustal thinning during the Late Cretaceous to Late Miocene. Furthermore, Müller *et al.* (2012) did not model crustal thinning for the Mount Lofty or Flinders Ranges, which is not plausible, considering the St Vincent Basin is a rift basin with subsidence in the Paleogene inferred from the oldest unit in the basin – Cape Jervis Formation (Alley and Lindsay, 1995).

Our results indicate that the middle Eocene to middle Miocene is dominated by N–S extension whereas Müller *et al.* (2012) suggests the Eocene is dominated by E–W compression evolving in the Miocene to NW–SE compression (Table 3). Interestingly, our Eocene models match E–W  $\sigma_H$  orientations predicted by Müller *et al.* (2012) but the tectonic stress state is contrary (Table 3). We observe evidence of early E–W compression structures in the Eocene Eyre Formation or Cretaceous Parabarana Sandstone that support the Eocene or Miocene models by Müller *et al.* (2012) (Figure 6). In addition, periods of quiescence presumably reflect short-lived attainment of an equilibrium stress state, and thus, small changes in the stress state could cause both extension and compression and might explain epeirogenic block movements described by Tokarev (2005) or the transition between Stage 2 and 3 as described in this study.

**Table 3.** Comparison chart of Cenozoic paleostress models for the Mount Lofty Ranges and Flinders Ranges. Green coloured text indicates similarities between the models and red colour text indicates conflicting models.

Time period	Muller <i>et al.</i> (2012)	Lubiniecki <i>et al.</i> (2019)	Stage
Late Pleistocene	Flinders $\sigma_H$ : E–W Lofty: $\sigma_H$ : NW–SE Regime: Compression	Flinders $\sigma_H$ : E–W Lofty $\sigma_H$ : E–W Regime: compression	5
Pliocene–late Pleistocene	Clockwise rotation $\sigma_H$ to E–W	Flinders $\sigma_H$ : ENE–WSW Lofty: $\sigma_H$ : NW–SE Regime: compression Clockwise rotation $\sigma_H$ to E–W	4
Late Miocene	Flinders $\sigma_H$ : NE–SW Lofty: $\sigma_H$ : N–S Regime: compression	Flinders $\sigma_H$ : N–S Lofty $\sigma_H$ : N–S Regime: compression	3
Early–middle Miocene	$\sigma_H$ : NW–SE Regime: compression	$\sigma_H$ : E–W Regime: NS extension	2
Eocene	$\sigma_H$ : E–W Regime: compression Low magnitudes stress	$\sigma_H$ : E–W Regime: NS extension	2
Late Cretaceous	$\sigma_H$ : N–S Regime: compression Substantially uncertain	$\sigma_H$ : NW–SE Regime: NE–SW extension	1

Müller *et al.* (2012) suggests crustal shortening has dominated since the late Miocene, subject to N–S  $\sigma_H$  in the Mount Lofty Ranges and NE–SW  $\sigma_H$  in the Flinders Ranges during the late Miocene pulse (Table 3). However, we found no evidence to indicate opposing paleostress orientations during this period, rather a comparable N–S compression for both Mount Lofty Ranges and Flinders Ranges (Figure 6). Late Miocene deformation of southeastern Australian dep-

ocentres is consistent (e.g. Holford *et al.*, 2011a), further supporting our model of harmonious paleostress.

The greatest similarity between the model presented by Müller *et al.* (2012) and our paleostress model occurs during the most recent period of neotectonic history. For example, we both suggest NW–SE  $\sigma_H$  in the Mount Lofty Ranges during the Pliocene to late Pleistocene and E–W  $\sigma_H$  in the Flinders Ranges during the late Pleistocene to Present (Table 3) whereas

Müller *et al.* (2012) suggested NW–SE  $\sigma_H$  has dominated the Mount Lofty Ranges from the Pliocene to Present. However, Hillis *et al.* (2008) indicated that both Mount Lofty Ranges and Flinders Ranges are currently subject to E–W  $\sigma_H$ , matching our model (Figure 6). Müller *et al.* (2012) noted increased variability in  $\sigma_H$  at this stage of their model compared to other times and demonstrated a clockwise rotation of  $\sigma_H$ .

### Relevance for regional neotectonics

Post-rift compression along the southern Australian passive margin is well-documented with consensus for Eocene onset and distribution of compressional strain accommodation, since the final breakup of Antarctica from Australia (e.g. Dickinson *et al.*, 2002; Hillis *et al.*, 2008; Holford *et al.*, 2011a; Holford *et al.*, 2014; Sandiford, 2003). The St Vincent Basin exhibits deformation characteristics similar to those of neighbouring basins, in particular those of the western Otway Basin (to the SE) and the Eucla Basin (to the W). The Otway Basin exemplifies continual mid Eocene–Pliocene compression via long-wavelength folding and reverse-faulting (Duddy *et al.*, 2003; Holford *et al.*, 2010; Holford *et al.*, 2011a; Tuit *et al.*, 2011), with peak deformation from late Miocene–early Pliocene coeval with a well-documented angular unconformity (Dickinson *et al.*, 2002; Sandiford *et al.*, 2004). The Otway Basin exhibits neotectonic features indicating a NW–SE-compressive stress that has developed since the middle Eocene; such features are observed margin wide (Holford *et al.*, 2014). In the west, the Eucla Basin shows minor signs of faulting (Clark *et al.*, 2012), with minor eastward tilting and uplift (Holford *et al.*, 2011a; Hou *et al.*, 2006; Sandiford, 2007).

Pulses of crustal shortening are evident during the middle Eocene and late Mio-

cene–Pliocene rocks in the Otway Basin (e.g. Debenham *et al.*, 2018). However, deformation in the Otway Basin is not restricted to these time intervals (Holford *et al.*, 2014). Our results for the St Vincent Basin agree with those of Holford *et al.* (2014) with the deformation bands documented in this study evolved under a dynamic regional stress regime that spans the Late Cretaceous to Present (Figure 6). Therefore, intracontinental strain accommodation in the St Vincent Basin and Lake Eyre Basin is not constrained to the late Miocene–Pliocene and Pleistocene pulses of deformation (Figure 6) with our model demonstrating that the most recent stress state has only been active since the late Pleistocene post 100 Ka. These developments have significant implications for hydrocarbon and economic mineral exploration because the structures outlined here influence the way fluids flow through the subsurface. The addition of temporal constraints to fault evolution and development of sedimentary structures may enhance our understanding of palaeofluid flow and vector modelling.

### Conclusions

- We have mapped 737 deformation bands and 397 fractures depicting five Cenozoic generations of paleostress. Stage 1: NW–SE extension (early Paleocene–early Eocene). Stage 2: N–S extension (middle Eocene–middle Miocene). Stage 3: N–S compression (late Miocene–early Pliocene). Stage 4: NW–SE compression (middle Pliocene–late Pleistocene). Stage 5: E–W compression (late Pleistocene–Present-day).
- The Mount Lofty Ranges and Flinders Ranges evolved from extensional to compressional tectonics regimes in the late Miocene.

The associated exhumation and denudation resulted in a rotation of  $\sigma_H$  from NW–SE to E–W.

- Quantitative paleostress analysis conducted in this study does not support the paleostress model of Müller *et al.* (2012). Although the two models exhibit similarities, for the most part the models disagree. Our model is founded on physical structural evidence, while Müller *et al.* (2012) is speculative of paleostress vector.
- Deformation bands are excellent indicators of discrete changes in the local and regional stress regime. This characteristic makes their analysis an effective tool for constraining the temporal evolution of paleostress.

### Acknowledgements

Doug and Margaret Sprigg have been very kind and supportive, allowing us access to the Arkaroola Resort and Wilderness Sanctuary for fieldwork. We also thank Rowan Hansberry, Morgan Blades, Kamini Bhowany, Braden Morgan, and Jonathan Berthiaume for their helpful discussions and field assistance.

### Funding

We thank the Australian Research Council (DP1601158) and the Government of South Australia's Department of State Development and Geological Survey of South Australia for their financial support.

### References

- Alley, N. F., 1998, Cainozoic stratigraphy, palaeoenvironments and geological evolution of the Lake Eyre Basin: *Palaeogeography, Palaeoclimatology, Palaeoecology*, v. 144, no. 3, p. 239-263.
- Alley, N. F., and Lindsay, J. M., 1995, The Phanerozoic, Drexel J. F. and Preiss W. V. (eds) *The Geology of South Australia, Volume 2*, Geological Survey of South Australia Bulletin 54, p. 152.
- Allmendinger, R. W., Cardozo, N., and Fisher, D. M., 2012, *Structural geology algorithms: vectors and tensors*, New York, Cambridge University Press.
- Anderson, E. M., 1951, *The dynamics of faulting and dyke formation with applications to Britain*, Hafner Pub. Co.
- Aydin, A., and Johnson, A., 1978, Development of faults as zones of deformation bands and as slip surfaces in sandstone: *Pure and Applied Geophysics*, v. 116, no. 4-5, p. 931-942.
- Cann, J. H., Lower, C. S., and Jago, J. B., 2014, Provenance and sediment characteristics of contemporary gravel deposits at Sellicks Beach, eastern shore of Gulf St Vincent, South Australia: *Australian Journal of Earth Sciences*, v. 61, no. 6, p. 819-836.
- Célérier, J., Sandiford, M., Hansen, D. L., and Quigley, M., 2005, Modes of active intraplate deformation, Flinders Ranges, Australia: *Tectonics*, v. 24, no. 6, p. n/a-n/a.
- Clark, D., McPherson, A., and Van Dissen, R., 2012, Long-term behaviour of Australian stable continental region (SCR) faults: *Tectonophysics*, v. 566, p. 1-30.
- Debenham, N., King, R. C., and Holford, S. P., 2018, The influence of a reverse-reactivated normal fault on natural fracture geometries and relative chronologies at Castle Cove, Otway Basin: *Journal of Structural Geology*, v. 112, p. 112-130.

- Denham, D., Alexander, L., and Worotnicki, G., 1979, Stresses in the Australian crust: evidence from earthquakes and in-situ stress measurements: *BMR Journal of Australian Geology and Geophysics*, v. 4, no. 4, p. 289-295.
- Dickinson, J. A., Wallace, M. W., Holdgate, G. R., Gallagher, S. J., and Thomas, L., 2002, Origin and Timing of the Miocene-Pliocene Unconformity in Southeast Australia: *Journal of Sedimentary Research*, v. 72, no. 2, p. 288-303.
- Drexel, J. F., and Preiss, W. V., 1995, The geology of South Australia, Volume 2. The Phanerozoic, South Australia Geological Survey. Bulletin, 54.
- Duddy, I., Erout, B., Green, P., Crowhurst, P., and Boulton, P., 2003, Timing constraints on the structural history of the western Otway Basin and implications for hydrocarbon prospectivity around the Morum High, South Australia: *The APPEA Journal*, v. 43, no. 1, p. 59-83.
- Fairburn, B., 1998, The Willunga Embayment - a stratigraphic revision: *Mineral Resources of South Australia*, v. 11, p. 35-41.
- Flöttmann, T., and Cockshell, C. D., 1996, Palaeozoic basins of southern South Australia: New insights into their structural history from regional seismic data: *Australian Journal of Earth Sciences*, v. 43, no. 1, p. 45-55.
- Foden, J., Elburg, M., xa, A, Dougherty, x, Page, J., and Burt, A., 2006, The Timing and Duration of the Delamerian Orogeny: Correlation with the Ross Orogen and Implications for Gondwana Assembly: *The Journal of Geology*, v. 114, no. 2, p. 189-210.
- Fossen, H., Schultz, R. A., Shipton, Z. K., and Mair, K., 2007, Deformation bands in sandstone: a review: *Journal of the Geological Society of London*, v. 164, no. 4, p. 755-769.
- Fossen, H., Schultz, R. A., and Torabi, A., 2011, Conditions and implications for compression band formation in the Navajo Sandstone, Utah: *Journal of Structural Geology*, v. 33, no. 10, p. 1477-1490.
- Foster, D., Murphy, J., and Gleadow, A., 1994, Middle tertiary hydrothermal activity and uplift of the northern flinders ranges, South Australia: Insights from apatite fission-track thermochronology: *Australian Journal of Earth Sciences*, v. 41, no. 1, p. 11-17.
- Gaina, C., Müller, D. R., Royer, J.-Y., Stock, J., Hardebeck, J., and Symonds, P., 1998, The tectonic history of the Tasman Sea: A puzzle with 13 pieces: *Journal of Geophysical Research: Solid Earth*, v. 103, no. B6, p. 12413-12433.
- Hillis, R., and Reynolds, S., 2000, The Australian stress map: *Journal of the Geological Society*, v. 157, no. 5, p. 915-921.
- , 2003, In situ stress field of Australia: *Geological Society of America Special Papers*, v. 372, p. 49-58.
- Hillis, R. R., Sandiford, M., Reynolds, S. D., and Quigley, M. C., 2008, Present-day stresses, seismicity and Neogene-to-Recent tectonics of Australia's 'passive' margins: intraplate deformation controlled by plate boundary forces: *Geological Society, London, Special Publications*, v. 306, no. 1, p. 71-90.
- Holford, S., Hillis, R., Duddy, I., Green, P., Tuitt, A., and Stoker, M., 2010, Impacts of Neogene-Recent compressional deformation and uplift on hydrocarbon prospectivity of the passive southern Australian margin: *The APPEA Journal*, v. 50, no. 1, p. 267-286.
- Holford, S., Hillis, R. R., Duddy, I. R., Green, P. F., Stoker, M., Tuitt, D., Backe, G., Tassone, D. R., and MacDonald, J. D., 2011a, Cenozoic post-breakup compressional deformation and exhumation of the southern Australian margin: *APPEA Journal*, v. 51, p. 613.
- Holford, S. P., Green, P. F., Duddy, I. R., Turner, J. P., Hillis, R. R., and Stoker, M. S., 2009,

- Regional intraplate exhumation episodes related to plate-boundary deformation: *Geological Society of America Bulletin*, v. 121, no. 11-12, p. 1611-1628.
- Holford, S. P., Hillis, R. R., Duddy, I. R., Green, P. F., Tassone, D. R., and Stoker, M. S., 2011b, Paleothermal and seismic constraints on late Miocene-Pliocene uplift and deformation in the Torquay sub-basin, southern Australian margin: *Australian Journal of Earth Sciences*, v. 58, no. 5, p. 543-562.
- Holford, S. P., Hillis, R. R., Hand, M., and Sandiford, M., 2011c, Thermal weakening localizes intraplate deformation along the southern Australian continental margin: *Earth and Planetary Science Letters*, v. 305, no. 1, p. 207-214.
- Holford, S. P., Tuitt, A. K., Hillis, R. R., Green, P. F., Stoker, M. S., Duddy, I. R., Sandiford, M., and Tassone, D. R., 2014, Cenozoic deformation in the Otway Basin, southern Australian margin: implications for the origin and nature of post-breakup compression at rifted margins: *Basin Research*, v. 26, no. 1, p. 10-37.
- Hou, B., Alley, N. F., Frakes, L. A., Stoian, L., and Cowley, W. M., 2006, Eocene stratigraphic succession in the Eucla Basin of South Australia and correlation to major regional sea-level events: *Sedimentary Geology*, v. 183, no. 3-4, p. 297-319.
- Jayawardena, C. L., 2013, Characteristics of neotectonic faulting in the Mount Lofty and Flinders Ranges, South Australia [Unpublished Ph.D. thesis]: University of Wollongong.
- Krassay, A., Cathro, D., and Ryan, D., 2004, A regional tectonostratigraphic framework for the Otway Basin, in D. R. J. P. J. Boulton, a. S., C. Lang, ed., *Eastern Australasian Basins Symposium II: Adelaide, South Australia*, Petroleum Society of Australia, p. 97-116.
- Mitchell, M. M., Kohn, B. P., O'Sullivan, P. B., Hartley, M. J., and Foster, D. A., 2002, Low-temperature thermochronology of the Mt Painter Province, South Australia: *Australian Journal of Earth Sciences*, v. 49, no. 3, p. 551-563.
- Müller, R. D., Dyksterhuis, S., and Rey, P., 2012, Australian paleo-stress fields and tectonic reactivation over the past 100 Ma: *Australian Journal of Earth Sciences*, v. 59, no. 1, p. 13-28.
- Norvick, M. S., and Smith, M. A., 2001, Mapping the plate tectonic reconstruction of southern and southeastern Australia and implications for petroleum systems: *The AAPG Bulletin* v. 41, no. 15-35.
- Paul, E., Flöttmann, T., and Sandiford, M., 1999, Structural geometry and controls on basement-involved deformation in the northern Flinders Ranges, Adelaide Fold Belt, South Australia: *Australian Journal of Earth Sciences*, v. 46, no. 3, p. 343-354.
- Potts, G. J., and Reddy, S. M., 1999, Construction and systematic assessment of relative deformation histories: *Journal of Structural Geology*, v. 21, no. 8, p. 1245-1253.
- Preiss, W., 1990, A stratigraphic and tectonic overview of the Adelaide Geosyncline, South Australia. J.B Jago, P.s Moore (Eds): *The Evolution of a Late Precambrian-Early Palaeozoic Rift Complex: The Adelaide Geosyncline*, Geological Society of Australia, Special Publication, v. 16, p. 1-33.
- , 2019, The tectonic history of Adelaide's scarp-forming faults: *Australian Journal of Earth Sciences*, v. 66, no. 3, p. 305-365.
- Quigley, M., Sandiford, M., Fifield, L. K., and Alimanovic, A., 2007, Landscape responses to intraplate tectonism: Quantitative constraints from <sup>10</sup>Be nuclide abundances: *Earth and Planetary Science Letters*, v. 261, no. 1-2, p. 120-133.
- Quigley, M. C., Cupper, M. L., and Sandiford, M., 2006, Quaternary faults of south-central Australia: Palaeoseismicity, slip rates and origin: *Australian Journal of Earth Sciences*, v. 53, no. 2, p. 285-301.
- Sandiford, M., 2003, Neotectonics of southeast-

- ern Australia: linking the Quaternary faulting record with seismicity and in situ stress: *Geological Society of America Special Papers*, v. 372, p. 107-119.
- Sandiford, M., 2007, The tilting continent: A new constraint on the dynamic topographic field from Australia: *Earth and Planetary Science Letters*, v. 261, no. 1-2, p. 152-163.
- Sandiford, M., 2008, Ground motion response spectra, Four Mile Project: Pasadena, California, URS.
- Sandiford, M., Quigley, M., de Broekert, P., and Jakica, S., 2009, Tectonic framework for the Cenozoic cratonic basins of Australia: *Australian Journal of Earth Sciences*, v. 56, no. sup1, p. S5-S18.
- Sandiford, M., Wallace, M., and Coblenz, D., 2004, Origin of the in situ stress field in south-eastern Australia: *Basin Research*, v. 16, no. 3, p. 325-338.
- Scheibner, E., 1999, The Geological Evolution of New South Wales: A Brief Review, Department of Mineral Resources.
- Schellart, W. P., and Spakman, W., 2015, Australian plate motion and topography linked to fossil New Guinea slab below Lake Eyre: *Earth and Planetary Science Letters*, v. 421, p. 107-116.
- Sprigg, R., 1946, Reconnaissance geological survey of portion of the western escarpment of the Mount Lofty Ranges: *Transactions of the Royal Society of South Australia*, v. 69, p. 277-304.
- Tokarev, V., 2005, Neotectonics of the Mount Lofty Ranges, South Australia [PhD Thesis]: University of Adelaide.
- Tokarev, V., Sandiford, M., and Gostin, V., 1999, Landscape evolution in the Mount Lofty Ranges: implications for regolith development, *in* Taylor, G., and Pain, C., eds., *New Approaches to an Old Continent*, Proceedings of Regolith '98, 3rd Australian Regolith Conference: Kalgoorlie, WA, Cooperative Research Centre for Landscape & Mineral Exploration, Perth, p. 131-139.
- Tondi, E., Antonellini, M., Aydin, A., Marchegiani, L., and Cello, G., 2006, The role of deformation bands, stylolites and sheared stylolites in fault development in carbonate grainstones of Majella Mountain, Italy: *Journal of Structural Geology*, v. 28, no. 3, p. 376-391.
- Tuitt, A., Holford, S., Hillis, R., Underhill, J., Ritchie, D., Johnson, H., Hitchen, K., Stoker, M., and Tassone, D., 2011, Continental margin compression: a comparison between compression in the Otway Basin of the southern Australian margin and the Rockall-Faroe area in the northeast Atlantic margin: *The APPEA Journal*, v. 51, no. 1, p. 241-258.
- Webb, B., 1958, Summary of tectonics and sedimentation: The geology of South Australia. *Journal of the Geology Society of Australia*, v. 5, p. 136-149.
- Williams, G. E., 1973, Late Quaternary piedmont sedimentation, soil formation and palaeoclimates in arid South Australia: *Zeitschrift für Geomorphologie*, v. 17, p. 102-125.

# CHAPTER 3

Lubiniecki, D. C., White S. R. S., King R. C., Holford S. P., Bunch M. A., Hill, S. M. (2019). *Structural evolution of carbonate-hosted cataclastic bands adjacent to a major neotectonic fault, Sellicks Beach, South Australia*. *Journal of Structural Geology* 126, 11-24. DOI: 10.1016/j.jsg.2019.05.004

# Statement of Authorship

Title of Paper	Structural evolution of carbonate-hosted deformation bands adjacent to a major neotectonic fault, Sellicks Beach, South Australia
Publication Status	<input checked="" type="checkbox"/> Published <input type="checkbox"/> Accepted for Publication <input type="checkbox"/> Submitted for Publication <input type="checkbox"/> Unpublished and Unsubmitted work written in manuscript style
Publication Details	LUBINIECKI, D. C., WHITE, S. R. S., KING, R. C., HOLFORD, S. P., BUNCH, M. A. & HILL, S. 2019. Structural evolution of carbonate-hosted cataclastic bands adjacent to a major neotectonic fault, Sellicks Beach, south Australia. <i>Journal of Structural Geology</i> , 126, 11-24.

## Principal Author

Name of Principal Author (Candidate)	Drew Lubiniecki		
Contribution to the Paper	Completed fieldwork, collected and interpreted data, collected and analysed samples, wrote and prepared manuscript, acted as corresponding author.		
Overall percentage (%)	70%		
Certification:	This paper reports on original research I conducted during the period of my Higher Degree by Research candidature and is not subject to any obligations or contractual agreements with a third party that would constrain its inclusion in this thesis. I am the primary author of this paper.		
Signature	_____	Date	<b>24/9/2019</b>

## Co-Author Contributions

By signing the Statement of Authorship, each author certifies that:

- i. the candidate's stated contribution to the publication is accurate (as detailed above);
- ii. permission is granted for the candidate to include the publication in the thesis; and
- iii. the sum of all co-author contributions is equal to 100% less the candidate's stated contribution.

Name of Co-Author	Samuel White		
Contribution to the Paper	Conducted original fieldwork, sample collected, and analysis.		
Signature	_____	Date	9/9/2019

Name of Co-Author	Rosalind King		
Contribution to the Paper	Supervised fieldwork, aided in collection of data and samples, helped with data interpretation and manuscript revision.		
Signature	_____	Date	18/9/2019

Name of Co-Author	Simon Holford		
Contribution to the Paper	Supervised fieldwork, aided in collection of data and samples, helped with data interpretation and manuscript revision.		
Signature		Date	15/5/19

Name of Co-Author	Mark Bunch		
Contribution to the Paper	Supervised fieldwork, aided in collection of data and samples, helped with data interpretation and manuscript revision.		
Signature		Date	18/09/2019

Name of Co-Author	Steven Hill		
Contribution to the Paper	Financial support, government correspondent, and overall concept of thesis.		
Signature		Date	11/9/19

Please cut and paste additional co-author panels here as required.

---

## Structural evolution of carbonate-hosted deformation bands adjacent to a major neotectonic fault, Sellicks Beach, South Australia

---

### Abstract

---

Deformation bands are common fault-related strain features found in upper crustal granular highly porous sedimentary rocks. However, the majority of research has focused on siliciclastic-related case studies, resulting in a knowledge gap surrounding the nomenclature and implications of carbonate-hosted cataclastic bands. We present a systematic case study of carbonate-hosted deformation bands in the Oligocene–Miocene Port Willunga Formation (PWF) exposures along the wave-cut platforms at Sellicks Beach, South Australia. Sellicks Beach provides an exceptional location to study carbonate-hosted deformation bands because of the unique juxtapositions of the PWF, a carbonate grainstone offset by the NE-SW striking Willunga Fault, and metasedimentary basement. The Willunga Fault is a steep SE-dipping present-day active reverse fault that previously accommodated deposition in a Cenozoic half-graben. We have conducted a comprehensive structural analysis of 269 PWF deformation bands that formed as a result of strain induced by the Willunga Fault. Our model identifies three sets of shear-enhanced compaction bands (SECBs), and one set of pure compaction bands (PCBs) within the PWF. The PWF deformation bands display a range of cataclasis intensity, named here as crush micro-breccia (0–10% gm) and protocataclastic bands (10–50% gm) defined by the percentage of microscopic fine-grained groundmass (gm), the product of comminution, stylolite formation, and cementation. Petrophysical analysis indicates that crush micro-breccia bands reduce permeability between 0.0–0.75 orders of magnitude, and protocataclastic bands reduce permeability between 0.25–1.75 orders of magnitude relative to host rock. Our results indicate that PWF deformation bands are a useful proxy for cataclasis intensity, forming the foundation for a new classification scheme to describe cataclastic deformation bands, specifically applied to carbonate rocks.

**Keywords:** Willunga Fault, St. Vincent Basin, cataclasis intensity, fault history, Mount Lofty Ranges

---

### 1. Introduction

Deformation bands are millimetre-wide tabular zones of localized strain that form in porous clastic rocks such as sandstones, carbonate grainstones, and chalks; they arguably represent the most common strain feature in porous granular rocks (Fossen et al., 2007). Strain is accommodated by pore-space collapse, resulting from compaction during burial, or high deviatoric stress, e.g. fault-induced strain (Fossen et al., 2007). Disaggregation bands form by breaking up of grain-bonding cements, and accommodate strain through grain-boundary sliding; whereas cataclastic bands form

by comminution (Fossen et al., 2007). In siliciclastic rocks, disaggregation bands are generally the first to form in a burial sequence, prior to lithification when porosity is high and confining pressure and burial depth are low (Antonellini et al., 1994; Fossen et al., 2007; Skurtveit et al., 2013). Cataclastic bands form with increasing burial depth or confining pressure, in well-cemented formations with low porosity (Antonellini et al., 1994; Skurtveit et al., 2013). Cataclasis in carbonate grainstone is usually mediated by pressure solution (Antonellini et al., 2014b; Micarelli et al., 2006; Tondi et al., 2006). Therefore, the intensity of comminution and pressure solution is

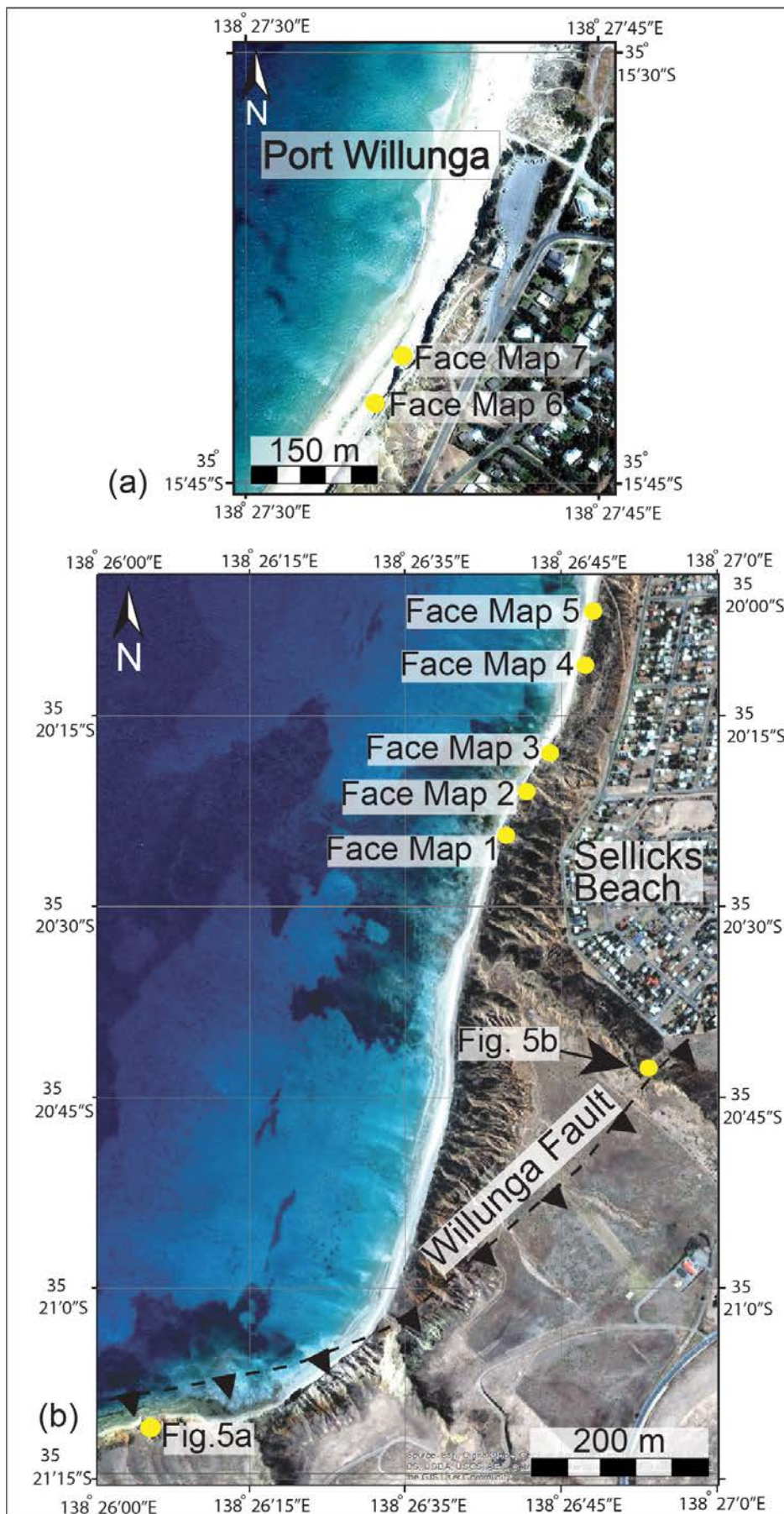


**Figure 1.** (a) Map of Port Willunga illustrating the spatial relationship between Face Maps 6 and 7. (b) Map of Sellicks Beach illustrating the spatial relationships between Face Maps 1-5, Fracture Maps 1 and 2, Cactus Canyon, and the Willunga Fault.

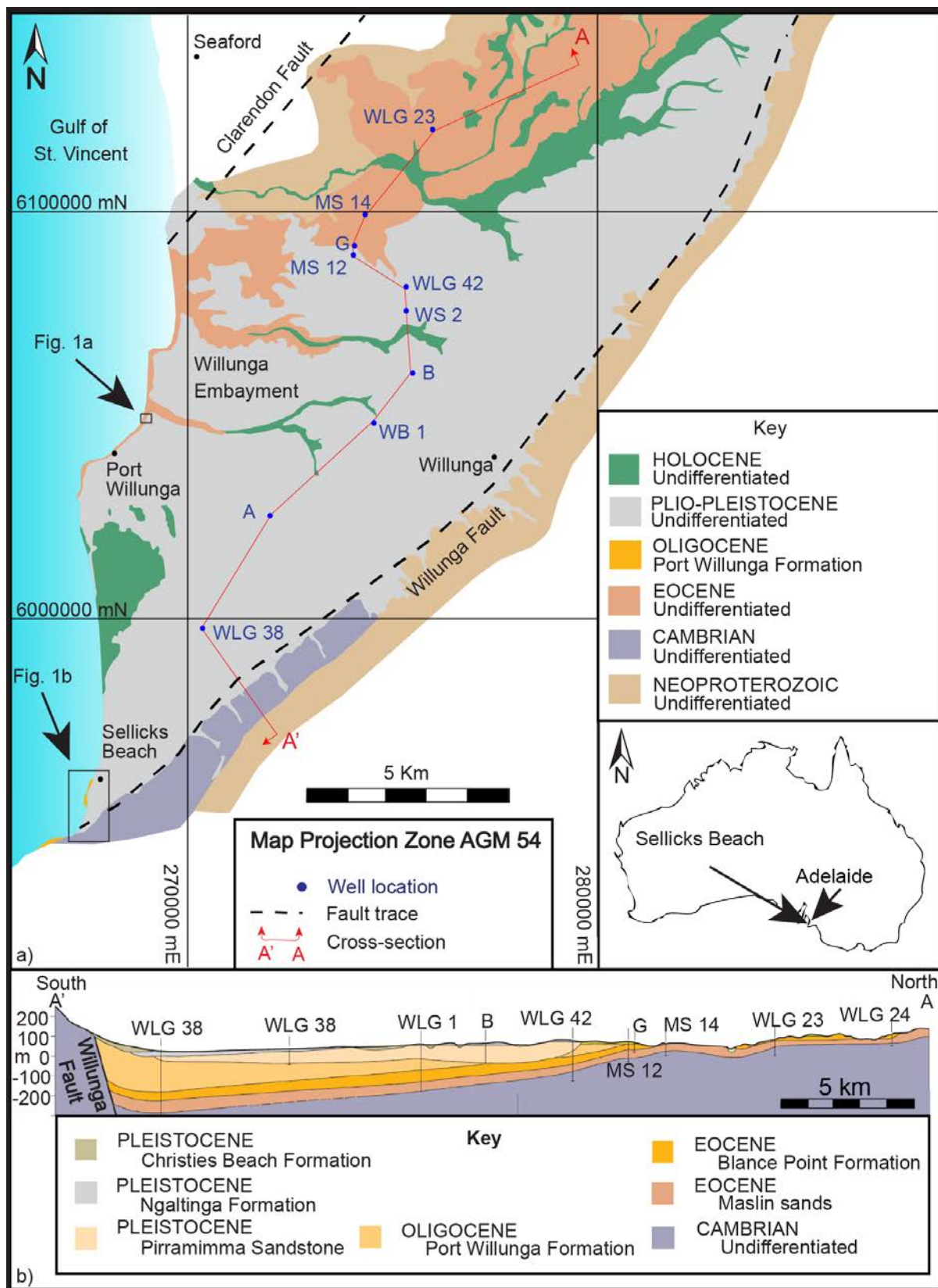


**Figure 2. (a)** Geological map of the Willunga Embayment, highlighting study areas **Figure 1a** and **Figure 1b**, modified after Fairburn, (1998); **(b)** Cross section of the Willunga Embayment modified after Fairburn, (1998).

analogous to strain intensity. Ballas et al. (2012) applied the widely-used fault-rock classification scheme by Sibson (1977) to the intensity of cataclasis in sandstone-hosted deformation bands. This comparison linked factors that control permeability, such as tectonic regime, presence of a fault, burial depth, host rock porosity, grain size, and sorting. However, the fault rock classification scheme of Sibson (1977) has yet to be applied to carbonate-hosted deformation bands.

The majority of documented case studies involving deformation bands focus on sandstones (e.g. Antonellini and Mollema, 2015; Aydin et al., 2006; Ballas et al., 2015; Fossen and Hesthammer, 1997); this has resulted in a comparative lack of knowledge on carbonate-hosted deformation bands (e.g. Antonellini et al., 2014b; Cilona et al., 2012; Rath et al., 2011; Rotevatn et al., 2016; Tondi, 2007). This knowledge gap has resulted in a lack of attention to detail applied to the mechanical classification of carbonate-hosted deformation bands. Antonellini et al. (2014b) and Rotevatn et al. (2016) developed simple kinematic classification schemes for carbonate-hosted deformation bands (e.g. compactive and pure shear bands); however, the classification schemes leave no room for increased levels of mechanical strain induced by cataclasis in carbonate rocks. The lack of detail for carbonate cataclasis classification is a result of the relatively few case studies applied to carbonate deformation bands. It is therefore important to explore the intricate relationship of mechanical strain and cataclasis intensity of the carbonate cataclastic deformation bands.

This study defines the structural evolution of carbonate-hosted deformation bands in the attempt to elucidate discrete changes in cataclasis intensity. Despite

recent work, the need remains for a universal classification scheme that defines the cataclasis intensity of deformation bands in carbonate rocks. Carbonate grainstone at Sellicks Beach is made up of moderately sorted delicate bioclastic grains of varying type and shape. These characteristics make disaggregation difficult, if not impossible, without the addition of comminution to accommodate displacement and strain. Our observations indicate that there is a range in cataclasis intensity within the Oligocene–late Miocene PWF grainstone at Sellicks Beach, South Australia. Thus, the carbonate grainstone-hosted deformation bands observed in this study do not fit the existing classification models (e.g. Antonellini and Aydin, 1994; Rotevatn et al., 2016). We rectify this problem by retrofitting the fault rock classification scheme by Sibson (1977) to classify cataclasis intensity of carbonate deformation bands. Ballas et al. (2012) successfully applied this classification scheme to siliciclastic rocks, and thereby have provided an opportunity to objectively relate similar and differing characteristics of deformation bands formed in carbonate and siliciclastic grainstone. For the first time, we report the microstructural evolution of the carbonate-hosted deformation bands of the Oligocene–late Miocene PWF using this classification system.

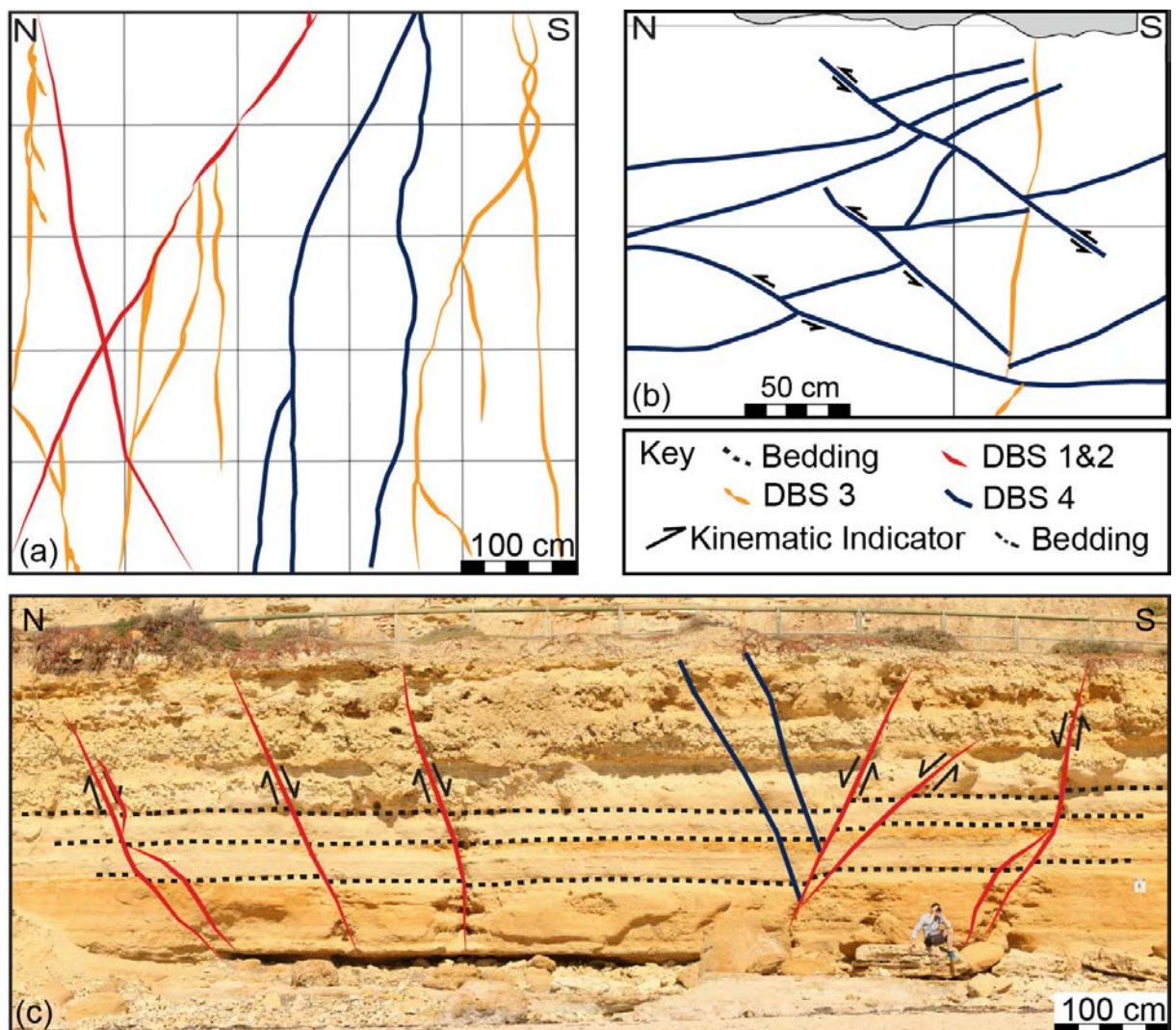
## 2. Geological setting of the Willunga Embayment

### 2.1 Structural setting and neotectonic history

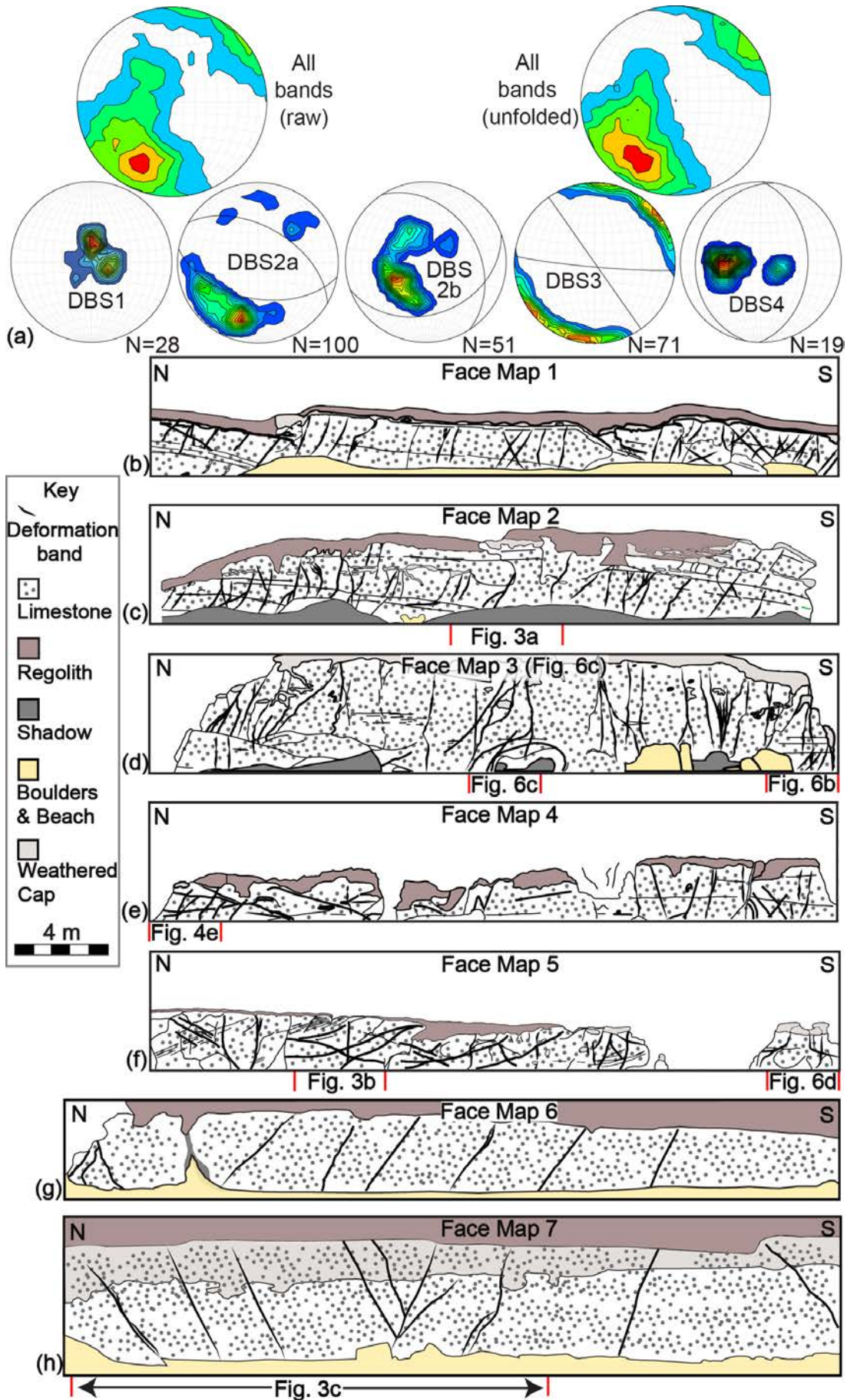
Sellicks Beach is located at the southern edge of the Cenozoic Willunga Embayment, adjacent to the Willunga Fault, which is one of the most prominent neotectonic structures in southeastern Australia (Fig. 1). The Willunga Fault is recognised by the occurrence of steep cliffs along the Sellicks Hill scarp face,

young topography, and recent drainage patterns (Sandiford, 2003). The Willunga Embayment forms the southern section of the larger Cenozoic-age St. Vincent Basin, bound to the south by the Willunga Fault and to the north by the Clarendon Fault (Fig. 2a). The Willunga Fault originally formed as a bounding fault to a NNE-SSW oriented half-graben associated with final separation of Australia from Antarctica during the middle Eocene (Flöttmann and Cockshell, 1996; Holford et al., 2011a; Norvick and Smith, 2001). Oligocene–Miocene extension resulted

in subsidence of the St. Vincent Basin; increased accommodation space allowed marine transgression and deposition of the PWF (Tokarev, 2005). Subsidence dominated until the late Miocene–Pliocene when regional tectonic compression triggered uplift, erosion, and the formation of low-angle unconformities within the St. Vincent Basin (Sandiford, 2003; Tokarev, 2005). Correlation of interglacial benches in the hanging wall and footwall implies reverse-sense movement on near-vertical exposures of the Willunga Fault with time-averaged verti-



**Figure 3.** (a) Grid map illustrating the spatial relationships between Deformation Band Set 2, 3, and 4 in plan-view (Face Map 2). (b) Face map illustrating the spatial relationships between Deformation Band Set 3 and 4 in cross-section view (Face Map 5). (c) Photograph of a graben-like structure depicting Deformation Band Set 2 within the Blanche Point Formation at Port Willunga (Face Map 7).



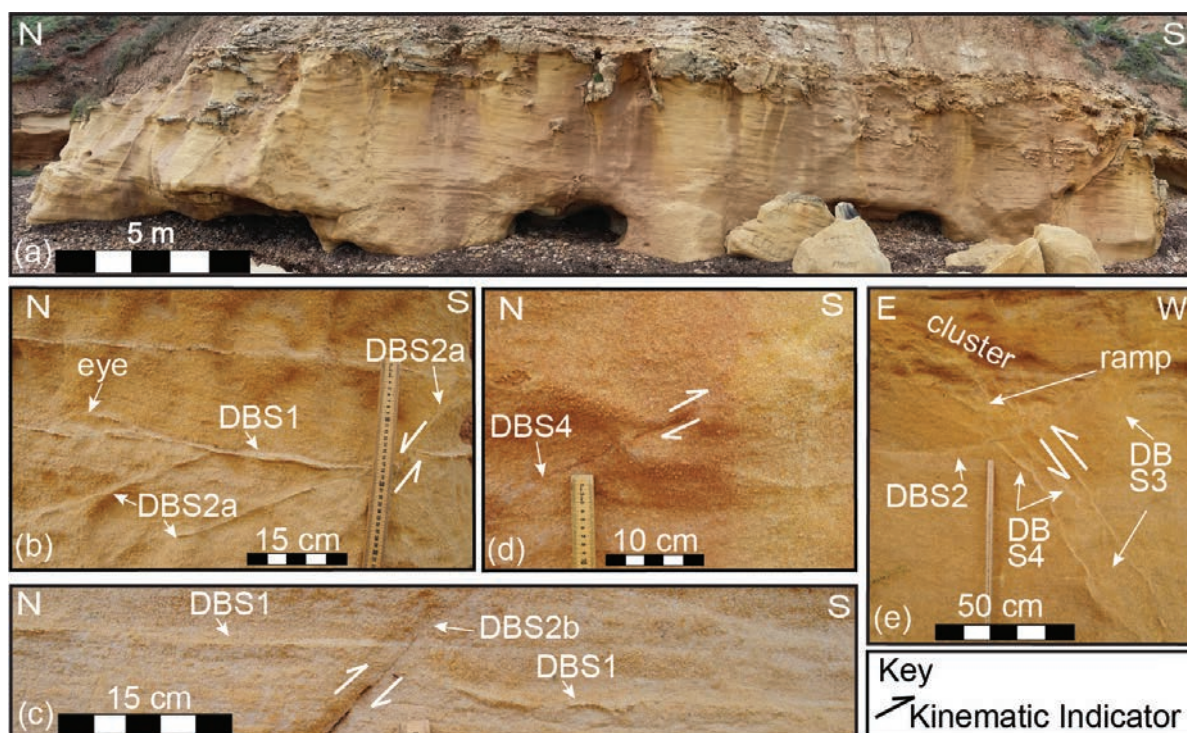


**Figure 5.** Photographs depicting the crosscutting relationships between Deformation Band Sets 1–4, and highlighting the principal stress evolution. **(a)** Photograph of Face Map 3 illustrating a typical Port Willunga Formation outcrop at Sellicks Beach. **(b)** Deformation Band Set 2 crosscutting Deformation Band Set 1 (normal displacement). **(c)** Deformation Band Set 2 crosscutting Deformation Band Set 1 (reverse displacement). **(d)** Deformation Band Set 4 crosscutting Deformation Band Set 2 (reverse displacement). **(e)** Deformation Band Set 4 crosscutting Deformation Band Set 3 (reverse displacement).

cal displacement of 50 to 70 m per Myr (Sandiford, 2003). Uplift and increased erosion of Neoproterozoic and Cambrian rocks SE of the Willunga Fault resulted in generation of the Quaternary alluvial fan sediments, which unconformably overlie the PWF at Sellicks Beach (Cann et al., 2014).

## 2.2 Geology of the Port Willunga Formation

The Willunga Fault marks the contact between the Cenozoic St. Vincent Basin

and late Proterozoic–Early Phanerozoic Adelaidean basement, juxtaposing the PWF with the Cambrian Heatherdale Shale (Fig. 2). The PWF is Oligocene–late Miocene in age and is separated from the overlying Quaternary alluvial fan sediments by an angular unconformity (Cann et al., 2014; Sandiford, 2003). The PWF comprises pale yellow–yellowish white carbonate grainstone, which contains fragmented bryozoan, brachiopod, bivalve, and echinoid shells. Bioclasts exhibit a sub-rounded to sub-angular shape, and moderate sorting;

**Figure 4.** (Page 66) Face maps highlighting deformation band structures in the Port Willunga Formation (locations provided in Figure 1). **(a)** Face Map 1 oriented north-south (location: Sellicks Beach). **(b)** Face Map 2 oriented north-south (location: Sellicks Beach). **(c)** Face Map 3 oriented north-south (location: Sellicks Beach). **(d)** Face Map 4 oriented north-south (location: Sellicks Beach). **(e)** Face Map 5 oriented north-south (Location: Sellicks Beach). **(f)** Face Map 6 oriented north-south (location: Port Willunga). **(g)** Face Map 7 oriented north-south (location: Port Willunga).

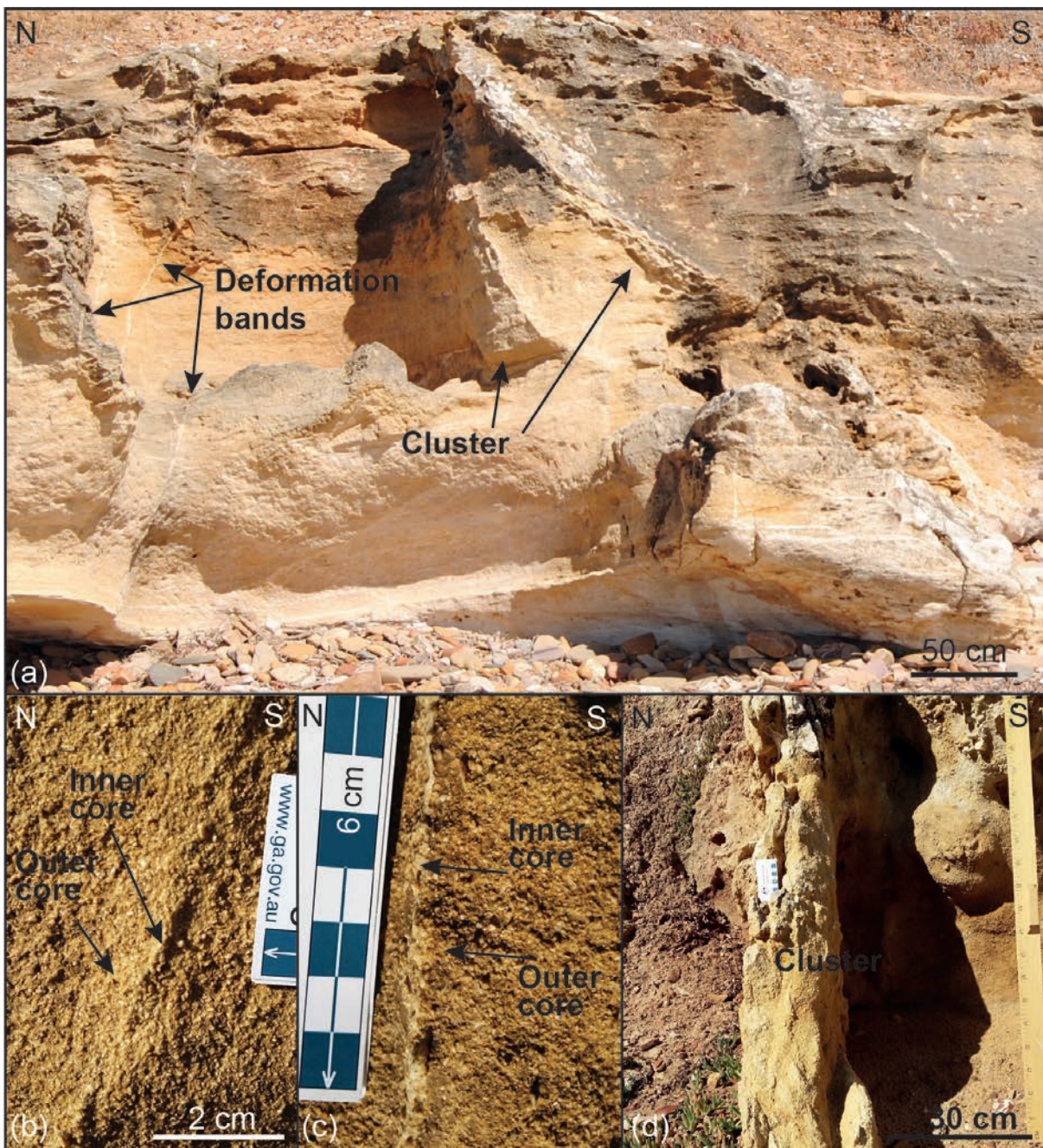


**Figure 6.** (a) Photograph of deformation band clusters at Sellicks Beach (AGM 267726E 6086230N Zone 54). (b) Photograph of typical crush microbreccia texture. (c) Photograph of typical protocataclastic texture. (d) Photograph of a deformation band cluster at Sellicks Beach.

bioclasts range in size from 0.1–2.0 mm. Fine-grained magnetite occurs throughout the PWF, including within deformation band zones at Sellicks Beach and Port Willunga. Occasional accumulations of detrital magnetite are preferentially sorted in beach sands immediately down slope from outcrop of the PWF. Mag-

netite grains are predominantly <1 mm in diameter. Pyrite and glauconite have also been noted to occur in the PWF from borehole samples (Cooper, 1979). Fine grained bladed calcite cement is observed in thin section within intergranular pore spaces and radially within void fossil chambers. The shallow marine sedimen-

tary rock of the PWF varies in thickness laterally due to subsequent erosion, from 9–150 m over 15 km (Fig. 2b) (Cooper, 1979). The PWF is poorly exposed at the surface and only crops out in low cliffs at Sellicks Beach and Port Willunga (Fig. 2a). Differential elevation of the PWF limestone between the Willunga Fault hanging wall and footwall, infers vertical displacement of  $\approx 240$  m since the early Miocene (Sandiford, 2003; Tokarev et al., 1999).

### 3. Methods

In outcrop, visually different deformation bands were measured and sampled to conduct structural, petrophysical, and optical investigations. Structures were measured in the field, then categorized based on their observable textures. Structural analysis was conducted using

stereonet diagrams produced by Stereonet9 (Allmendinger et al., 2012). Deformation bands were categorized into sets based on their orientation and geometry following the Andersonian theory of faulting (Anderson, 1905). The sequence in which the sets developed allowed us to define the structural evolution local to the Willunga Fault. We have identified five distinct sets of deformation bands, consecutively named based on mutually exclusive kinematic relationships.

At Sellicks Beach, the PWF exhibits open fold geometry with the fold axis oriented NE–SW. Folded late Pleistocene gravels of the Pooraka Formation in the nearby Sellicks Region exhibits similar fold orientation and was estimated to be no older than 125 Ka by Jayawardena (2013). We have inferred the open folds within the PWF to have occurred concu-

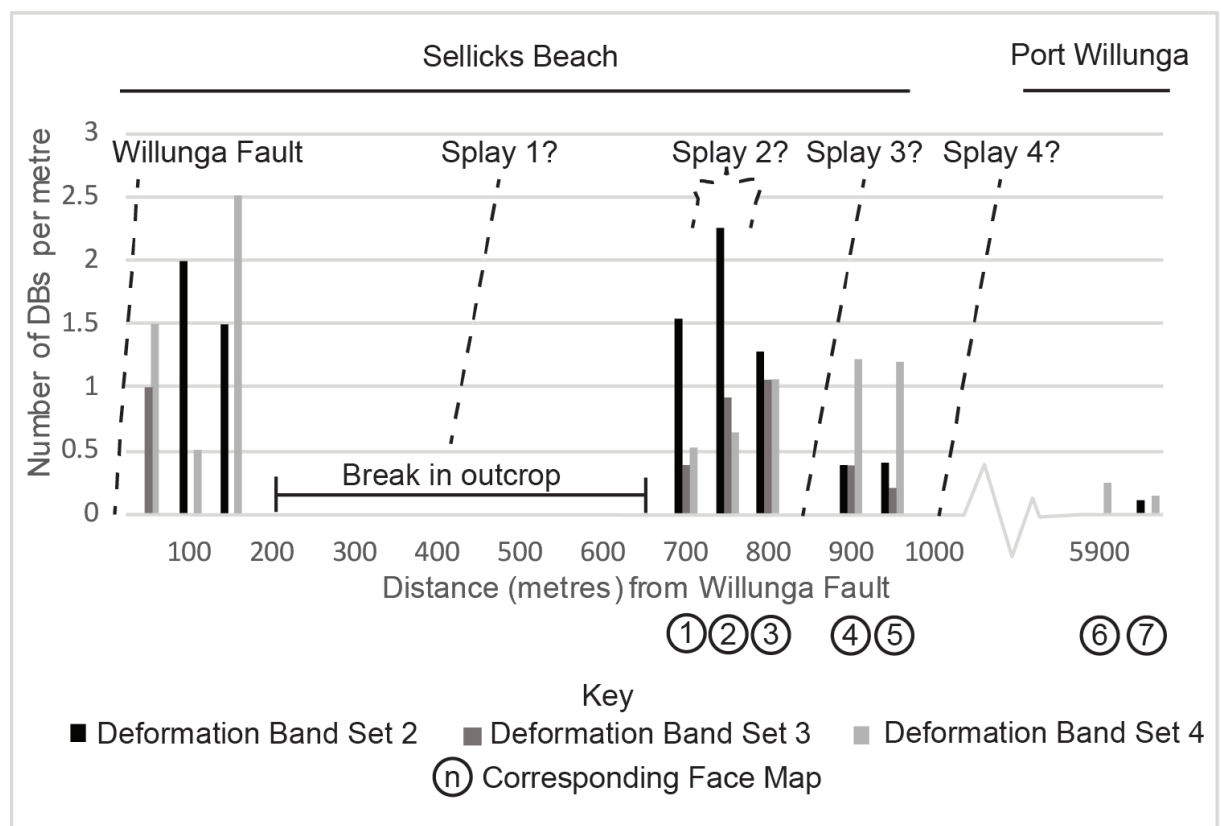


**Figure 7.** A distribution diagram highlighting the spatial density of Deformation Band Sets 2, 3, 4, and the potential distribution of Willunga Fault splays in the Port Willunga Formation at Sellicks Beach and Port Willunga.

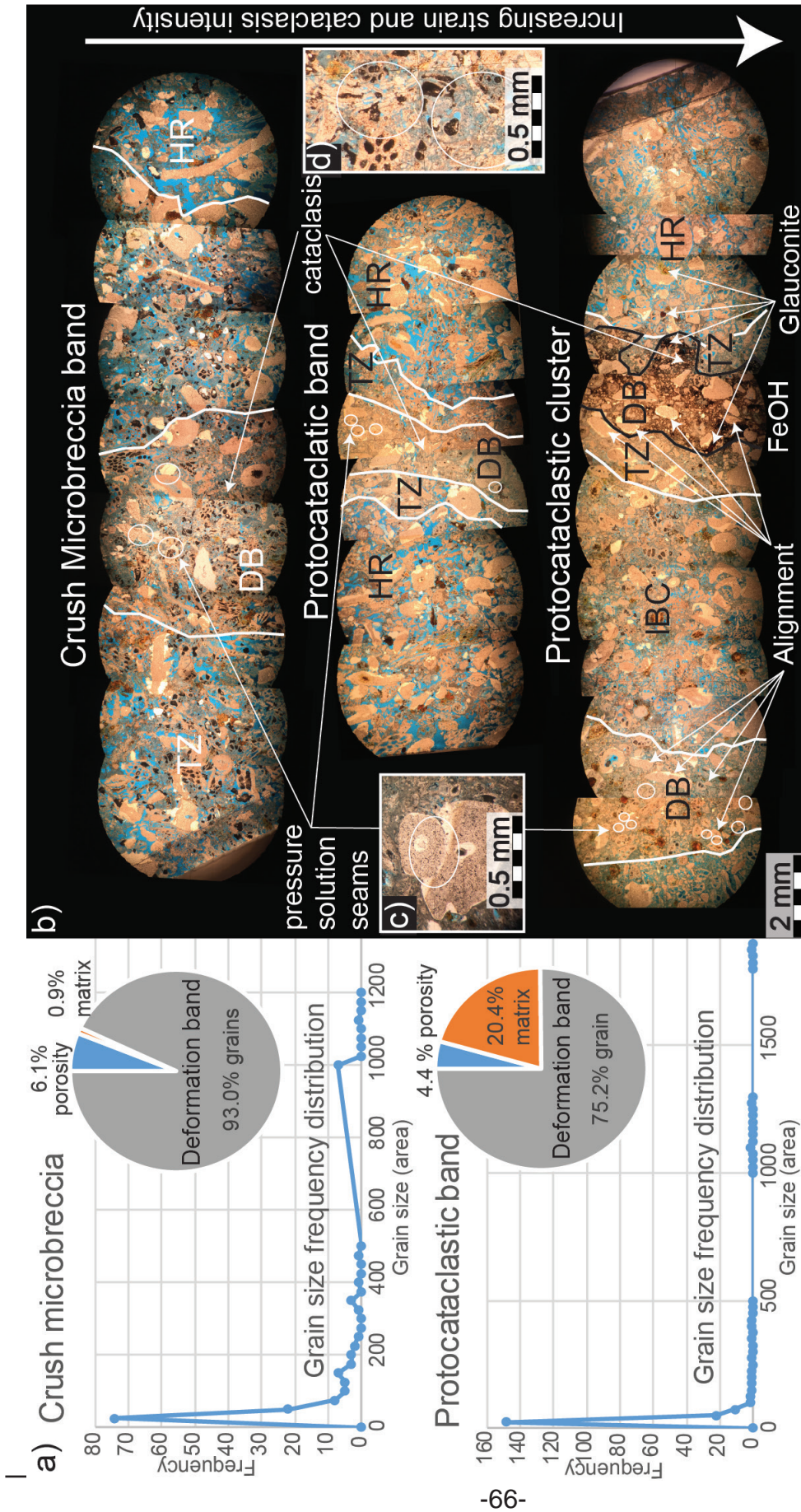


**Figure 8.** Micrographs of Port Willunga Formation cataclastic bands highlighting a progressive sequence of increasing cataclasis intensity, based on the matrix/grain ratio calculated by grain size distribution. DB: deformation band, TZ: transition zone, HR: host rock, IBC: interband compaction. **(a)** (left) Histograms highlighting the grain size distribution and matrix/grain ratio of crush microbreccia bands and protocataclastic bands; **(b)** (top) Microbreccia deformation band; (middle) protocataclastic deformation band with calcium carbonate cement; (bottom) protocataclastic deformation band with iron hydroxide cement. **(c)** Pressure solution seams within all micrographs. **(d)** Grain fracturing within all micrographs.

rently DBS3, which altered the orientation of DBS1–3. We corrected for the recent change in orientation by unfolding to the present-day bedding (bedding range: 30/177–08/098). Deformation bands are recorded in one grid map (Fig. 3a), and seven highly detailed face maps covering 80–210 m<sup>2</sup> of vertical cliff faces at Sellicks Beach and Port Willunga (Fig. 4). The one-metre grid diagram of a wave-cut platform covers 25 m<sup>2</sup> in plan-view, and is located in front of Face Map 2 (Fig. 3a). We have also constructed an additional face map excerpt from Face Map 5 in cross section view to highlight cross-cutting relationships (Fig. 3b). We used the frequency and distribution of individual DBS to gain understanding of the activity of the Willunga Fault at Sellicks Beach. Frequencies of individual DBS was calculated to an average per metre and plotted on a histogram chart to represent the distribution.

Microstructural analyses were undertaken on six samples containing deformation bands and two samples containing host rock to incorporate the cataclastic textures observed at Sellicks Beach. Samples were collected from Face Map 1–5 at Sellicks Beach from grab samples to protect the natural beauty of the outcrop (Fig. 4). Preparation included cutting sample perpendicular to deformation band strike and impregnation with blue dyed to indicate pore space. Petrophysical analysis was conducted using thin sections, plug samples, and a handheld permeameter. Thin sections were digitally photographed to calculate 2D porosity using JMicroVision© image analysis software. Eight plugs were cut from the Sellicks Beach samples and analysed using a modified Archimedes method to calculate absolute porosity (after Wong, 1999). Permeability was measured perpendicular to strike in the field using TinyPerm III Portable Air Permeameter by New England Research. The permeameter was calibrated by New England Research

and provides reliable permeability values ranging from 1 mD to 10 D. Outcrop was carefully scrapped with a putty knife and brushed clean prior to measurement. Data was collected in flat spots using a 6 mm rubber nozzle to support a good a seal and prevent air leaking from the permeameter. Grain particle size distributions of the different observable cataclastic textures was calculated using JMicroVision© image analysis software. Particle size distribution was used to distinguish particle area matrix and particle area grains, using 62.5 µm as the cut-off for matrix and grains after Bjørk et al. (2009). Lack of high-resolution images made cement recognition difficult and may result in small error.

#### 4. Structural data from the Port Willunga Formation

Here we describe the local- and micro-structural analysis of 269 deformation bands mapped within the PWF.

##### 4.1 Geometrical and structural observations of the Port Willunga Formation cataclastic bands

Deformation Band Set 1 (DBS1) is bedding parallel, showing no signs of shear displacement (Fig. 4a). The set comprises 28 deformation bands that exhibit a wavy characteristic, with wavelengths ranging from 5–10 mm. They appear as discrete structures ranging in thickness from 1–2 mm, and in clusters spanning up to 15 cm. DBS1 exhibits shallowly dipping limbs (i.e. 15–20°) to the S and NW at Sellicks Beach, reflecting the regional structure (Fig. 4a). At Port Willunga however, DBS1 is planar and dips shallowly (i.e. 10°) to the south. Stereonet analysis highlighted an ENE-WSW axial plane with a gentle WSW plunging fold axis, implying the maximum principal stress ( $\sigma_1$ ) was orientated NNW-SSE at the time of folding, subsequent to the formation of DBS1 (Fig. 4a). Bedding

and thus the dip of DBS1 progressively steepens towards the south, reaching up to  $65^\circ$  dipping north at the southern end of Sellicks Beach, within 5 m of the Willunga Fault.

Deformation Band Set 2 (DBS2) is sub grouped into two sections due to their similar geometry. We have measured 100 conjugate deformation bands that we assign to Deformation Band Set 2a (DBS2a); these bands strike range from E–W to NW–SE and averagely dips  $55^\circ$  towards the south and  $55^\circ$  towards the NE, respectively (Fig. 4a). Offsetting kinematic indicators of DBS1 are consistent with up to 4 mm normal-displacement, (DBS2a) (Fig. 5b). We have measured 51 conjugate deformation bands that we assign to Deformation Band Set

2b (DBS2b); these bands strike range from ENE–WSW dipping  $35^\circ$  towards the SE, and NW–SE and  $35^\circ$  towards the NE, respectively (Fig. 4a). Deformation Band Set 2 and 3 forms clusters of deformation bands up to 110 mm wide that converge to a single point before disappearing below the beach surface (Fig. 4d); these clusters are separated by metre-wide scale zones of undeformed host rock. Offsetting kinematic indicators of DBS1 are consistent with reverse-displacement (DBS2b), with up to 4 cm displacement (Fig. 5c). Slip-surfaces are observed forming a mild graben-like structure in Face Map 7, conforming to the geometry that define DBS1 (Fig. 3c).

We have measured 71 near-vertical deformation bands that we assign to Defor-

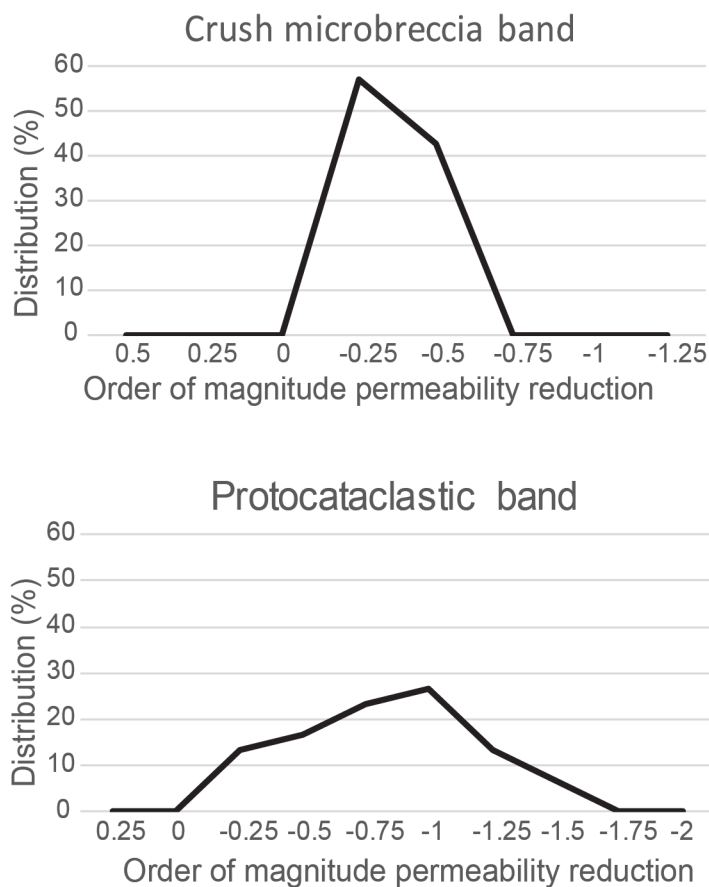


**Figure 9.** Histograms illustrating the distribution of cataclasis intensity permeabilities, represented by order of magnitude reduction.

	<b>Sibson, 1977</b>	<b>Ballas et al., 2015</b>	<b>This study</b>
<b>Classification scheme</b>	Textural classification of fault rocks	Cataclasis intensity classification scheme for siliciclastic-hosted deformation bands serving as a function for permeability	Cataclasis intensity classification scheme for carbonate-hosted deformation bands (DB)
<b>Low intensity cataclasis</b>	Crush micro-breccia (0-10% matrix)	Single strands of breccia (0-10% matrix)	Crush micro-breccia: <ul style="list-style-type: none"> <li>- Aperture: 1-5mm</li> <li>- Inner zone bioclasts are sub-aligned to aligned</li> <li>- Outer margin bioclasts are sub-aligned to DB orientation</li> <li>- Compaction extensive</li> <li>- Grain crushing minor</li> <li>- Pressure solution seams major</li> <li>- 0–10% deformation band matrix</li> </ul>
<b>Moderate intensity cataclasis</b>	Protocataclasite (10-50% matrix)	Single or a few strands of protocataclastic (10-50% matrix)–cataclastic bands (50-90% matrix)	Protocataclastic band: <ul style="list-style-type: none"> <li>- Aperture: 1-3mm</li> <li>- Sharp contrast between host rock and DB</li> <li>- Inner margin bioclasts display sub-alignment with DB. Bioclasts exhibit intense fracturing</li> <li>- Outer margin bioclasts align parallel to DB orientation</li> <li>- Grain crushing major</li> <li>- Pressure solution seams major</li> <li>- 10–50% deformation band matrix</li> </ul>
<b>High intensity cataclasis</b>	Cataclasite (50-90% matrix)	Band clusters, several strands of cataclastic bands (50-90% matrix)	Cataclastic band: <ul style="list-style-type: none"> <li>- Description N/A</li> <li>- 50–90% deformation band matrix</li> </ul>
<b>Ultrahigh intensity cataclasis</b>	Ultracataclasite (90-100% matrix)	Fault core, cataclastic (50-90% matrix)–ultracataclastic (90-100% matrix) band textures along slip surface	Ultracataclastic band: <ul style="list-style-type: none"> <li>- Description N/A</li> <li>- 90–100% matrix</li> </ul>

**Table 1.** Cataclasis classification scheme comparison chart.

Conjugate set	Set A				Set B				Dihe-dral angle	n
	Strike	Avg. strike	Dip dir.	Avg. dip	Strike	Avg. strike	Dip dir.	Avg. dip		
Stage 6	186	N-S	276	21	352	N-S	082	34	55	12
Stage 5	X	X	X	X	234	NE-SW	324	30	NA	10
Stage 4	154	NNW-SSE	NA	90	025	NNE-SSW	NA	90	NA	873
Stage 3	217	NE-SW	307	62	050	NE-SW	140	66	54	9
Stage 2	X	X	X	X	085	E-W	265	60	X	2
Stage 1	X	X	X	X	X	X	X	X	X	X

**Table 2:** Table of samples collected for porosity analysis at Sellicks Beach.

mation Band Set 3 (DBS3), with strikes ranging from WSW-ENE to N-SE (Fig. 4a). These deformation bands exhibit a wavy geometry with wavelengths ranging from 5–25 mm (Fig. 5e). This set forms individual structures ranging from 2–5 mm thickness, as well as anastomosing clusters of 3 to 10 bands ranging from 4–15 mm in width. There are no kinematic indicators that define shear displacement for DBS3.

We have measured 19 conjugate deformation bands that we assign to Deformation Band Set 4 (DBS4), with mean dihedral angles of 56° (Fig. 4a). This set is defined on the basis of its strike, ranging from NW-SE to N-S, and has an average dip of 53° towards the NE and SW (Fig. 4a). Individual bands have planar geometries, with thicknesses that range from 1–2 mm. Clusters of deformation bands have widths of up to 11 cm made up of 40–50 bands (Fig. 6a and Fig. 6d). At Sellicks Beach, DBS4 is observed to offset Sets 1, 2, and 3, with reverse-sense displacements of up to 10 cm (Fig. 5d and Fig. 5e respectively).

Discrete band segments commonly form ramp and eye structures (Fig. 5e and Fig. 5b respectively). Ramp structures connect two discrete deformation bands

that are offset from each other, whereas eye structures connect two discrete bands that are coplanar (Antonellini et al., 1994).

#### 4.2 Distribution and frequencies of the Port Willunga Formation deformation bands

The distribution of all DBS is uniform at Face Map 3 (Fig. 5a), coinciding with a pattern changes observed in the distribution of DBS2–4 (Fig. 7). The frequency of DBS2–4 generally increase with decreasing distance towards the Willunga Fault (Fig. 7). Deformation Band Set 1 is bedding parallel, and thus does not display any spatial variation between Face Maps 1–5. However, DBS1 is absent in Face Maps 6 and 7 (Fig. 4). Deformation Band Set 2, 3, and 4 are not spatially consistent, following different frequency and distribution trends with respect to the Willunga Fault (Fig. 7). The spatial distribution of DBS2a appears to be bimodal, peaking at the Willunga Fault and Face Map 2 (Fig. 7). However, important gaps in our database exist due to lack of outcrop. Deformation Band Set 3 also exhibits a bimodal distribution, peaking at the Willunga Fault and Face Map 3. The distribution of DBS4 appears to be trimodal, peaking at the Willunga Fault,

150 m from the Willunga Fault, and Face Maps 4–5. We note the lack of outcrop at Sellicks Beach may influence these results. Deformation Band Set 2, 3, and 4 located at Face Map 4 and Face Map 5 exhibit a mirrored distribution, based on the number of deformation bands per metre (Fig. 7). Here, DBS4 peaks at 1.2 deformation bands in one metre, just over three times more than that of DBS2 and DBS3. Face Maps 1–3 show a similar north-skewed distribution of DBS3 and DBS4; however, DBS2a shows a normal distribution, peaking at Face Map 2 (Fig. 7). Outcrop is scarce within 150 m of the Willunga Fault; PWF deformation bands show no clear trends or distributions for individual DBS within this range.

#### 4.3 Microstructural and petrographic characteristics and of carbonate-hosted deformation bands cataclastic textures

We observed two distinct cataclasis textures within the PWF, named crush micro-breccia and protocataclastic bands, adapted from the fault rock mechanism model by Sibson (1977) to incorporate carbonate deformation bands (Table 1). Microstructural and petrographic analysis listed in this section was conducted to investigate their characteristics.

Low intensity cataclasis textures appear in the field as positive relief structures with gradational boundaries between host rock and deformation band, with visible sub-aligned grains oriented to band (Fig. 6b). These bands are referred to as crush micro-breccia. Crush micro-breccia bands exhibit multiphase band zonation, previously described in carbonate grainstone cataclastic bands (e.g. Rath et al., 2011; Rotevatn et al., 2016; Tondi, 2007). The grain randomness contrast between host rock and deformation band is subtle, grading from randomly oriented bioclasts into a discrete zone of uniformly

oriented bioclasts in the outer zone. The inner zone is defined by sub-aligned and aligned bioclasts parallel to the strike of the deformation band, and an outer zone of sub-aligned bioclasts. Compaction and pore space reduction relative to host rock is extensive and mainly contained within the inner zone. The cumulative width of the inner and outer zones, ranges from 2.0–5.0 mm (Fig. 8b). Interestingly, comminution is minimal and is only accommodated by mechanically-weak fossils (e.g. collapsed bryozoan lattices); it does not occur in the stronger fossils (e.g. bivalves) (Fig. 8d). The occurrence of sutured grain boundaries with serrated edges observed at grain-to-grain contacts, is extensive within the inner zone (Fig. 8c). Crush micro-breccia bands are present in DBS1–4; these cataclasis textures show no clear relationship with the spatial distribution of DBS. Particle size distributions were calculated for crush micro-breccia band, showing a positive skew and wide range and the inner zone matrix accounts for 0.9% of the total volume (Fig. 8a). The particle size distribution results fall within the crush micro-breccia parameter by Sibson (1977), where the comminuted matrix must account for 0–10% (Table 1).

Moderate intensity cataclasis textures appear in the field as positive relief structures with sharp contrast boundaries between host rock and deformation band (Fig. 6c). These bands are referred to as protocataclastic bands. Protocataclastic bands exhibit multiphase band zonation, similar to carbonate grainstone bands described by Rotevatn et al. (2016). However, the alignment of bioclasts occurs in opposite zones from crush micro-breccia bands (Table 1). The outer zone bioclasts align parallel to the deformation band and form a sharp contact between the host and outer margin. The outer zone exhibits extensive compaction and moderate comminution of delicate fos-

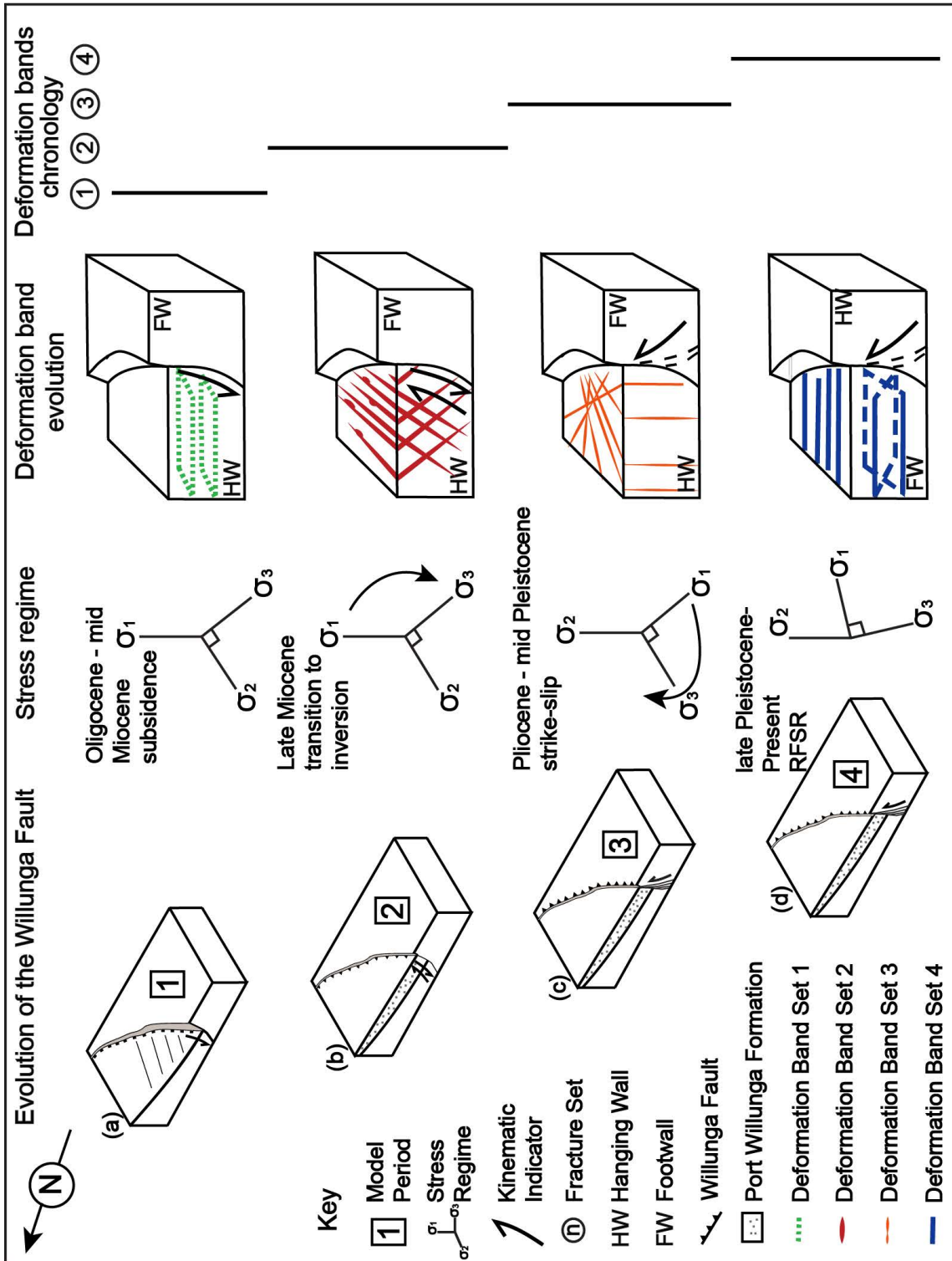


**Figure 10.** A schematic block diagram illustrating the neotectonic evolution of deformation bands and fractures in formations adjacent to the Willunga Fault: **(a)** Oligocene–late Miocene: deposition of Port Willunga Formation sediments in a normal fault stress regime, synchronous with the development of Deformation Band Set 1; **(b)** late Miocene: transition from a normal fault stress regime to a reverse fault stress regime (i.e. St. Vincent Basin inversion); **(c)** late Miocene: inversion coupled with sedimentary unloading of the St. Vincent Basin resulted in the clockwise rotation of  $\sigma_H$  from NNW-SSE to E-W; **(d)** late Pleistocene–Present day: E-W compression coupled with production of newly formed nearly-vertical Willunga Fault splays dipping towards the SW.

sils. The inner zone bioclasts exhibit sub-alignment with the deformation band (i.e. some grains align parallel to the band and some grains are oriented randomly), extensive compaction and comminution (i.e. breakdown and crushing of all bioclasts). The cumulative thickness of the inner and outer zones, ranges from 1.0–3.0 mm (Fig. 8). Sutured grain boundaries with serrated edges are observed at grain-grain contacts within the inner zone (Fig. 8c). Particle size distributions were calculated, showing a positive skew and wide range and the inner zone cataclastic matrix accounts for 20% of the total band volume (Fig. 8a). The particle size distribution results fall within the protocataclastic parameter by Sibson (1977), where the comminuted matrix must account for 10–50% (Table 1).

#### 4.4 Porosity and permeability

Crush micro-breccia band porosities calculated for samples 1G and 2G are 5.2% and 6.2% respectively. The absolute porosity of sample 1G containing both deformation band and host rock, is 31.2% (Table 2). Crush micro-breccia bands show a wide range in permeability results, ranging from  $1.8 \times 10^3$  mD to  $3.4 \times 10^3$  mD. Host-rock permeability averaged  $3.8 \times 10^3$  mD. Permeability analysis of eight crush micro-breccia bands indicates permeability reductions relative to host rock ranging from 0.0 up to 0.75 orders of magnitude (Fig. 9). Protocataclastic band porosities calculated for samples 5S and 6S, are 4.6% and 2.8% respectively. The absolute porosities of samples 5S and 6S containing both deformation band and host rock are 32.9% and 35.7% respectively (Table 2). Protocataclastic bands show a wide range in permeability results, ranging from  $2.47 \times 10^2$  mD to  $2.7 \times 10^3$  mD. Permeability analysis of 27 protocataclastic bands indicates permeability reductions relative to host rock ranging from ~0.25-

1.75 orders of magnitude (Fig. 9). Protocataclastic bands are present in DBS1–4; these cataclasis textures show no clear relationship with the spatial distribution of DBS. Cementation preferentially occurs along deformation band boundaries and is mainly observed in the protocataclastic bands. A radial isopachous fringe of fine grained acicular calcite is observed in thin section views of both intergranular pore spaces and void fossil chambers, in both deformation bands and host rock (Fig. 8). Void fossil chambers are well preserved. Dull black iron-hydroxide (i.e. goethite) cement is observed in both crush micro-breccia and protocataclastic bands, including all DBS within the PWF. Goethite is localized within the deformation band where present and does not occur within the host rock (Fig. 8). However, calcite cement is more prevalent of the PWF deformation bands. Two of eight samples collected from Sellicks Beach are protocataclastic bands cemented with goethite; these bands exhibit the lowest porosity (e.g. 1.8%), as calculated from sample 3B (Table 2). Protocataclastic bands cemented with goethite exhibit further reduced protocataclastic band porosity by at least ~1.0%. This is shown by comparing samples 3B and 4B (1.8% and 1.8% porosity respectively) containing iron-hydroxide cement with sample 5S and 6S (4.6% and 2.6% porosity respectively) containing calcite cement (Table 2).

#### 5. Discussion: The structural evolution of carbonate-hosted deformation bands within the Port Willunga Formation

There is a general lack of documented case studies focused on the sequential development of carbonate-hosted deformation bands, in comparison to those within sandstones which have been well studied (e.g. Agosta et al., 2010; Antonellini et al., 2008; Cilona et al., 2014;

Cooke et al., 2018; Michie, 2015; Tavani et al., 2018; Tavani et al., 2016; Ton-di et al., 2012; Wennberg et al., 2013; Wennberg and Rennan, 2018). Here, we provide a structural synthesis that reconciles the intricate geometrical and microstructural relationships observed in the cataclastic deformation bands within the PWF.

### 5.1 *The role of cement in deformation band porosity*

Iron-hydroxide cement is a secondary bonding cement found within PWF deformation bands. We attribute the origin of the iron-hydroxide cement to the presence of sedimentary pyrite and oxidizing glauconite. Glauconite is an iron-aluminium-rich detrital mineral with a hard siliceous shell, which readily oxidizes into iron oxide i.e. magnetite and goethite (El-Sharkawi and Al-Awadi, 1982; Prather, 1905). Goethite is a common weathering product of siderite, magnetite, and pyrite (Prather, 1905). Therefore, we make the interpretation that the fine grained magnetite found within the PWF and adjacent sands to be the result of oxidized glauconite, producing a readily available source of iron-oxide for the observed iron-hydroxide cemented deformation bands at Sellicks Beach and Port Willunga (Fig. 8).

Calcite is the main bonding cement found within the PWF deformation bands, unsurprisingly given the host formation is carbonate grainstone. Normally, deformation band cement is sourced from circulating ionic-rich formation fluids that readily react with fresh grain surfaces resulting from grain-boundary sliding and grain fracture. Cooke et al. (2018) suggested limited diagenesis within the Maltese Globigerina Limestone supported high initial porosity and poor lithification, which enhanced granular flow, pore space collapse, and permeability reduc-

tion. However, our results stray from those of Cooke et al. (2018). Pre-exposed surfaces of the host rock do not react with the formation fluids because diagenetic clays have usually formed a non-reactive barrier around the host rock grains (Fossen et al., 2007). Radial fine grained bladed calcite observed within void fossil chambers in both host rock and deformation bands of the PWF is indicative that the initial formation cement fluid was marine (Land, 1970). However, serrated and sutured grain boundaries at grain-grain contact points indicates the deformation bands have been subject to intergranular pressure solution, interpreted here as potential source of deformation band cement (Fig. 8c). Similar observations have been made in chalk and carbonate grainstone (e.g. Aydin et al., 2010; Gaviglio et al., 2009; Kaminskaite et al., 2019; Tondi, 2007; Tondi et al., 2016). This artefact is caused by disaggregation and mainly by cataclasis, which produce highly reactive fresh grain surfaces, and pressure solution which causes bioclastic pressure solution seams at grain boundaries. Pressure solution cement then precipitates in nearby void space. These processes collectively favour chemical precipitation of cement (e.g. Rustichelli et al., 2012).

### 5.2 *Carbonate cataclasis textures: a proxy for cataclasis intensity*

Two cataclasis textures are observed within PWF carbonate-hosted deformation bands, indicating two distinct phases of cataclasis development (Table 1). They therefore provide a proxy for cataclasis intensity. This proxy is based on textural characteristics of the carbonate and the degree of comminution, which are related to grain size distribution. We have described the textural characteristics of the cataclastic deformation bands listed in Table 1, using the fault rock textural classification scheme of Sibson

(1977) as a standard for cataclasis intensity. The deformation band matrix calculated from samples collected at Sellicks Beach falls within the appropriate range for crush micro-breccia and protocataclasis deformation (Table 1). Cataclasis intensity has been previously proposed by Antonellini et al. (2014b) and documented by Rotevatn et al. (2016). However, this classification scheme limits the documentable intensity of cataclasis. Rather, cataclastic bands are classified as cataclasis dominant or pressure solution dominant (Antonellini et al., 2014b; Rotevatn et al., 2016). However, nomenclature already exists for pressure solution dominant deformation bands (i.e. solution bands) (Fossen et al., 2007). We suggest the cataclasis intensity scheme of Sibson (1977) provides universal nomenclature for all cataclastic structures. This classification scheme is already used by Ballas et al. (2012) to describe siliciclastic cataclastic bands and appears to be applicable for carbonate-hosted deformation bands.

Cataclastic textures within the PWF exhibit a range of grain-grain relationships and fracturing mechanisms, evident specifically by bioclast shape, size, and orientation listed in Table 1. These are similar to what has been demonstrated in previous carbonate-based studies (Antonellini et al., 2014b; e.g. Baud et al., 2009; e.g. Baxevanis et al., 2006; Rotevatn et al., 2016; Vajdova et al., 2012; Vajdova et al., 2010). Microstructural analysis suggests crush micro-breccia accommodates intraparticle porosity collapse by flattening void fossil chambers via fracture. Intraparticle porosity collapse is accommodated by grain-boundary sliding, which also results in the alignment of elongate grains (Fig. 8b). Grain fracturing occurs primarily for, but is not limited to, mechanically weak fossils (e.g. bryozoan and gastropods), whereas mechanically strong fossils (e.g.

brachiopods and bivalves) are generally well-preserved and show only minor signs of post-depositional strain in crush micro-breccia. These more robust bioclasts types are heavily fractured but not heavily crushed, meaning the original bioclast itself remains easily identifiable (Fig. 8b). Delicate fossils like thin-wall chambered organisms and bryozoan lattice structures create potential weaknesses for fracture initiation. The irregular fossil shape promotes interlocking grain relationships and demote non-destructive granular flow, similar to what has been observed in echinoid fragments by Rotevatn et al. (2016) and foraminifera shell molds in chalk by Kaminskaite et al. (2019). This supports the notion that deformation initiates at irregularly shaped pore space observed by Zhu et al. (2010). Therefore, we make the interpretation that delicate bioclasts like intact bryozoan clasts promote mild cataclasis via fracture and disaggregation, which form the crush micro-breccia band textures observed at Sellicks Beach.

In contrast, protocataclastic bands exhibit full-fledged comminution and homogenization of bioclasts making the proto-fossil unidentifiable in most cases, similar to Antonellini et al. (2014b) and Rotevatn et al. (2016) (Fig. 8). Poor preservation of intact fossils with void fossil chambers and observable grain fracturing, yet low magnitude grain size reduction relative to host rock infers that these bands exhibit low magnitude of cataclasis intensity. Alignment of bioclast grains with the orientation of the deformation band suggests grain-boundary sliding accommodated rotation and alignment of bioclasts. The transition from low intensity cataclasis to moderate intensity cataclasis indicates that strain intensity has increased. We speculate changes in strain intensity may be caused by enhanced plate-scale forces accommodated by the Willunga Fault (e.g. Holford et al., 2011b). Chang-

es at the plate boundary resulted in the well-documented Willunga Fault inversion (e.g. Sandiford et al., 2009). We suggest Willunga Fault inversion resulted in burial depth fluctuations of the PWF, which caused local changes in the principal stress magnitudes (Fig. 10).

### 5.3 Structural evolution of the Willunga Fault

The chronological order of development for individual DBS was determined through observations of kinematic crosscutting relationships (Fig. 5). Deformation Band Set 4 crosscuts all other sets, indicating that it must be the youngest. Deformation Band Set 3 is not observed to be crosscut by DBS1 or DBS2a; given it is only crosscut by DBS4, this must be the third generation of deformation bands. We suggest DBS2a formed prior to DBS2b considering DBS2a implies extensional stress state geometry and DBS2b implies compressional stress state geometry (Fig. 4), given the local stress state evolved from extension to compression in the late Miocene (Tokarev, 2005). Deformation Band Set 2a and 2b crosscuts DBS1, indicating DBS1 is the oldest set.

We present a model that highlights the coevolution of low- and moderate-intensity cataclastic deformation bands, the result of burial depth and subsequent changes to the lithostatic load during reactivation of the Willunga Fault (Fig. 10). Deformation band architecture is governed by the principal stresses at the time of formation, making their strain features an excellent indicator of discrete changes in stress regime. The oldest documented structures at Sellicks Beach are DBS1, based on mutually exclusive crosscutting relationships with DBS1–3. We make the interpretation that DBS1 is PCB due to the lack of shearing, likely formed while primary porosity was high,

as a result of burial and diagenesis of the PWF sensu Tondi et al. (2006) (Fig. 10a). Deformation Band Set 2 (i.e. SECB) indicates this set formed next under a normal fault stress regime – where vertical stress ( $\sigma_v$ ) > maximum horizontal stress ( $\sigma_H$ ) > (minimum horizontal stress ( $\sigma_h$ )). Subsidence of the PWF increased accommodation space for sedimentation, enhancing the lithostatic load and increasing  $\sigma_v$  in the hanging wall of the Willunga Fault (i.e. the Willunga Embayment) (Fig. 10b). We postulate that the normal fault stress regime existed throughout the period of PWF sedimentation (i.e. Oligocene–late Miocene), providing a steadily increasing lithostatic load. Initial loading of the PWF would have resulted in a relatively low  $\sigma_v$  during the beginning of the Oligocene, producing low intensity strain features (i.e. crush micro-breccia); throughout the Oligocene and into the Miocene  $\sigma_v$  would have increased with higher lithostatic load, producing higher intensity strain features.

The late Miocene compressive pulse is well documented in southeast Australia (e.g. Holford et al., 2010; Holford et al., 2009; Holford et al., 2014; Sandiford, 2003), resulting in a disconformity at the upper boundary of the PWF (Tokarev, 2005). This pulse of compression caused inversion of the Willunga Embayment and increased  $\sigma_H$  (where  $\sigma_H > \sigma_v > \sigma_h$ ) resulting in formation of DBS2a. In a reverse fault stress regime uplift of the hanging wall will reduce  $\sigma_v$  due to erosion of hanging wall sediments, subsequently decreasing lithostatic load and  $\sigma_v$ . Therefore, cataclasis intensity would have begun to decrease at the late Miocene due to denudation and reduced lithostatic load of Willunga Embayment stratigraphy (Fig. 10b).

Tokarev (2005) and Jayawardena (2013) postulate that the Willunga Fault is partitioned into a series of fault splays that

resulted in the Willunga Fault hanging wall section being switched from Willunga Embayment stratigraphy to metasedimentary basement rocks of Willunga Hill (former footwall rocks). This change in fault orientation would have halted denudation of Willunga Embayment sediments and would have led to resumption of increasing sediment load by denudation of the adjacent uplifted basement and its sedimentation into the Willunga Embayment basin, increasing  $\sigma_v$  (where  $\sigma_h > \sigma_v > \sigma_h$ ). The change in Willunga Fault splay orientation resulted in the formation of DBS3, a set of strike-slip fault stress regime deformation bands.

The Willunga Fault switch produced a series of SE dipping splays denuding the metasediment basement and resulting in differential loading of the Willunga Fault by changes in hanging wall/footwall elevation. The high topographic relief of Willunga Hill results in a differential elevation of 350–430 m between the Willunga Hill hanging wall and Sellicks Beach footwall blocks in the present day, where rocks dip below sea level (Fig. 10d). The magnitude of differential elevation would have been greater prior to denudation in the past. Denudation of the newly formed hanging wall would have decreased  $\sigma_v$  in the hanging wall, thereby unloading lithostatic pressure acting upon overridden sediment package of the footwall block adjacent to the Willunga Fault, therefore decreasing  $\sigma_v$  for Willunga Embayment sediments located there (where  $\sigma_h > \sigma_h > \sigma_v$ ). This resulted in the formation of DBS4, a set of SECB. DBS4 formed most recently under reverse fault stress state. Thus,  $\sigma_v$  likely decreased resulting in cataclasis intensity decreasing (where  $\sigma_h > \sigma_h > \sigma_v$ ). The folded late Pleistocene Pookara Formation noted by Jayawardena (2013) indicates this stress state lasted until the end of the Pleistocene.

A by-product of our model constrains the

timing and evolution of palaeostress in the St. Vincent Basin, useful for developing temporal constraints on the timing of folding and emplacement of petroleum or mineral deposits. For example, Cenozoic compression in SE Australia resulted in basin inversion, amplifying anticline traps thereby influencing the location of hydrocarbons plays in the southern margin (Hillis et al., 2008; Holford et al., 2014). Similarly, Carboniferous compression in eastern Australia resulted in the formation of anticlines and subsequent saddle reef gold (Windh, 1995). Taken together, this demonstrates the necessity to define timing of changes to the palaeostress regime. We strongly suggest deformation bands are a sensitive indicator of local changes in the stress regime and therefore provide a method to unravel the evolution of stress and fault history.

#### 5.4 Willunga Fault splays

Grainstones accommodate strain by the process of pore space collapse, thereby forming discrete zones of localized strain rather than typical gouge zones observed in a rocks with poor primary porosity (Fossen et al., 2007). This difference in strain accommodation makes the precise location of sandstone and carbonate grainstone faults hard to pinpoint. We use the distribution of deformation bands observed in this study to indicate the potential location of carbonate grainstone fault splays named Splay 1–4. The distributions suggest an approximate location and array of fault mechanisms within the PWF based on strain frequencies in DBS2a, DBS3, and DBS4. To accommodate the strain distribution within the PWF, we assume the location of at least four Willunga Fault splays, with failures including high angle reverse and normal fault motion, and strike-slip fault motion. The idea of a partitioned Willunga Fault was first suggested by Tokarev (2005) and supported by Jayawardena (2013).

The apparent bimodal distribution frequency of DBS2a (i.e. normal fault bands) may infer a high angle normal fault strain accommodation at the Willunga Fault. Interestingly, a higher distribution is noted at Face Map 2 (Fig. 7). This correlation may imply the location of a fault splay (Splay 2) near Face Map 2 (Fig. 10c). The apparent unimodal distribution frequency of DBS3 (i.e. strike slip fault bands) may infer of a strike-slip fault strain accommodation located at Face Map 3 (Fig. 7). This pattern coincides with inflection points observed in the distribution of DBS2a and DBS4, indicating a shift in strain distribution in the PWF (Fig. 7). This correlation may imply the location of a fault splay (Splay 3) between Face Map 3 and Face Map 4 (Fig. 10c). The apparent trimodal frequency distribution of DBS4 (i.e. reverse fault bands) may infer enhanced strain accommodation at the frequency peaks located at the Willunga Fault, the break in outcrop (Splay 1), between Face Map 3 and Face Map 4 (Splay 3), and north of Face Map 5 (Splay 5). The apparent distribution peaks support the notion that the most recent period of reverse-faulting triggered the development of splay faults at these suggested localities (Fig. 7). The break in outcrop – perhaps an indication of faulting itself due to the lateral irregularity in PWF outcrop – represents a significant distance along Sellicks Beach that may host many unseen splay faults.

### *5.5 Implications for fluid flow in the Port Willunga Formation*

Ballas et al. (2015) suggested permeability is a function of cataclasis intensity in siliciclastic sandstones, whereby enhanced comminution is associated with permeability reduction. We argue that the cataclasis classification scheme used by Ballas et al. (2012) can also be applied to understand deformation band permeability

in carbonate rocks. We have compared the petrophysical characteristics of carbonate protocataclastic bands to carbonate crush micro-breccia bands, finding protocataclastic band porosity reductions between 1.6-3.4% greater than for crush micro-breccia and up to nearly two orders of magnitude reduction for permeability (Fig. 9). This suggests the permeability function developed by Ballas et al. (2015) would hold true for carbonate grainstone, whereby permeability is a function of cataclasis intensity in carbonate grainstones, with permeability reduced with increasing cataclasis. Singular cataclastic bands porosities and permeabilities are comparable to those measured by Rath et al. (2011), Antonellini et al. (2014b), Tondi et al. (2016), and Kaminskaite et al. (2019). However, these cases obtained higher magnitude reductions as their petrophysical data incorporated cataclastic clusters.

Protocataclastic bands containing iron-hydroxide cements exhibit the lowest overall deformation band porosities (e.g. 1.8%) and have lowest permeabilities relative to host rock within the PWF (e.g. nearly two orders of magnitude reduction) (Fig. 9). Therefore, we suggest that protocataclastic bands have the highest influence on fluid migration in the PWF. However, low band connectivity and band intersections represent zones of enhanced permeability and would be expected to permit fluid flow around and between the bands. Deformation Band Sets 3 and 4 form wide clusters, with widths measuring up to 11 cm (Fig. 4). Intrinsic permeability of the host rock between these clusters may not be significantly affected. Flow normal to the clusters will be subject to a permeability that is the net thickness-weighted harmonic mean of permeabilities for the cluster zones and inter-cluster zones. This permeability will be orders of magnitude lower than for cluster-parallel flow,

which will be the net thickness-weighted arithmetic mean of respective permeabilities e.g. Rotevatn et al. (2017); Rotevatn et al. (2016); Tondi et al. (2016). Another perspective would be to consider these clusters as no-flow zones that effectively eliminate some of the cross-sectional area available for cluster-parallel flow. In this respect, their presence would reduce volumetric flow rate in this direction. These arguments imply that deformation bands should reduce bulk permeability and align the permeability tensor of the PWF parallel to them wherever they occur, i.e. up to 1 km from the Willunga Fault (Fig. 7).

Carbonate-hosted deformation bands can have a permeability altering effect within a fault damage zone due to deformation band-induced permeability anisotropy, which in effect decreases bulk permeability and enhances flow in a preferred direction (e.g. Zambrano et al., 2017). As argued above, fluid generally flows parallel to the strike of conjugate deformation bands, rather than across a fault damage zone (Fossen and Bale, 2007). In undeformed host rock, maximum permeability is usually parallel to bedding, resulting from depositional alignment of sediment layers of particular textural maturity that is usually parallel to sub-parallel with zones of equal burial stress and compaction (Farrell et al., 2014; Zambrano et al., 2017). If we consider the PWF as a confining reservoir or aquifer, maximum permeability should therefore be parallel to the shallow southward dipping beds within the PWF. However, DBS3 and DBS4 form wide cluster zones and DBS2a–4 are oriented obliquely to bedding. This case study may infer compartmentalisation by the formation of semi-discrete chambers between which pore fluid pressures could develop without being able to equalise. However, the sealing capabilities of these cataclastic bands should not be consid-

ered 100% effective, as their thickness and continuity is heterogeneous (Antonellini et al., 2014a). Gravity driven meteoric water flows south-westward from on-shore recharge zones down-dip towards Sellicks Beach. This is apparent near the Willunga Fault, where we observe natural spring water emanating from the beach sands in isolated saturated patches adjacent to the outcrop.

## 6. Conclusions

- We present a uniform classification scheme for cataclastic carbonate deformation bands following the fault classification scheme used to define fault rocks. We have mapped 28 PCBs and 241 SECBs within the Oligocene-Miocene PWF, which define the structural evolution of the Willunga Fault.
- The cataclastic deformation bands within the PWF show a hierarchy of pore space and grain-size reduction based on their degree of disaggregation, comminution, pressure solution and cementation. Comminution increases with increasing deviatoric stress and thus defines a proxy for cataclasis intensity in carbonate rocks. We define these cataclastic intensities as crush micro-breccia and proto-cataclastic textures. Cataclasis intensity may also be used as proxy for permeability, as protocataclastic bands have the greatest permeability reducing effect in the PWF.
- Cataclasis is the primary controlling formation mechanism within the PWF deformation bands; disaggregation, pressure solution, and cementation also supportive deformation mech-

anism. Cementation is present both syn- and post-deformation.

- The majority of deformation is hosted within the hanging wall of the Willunga Fault, similar to our findings of DBS1 and DBS2a, which both formed within the hanging wall block of the Willunga Fault. However, the Willunga Fault blocks changed hanging wall/footwall relationship, resulting in DBS3 and DBS4 forming within the footwall block adjacent to the Willunga Fault.
- Our fault model shows that deformation bands are sensitive to the local stress regime; their interpretation therefore provides a method by which to unravel fault history. This work is widely applicable to regional basin evolution models, fundamental for modelling the development of petroleum and mineral deposits.

### Acknowledgements

We thank the Australian Research Council (DP1601158) and the Government of South Australia's Department of State Development and Geological Survey of South Australia for their financial support. We also thank Steve Hore, Tania Davies, Peter Reynolds, Hilary Pask, and Jonathan Berthiaume for their helpful discussions and field assistance.

### References

- Agosta, F., Alessandrini, M., Tondi, E., and Aydin, A., 2010, Oblique normal faulting along the northern edge of the Majella Anticline, central Italy: Inferences on hydrocarbon migration and accumulation: *Journal of Structural Geology*, v. 32, no. 9, p. 1317-1333.
- Allmendinger, R. W., Cardozo, N., and Fisher, D. M., 2012, *Structural geology algorithms: vectors and tensors*, New York, Cambridge University Press.
- Anderson, E. M., 1905, The dynamics of faulting: *Transactions of the Edinburgh Geological Society*, v. 8, no. 3, p. 387-402.
- Antonellini, M., and Aydin, A., 1994, Effect of faulting on fluid flow in porous sandstones: petrophysical properties: *AAPG bulletin*, v. 78, no. 3, p. 355-377.
- Antonellini, M., Cilona, A., Tondi, E., Zambrano, M., and Agosta, F., 2014a, Fluid flow numerical experiments of faulted porous carbonates, northwest Sicily (Italy): *Marine and Petroleum Geology*, v. 55, p. 186-201.
- Antonellini, M., and Mollema, P. N., 2015, Polygonal deformation bands: *Journal of Structural Geology*, v. 81, p. 45-58.
- Antonellini, M., Petracchini, L., Billi, A., and Scrocca, D., 2014b, First reported occurrence of deformation bands in a platform limestone, the Jurassic Calcare Massiccio Fm., northern Apennines, Italy: *Tectonophysics*, v. 628, p. 85-104.
- Antonellini, M., Tondi, E., Agosta, F., Aydin, A., and Cello, G., 2008, Failure modes in deep-water carbonates and their impact for fault development: Majella Mountain, Central Apennines, Italy: *Marine and Petroleum Geology*, v. 25, no. 10, p. 1074-1096.
- Antonellini, M. A., Aydin, A., and Pollard, D. D., 1994, Microstructure of deformation bands in porous sandstones at Arches National Park, Utah: *Journal of Structural*

- Geology, v. 16, no. 7, p. 941-959.
- Aydin, A., Antonellini, M., Tondi, E., and Agosta, F., 2010, Deformation along the leading edge of the Maiella thrust sheet in central Italy: *Journal of Structural Geology*, v. 32, no. 9, p. 1291-1304.
- Aydin, A., Borja, R. I., and Eichhubl, P., 2006, Geological and mathematical framework for failure modes in granular rock: *Journal of Structural Geology*, v. 28, no. 1, p. 83-98.
- Ballas, G., Fossen, H., and Soliva, R., 2015, Factors controlling permeability of cataclastic deformation bands and faults in porous sandstone reservoirs: *Journal of Structural Geology*, v. 76, p. 1-21.
- Ballas, G., Soliva, R., Sizun, J.-P., Benedicto, A., Cavailles, T., and Raynaud, S., 2012, The importance of the degree of cataclasis in shear bands for fluid flow in porous sandstone, Provence, France: *AAPG bulletin*, v. 96, no. 11, p. 2167-2186.
- Baud, P., Vinciguerra, S., David, C., Cavallo, A., Walker, E., and Reuschlé, T., 2009, Compaction and Failure in High Porosity Carbonates: Mechanical Data and Microstructural Observations, *in* Vinciguerra, S., and Bernabé, Y., eds., *Rock Physics and Natural Hazards*: Basel, Birkhäuser Basel, p. 869-898.
- Baxevanis, T., Papamichos, E., Flornes, O., and Larsen, I., 2006, Compaction bands and induced permeability reduction in Tuffeau de Maastricht calcarenite: *Acta Geotechnica*, v. 1, no. 2, p. 123-135.
- Bjørk, T. E., Mair, K., and Austrheim, H., 2009, Quantifying granular material and deformation: Advantages of combining grain size, shape, and mineral phase recognition analysis: *Journal of Structural Geology*, v. 31, no. 7, p. 637-653.
- Cann, J. H., Lower, C. S., and Jago, J. B., 2014, Provenance and sediment characteristics of contemporary gravel deposits at Sellicks Beach, eastern shore of Gulf St Vincent, South Australia: *Australian Journal of Earth Sciences*, v. 61, no. 6, p. 819-836.
- Cilona, A., Baud, P., Tondi, E., Agosta, F., Vinciguerra, S., Rustichelli, A., and Spiers, C. J., 2012, Deformation bands in porous carbonate grainstones: Field and laboratory observations: *Journal of Structural Geology*, v. 45, p. 137-157.
- Cilona, A., Faulkner, D. R., Tondi, E., Agosta, F., Mancini, L., Rustichelli, A., Baud, P., and Vinciguerra, S., 2014, The effects of rock heterogeneity on compaction localization in porous carbonates: *Journal of Structural Geology*, v. 67, p. 75-93.
- Cooke, A. P., Fisher, Q. J., Michie, E. A. H., and Yielding, G., 2018, Investigating the controls on fault rock distribution in normal faulted shallow burial limestones, Malta, and the implications for fluid flow: *Journal of Structural Geology*, v. 114, p. 22-42.
- Cooper, B. J., 1979, Eocene to Miocene stratigraphy of the Willunga Embayment: *Geological Survey of South Australia*, v. 50, p. 1-97.
- El-Sharkawi, M. A., and Al-Awadi, S. A., 1982, Alteration products of glauconite in Burgan oil field, Kuwait: *Journal of Sedimentary Petrology*, v. 52, no. 3, p. 999-1002.
- Fairburn, B., 1998, The Willunga Embayment - a stratigraphic revision: *Mineral Resources of South Australia*, v. 11, p. 35-41.
- Farrell, N. J. C., Healy, D., and Taylor, C. W., 2014, Anisotropy of permeability in faulted porous sandstones: *Journal of Structural Geology*, v. 63, p. 50-67.
- Flöttmann, T., and Cockshell, C. D., 1996, Palaeozoic basins of southern South Australia: New insights into their structural history from regional seismic data: *Australian Journal of Earth Sciences*, v. 43, no. 1, p. 45-55.
- Fossen, H., and Bale, A., 2007, Deformation bands and their influence on fluid flow: *AAPG Bulletin*, v. 91, no. 12, p. 1685-1700.

- Fossen, H., and Hesthammer, J., 1997, Geometric analysis and scaling relations of deformation bands in porous sandstone: *Journal of Structural Geology*, v. 19, no. 12, p. 1479-1493.
- Fossen, H., Schultz, R. A., Shipton, Z. K., and Mair, K., 2007, Deformation bands in sandstone: a review: *Journal of the Geological Society of London*, v. 164, no. 4, p. 755-769.
- Gaviglio, P., Bekri, S., Vandycke, S., Adler, P., Schroeder, C., Bergerat, F., Darquennes, A., and Coulon, M., 2009, Faulting and deformation in chalk: *Journal of structural geology*, v. 31, no. 2, p. 194-207.
- Hillis, R. R., Sandiford, M., Reynolds, S. D., and Quigley, M. C., 2008, Present-day stresses, seismicity and Neogene-to-Recent tectonics of Australia's 'passive' margins: intraplate deformation controlled by plate boundary forces: *Geological Society, London, Special Publications*, v. 306, no. 1, p. 71-90.
- Holford, S., Hillis, R., Duddy, I., Green, P., Tuitt, A., and Stoker, M., 2010, Impacts of Neogene-Recent compressional deformation and uplift on hydrocarbon prospectivity of the passive southern Australian margin: *The APPEA Journal*, v. 50, no. 1, p. 267-286.
- Holford, S., Hillis, R. R., Duddy, I. R., Green, P. F., Stoker, M., Tuitt, D., Backe, G., Tassone, D. R., and MacDonald, J. D., 2011a, Cenozoic post-breakup compressional deformation and exhumation of the southern Australian margin: *APPEA Journal*, v. 51, p. 613.
- Holford, S. P., Green, P. F., Duddy, I. R., Turner, J. P., Hillis, R. R., and Stoker, M. S., 2009, Regional intraplate exhumation episodes related to plate-boundary deformation: *Geological Society of America Bulletin*, v. 121, no. 11-12, p. 1611-1628.
- Holford, S. P., Hillis, R. R., Hand, M., and Sandiford, M., 2011b, Thermal weakening localizes intraplate deformation along the southern Australian continental margin: *Earth and Planetary Science Letters*, v. 305, no. 1, p. 207-214.
- Holford, S. P., Tuitt, A. K., Hillis, R. R., Green, P. F., Stoker, M. S., Duddy, I. R., Sandiford, M., and Tassone, D. R., 2014, Cenozoic deformation in the Otway Basin, southern Australian margin: implications for the origin and nature of post-breakup compression at rifted margins: *Basin Research*, v. 26, no. 1, p. 10-37.
- Jayawardena, C. L., 2013, Characteristics of neotectonic faulting in the Mount Lofty and Flinders Ranges, South Australia [Unpublished Ph.D. thesis]: University of Wollongong.
- Kaminskaite, I., Fisher, Q. J., and Michie, E. A. H., 2019, Microstructure and petrophysical properties of deformation bands in high porosity carbonates: *Journal of Structural Geology*, v. 119, p. 61-80.
- Land, L. S., 1970, Phreatic versus vadose meteoric diagenesis of limestones: evidence from a fossil water table: *Sedimentology*, v. 14, no. 3-4, p. 175-185.
- Micarelli, L., Benedicto, A., and Wibberley, C. A. J., 2006, Structural evolution and permeability of normal fault zones in highly porous carbonate rocks: *Journal of Structural Geology*, v. 28, no. 7, p. 1214-1227.
- Michie, E. A. H., 2015, Influence of host lithofacies on fault rock variation in carbonate fault zones: A case study from the Island of Malta: *Journal of Structural Geology*, v. 76, p. 61-79.
- Norvick, M. S., and Smith, M. A., 2001, Mapping the plate tectonic reconstruction of southern and southeastern Australia and implications for petroleum systems: *The APPEA Journal* v. 41, no. 15-35.
- Potts, G. J., and Reddy, S. M., 1999, Construction and systematic assessment of relative deformation histories: *Journal of Structural Geology*, v. 21, no. 8, p. 1245-1253.
- Prather, J. K., 1905, Glauconite: *The Journal of*

- Geology, v. 13, no. 6, p. 509-513.
- Rath, A., Exner, U., Tschegg, C., Grasemann, B., Laner, R., and Draganits, E., 2011, Diagenetic control of deformation mechanisms in deformation bands in a carbonate grainstone: *AAPG Bulletin*, v. 95, no. 8, p. 1369-1381.
- Rotevatn, A., Fossmark, H. S., Bastesen, E., Thorsheim, E., and Torabi, A., 2017, Do deformation bands matter for flow? Insights from permeability measurements and flow simulations in porous carbonate rocks: *Petroleum Geoscience*, v. 23, no. 1, p. 104-119.
- Rotevatn, A., Thorsheim, E., Bastesen, E., Fossmark, H. S. S., Torabi, A., and Sælen, G., 2016, Sequential growth of deformation bands in carbonate grainstones in the hangingwall of an active growth fault: Implications for deformation mechanisms in different tectonic regimes: *Journal of Structural Geology*, v. 90, p. 27-47.
- Rustichelli, A., Tondi, E., Agosta, F., Cilona, A., and Giorgioni, M., 2012, Development and distribution of bed-parallel compaction bands and pressure solution seams in carbonates (Bolognano Formation, Majella Mountain, Italy): *Journal of Structural Geology*, v. 37, p. 181-199.
- Sandiford, M., 2003, Neotectonics of southeastern Australia: linking the Quaternary faulting record with seismicity and in situ stress: *Geological Society of America Special Papers*, v. 372, p. 107-119.
- Sandiford, M., Quigley, M., de Broekert, P., and Jakica, S., 2009, Tectonic framework for the Cenozoic cratonic basins of Australia: *Australian Journal of Earth Sciences*, v. 56, no. sup1, p. S5-S18.
- Sibson, R. H., 1977, Fault rocks and fault mechanisms: *Journal of the Geological Society*, v. 133, no. 3, p. 191-213.
- Skurtveit, E., Torabi, A., Gabrielsen, R. H., and Zoback, M. D., 2013, Experimental investigation of deformation mechanisms during shear-enhanced compaction in poorly lithified sandstone and sand: *Journal of Geophysical Research*, v. 118, no. 8, p. 4083-4100.
- Tavani, S., Granado, P., Balsamo, F., Pizzati, M., Cantarero, I., Corradetti, A., and Muñoz, J., 2018, Shear-enhanced compaction-solution bands in quartz-rich calcarenites of the Cotiella Massif (Spanish Pyrenees): *Journal of Structural Geology*, v. 114, p. 274-279.
- Tavani, S., Vitale, S., Grifa, C., Iannace, A., Parente, M., and Mazzoli, S., 2016, Introducing dolomite seams: hybrid compaction-solution bands in dolomitic limestones: *Terra Nova*, v. 28, no. 3, p. 195-201.
- Tokarev, V., 2005, Neotectonics of the Mount Lofty Ranges, South Australia [PhD Thesis]: University of Adelaide.
- Tokarev, V., Sandiford, M., and Gostin, V., 1999, Landscape evolution in the Mount Lofty Ranges: implications for regolith development, *in* Taylor, G., and Pain, C., eds., *New Approaches to an Old Continent, Proceedings of Regolith '98, 3rd Australian Regolith Conference: Kalgoorlie, WA, Cooperative Research Centre for Landscape & Mineral Exploration, Perth*, p. 131-139.
- Tondi, E., 2007, Nucleation, development and petrophysical properties of faults in carbonate grainstones: Evidence from the San Vito Lo Capo peninsula (Sicily, Italy): *Journal of Structural Geology*, v. 29, no. 4, p. 614-628.
- Tondi, E., Antonellini, M., Aydin, A., Marchegiani, L., and Cello, G., 2006, The role of deformation bands, stylolites and sheared stylolites in fault development in carbonate grainstones of Majella Mountain, Italy: *Journal of Structural Geology*, v. 28, no. 3, p. 376-391.
- Tondi, E., Cilona, A., Agosta, F., Aydin, A., Rustichelli, A., Renda, P., and Giunta, G., 2012, Growth processes, dimensional parameters and scaling relationships of two conjugate sets of compactive shear

- bands in porous carbonate grainstones, Favignana Island, Italy: *Journal of Structural Geology*, v. 37, p. 53-64.
- Tondi, E., Rustichelli, A., Cilona, A., Balsamo, F., Storti, F., Napoli, G., Agosta, F., Renda, P., and Giorgioni, M., 2016, Hydraulic properties of fault zones in porous carbonates, examples from central and southern Italy: *Italian Journal of Geosciences*, v. 135, no. 1, p. 68-79.
- Vajdova, V., Baud, P., Wu, L., and Wong, T.-f., 2012, Micromechanics of inelastic compaction in two allochemical limestones: *Journal of Structural Geology*, v. 43, p. 100-117.
- Vajdova, V., Zhu, W., Natalie Chen, T.-M., and Wong, T.-f., 2010, Micromechanics of brittle faulting and cataclastic flow in Tavel limestone: *Journal of Structural Geology*, v. 32, no. 8, p. 1158-1169.
- Wennberg, O. P., Casini, G., Jahanpanah, A., Lapponi, F., Ineson, J., Wall, B. G., and Gillespie, P., 2013, Deformation bands in chalk, examples from the Shetland Group of the Oseberg Field, North Sea, Norway: *Journal of Structural Geology*, v. 56, p. 103-117.
- Wennberg, O. P., and Rennan, L., 2018, A brief introduction to the use of X-ray computed tomography (CT) for analysis of natural deformation structures in reservoir rocks: Geological Society, London, Special Publications, v. 459, no. 1, p. 101-120.
- Windh, J., 1995, Saddle reef and related gold mineralization, Hill End gold field, Australia; evolution of an auriferous vein system during progressive deformation: *Economic Geology*, v. 90, no. 6, p. 1764-1775.
- Wong, P., 1999, *Methods in the physics of porous media*: Elsevier, v. 35, p. 361.
- Zambrano, M., Tondi, E., Mancini, L., Arzilli, F., Lanzafame, G., Materazzi, M., and Torrieri, S., 2017, 3D Pore-network quantitative analysis in deformed carbonate grainstones: *Marine and Petroleum Geology*, v. 82, p. 251-264.
- Zhu, W., Baud, P., and Wong, T.-f., 2010, Micro-mechanics of cataclastic pore collapse in limestone: *Journal of Geophysical Research: Solid Earth*, v. 115.

---

# CHAPTER 4

---

# Statement of Authorship

Title of Paper	The effects of dilation bands on uranium mineralization in sedimentary sequences: a case study from the Flinders Ranges, South Australia
Publication Status	<input type="checkbox"/> Published <input type="checkbox"/> Accepted for Publication <input type="checkbox"/> Submitted for Publication <input checked="" type="checkbox"/> Unpublished and Unsubmitted work written in manuscript style
Publication Details	Lubiniecki, Drew Christopher, et al. "The effects of dilation bands on uranium mineralization in sedimentary sequences: a case study from the Flinders Ranges, South Australia" Journal of Geology (2019).

## Principal Author

Name of Principal Author (Candidate)	Drew Lubiniecki		
Contribution to the Paper	Completed fieldwork, collected and interpreted data, collected and analysed samples, wrote and prepared manuscript, acted as corresponding author.		
Overall percentage (%)	75%		
Certification:	This paper reports on original research I conducted during the period of my Higher Degree by Research candidature and is not subject to any obligations or contractual agreements with a third party that would constrain its inclusion in this thesis. I am the primary author of this paper.		
Signature		Date	05/04/19

## Co-Author Contributions

By signing the Statement of Authorship, each author certifies that:

- i. the candidate's stated contribution to the publication is accurate (as detailed above);
- ii. permission is granted for the candidate to include the publication in the thesis; and
- iii. the sum of all co-author contributions is equal to 100% less the candidate's stated contribution.

Name of Co-Author	Simon Holford		
Contribution to the Paper	Supervised fieldwork, aided in collection of data and samples, helped with data interpretation and manuscript revision.		
Signature		Date	5/4/19

Name of Co-Author	Rosalind King		
Contribution to the Paper	Supervised fieldwork, aided in collection of data and samples, helped with data interpretation and manuscript revision.		
Signature		Date	5/4/2019

Name of Co-Author	Mark Bunch		
Contribution to the Paper	Supervised fieldwork, aided in collection of data and samples, helped with data interpretation and manuscript revision.		
Signature		Date	05/04/2019

Name of Co-Author	Stephen Hore		
Contribution to the Paper	Supervised fieldwork, aided in collection of data and samples, and helped with data interpretation.		
Signature		Date	8/4/19

Name of Co-Author	Steven Hill		
Contribution to the Paper	Financial support, government correspondent, and overall concept of thesis.		
Signature		Date	2/4/19

Please cut and paste additional co-author panels here as required.

---

# The effects of dilation bands on uranium mineralization in sedimentary sequences: a case study from the Flinders Ranges, South Australia

---

## Abstract

Deformation bands form as discrete zones of localised strain in granular-sedimentary rocks, resulting in pore volume alteration. The presence of dilation bands at the Dead Tree section — within the step over zone of the Paralana and Four Mile faults — demonstrates localised fault-related extension and enhanced subsurface fluid flow. The Dead Tree section provides a natural laboratory to study mineralised fluid pathways, located intermediately between the uplifted radiogenic Mt. Painter Inlier and the Four Mile uranium deposit. We have documented and analysed 286 individual deformation bands using a permeameter, micro computed tomography, stereonet software, digital image analysis software, and petrographic microscopy. Field observations indicate that palaeo-redox roll front deposits rich in uranium (57 ppm) and thorium (706 ppm) are spatially correlated with the dilation bands documented in this study. We present a conceptual model to account for the microstructural evolution of dilational bands. This work may have economic implications for pre-drilling exploration of sedimentary-hosted copper and uranium mineralisation systems.

**Keywords:** Sedimentary-hosted mineralisation, uranium, Paralana Fault dilation band, deformation band, Flinders Ranges, Lake Lyre Basin

---

## 1.0 Introduction

Deformation bands are discrete, millimetre to centimetre wide tabular zones of localised strain that form as a result of faulting within porous granular sedimentary rocks (Fossen et al., 2007). Deformation bands accommodate strain pore space collapse (compaction band) or pore space inflation (dilation band), invoking mechanical deformation processes like grain boundary sliding, grain fracture, grain alignment, pressure solution, and/or cementation (Fossen et al., 2007). Dilation bands have been predicted theoretically (e.g. Bésuelle, 2001b), produced in lab experiments (e.g. Bésuelle, 2001a), and rarely observed in the field (e.g. Alikarami and Torabi, 2015; Antonellini et al., 1994; Du Bernard et al., 2002; Exner et al., 2013; Lommatzsch et al., 2015), resulting in a literature gap (e.g. Schultz and Siddharthan, 2005). Dilation bands are characterised by volumetric strain and enlarged intra-band pore spac-

es relative to host rock (Du Bernard et al., 2002), resulting in permeability anisotropy within fault zones (sensu Farrell et al., 2014). Increased porosity significantly enlarges pore throat diameters, resulting in enhanced permeability and the formation of conductive fluid conduits (Schultz and Siddharthan, 2005).

The origin and development of the sedimentary-hosted Four Mile uranium deposit in the northern Flinders Ranges, South Australia, and by extension the adjacent Beverly uranium deposit, is a subject of some debate, with both meteoric- and basement-sourced fluid models having been proposed for their genesis (e.g. Brugger et al., 2005; Haynes, 1975; Wilson, 2015; Wülser et al., 2011). However, geologically-recent faulting and related brittle deformation structures have rarely been considered important factors controlling mineralisation. Deformation bands are brittle deformation structures and their impacts on fluid flow in petro-

leum reservoirs is well documented (e.g. Fossen and Bale, 2007; Rotevatn et al., 2013). For example, deformation bands have been used as important indicators of faulting and structural permeability (e.g. Fossen and Bale, 2007; Ngwenya et al., 2003; Rotevatn et al., 2013). More specifically, compaction band arrays may baffle fluid flow, influence flow patterns, and cause compartmentalisation of fluids (Eichhubl et al., 2004; Sternlof et al., 2004; Taylor and Pollard, 2000). However, there is a poor understanding concerning the development of dilational deformation bands and their impacts on mineralising fluid flow.

Current mineralisation models for the Four Mile and Beverley uranium deposits are over-simplified and neglected to consider Paralana and Four Mile fault geometry in their analyses (e.g. Wilson, 2015; Wülser et al., 2011). A recent study by Skirrow et al. (2009) suggested an incomplete conceptual model of the regional and local geological controls of uranium mineralisation in the Lake Frome Region and therefore, there may be larger deposits that are yet to be discovered. The Four Mile uranium deposit is hosted within the Eyre Formation, an Eocene kaolinized quartz sandstone located eleven kilometres northwest of Beverley and less than one kilometre from the range front (Alliance, 2009). The Dead Tree section is located along the eastern flank of the northern Flinders Ranges in South Australia, intermediately between the uplifted radiogenic Mt. Painter Inlier and the Four Mile West Uranium deposit, providing exceptional exposures of anomalously high uranium- and thorium-bearing palaeo-redox roll fronts (Hore and Hill, 2009). The Dead Tree section provides an excellent natural analogue for the sub-surface Uranium deposits because the Eyre Formation outcrop demonstrates

a potential palaeo fluid pathway from source to deposit. This is the first documented case study relating deformation bands to sedimentary-hosted mineralisation.

We present a geomechanic study focused on elucidating the microstructural evolution of dilational deformation bands and their relationships to sedimentary-hosted uranium mineralisation in the northern Flinders Ranges, South Australia. Permeability enhancing dilation bands have been identified within the Eyre Formation at the Dead Tree section. We define their microstructural evolution and provide a four stage evolution model that demonstrates cyclic pore space enhancement, subsequent cementation, and finally fracture via crack propagation. The evidence we present suggests that the dilation bands documented here have evolved into discrete fluid conduits, potentially facilitating uranium-rich fluid flow from the Mount Painter Inlier into the Lake Eyre Basin. We demonstrate that a transtensional fault jog connecting two sections of the Paralana Fault near the Dead Tree section is responsible for localised extension and accommodation of volumetric strain (i.e. dilation bands) within the Eyre Formation. Our conceptual models are based on fundamental structural principles and can be easily adapted to other localities using our framework of geological field mapping methods; combined these may provide a cheap exploration tool for mineral exploration further along the eastern front of the northern Flinders Ranges and in other range settings with high abundances of economic minerals like uranium and copper.

## **2.0 Geological Setting**

The northern Flinders Ranges are well known for its abundance in uranium

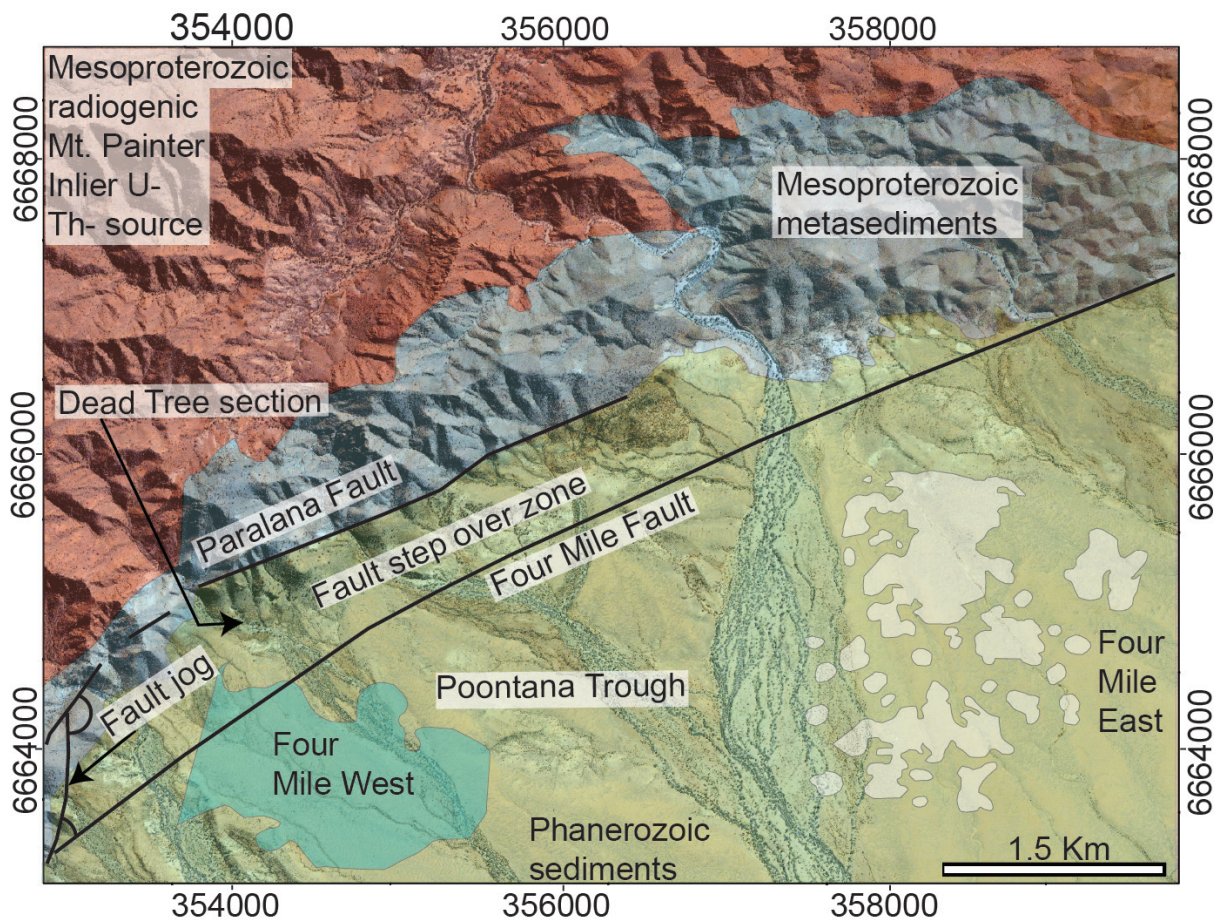


**Figure 1.** Geological map of the Dead Tree section.

mineralisation, e.g., Mount Gee, Beverley, and Four Mile uranium deposits, all located within 15 km radius (Wülser et al., 2011). The Four Mile uranium deposit is hosted within the Eyre Formation and is well exposed along the range front at the Dead Tree section (Fig. 1) (Alliance, 2009; Hore and Hill, 2009). The Dead Tree section is flanked by the Paralana Fault, situated along the edge of the Mesoproterozoic–Neoproterozoic Mt. Painter Inlier granites, gneisses, and Adelaidean Sequence metasediments (Hore and Hill, 2009). The Paralana Fault initially developed as an extensional fault during the Middle Proterozoic, and has been intermittently active since (Preiss, 1990). The Paralana fault inverted during the Cambrian–Ordovician Delamerian Orogeny, which caused intense deformation of the Adelaidean cover sediments,

including exhumation and denudation of the radiogenic Mount Painter and Mount Babbage Inliers (Paul et al., 1999).

The Eyre Formation is composed of kaolinized sandstones and siltstones that were deposited by braided streams during subsidence of the Lake Eyre Basin in the middle Eocene; it disconformably overlies Mesozoic sandstones and shales (Drexel and Preiss, 1995). At the Dead Tree section, the Eyre Formation is layered, alternating from fine-grained sandstone to coarse-grained sandstone stained with iron oxide. The Delamerian Orogeny uplifted and deformed the Adelaidean Sequence originally during the Late Cambrian (Foden et al., 2006). However, recent strain accommodation and neotectonic uplift in the Flinders Ranges has resulted from redistribution

Name	$\sigma_H$	Stress Regime	Set A				Set B				Dihedral angle
			Strike	Average strike	Dip direction	Average dip	Strike	Average strike	Dip	Average dip	
EF4b	NE-SW	Strike-slip	228	NE-SW	-	87	114	NW-SE	-	86	66°
EF4a	NE-SW	Reverse	129	NW-SE	SW	42	012	N-S	E	27	60°
EF3	NW-SE	Reverse	229	NE-SW	NW	17	021	N-S	E	45	60°
EF2b	N-S	Strike-slip	319	NW-SE	-	85	206	NE-SW	-	82	68°
EF2a	N-S	Reverse	319	NW-SE	NE	40	051	NE-SW	SE	38	54°
EF1	E-W	Normal	265	E-W	N	47	265	E-W	S	67	68°

**Table 1.** Table of deformation band data observed from the Eyre Formation at the Dead Tree section.

of Indo-Australian Plate boundary stresses (Hillis et al., 2008). Redistribution of intraplate strain accommodation resulted in Quaternary reverse faulting along the Paralana Fault zone (e.g. Quigley et al., 2006; Sandiford, 2003).

### 3.0 Methods

Deformation bands were analysed using micro computed tomography (CT) to produce a 3D porosity model to help visualise the vuggy third order pore space (Fig. 3c). Porosity was first analysed using digital image analysis software called Image J, then results were matched for thresholds using CTan software. Images produced with CTan demonstrates intricate network of elongated third order pore space within the dilation bands (Fig. 3c). To further constrain petrophysical characteristics of deformation bands and host rock, we quantified permeability in the field using a TinyPerm III Portable Air Permeameter by New England Research. Permeability was measured perpendicular to strike in the field. The permeameter was calibrated by New England Research and provides reliable permeability values ranging from 1 mD to

10 D. Outcrop was carefully scrapped with a putty knife and brushed clean prior to measurement. Data was collected in flat spots using a 6 mm rubber nozzle to support a good a seal and prevent air leaking from the permeameter. Permeability analysis were conducted on the alternating coarse- and fine- grained strata within the host rock at the Dead Tree section.

### 4.0 Structural Data

#### 4.1 Field observations

We have observed and recorded 286 deformation bands within the Eyre Formation at the Dead Tree section (Fig. 2). Deformation bands there appear in two forms: Type 1) well-cemented; and Type 2) friable. Well-cemented bands are bonded with white and pink silica cement, and contain an intricate network of elongated vuggy pore space (>1mm vugs) and interstitial quartz grains visible in hand samples (Fig. 3a). All Type 1 deformation bands exhibit red hematite staining on outer surfaces of the cement. Friable bands are reduced to mainly non-consolidated, fine-grained white

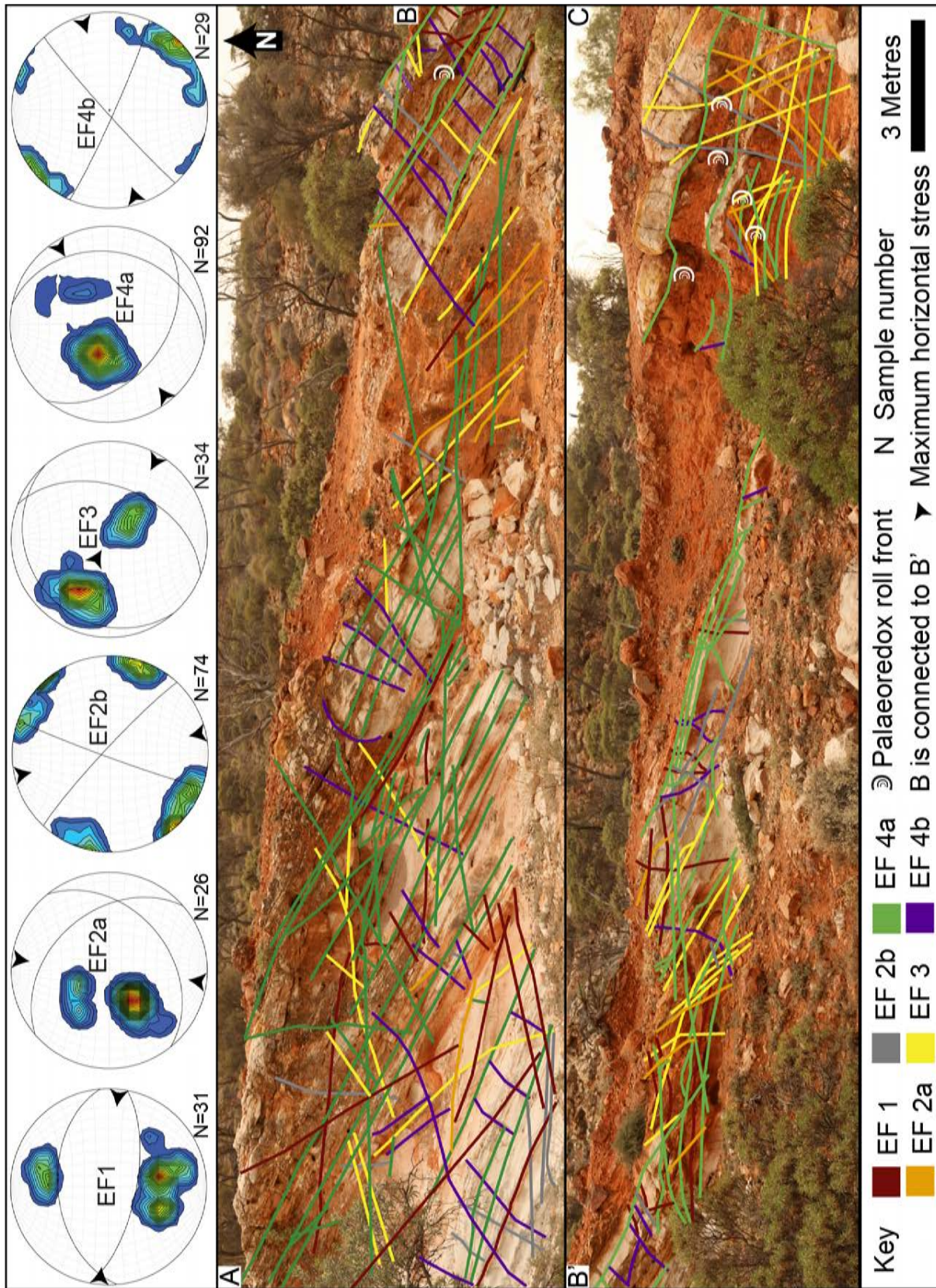


**Figure 2.** Detailed face maps of the deformation bands within the Eyre Formation, cropping out at the Dead Tree section; B connects with B'. Stereonet diagrams demonstrate the structural evolution of deformation bands at the Dead Tree section.

siliceous dust, with remnant quartz grains and fragments of preserved cement. Individual deformation of both types of bands display thicknesses ranging from 1–6 mm, with large clusters reaching thicknesses of up to 50 mm (Fig. 3a). Shear-offsets of bedding and other deformation bands range in magnitude from 1–8 cm (Fig. 2). We note that the vuggy cement absorbed a vast amount of epoxy via wicking action when preparing samples for thin sections, infiltrating the entire deformation band leaving the adjacent host rock void of epoxy. This implies high porosity and permeability relative to host rock.

Deformation bands were classified following the scheme described by Aydin et al. (2006), and categorized based on: a) their orientation relative to bedding (unfolded to 30/110); b) presence of observable shear offset; c) geometry; and d) cross-cutting relationships. Structural measurements were collected in the field, then processed and analysed using Stereonet and Gigapan high-resolution imagery. Individual deformation bands are grouped into six individual sets that can be further grouped into four generations defined by their inferred palaeostress, named Eyre Formation (EF) 1–4 (Table 1). Eyre Formation 1 bands are friable and strike east-west, dipping moderately towards the north and south (Fig. 2). Eyre Formation 2a bands are well cemented and strike north-east-southwest and northwest-southeast, dipping shallowly towards the southeast and northeast, respectively (Fig. 2). Eyre Formation 2b bands are well cemented and strike north northeast-south southwest and northwest-southeast, dipping near vertical (Fig. 2). Eyre Formation 3 bands encompass both well cemented and friable, striking northeast-southwest and dipping shallowly towards the

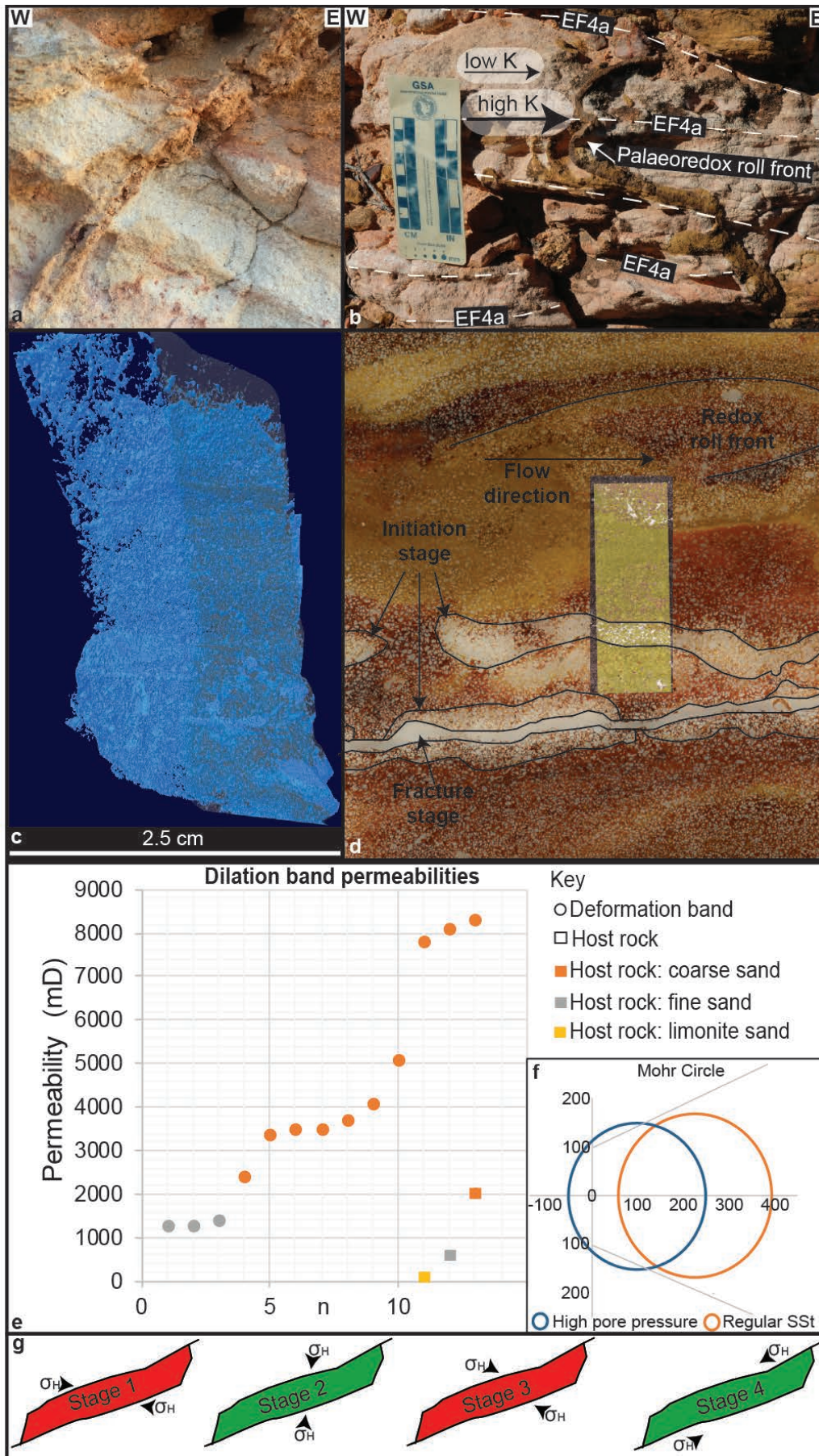
northwest and southeast (Fig. 2). Eyre Formation 4a bands are well cemented, iron oxide stained (Fig. 3a), and strike northwest-southeast and north-south, dipping shallowly towards the southwest and east, respectively (Fig. 2). Eyre Formation 4b bands are well-cemented, iron-oxide stained (Fig. 3a), and strikes east northeast-west southwest and west northwest-east southeast, dipping nearly vertical (Fig. 2). Deformation band sets EF2 and EF4 from groups of two individual sets because their consecutive formation based on cross-cutting relationships and imply similar maximum horizontal stress orientations (i.e., EF2a–EF2b, EF4a–EF4b; Fig. 2).

#### 4.2 Microstructural analysis

We conducted a microstructural analysis on eight thin sections using an optical microscope, highlighting a four-stage evolution sequence, from nascent deformation bands to thoroughgoing fractures. This was based on observed relationships between quartz grains, pore space, and host wall rock. The observed evolutionary sequence is as follows:

Stage 0) Undeformed host rocks exhibit multiple grain-grain contact points per grain, syntaxial quartz overgrowth, and randomly enlarged pore space between grain contact points (Fig. 4a).

Stage 1) The nascent stage of deformation band development is characterised by simple shear dilation of grain-grain contact points, breaking of syntaxial grain-bonding cements, and formation of epitaxial iron-hydroxide cement (Fig. 4b). Observed features that illustrate initial dilation are enhanced pore space between grains, decreasing grain boundary contact points, and minor remnants of quartz overgrowth cement (Fig. 3c & 4b).



Stage 2) The juvenile stage of deformation band development is characterized by cement dissolution, defined by appearance of third-order elongated vuggy porosity. We define first order porosity as primary, second order porosity as enlarged primary porosity (i.e., dilation band) now filled with quartz cement, and third order porosity are the dissolution vugs forming within the quartz cement. Epitaxial iron-hydroxide appears on quartz grains, and on the rims of the enlarged vuggy third-order porosity (Fig. 4c).

Stage 3) The mature stage of deformation band development is characterised by observable gradation in the decrease of grain contact points from host rock into dilation band. The host rock walls are completely separated, bound by cement, and cohesive gradation of dilatant grains. A thick band of zoned cement (e.g. 5–15 mm) binds the dispersed interstitial grains and third-order vuggy porosity. Epitaxial iron-hydroxide is observed on quartz grains, filling pore space in host rock, and on the rims of the enlarged vuggy porosity; syntaxial quartz cement forms the main band binding structure (Fig. 3c & 4d).

Stage 4) The fracture stage deformation development is characterised by dilation of individual grains within wall rock, with sharp cusped boundaries enveloping syntaxial quartz cement infill. Quartz cement is observed encompassing rafts of floating wall rock and forming third order porous vugs, which themselves exhibit epitaxial iron hydroxide

rims (Fig. 4e).

### 4.3 Porosity and permeability

Pore space observed in Figure 4b–4e has been subsequently infilled with epitaxial iron-hydroxide cement (Fig. 4b), and syntaxial silica (Fig. 4c–4e) and retains no original or secondary porosity. Deformation bands with intact secondary porosity exist (Fig. 3d) but are difficult to distinguish in the field because they blend in with the kaolinized sandstone. Third-order pore space vugs appear in Figure 4c–4e within pre-existing cemented deformation bands that are composed mainly of silica cement. Vugs are elongated, and not obviously well connected in two-dimensional cross sections (Fig. 4c–4e). However, Micro CT indicates 16.1% of deformation band space comprises pore space within sample DL1, of which 14.5% is open porosity from a dilation band hosted within fine-grained sand (Fig. 3c). These results imply that 90% of deformation pore space is readily available to conduct fluid flow.

Permeability analysis highlights the contrast between the highly permeable hematite-stained coarse-grained sediments (avg. 2040 mD), and the low permeability, fine-grained kaolinized sediments (avg. 638.7 mD) (Fig. 3e). Interestingly, thin layers of limonite-stained sediments exhibit the lowest overall average permeability of 123.9 mD. We sampled permeability on 12 cemented deformation bands, with results indicating an average permeability of 7,600 mD with a standard deviation of 4,055 mD. Permeability data reveals a linear trend of increasing per-

**Figure 3.** (a) Photograph of a dilation band observed at the Dead Tree section. (b) Photograph of a dilation band cross-cutting a dilation band observed at the Dead Tree section. (c) Computed Tomography (CT) image of a dilation band sampled from the Dead Tree section. (e) Dot plot illustrating dilation band permeabilities measured at the Dead Tree section. (f) Mohr Circle illustrating an increase in pore pressure. (g) Conceptual structural evolution model of the Paralana-Four Mile fault zone.

meability with increasing grain size (Fig. 3e).

#### *4.4 Palaeo-redox roll fronts*

Eyre Formation sandstone-hosted palaeo-redox roll fronts are the main style of uranium mineralisation at the Four Mile deposit (Alliance, 2009). Hore and Hill (2009) documented and analysed a series of palaeo-redox roll fronts rich in uranium and thorium within the Eyre Formation at the Dead Tree section (mapped in Figure 2). Palaeo-redox roll fronts contain uranium concentrations that range from 20 ppm to 57 ppm and anomalously high thorium concentrations that range from 25 ppm to 706 ppm (Hore and Hill, 2009). The palaeo-redox roll fronts exhibit lobate morphologies and they exhibit a distinct spatial relationship with the deformation bands documented in this study (Fig. 3b). Palaeo-redox roll fronts either form parallel to the east-dipping planes of EF3 (in one case the palaeo-redox front cross-cuts EF3), or cross-cut the east-dipping planes of EF4a (Fig. 2). Figure 3d demonstrates this coupled relationship by the juxtaposition of palaeo-redox roll fronts to parallel fractures and deformation bands. Deformation bands do not displace palaeo-redox fronts in the way they offset bedding surfaces. However, dilation bands seem to influence the morphology of the palaeo-redox fronts where coupled by causing an inverse lobate form to what would normally be expected of fluids migrating down-dip (Fig. 3b). We suggest this unique relationship implies higher flow rates of U and Th-bearing fluids along the dilation band relative to host rock; a model supported by higher measured dilation band permeabilities and lower measured host rock permeabilities (Fig. 3e). The enhanced permeability of dilation bands may explain the observation that epoxy

resin became wicked through samples when preparing for thin sections.

### **5.0 Discussion: Structural evolution of deformation bands at the Dead Tree section**

Here, we present a regional and microstructural analysis demonstrating the evolution of shear-enhanced dilation bands into fractures, and an association between their petrophysical properties and localised uranium mineralisation. Intrinsic factors that control the development of deformation bands include: confining pressure, deviatoric stress, pore fluid pressure, degree of lithification, mineralogy, grain size, grain shape, and sorting (Fossen et al., 2007). We argue that fault geometry, high pore fluid pressure, poor lithification, and low confining pressure are the main mechanical factors controlling the development of deformation bands at the Dead Tree section, and we explore their potential role in enabling meteoric fluid migration from the Flinders Ranges to the nearby economic uranium deposits.

#### *5.1 Conceptual development model of dilational deformation bands*

Field observations and microstructural analysis of the Dead Tree section deformation bands demonstrates that simple shear is responsible for positive volumetric strain (dilation), which progressively evolved into discrete fracture via crack propagation (Fig. 4). Dilation bands increase pore volume relative to host rock (Fossen et al., 2007), as observed in Figures 4b–4e. At the Dead Tree section, dilation bands occur in and intersect alternating coarse- and fine-grained strata, showing no remnant signs of comminution (Fig. 4); this is indicative of shallow burial depths (<1 km) at the time of their formation (*sensu* Fossen et al., 2007).

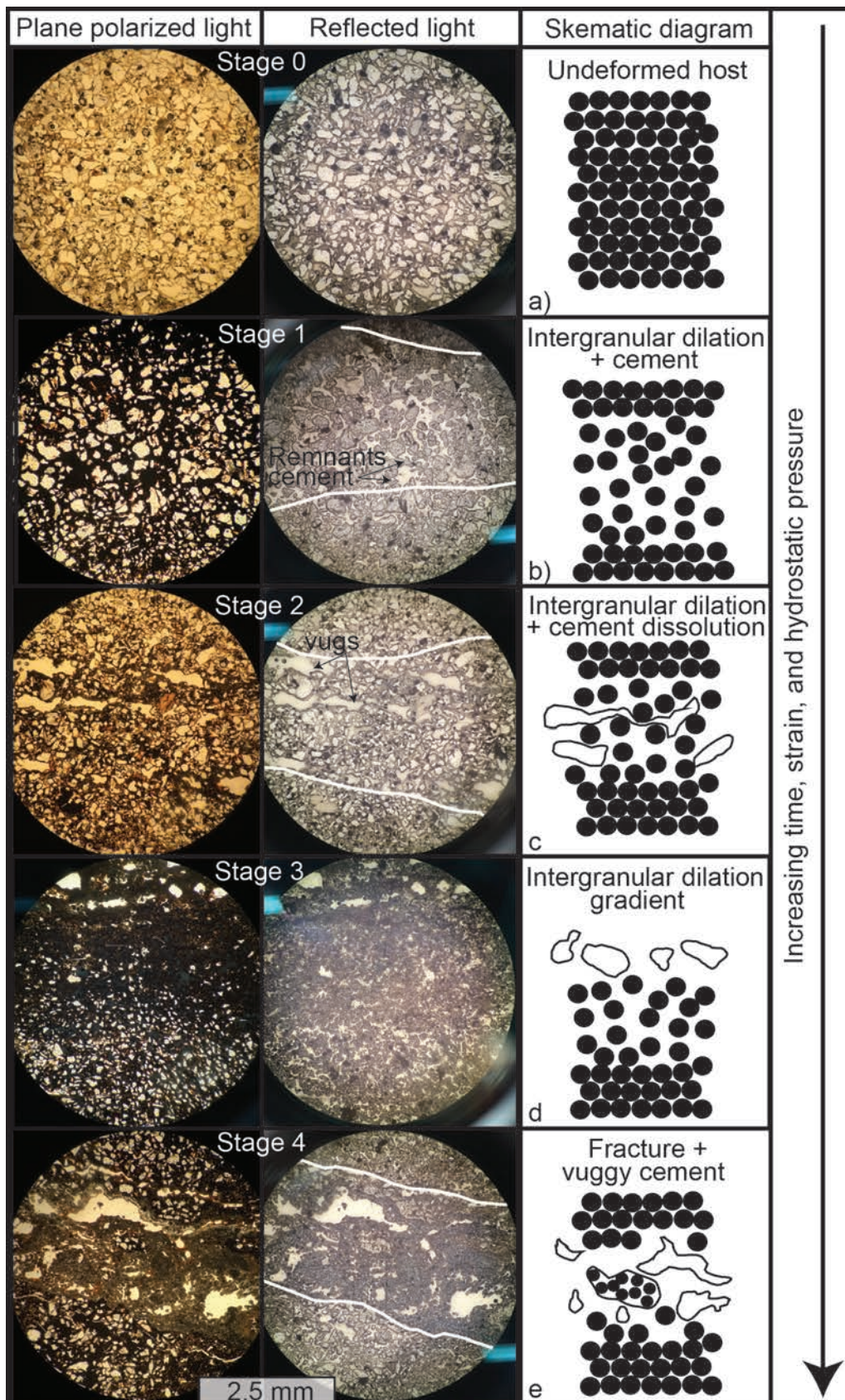


**Figure 4.** Conceptual model illustrating the microstructural evolution of dilation bands observed at the Dead Tree section. **(a)** Host rock; **(b)** Stage 1; **(c)** Stage 2; **(d)** Stage 3; **(e)** Stage 4.

Microstructural analysis illustrates a clear evolution of a dilation band into a fracture, which we envisage occurred in four successive stages. The nascent stage of our model (Stage 1) occurs by intergranular disaggregation and dilation of individual grains, causing mechanical and chemical precipitation of multiple cements (Fig. 3d & 4b). This has been similarly conceptualised by Exner et al. (2013). For example, dilation bands created conduits of high porosity and permeability, which provided space for meteoric fluid flow and promoted iron-hydroxide cement precipitation. We suggest that intergranular dominated dilation (i.e. pore volume increase; *sensu* Bésuelle, 2001a) was promoted by low vertical stress and high lateral stress loading (i.e. compaction and compression) of permeable fluid-saturated sedimentary rocks, resulting in tensile failure (Fig. 3f).

A change in reservoir chemistry is inferred from observations of dissolution of iron-hydroxide cements and responsible for Stage 2 of our model. We suggest this process is responsible for cavity formation and the third-order vuggy pore network observed with remnant iron-hydroxide rims (Fig. 4c). Exner et al. (2013) also noted dissolution of Fe-dolomite cement in his model. Discontinuities between band walls initiates as deformation bands continue to grow with contemporaneous precipitation of syntaxial cement (Fig. 4d). Multiple layering of syntaxial cement indicates multiple fluid influxes and implies that fluid influx may be responsible for growth and widening of dilation bands. Therefore, we suggest iron oxide and siliceous cement precipitates out of solution and into the newly formed third-order pore space. Iron oxide dissolves out of deformation bands, leaving siliceous cement behind, and forming elongated vuggy pores within

deformation bands.

The final and most strain intensive stage (Stage 4) of deformation occurs via crack propagation, resulting in tensile fracturing of the host-rock (Fig. 4e). Observations of floating host-rock islands surrounded by silica cements and sharp host rock boundaries support this interpretation (Fig. 4e). Cuspate textures on host rock wall edges in Figure 4e indicate chemical dissolution of the host wall rock and presence of corrosive fluids. Therefore, we suggest tensile mechanical fracturing of host rock occurred along weakened pre-existing dilation bands. We believe these stages best represent the progressive development of dilation bands within the Eyre Formation.

### *5.2 The impacts of shear dilation bands on permeability enhancement*

The main application of this study is an exploration tool for geologists. Scanning Electron Microscope images, micrographs, handheld permeameter results, and micro CT results demonstrates that dilation bands enhance permeability relative to surrounding host rocks and enhance fluid flow between the Flinders Ranges and Lake Eyre Basin. Optical microscope and SEM images demonstrate that pore space dilates within discrete parallel deformation bands (Fig. 3d). Micro CT results indicate dilation bands contain an intricate network of well connected (i.e. 14.5% open pore space) third-order vuggy pore space (Fig. 3c). Additionally, permeameter results imply dilation bands are characterised by enhanced permeability relative to the adjacent host rock (Fig. 3e). These relationships strongly imply that dilation bands are associated with enhanced permeability of the Eyre Formation at the Dead Tree section, and thus likely

represent preferential conduits for fluid flow. Field observations indicate dilation bands form in clusters (Fig. 3a), similar to compaction bands (e.g. Aydin, 1978; Main et al., 2000). Moreover, pink iron-stained cemented EF4a and EF4b bands indicate high concentrations of iron in the formation fluid during cement precipitation, supporting the notion of fluid flow enhancement via a conduit formed by dilation bands. In stark contrast, carbonate-hosted dilation bands have been observed as complete seals, reducing porosity and permeability (e.g. Kaminskaite et al., 2019)

Deformation bands may exert strong controls on fluid flow in the shallow crust, either by enhancing porosity and forming conduits for fluid migration, or decreasing porosity and forming retarding barriers that preferentially orient fluids (Fossen et al., 2007), especially in the vadose zone where hydrostatic pressure is low (Sigda et al., 1999). The Eyre Formation is a regional aquifer characterised by a silcrete overprint and overlain by the Namba Formation, a regional aquitard (Drexel and Preiss, 1995). The Dead Tree section is situated on the eastern flank of the northern Flinders Ranges, where the aquifer recharges above the vadose zone. Therefore, we suggest that the deformation bands within the uppermost unsaturated crust at the Dead Tree section and around the Four Mile region will have the greatest impact on sub-surficial meteoric fluids flowing from the Mt. Painter Inlier into the Lake Eyre Basin.

We argue that dilation bands support fluid mixing between fine-grained layers that are void of iron oxide. Permeability data for fine-grained, kaolinized sediment layers (i.e. fine sandstone and limonite siltstone) are low (Fig. 3e), and suggest a stratigraphic lateral control on meteoric

fluids, and fluid compartmentalization, based on the lack of iron-oxide stain in fine-grained kaolinized layers (Fig. 2). We argue that the dilational deformation bands documented provide a network for fluid mixing between fine-grained compartmentalized layers. Handheld permeameter results have a high standard deviation, likely reflecting the heterogeneous distribution of the large porous vugs. Mixing fluids between compartmentalised layers may result in conditions favourable for redox.

Palaeo-redox roll fronts containing elevated levels of uranium and thorium crop out within the Eyre Formation at the Dead Tree section. Considering its unique location between the radiogenic Mount Painter Inlier and the Four Mile Uranium deposit, this field site therefore represents a key outcrop for understanding mineralising fluid pathways from source to deposit. Field observations indicate an unequivocal spatial correlation between the palaeo-redox roll fronts forming in the coarse-grained iron-oxide stained sandstone layers, and EF3 and EF4a bands. Palaeo-redox roll fronts form a distinct spatial relationship with the west dipping bands of EF3 and EF4a (Fig. 2). We infer a temporal sequence by which the precipitation of palaeo-redox roll fronts followed development of deformation band set EF4. Cross-cutting relationship indicates the palaeo-redox roll front deposit formed around deformation band (Fig. 3). Micro CT results suggest that this relationship is mutually exclusive, and that fluid continued to pass through the dilation band and mineralised fluid front after redox front precipitation (Fig. 3c). Parallelism between redox fronts, dilation bands, and fractures observed in petrographic and SEM images also supports the notion that dilation bands of this study are spatially correlat-

ed with the palaeo-redox roll fronts rich in uranium and thorium (Fig. 3d). These parallel and cross-cutting relationships indicate that dilation bands within the Eyre Formation acted as fluid conduits and supported fluid flow between the northern Flinders Ranges and the Lake Eyre Basin.

### 5.3 A fault jog model for dilational deformation bands and uranium mineralisation at Four Mile

The Dead Tree section sits within a fault step over zone (the Poontana Trough) of the Paralana Fault and Four Mile Fault (Fig. 1). Fault jogs are prone to volumetric strain accumulation and are characterised by the formation of rhomb pull-apart basins in the fault step over zone (e.g. Aydin and Nur, 1982; Basile and Brun, 1999). Pull-apart basins are structurally controlled by two overlapping parallel en echelon faults (in this case Paralana and Four Miles faults), which create a localised area of extension undergoing crustal shortening, causing subsidence that is spatially restricted to the zone overlap. We suggest that this type of pull-apart basin model could potentially account for tensile volumetric strain and the formation of dilation bands observed at the Dead Tree section (Fig. 2).

When near-vertically dipping faults deviates from strike, fault bends and steps link parallel fault trends, which become favourable locations for transtensional and transpressional stress when the orientation of the regional maximum horizontal stress aligns with the obtuse angle of the fault and fault jog (Fig. 1). For example, N-S and NE-SW oriented maximum horizontal stress – as inferred during the formation of EF2 and EF4 – creates localised tension in the fault step over zone of the Paralana Fault and Four

Mile Fault (Fig. 3g). A rock in a compressional regime undergoing tension is at an advantage to develop positive volumetric strain (dilation) because localised tension promotes fluid flow and enhances pore pressure. Thus, if the pore pressure of the area undergoing tension is higher than the lithostatic pressure of the formation, a dilational deformation band will form (Fig. 3f). Dilational volumetric strain is common in shallow formations and likely responsible for the well-cemented, shallowly dipping dilation bands (e.g. EF2a, EF2b, EF4a, EF4b) observed at the Dead Tree section (Fig. 5). However, the maximum horizontal stress oriented E-W and NW-SE aligns with the acute angle of the fault and the fault jog resulting in transpression, which led to the formation of compaction deformation bands as observed in friable and dusty EF1 compaction bands (Fig. 5).

The Dead Tree section provides a missing link between the radiogenic Mt. Painter Inlier uranium source and the Four Mile uranium deposit because of its unique location between the two. The structures documented in this study support fluid flow between the Mesoproterozoic Mt. Painter Inlier to the west and the Mesozoic and Cenozoic sediments in the Frome Embayment and Lake Eyre Basin to the east. We would expect to find concentrations of deformation bands and fractures in sediments adjacent to Four Mile, Pannikin, and Beverley uranium deposits because of the spatial relationship adjacent to a major neotectonic fault system comprising the Paralana Fault, the Four Mile Fault, and the Poontana Fault. Our results from the Dead Tree section confirm the notion that deformation bands have potentially enhanced fluid flow between uranium source and uranium deposit, and may be used analogously to other local uranium mineral

systems by detailed structural mapping of large scale faults.

## 6.0 Introduction

- We have documented 286 deformation bands within the Eocene Eyre Formation at the Dead Tree section, northern Flinders Ranges, South Australia, which form four sets of shear-enhanced dilation bands. The dilation bands have evolved through a four-stage microstructural evolution from shear-enhanced dilation bands into fractures via crack propagation.
- We suggest a fault jog model for the origin and development of dilation bands at the Dead Tree section and by extension uranium mineralisation at the Four Mile deposit. Localised transtension accommodated enhanced volumetric strain, resulting in dilational deformation bands, which formed fluid conduits for meteoric fluid transportation from source to deposit. Palaeo-redox roll fronts rich in uranium and thorium exhibit an unequivocal spatial correlation to the final stage of deformation band evolution.
- The dilation bands and fractures observed in this study increase the effective permeability of the Eyre Formation at the Dead Tree section. These structures enhance fluid flow between the Mount Painter Inlier and the Four Mile uranium deposit, and may have played a role in dictating the location of the Four Mile uranium deposit.

## Acknowledgements

We thank the Government of South Australia's Department of State Development Geological Survey of South Australia, International Geological Congress travel grant scheme, and Eric Rudd Memorial Scholarship for their financial support. Doug and Margaret Sprigg have been very kind and supportive, allowing us access to the Arkaroola Resort and Wilderness Sanctuary for fieldwork. We also thank Rowan Hansberry, Morgan Blades, Kamini Bhowany, and Jonathan Berthiaume for their helpful discussions and field assistance.

## Data Availability Statement

The authors confirm that the data supporting the findings of this study are available within the article.

## References

- Alikarami, R., and Torabi, A., 2015, Micro-texture and petrophysical properties of dilation and compaction shear bands in sand: *Geomechanics for Energy and the Environment*, v. 3, p. 1-10.
- Alliance, 2009, Quarterly report - for the period ending 30 June 2009.
- Antonellini, M. A., Aydin, A., and Pollard, D. D., 1994, Microstructure of deformation bands in porous sandstones at Arches National Park, Utah: *Journal of Structural Geology*, v. 16, no. 7, p. 941-959.
- Aydin, A., 1978, Small faults formed as deformation bands in sandstone: *Pure and Applied Geophysics*, v. 116, no. 4-5, p. 913-930.
- Aydin, A., Borja, R. I., and Eichhubl, P., 2006, Geological and mathematical framework for failure modes in granular rock: *Journal of Structural Geology*, v. 28, no. 1, p. 83-98.
- Aydin, A., and Nur, A., 1982, Evolution of pull-apart basins and their scale independence: *Tectonics*, v. 1, no. 1, p. 91-105.
- Basile, C., and Brun, J. P., 1999, Transtensional faulting patterns ranging from pull-apart basins to transform continental margins: an experimental investigation: *Journal of Structural Geology*, v. 21, no. 1, p. 23-37.
- Bésuelle, P., 2001a, Compacting and dilating shear bands in porous rock: Theoretical and experimental conditions: *Journal of Geophysical Research*, v. 106, no. B7, p. 13435-13442.
- Bésuelle, P., 2001b, Evolution of strain localisation with stress in a sandstone: brittle and semi-brittle regimes: *Physics and Chemistry of the Earth, Part A: Solid Earth and Geodesy*, v. 26, no. 1-2, p. 101-106.
- Brugger, J., Long, N., McPhail, D., and Plimer, I., 2005, An active amagmatic hydrothermal system: the Paralana hot springs, Northern Flinders Ranges, South Australia: *Chemical Geology*, v. 222, no. 1-2, p. 35-64.
- Drexel, J. F., and Preiss, W. V., 1995, The geology of South Australia, Volume 2. The Phanerozoic, South Australia Geological Survey. Bulletin, 54.
- Du Bernard, X., Eichhubl, P., and Aydin, A., 2002, Dilation bands: A new form of localized failure in granular media: *Geophysical Research Letters*, v. 29, no. 24, p. 2176-2180.
- Eichhubl, P., Taylor, W. L., Pollard, D. D., and Aydin, A., 2004, Paleo-fluid flow and deformation in the Aztec Sandstone at the Valley of Fire, Nevada—Evidence for the coupling of hydrogeologic, diagenetic, and tectonic processes: *Geological Society of America Bulletin*, v. 116, no. 9-10, p. 1120-1136.
- Exner, U., Kaiser, J., and Gier, S., 2013, Deformation bands evolving from dilation to cementation bands in a hydrocarbon reservoir (Vienna Basin, Austria): *Marine and Petroleum Geology*, v. 43, p. 504-515.
- Farrell, N. J. C., Healy, D., and Taylor, C. W., 2014, Anisotropy of permeability in faulted porous sandstones: *Journal of Structural Geology*, v. 63, p. 50-67.
- Foden, J., Elburg, M., xa, A, Dougherty, x, Page, J., and Burt, A., 2006, The Timing and Duration of the Delamerian Orogeny: Correlation with the Ross Orogen and Implications for Gondwana Assembly: *The Journal of Geology*, v. 114, no. 2, p. 189-210.
- Fossen, H., and Bale, A., 2007, Deformation bands and their influence on fluid flow: *AAPG Bulletin*, v. 91, no. 12, p. 1685-1700.
- Fossen, H., Schultz, R. A., Shipton, Z. K., and Mair, K., 2007, Deformation bands in sandstone: a review: *Journal of the Geological Society of London*, v. 164, no. 4, p. 755-769.

- Haynes, R., 1975, Beverley sedimentary uranium orebody, Frome embayment, South Australia: Economic Geology of Australia & Papua New Guinea, Ed. CL Knight, Aus-IMM, Monograph, v. 5, p. 808-813.
- Hillis, R. R., Sandiford, M., Reynolds, S. D., and Quigley, M. C., 2008, Present-day stresses, seismicity and Neogene-to-Recent tectonics of Australia's 'passive' margins: intraplate deformation controlled by plate boundary forces: Geological Society, London, Special Publications, v. 306, no. 1, p. 71-90.
- Hore, S. B., and Hill, S. M., 2009, Palaeoredox fronts: setting and associated alteration exposed within a key section for understanding uranium mineralisation at the Four Mile West deposit: *Mesa Journal*, v. 55, p. 34-39.
- Kaminskaite, I., Fisher, Q. J., and Michie, E. A. H., 2019, Microstructure and petrophysical properties of deformation bands in high porosity carbonates: *Journal of Structural Geology*, v. 119, p. 61-80.
- Lommatzsch, M., Exner, U., Gier, S., and Grasmann, B., 2015, Dilatant shear band formation and diagenesis in calcareous, arkosic sandstones, Vienna Basin (Austria): *Marine and petroleum geology*, v. 62, p. 144-160.
- Main, I. G., Kwon, O., Ngwenya, B. T., and Elphick, S. C., 2000, Fault sealing during deformation-band growth in porous sandstone: *Geology*, v. 28, no. 12, p. 1131-1134.
- Ngwenya, B., Kwon, O., Elphick, S. C., and Main, I., 2003, Permeability evolution during progressive development of deformation bands in porous sandstones: *J. Geophys. Res.-Solid Earth*, v. 108, no. B7.
- Paul, E., Flöttmann, T., and Sandiford, M., 1999, Structural geometry and controls on basement-involved deformation in the northern Flinders Ranges, Adelaide Fold Belt, South Australia: *Australian Journal of Earth Sciences*, v. 46, no. 3, p. 343-354.
- Preiss, W., 1990, A stratigraphic and tectonic overview of the Adelaide Geosyncline, South Australia. J.B Jago, P.s Moore (Eds): *The Evolution of a Late Precambrian–Early Palaeozoic Rift Complex: The Adelaide Geosyncline*, Geological Society of Australia, Special Publication, v. 16, p. 1-33.
- Quigley, M. C., Cupper, M. L., and Sandiford, M., 2006, Quaternary faults of south-central Australia: Palaeoseismicity, slip rates and origin: *Australian Journal of Earth Sciences*, v. 53, no. 2, p. 285-301.
- Rotevatn, A., Sandve, T. H., Keilegavlen, E., Kolyukhin, D., and Fossen, H., 2013, Deformation bands and their impact on fluid flow in sandstone reservoirs: the role of natural thickness variations: *Geofluids*, v. 13, no. 3, p. 359-371.
- Sandiford, M., 2003, Neotectonics of southeastern Australia: linking the Quaternary faulting record with seismicity and in situ stress: *Geological Society of America Special Papers*, v. 372, p. 107-119.
- Schultz, R. A., and Siddharthan, R., 2005, A general framework for the occurrence and faulting of deformation bands in porous granular rocks: *Tectonophysics*, v. 411, no. 1, p. 1-18.
- Sigda, J. M., Goodwin, L. B., Mozley, P. S., and Wilson, J. L., 1999, Permeability alteration in small-displacement faults in poorly lithified sediments: Rio Grande rift, central New Mexico: *Faults and subsurface fluid flow in the shallow crust*, p. 51-68.
- Skirrow, R. G., Jaireth, S., Huston, D., Bastrakov, E., Schofield, A., Van der Wielen, S., and Barnicoat, A., 2009, Uranium mineral systems: processes, exploration criteria and a new deposit framework: *Geoscience Australia Record*, v. 20, no. 2009, p. 44.
- Sternlof, K., Chapin, J., Pollard, D., and Durlofsky, L., 2004, Permeability effects of deformation band arrays in sandstone: *AAPG bulletin*, v. 88, no. 9, p. 1315-1329.
- Taylor, W., and Pollard, D. D., 2000, Estimation of in situ permeability of deformation

bands in porous sandstone, Valley of Fire, Nevada: Water Resources Research, v. 36, no. 9, p. 2595-2606.

Wilson, T., 2015, Uranium and uranium mineral systems in South Australia - Third edition, Report Book 2015/00011, Department of State Development, South Australia, Adelaide

Wülser, P.-A., Brugger, J., Foden, J., and Pfeifer, H.-R., 2011, The Sandstone-Hosted Beverley Uranium Deposit, Lake Frome Basin, South Australia: Mineralogy, Geochemistry, and a Time-Constrained Model for Its Genesis: Economic Geology, v. 106, no. 5, p. 835-867.

---

# CHAPTER 5

---

# Statement of Authorship

Title of Paper	The structural evolution of deformation bands within the Manitou Falls Formation, Athabasca Basin, Canada, constrained by analysis of deformation bands.
Publication Status	<input type="checkbox"/> Published <input type="checkbox"/> Accepted for Publication <input type="checkbox"/> Submitted for Publication <input checked="" type="checkbox"/> Unpublished and Unsubmitted work written in manuscript style
Publication Details	Lubiniecki, Drew Christopher, et al. "The structural evolution of deformation bands within the Manitou Falls Formation, Athabasca Basin, Canada." Journal of Structural Geology (2019).

## Principal Author

Name of Principal Author (Candidate)	Drew Lubiniecki		
Contribution to the Paper	Completed fieldwork, collected and interpreted data, collected and analysed samples, wrote and prepared manuscript, acted as corresponding author.		
Overall percentage (%)	70%		
Certification:	This paper reports on original research I conducted during the period of my Higher Degree by Research candidature and is not subject to any obligations or contractual agreements with a third party that would constrain its inclusion in this thesis. I am the primary author of this paper.		
Signature		Date	05/04/19

## Co-Author Contributions

By signing the Statement of Authorship, each author certifies that:

- i. the candidate's stated contribution to the publication is accurate (as detailed above);
- ii. permission is granted for the candidate to include the publication in the thesis; and
- iii. the sum of all co-author contributions is equal to 100% less the candidate's stated contribution.

Name of Co-Author	Rosalind King		
Contribution to the Paper	Supervised fieldwork, aided in collection of data and samples, helped with data interpretation and manuscript revision.		
Signature		Date	5/4/2019

Name of Co-Author	Simon Holford		
Contribution to the Paper	Supervised fieldwork, aided in collection of data and samples, helped with data interpretation and manuscript revision.		
Signature		Date	5/4/19

Name of Co-Author	Mark Bunch		
Contribution to the Paper	Supervised fieldwork, aided in collection of data and samples, helped with data interpretation and manuscript revision.		
Signature		Date	05/04/2019

Name of Co-Author	Dave Thomas		
Contribution to the Paper	Industry correspondent, aided in fieldwork and overall concept of module.		
Signature	David J. Thomas	Date	April 1, 2019

Name of Co-Author	Arin Kitchen		
Contribution to the Paper	Aided in fieldwork.		
Signature		Date	July 29 2019

Name of Co-Author	Gary Delaney		
Contribution to the Paper	Financial support, government correspondent, and overall concept of thesis.		
Signature		Date	JULY 29 2019

Please cut and paste additional co-author panels here as required.

---

## Structural evolution of deformation bands within the Manitou Falls Formation, Athabasca Basin, Canada

---

### Abstract

We present the results of a structural study which constrains the geometry and evolution of basement faults by analysis of over 1700 deformation bands in order to better understand the role of local and far-field palaeostresses in the Athabasca Basin. This work presents primary results of the post 1.8 Ga structural evolution the Manitou Falls Group, associated with the Centennial and Fox Lake uranium deposits. We present a six stage regional palaeostress model for the Manitou Falls Group, based on the formation of deformation bands: Stage 1) NW–SE extension; Stage 2) E–W extension; Stage 3) NE–SW extension; Stage 4) NW–SE transpression; Stage 5) N–S compression; Stage 6) E–W compression. The deformation bands are interpreted to be temporally related to nearby faulting within the basin sandstone, implying structurally prospective areas associated with uranium mineralisation. Stage 4 of our structural analysis may be temporally related to similar deformation event proximal to the Peter-Dominique uranium deposit, which provided a K-Ar age of 1.3 Ga from sericite within the normal fault zone. We suggest that a period of dravite fluid alteration along trend of Fox Lake uranium deposit occurred simultaneously with the Stage 4 our palaeostress model. This work may enhance existing exploration and mineral models for Fox Lake and Centennial uranium deposits resource targeting.

**Keywords:** Athabasca Basin; Structural Evolution; Centennial Uranium Deposit; Fox Lake Uranium Deposit; Manitou Falls Formation; Deformation Band.

---

### 1.0 Introduction

Deformation bands are abundant in the late Paleoproterozoic Manitou Falls Group of the Athabasca Basin in northern Saskatchewan, Canada. A deformation band is a discrete zone of localized strain that forms as a result of compaction due to sediment loading and high deviatoric stress in porous, granular sedimentary rocks like sandstones (Fossen et al., 2007). Deformation bands were first documented in Arches National Park, Utah by Aydin (1978). Their discovery captured particular interest from the hydrocarbon industry, owing to the stark alteration to host rock petrophysical properties (e.g. Wong and Baud, 2012; Zhu et al., 2010). Deformation bands exhibit cohesive strain hardening nature, which govern their formation (e.g. Aydin, 1978). Deformation band develop as single bands (mm thickness scale) and

forming clusters or swarms (cm scale) (e.g. Antonellini et al., 1994; Aydin and Johnson, 1983). Clusters have the greatest potential to retard fluid flow, as their cumulative thicknesses (dm–m scale) is often many times that of a single band (1–2 mm) (e.g. Fossen and Bale, 2007; Rotevatn et al., 2013). Reduced permeability may result in compartmentalisation and altered fluid flow direction in aquifers and petroleum reservoirs (e.g. Antonellini and Aydin, 1994; Ballas et al., 2015; Fossen and Bale, 2007; Tondi et al., 2016). In addition to their negative effects on fluid flow, deformation bands may also kinematically dilate and produce a conduit of enhanced permeability relative to the host rock (e.g. Alikarami and Torabi, 2015; Aydin et al., 2006; Du Bernard et al., 2002; Exner et al., 2013). Deformation bands have been largely overlooked in economic mineral systems, surprising-

ly considering their petrophysical properties, resulting in a knowledge gap.

The post 1.8 Ga tectonic evolution of arguably the world's largest source of unconformity-related high-grade uranium, the Athabasca Basin, is unclear. The Athabasca Basin is comprised of four unconformable quartzose fluvial sequences that were deposited between 1.76 and 1.50 Ga (Ramaekers et al., 2007). The basal unconformity separates the Mesoproterozoic Athabasca Group sandstone from the Paleoproterozoic basement rocks of the Rae Province and Hearne Province (Fig. 1). Most Athabasca unconformity-style uranium deposits are spatially and genetically associated with reactivated basement faults that crosscut the subterranean unconformity (e.g. Hoeve and Sibbald, 1978; Hoeve

et al., 1980; Jefferson et al., 2007; Li et al., 2015; Li et al., 2017). The majority of previous tectonic studies in the region have focused on the ductile tectonic evolution, such as those related to the Trans-Hudson Orogeny (Annesley et al., 2005; Ansdell, 2005; e.g. Ashton et al., 2001; Bickford et al., 1990; Corrigan, 2012). Some Athabasca Basin tectonic events have been investigated, such as subsidence following the Trans-Hudson Orogeny (e.g. Annesley et al., 2005; Ashton et al., 2001; Pysklywec and Mitrovica, 2000; Ramaekers and Eccles, 2004). However, these works either bundle the entire brittle structural history of the Athabasca Basin into one event (e.g. Ashton et al., 2001), or focus solely on post orogenic subsidence (e.g. Ramaekers and Eccles, 2004). Understanding the

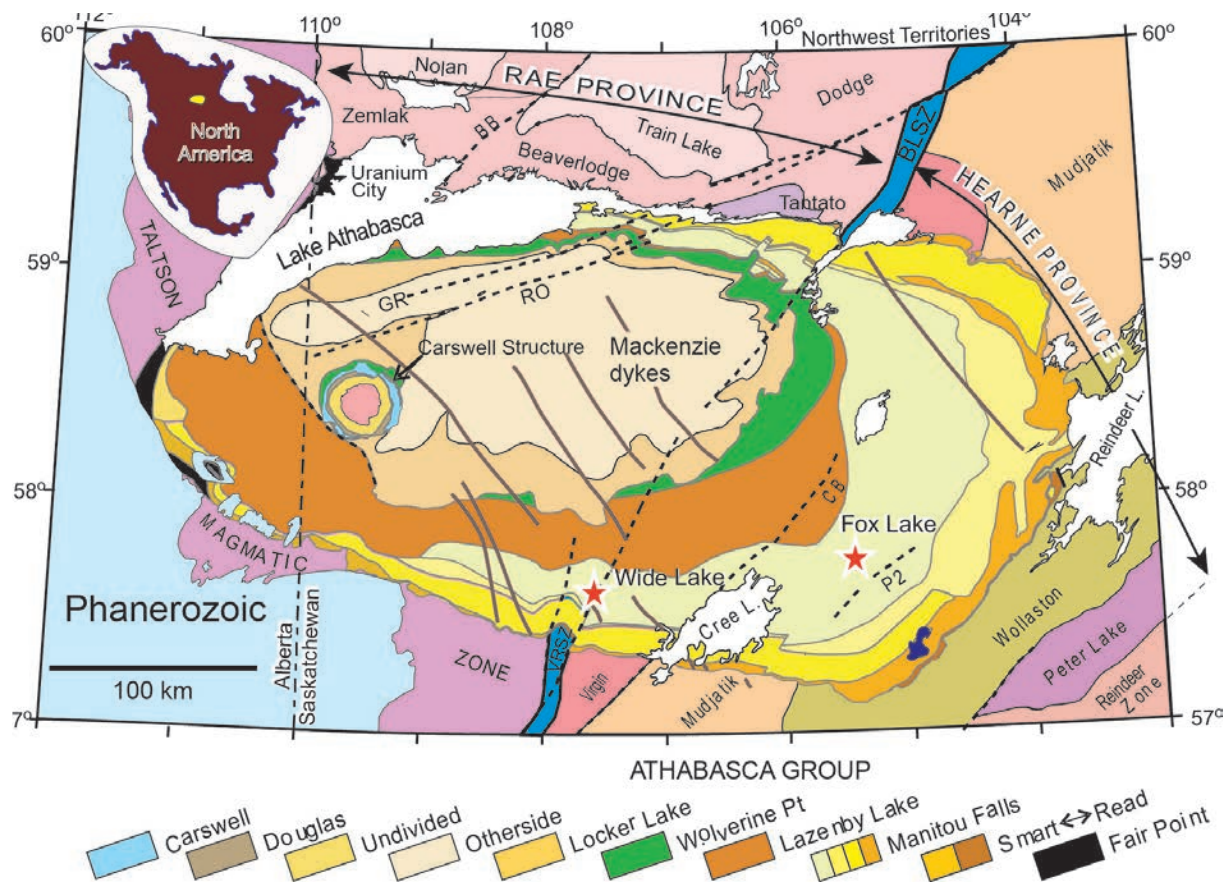


**Figure 1.** Geological map of the Athabasca Basin modified after Reid et al. 2014. Map key formations are listed from youngest to oldest (left to right).

structural evolution of the basin and therefore its fault-controlled mineral systems, requires a stage-by-stage analysis that should likely prove fundamental to exploration and future targeting of economically viable deposits (e.g. Cox et al., 2001; Micklethwaite et al., 2010). Given unconformity-related uranium mineralisation in the Athabasca Basin is directly related to circulating fluids through Athabasca Group cover successions, basement rocks, and fault zones (e.g. Hoeve and Sibbald, 1978); the potential role of deformation bands has not yet been investigated in detail.

There appears to be unequivocal spatial correlation between high-angle reverse faults, oblique transpressional faults, strike-slip faults, and high-grade unconformity-related uranium mineralisation (e.g. McArthur River, Cigar Lake, and Centennial uranium deposits) (e.g. Baudemont and Pacquet, 1999; Jefferson et al., 2007; Reid et al., 2014). Albeit, normal faults are not typically documented with mineralization in the basin (e.g. Baudemont and Fedorowich, 1996). Many post-sandstone faults associated with uranium mineralization are reactivated older basement faults that reflect an older history of pre-sandstone ductile and semi-brittle deformation. The spatial correlation of post-sandstone reactivated basement faults and shear zones with uranium mineralization indicates potential relationship of basement-hosted structures for localising mineralization responsible fluid flow in the Athabasca Basin. Besides confidential internal and unpublished company reports investigating fault reactivation histories and syn-mineralisation kinematic relationships little has been published on this topic in the public domain.

Fault system evolution is difficult to model

because they are typically characterised by dynamic stress states, which evolve with multiple episodes of reactivation (e.g. Debenham et al., 2018; Lubiniecki et al., 2019). Deformation bands can be used to constrain the palaeostress history of sedimentary basins and faults because their formation is intrinsically linked to palaeostress (Lubiniecki et al., 2019). Deformation bands can either form with respect to the regional palaeostress following the Andersonian conjugate model (e.g. Anderson, 1951; Ballas et al., 2015; Fossen et al., 2011), or in a Riedel shear system (e.g. Davis et al., 2000). Andersonian geometry is characterised by conjugate sets, which form a dihedral angle of approximately 60°, acutely bisected by the direction of maximum stress (Anderson, 1951). Riedel shear zones demonstrate a typical fracture pattern commonly associated with strike-slip faulting, specifically related to the orientation of the principal shear zone (i.e. fault) (Ahlgren, 2001). Thus, deformation bands provide an excellent tool to elucidate the structural evolution of faults and regional palaeostress because they conform to Andersonian and Riedel fault geometry (e.g. Ballas et al., 2015; Davis et al., 2000). These geometric characteristics combined with their cohesive and discrete nature of deformation bands make crosscutting relationships easily identifiable, underpinning our investigation of the tectonic evolution of sandstone faults and chronological implications of palaeostress within the Athabasca Basin. Thus, deformation bands provide excellent tool for resolving the post 1.8 Ga tectonic history of the Athabasca Basin.

This study aims to elucidate the structural evolution of the late Paleoproterozoic Athabasca Basin, with a specific focus on using deformation bands. We observed and recorded a suite of deformation

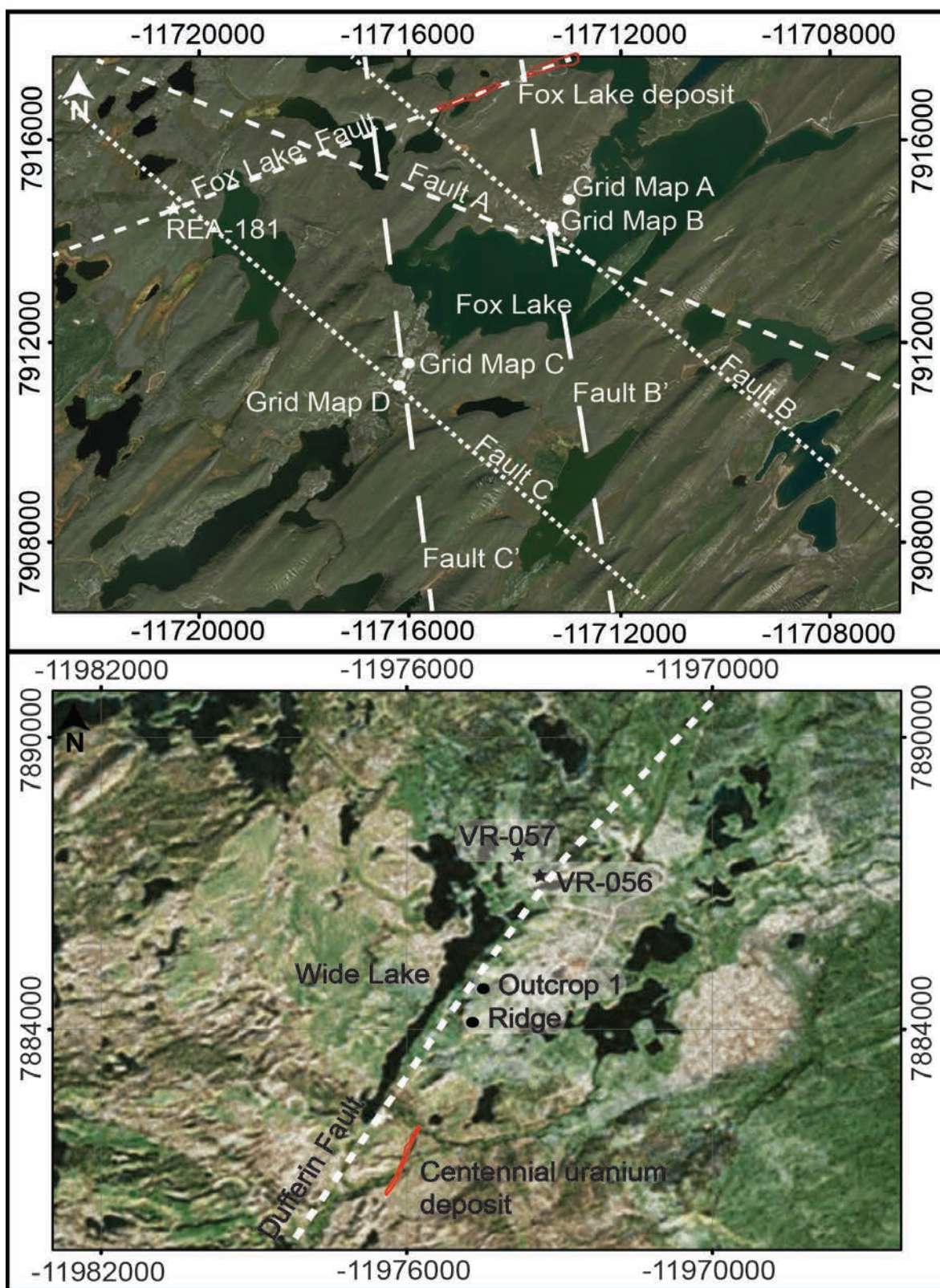


**Figure 2.** Satellite maps of the Fox Lake and Wide Lake regions. Red outlines define uranium mineralisation occurrences.

bands near the Fox Lake and Centennial uranium deposits to use as a discrete tectonic indicators of changes in the regional palaeostress state. We document 1713 deformation bands through surficial mapping and logging drill core of the late Paleoproterozoic Manitou Falls Group quartz arenite. This database provides constraints on the palaeostress evolution of the Athabasca Basin and role of faulting spatial associated with the nearby uranium Centennial and Fox Lake uranium deposits. Palaeostress histories in both study areas show a similar palaeostress history, a progressive evolution of extension, transpression, and finally compression.

## 2.0 Geological history of the Athabasca Basin

The crystalline basement underlying the Athabasca Basin is comprised of rocks of the Rae and Hearne provinces (Fig. 1). The two entities are heavily partitioned by numerous complicated fault arrays, which include the prominent Snowbird Tectonic Zone (Card et al., 2007), which separates them. The Snowbird Tectonic Zone is a 5 km wide shear zone, which is defined by the Virgin River Shear Zone (VRSZ) in the southern portion of the Athabasca Basin and Black Lake Shear Zone (BLSZ) in the northern part of the basin (Fig. 1). The Rae Province is dominated by orthogneisses and accreted to the Hearn and Slave cratons during the 2.0–1.9 Ga Taltson and Thelon orogenies (Card, 2016; Hoffman, 1988). Metasedimentary rocks are common in the Rae Province, cropping out N of the Athabasca Basin (e.g. Ashton et al., 2013) but are insignificant to the S (Card et al., 2014). The Hearne Province is dominated by Archean orthogneisses (e.g. Card et al., 2018). Although, high-grade siliciclastic metasedimentary rocks of

the Wollaston Supergroup locally mantle Archean inliers within the eastern part of the Athabasca Basin (e.g. Yeo et al., 2007).

The formation of the intracratonic Athabasca Basin of northern Saskatchewan and north-eastern Alberta is related to isostatic flexural sag, as a result of top crustal loading, which occurred in response to the rapid uplift near the end of the Trans Hudson Orogeny at 1.75 Ga (Hiatt and Kyser, 2007). The Athabasca Basin contains strata deposited in the Paleoproterozoic Jackfish Basin and Cree Basin, and the Mesoproterozoic Cree Basin and Mirror Basin (Bosman and Ramaekers, 2015). The study areas are located within the basin formations are temporarily constrained. For example, the age of the Wolverine Point Formation is constrained to 1644  $\pm$  13 Ma using zircon in tuff clasts (Rainbird et al., 2007). The Douglas Formation was dated using Re-Os, constrained to 1541  $\pm$  13 Ma (Creaser and Stasiuk, 2007). Deep weathering and intense erosion of the crystalline basement prior to deposition indicates the Cree Basin is younger than 1.75–1.78 Ga, the youngest retrograde metamorphic age of basement (Annesley et al., 1997). The Cree and Mirror basins formed between 1.80–1.50 Ga, which are constrained by Rb-Os and U-Pb methods (Ramaekers et al., 2007).

Palaeocurrent data indicating westerly flow infers the main source of sediments for the Manitou Falls Group was provided by the Trans Hudson Orogeny (Rainbird et al., 2007; Ramaekers et al., 2007). The basin strata largely consists of the Athabasca Supergroup fluvial quartz arenites, ordered imbricate from youngest to oldest in Figure 1. Extensive basin-wide unconformities marcate the stratigraphic extent of each basin

(Ramaekers et al., 2007). The Manitou Falls Group is located within the Cree Basin, exhibiting an overall fining upward succession of interbedded quartz-pebble conglomerate and quartz arenite. The Clampitt Formation and Dunlop Formation are stratigraphic equivalents, which were deposited in different deposystems (Fox Lake-Dunlop and Dufferin Lake approaches the Clampitt Formation boundary); they mark the onset of a rapid increase in clay intraclasts, indicating rapid and sustained increase in accommodation space; however, this may also reflect changes in climate e.g. increased seasonality and aridity (Ramaekers et al., 2007). Pagel (1975) suggested this spike in accommodation space led to the deep burial of the Manitou Falls Group. Basin-wide isopach maps indicate these deposits are analogues in size to modern 150 km wide Kosi megafans in the southern Himalayas (Ramaekers et al., 2007).

This study focusses on the Fox Lake area and the Wide Lake area of the Athabasca Basin. The Fox Lake area lies above more than seven hundred metres of Manitou Falls Group quartz arenite. Graphitic basement fault arrays are rooted in rocks of the Hearne Province, making good exploration targets for uranium exploration (e.g. Key Lake). The Fox Lake uranium deposit was discovered in 2015, spatially correlated to the graphitic fault system C10 Fault Zone and the basal unconformity of the Athabasca Basin (DeDecker, 2019; Rogers et al., 2017). This deposit displays a partitioned NE-SW trend at Fox Lake (Fig. 2). Wide Lake hosts the Centennial uranium deposit area and overlies the Snowbird Tectonic Zone in the southern Athabasca Basin, laying under 850 m to 900 m of Manitou Falls Group quartz arenites. Basement rocks entrained in the Snowbird Tectonic Zone are highly strained

rocks of the Rae Province, which include a relatively low-grade metasedimentary rock assemblage named the Virgin schist group (e.g., Card, 2016). The Dufferin Fault represents a reactivation of the NE-trending Snowbird Tectonic Zone, which has experienced over 200 m of NW over SE vertical displacement after deposition of the Manitou Falls Group (Card et al., 2007). The Centennial uranium deposit is situated 300–400 m E of the Dufferin Fault (Fig. 2). A network of diabase dikes and sills intrude the main Centennial uranium mineralisation (Alexandre et al., 2012). Main uranium mineralisation formed between 1.27–1.59 Ga, coinciding with emplacement of the diabase dikes at 1270 Ma, of which has since been partially mobilised at ca. 380 Ma (Alexandre et al., 2012).

### 3.0 Methods

This study uses a structural dataset comprising 1713 deformation bands. Data was collected from drill core and outcrops from Wide Lake (Fig. 2a) and Fox Lake (Fig. 2b). Here, the Manitou Falls Group quartz arenite was chosen to develop understanding of the histories of the Dufferin Fault and Fox Lake Fault.

In northern Saskatchewan, the landscape is covered by glacial features and deposits such as glacial till and drumlins, made obvious by the linear NE-SW trending features observed in satellite imagery (Fig. 2). Bright areas on satellite imagery indicating high solar albedo, assumed to be areas of outcropping sandstone (Fig. 2). Deformation bands were noted in both sparse and dense populations in these areas and mapped by a grid system in areas showing highest abundance (proximal to or within large clusters; Fig. 3). These grid maps were constructed from data collected in the field, individual-

ly mapped in 1x1 m blocks, then stitched together and digitized in digital image drafting software. Supplementing the outcrop data, structural measurements were also collected from drill hole (REA-181) located 4 kilometres W of Fox Lake, along the ENE-trending Fox Lake fault which hosts the Fox Lake uranium deposit (Fig. 2a).

At Wide Lake two drill holes, VR-56 and VR-57 (Table 1), REA-181 at Fox Lake (Table 2), and outcrops at Fox Lake (Table 3). Bedrock and drill core data was plotted on Stereonet diagrams using Stereonet9 by Allmendinger et al. (2012). Data clusters and corresponding conjugate sets were pulled out of the dataset individually. Stereonet plots highlight and define various structural data subsets. Individual stages were chronologically ordered based on the mutually exclusive cross-cutting relationships observed within the Manitou Falls Group at Fox Lake and Wide Lake. These relationships are segregated into the individual stages and displayed as a Younging Table (Table 4) (*sensu* Potts and Reddy, 2000). Individual structural analysis were completed for Fox Lake and Wide Lake deformation bands, then compared for trends and similarities, defining the stages of the palaeostress model.

Six samples of cataclastic bands were prepared for catholuminescence and electron microprobe (EM), using a Scanning Electron Microscope (SEM). Twenty-eight thin sections were prepared for transmitted light microscopy. Electron instrument samples were first analysed using the SEM to highlight intra-deformation band variations in silica cement, then spot analysed using the EM. Samples prepared for transmitted light microscopy were digitized, analysed using a petrographic microscope, then described in

terms of their petrographic and structural characteristics.

#### **4.0 Structural analysis of Fox Lake and Wide Lake deformation bands**

Here, we describe the 1713 deformation bands mapped within the Manitou Falls Group at Wide Lake (Centennial deposit) and Fox Lake (Fox Lake deposit), located in the southern and eastern Athabasca Basin, respectively (Fig. 2).

##### *4.1 Deformation bands within the Manitou Falls Group*

The deformation bands observed in this study were classified following Aydin et al. (2006) conforming to the basis of: a) orientation relative to bedding; b) geometry; c) presence/absence of observable shear relationships; and d) deformation mechanism. We have identified: three distinct types of formation kinematics within the Athabasca Group Manitou Falls Group, i) pure compaction band (PCB), ii) shear-enhanced compaction band (SECB), and iii) shear-enhanced dilation band (SEDB). Similarly, three distinct types of formation mechanisms were recognized: i) cataclastic band, ii) dissolution band, iii) dilative-cataclastic band, and iv) fracture.

##### *4.2 Geometric relationships of Fox Lake and Wide Lake deformation bands*

Four grid maps were constructed from outcrops at Fox Lake, which illustrates the spatial and geometric relationships of deformation bands within the heavily silicified Manitou Falls Group quartz arenites (Fig. 3). Deformation bands at Fox Lake display overstepping en echelon geometric patterns, consistent with Riedel shear zones (Fig. 4). Riedel shear arrays form synthetic R shears oriented 15° clockwise from the trace



Figure 3. Grid maps A–D of the deformation bands within the Manitou Falls Formation at Fox Lake.

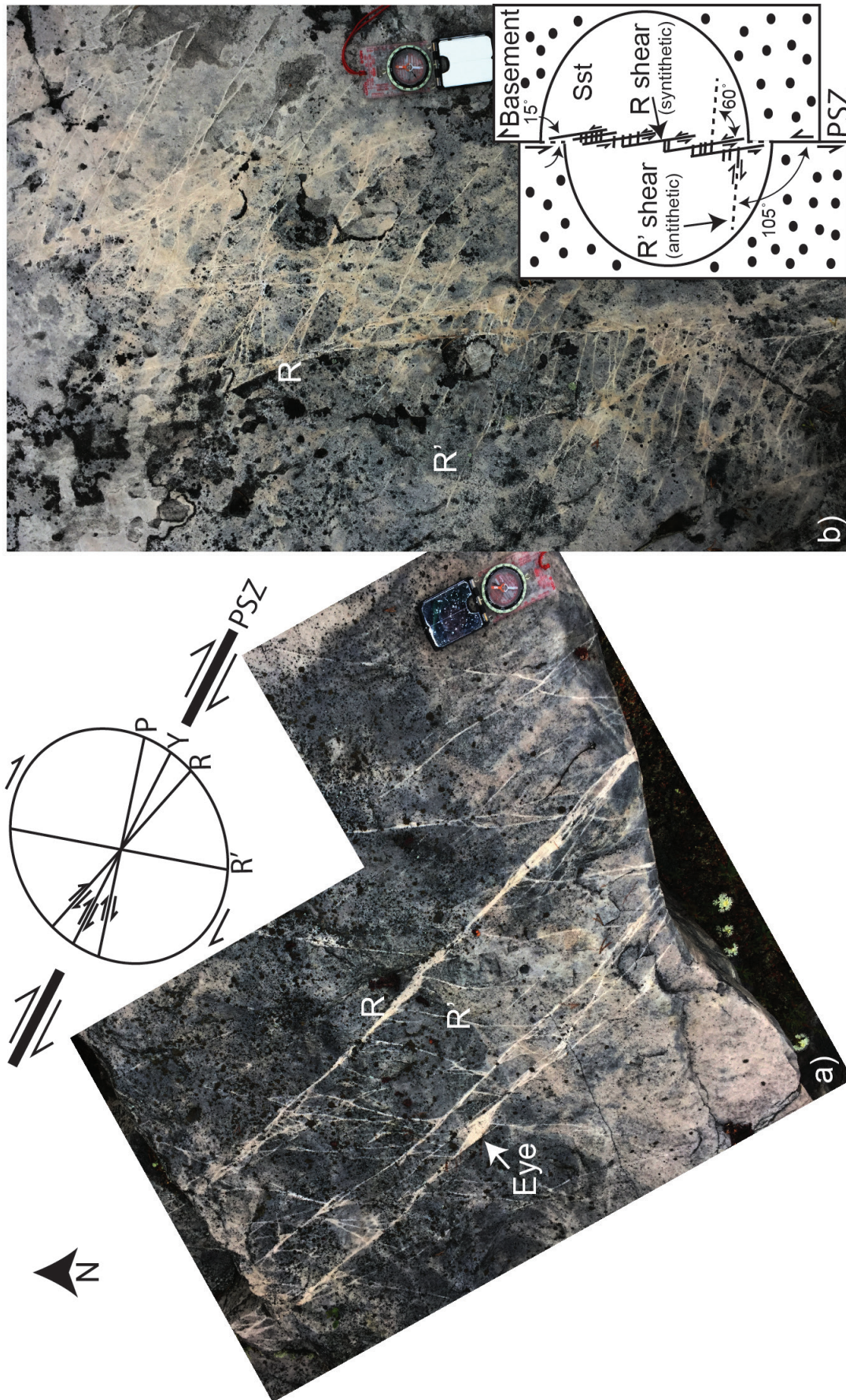
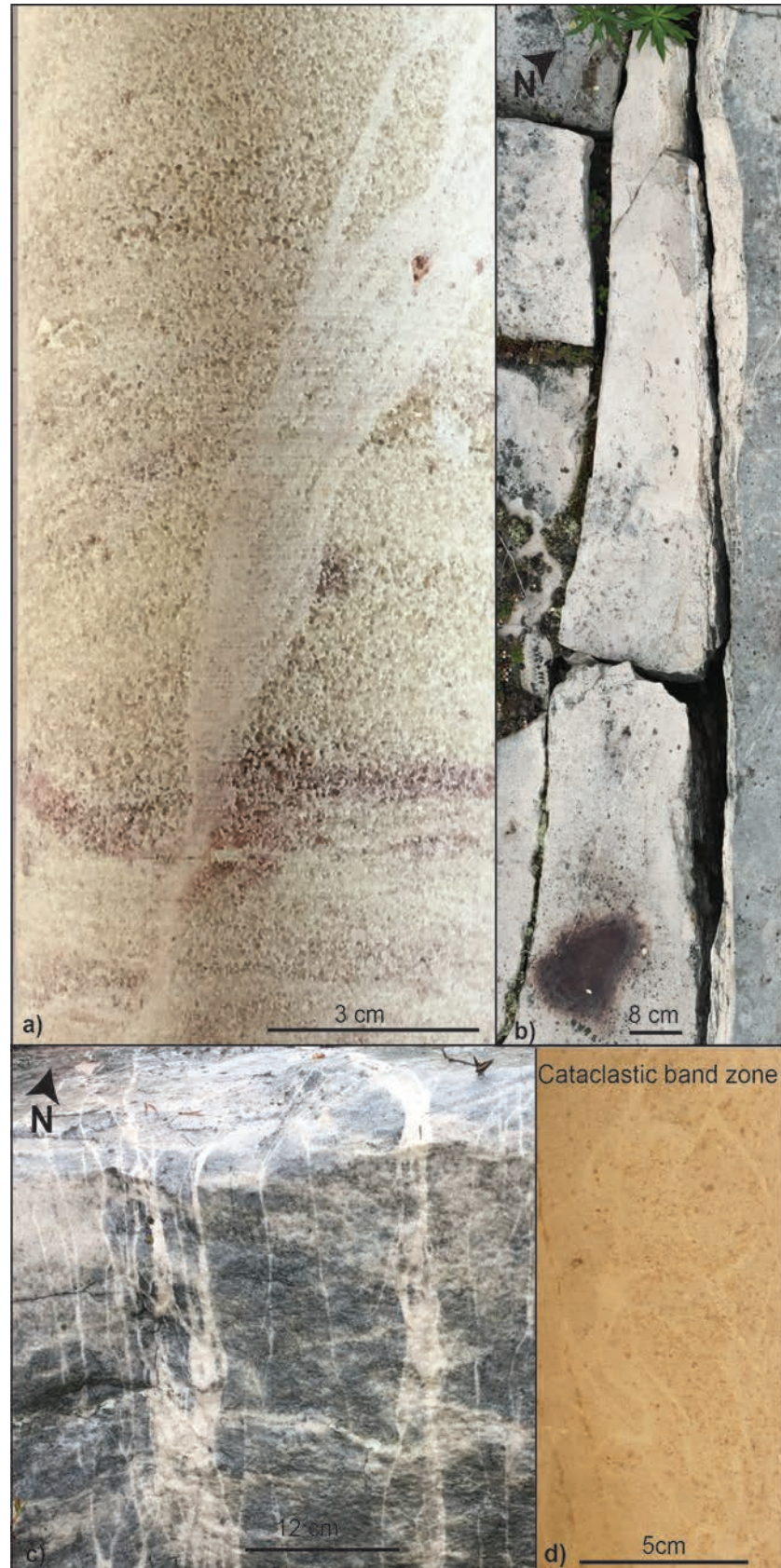
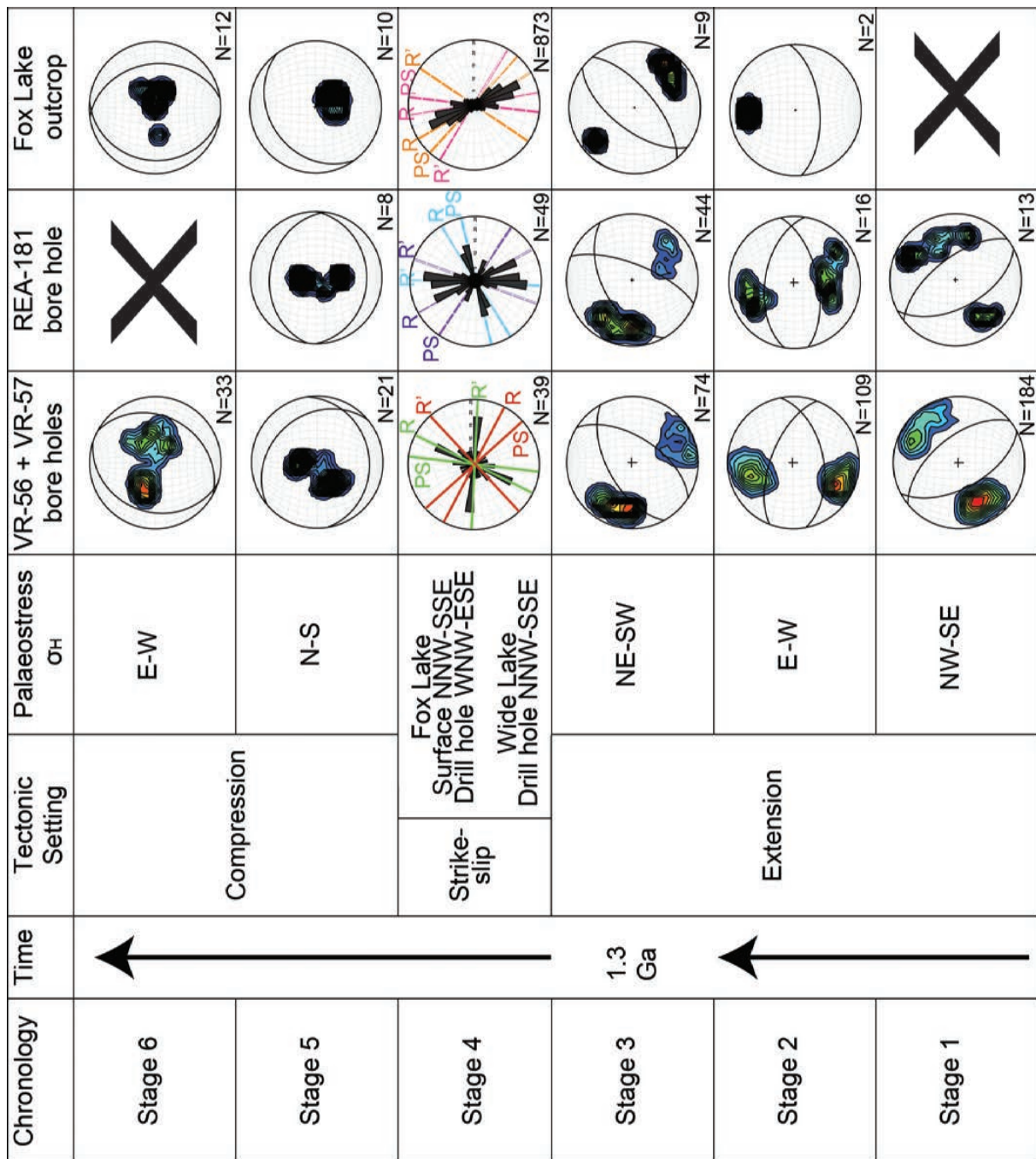


Figure 4. Photographs of cataclastic bands within the Manitou Falls Formation outcrop at Fox Lake conforming to Riedel shear geometry.



**Figure 5.** Photographs of cataclastic bands from the Manitou Falls Formation at Fox Lake: **a)** deformation band cluster in core; **b)** deformation band cluster in outcrop; **c)** face view of a Riedel shear zone cluster; **c)** face view of a Riedel Shear Zone and; **d)** high strain cataclastic band zone in core.



**Figure 6.** Stereonet diagrams illustrating the palaeostress evolution of basement faults underlying the Manitou Falls Group, Athabasca Basin. Principal shear zone is indicated by PS in Stage 4 stereonets.

of right handed strike-slip faults and 15° counter clockwise from the trace of left handed strike-slip faults (Fig. 4). R-shears are connected by an en echelon array of antithetic R'-shears oriented 60° clockwise from the trace of the right handed strike-slip fault and 60° counter

clockwise from the trace of left handed strike-slip faults (Fig. 4). Two sets of Riedel shear patterns were observed in the Fox Lake outcrop. The most prominent Riedel pattern observed ubiquitously at the Fox Lake conforms to NW-trending R-shears and NNE-trending R'-shears

	Set A				Set B					
Conjugate set	Strike	Avg. strike	Dip dir.	Avg. dip	Strike	Avg. strike	Dip dir.	Avg. dip	Dihedral angle	n
Stage 6	198	N-S	288	26	029	NNE-SSW	119	30	56	33
Stage 5	320	NW-SE	050	29	081	E-W	171	29	44	21
Stage 4	205	NNE-SSW	NA	90	094	E-W	NA	90	NA	39
Stage 3	241	NE-SW	331	59	032	NE-SW	122	58	69	74
Stage 2	291	E-W	021	62	079	E-W	169	52	73	109
Stage 1	152	NW-SE	242	58	321	NW-SE	051	58	65	184

**Table 1.** Deformation band dataset from Wide Lake drill holes VR-56 and VR-57.

	Set A				Set B					
Conjugate set	Strike	Avg. strike	Dip dir.	Avg. dip	Strike	Avg. strike	Dip dir.	Avg. dip	Dihedral angle	n
Stage 6	X	X	X	X	X	X	X	X	X	X
Stage 5	278	E-W	008	30	090	E-W	180	24	54	8
Stage 4	181	N-S	NA	90	068	E-W	NA	90	NA	49
Stage 3	241	NE-SW	331	53	021	NNE-SSW	111	70	68	44
Stage 2	279	E-W	009	53	078	E-W	168	61	69	16
Stage 1	322	NW-SE	052	63	152	NW-SE	242	55	63	13

**Table 2.** Deformation band dataset from Fox Lake drill hole REA-181.

	Set A				Set B					
Conjugate set	Strike	Avg. strike	Dip dir.	Avg. dip	Strike	Avg. strike	Dip dir.	Avg. dip	Dihedral angle	n
Stage 6	186	N-S	276	21	352	N-S	082	34	55	12
Stage 5	X	X	X	X	234	NE-SW	324	30	NA	10
Stage 4	154	NNW-SSE	NA	90	025	NNE-SSW	NA	90	NA	873
Stage 3	217	NE-SW	307	62	050	NE-SW	140	66	54	9
Stage 2	X	X	X	X	085	E-W	265	60	X	2
Stage 1	X	X	X	X	X	X	X	X	X	X

**Table 3.** Deformation band dataset from Fox Lake outcrop.

	Stage 1	Stage 2	Stage 3	Stage 4	Stage 5	Stage 6
Stage 1						
Stage 2	λ					
Stage 3	λ					
Stage 4		λ				
Stage 5	λ					
Stage 6		λ	λ			

**Table 4.** Younging table displaying cross-cutting relationships deformation bands observed within the Manitou Falls Formation.

(Fig. 4a). This Riedel shear is inferred right-handed with principal shear zone oriented NW-SE, confirmed by observed dextral R shears in outcrop (orange shears highlighted in Fig. 6). This Riedel shear is well developed in all grid maps (Fig. 3). A subsidiary Riedel shear pattern conforms to N-trending R-shears with W-NW-trending R'-shears (Fig. 4b). This Riedel shear is inferred left-handed with principal shear zone oriented N-S, confirmed by sinistral R shears observed in outcrop (pink shears highlighted in Fig. 6). This Riedel shear is best developed near Grid Map A (Fig. 2).

Two Riedel shears were interpreted from deformation bands measured in drill hole REA-181 at Fox Lake. The most prominent Riedel pattern observed conforms to NE-trending R-shears and N-trending R'-shears; this Riedel shear is inferred left-handed, with an ENE-trending principal shear zone (baby blue shears highlighted in Fig. 6). This ENE trending principal shear zone aligns with the trend of the Fox Lake uranium deposit, thereby defining the trend of the Fox Lake Fault

(Fig. 2). A subsidiary Riedel shear pattern observed in REA-181 conforms to NW-trending R-shears with NNE-trending R'-shears; this Riedel shear is inferred right-handed, with a NW-trending principal shear zone (purple shears highlighted in Fig. 6).

Two Riedel shears were interpreted from deformation bands measured in drill holes VR-56 and VR-57 at Wide Lake. The most prominent Riedel pattern observed conforms to NW-trending R-shears and E-trending R'-shears; this Riedel shear is inferred right-handed with a principal shear zone oriented NNE-SSW, confirmed by dextral R shears observed in outcrop (green shears highlighted in Fig. 6). This NNE trending principal shear zone correlates to the trend of the Dufferin Fault. A subsidiary Riedel shear pattern observed in REA-181 conforms to NW-trending R-shears with NE-trending R'-shears with an inferred NW-trending left-handed principal shear zone, confirmed by observed sinistral R shears in drill hole VR-57 (red shears highlighted in Fig. 6).

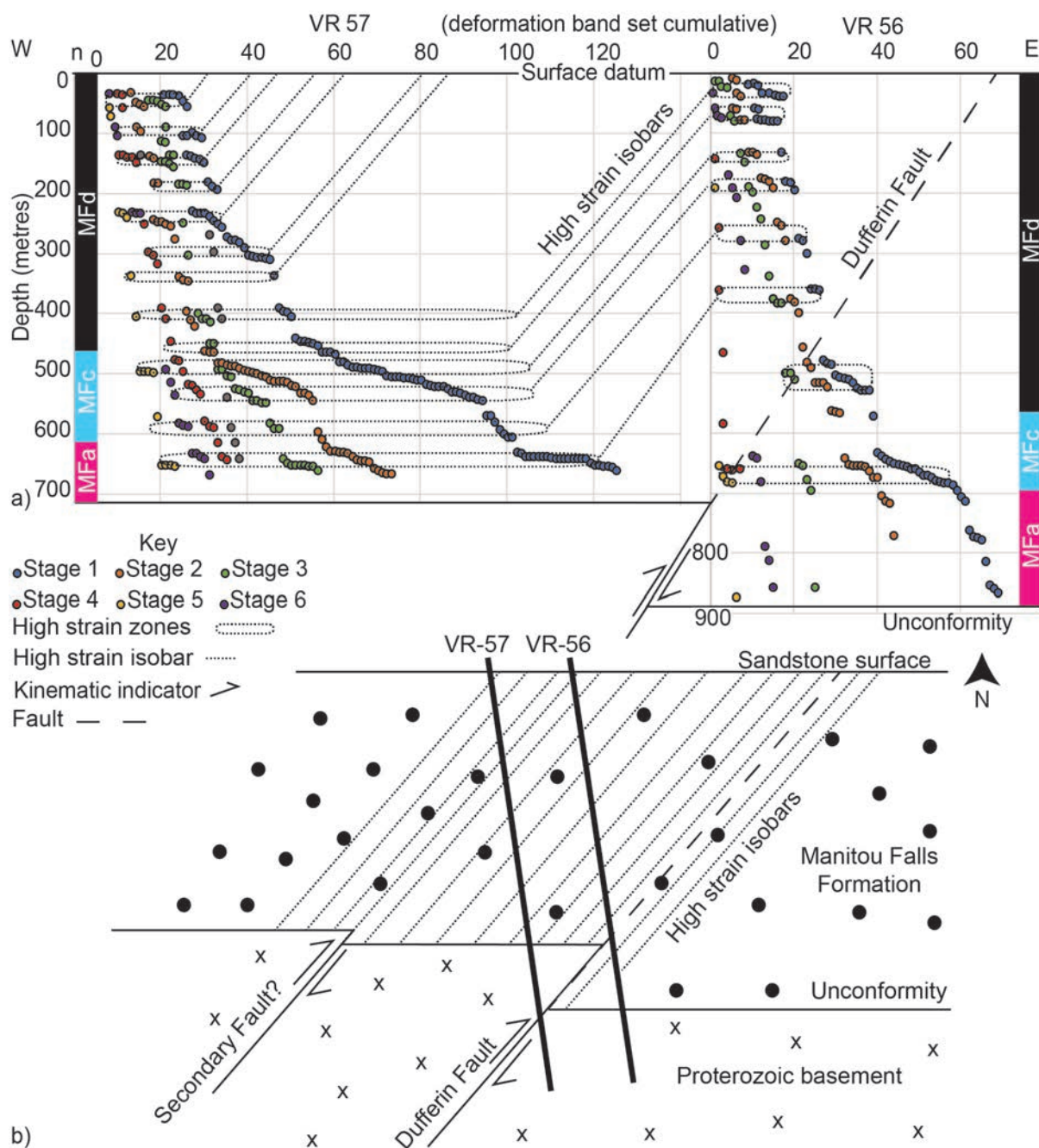


**Figure 7.** Dufferin Fault deformation band model representing drill holes VR56 and VR57 at Wide Lake (locations in Fig. 2): a) this set specific cumulative dot plot represents single deformation bands at the depth. Clumps of data reflect zones of high strain, linked by high strain zone isobars. MFa - Read Formation, MFc - Collins Formation, MFd - Clampitt/Dunlop Formation. b) Conceptual model of the Dufferin Fault.

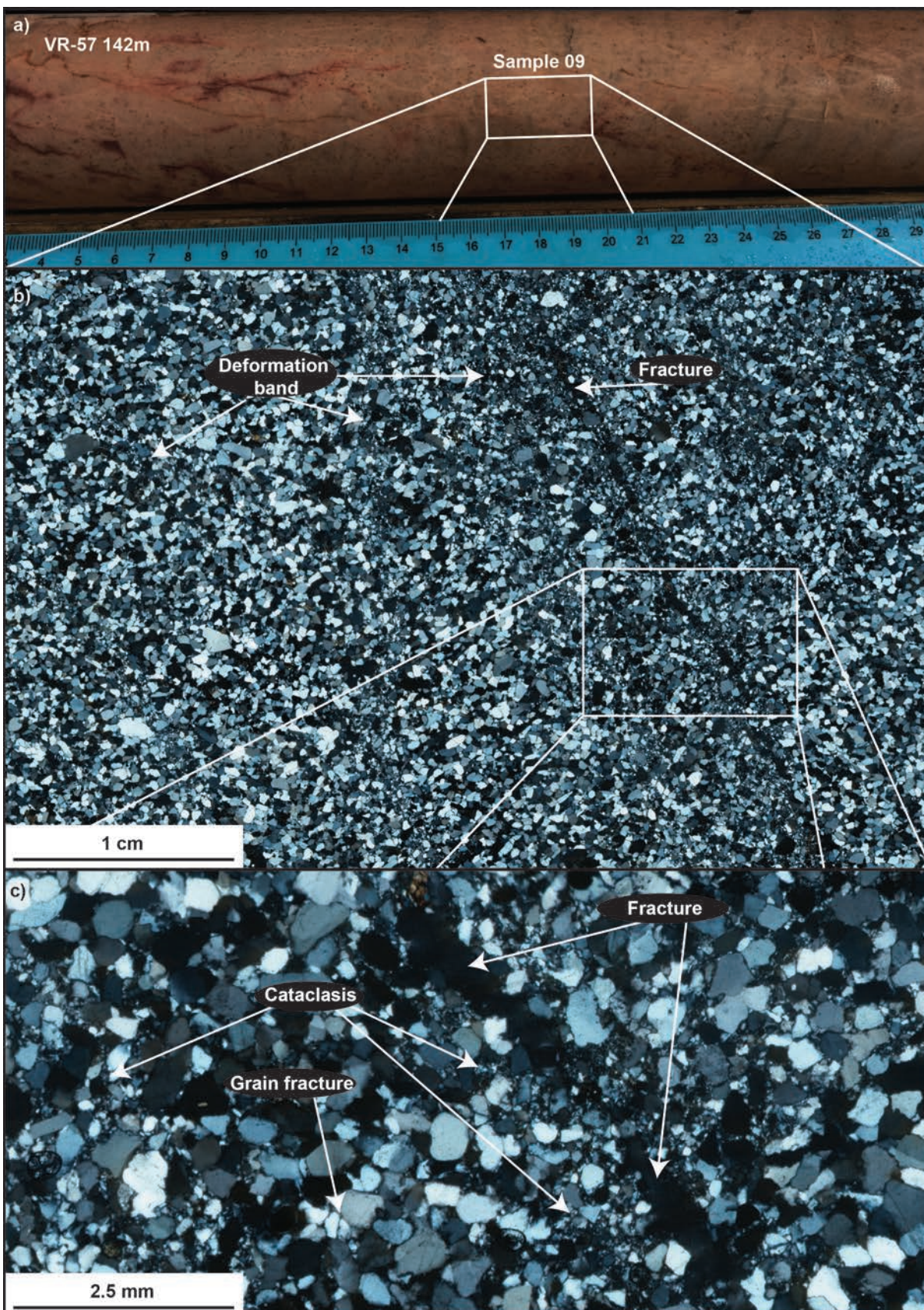


**Figure 8.** a) Photograph of a deformation band cluster zone collected from VR-57 at 142 m depth; b) micrograph under 4x lens highlighting fractures and deformation bands; and c) micrograph under 10x highlighting intraband cataclasis.

Individual R-shears range from 0.5–2.0 mm in thickness, with (Fig. 4). These bands appear to have both planar and anastomosing geometries creating islands of undeformed host rock (Fig. 5c). Cumulate thicknesses of up to 5 cm are noted in small cluster zones of R-shears and are metre scale in length, with a discontinuous, *en echelon* overstepping geometry (Fig. 4). Commonly, R-shears are connected by a deformation band eye, defined as a zone where two parallel deformation bands meet and join (Fig. 4b). Dextral and sinistral R-shears have offsets up to 10 cm in length. R'-shears are generally short (decimetre scale), discontinuous, and are composed of individual bands (2–4 mm) arranged in an *en echelon* overstepping geometry that connects R-shears (Fig. 4). Dextral and sinistral R'-shear have apparent offsets up to 1 cm in length. At the surface, dip-sense was difficult to determine due to the glacially polished outcrop surfaces; however, within core, both normal and reverse offsets of bedding and other deformation bands were observed.

Deformation bands at Fox Lake and Wide Lake with no obvious spatial or geometric relationship to Riedel shears are also observed with both planar and anastomosing geometries (Fig. 5). Individual bands range from 1–2 mm in thickness, while cumulate thicknesses of up to 10 cm are observed in large cluster zones (Fig. 5). These large clusters conform to the previously mentioned easterly and north-westerly orientations observed in Maps B and D, respectively (Fig. 2). In Map D, large cluster zones have been traced out for up to 50 m before being lost under the glacial till cover sequence (Fig. 5). Fractures are commonly observed forming along the margins of deformation bands. One polished slip surface, steep-dipping and NNW-strik-

ing, contained a striation with a pitch of 18°S in Grid Map A (Fig. 2). The widest cluster of cataclastic bands observed at Fox Lake were in excess of 9 cm wide (Fig. 5b). This clusters exhibited Mode I fractures and drusy quartz growth along the fractured wall rock contact of the deformation bands cluster. One Mode III fracture was observed near Grid Map D striking NNW-SSE, which crosscuts and pinches out into a rippled surface.

#### 4.3 Palaeostress model of the Manitou Falls Group

The regional palaeostress history of the Manitou Falls Group is interpreted to comprise six stages. This model does present uncertainty with the chronology and ordering of the structural sets, where cross-cutting relationships were not observed (Table 4).

##### 4.3.1 Stage 1

A total of 197 cataclastic bands are assigned to Stage 1, with the majority (184 bands) being from the Wide Lake area drill holes (VR-56 and VR-57). Stage 1 deformation bands strike NW and dip moderately towards the NE and SW (Fig. 6). Stage 1 bands exhibit normal kinematic offsets and fractures display reverse offsets at Wide Lake. At Fox Lake, Stage 1 bands are rarely observed in drill hole REA-181 (13 bands), while being entirely absent in outcrops.

##### 4.3.2 Stage 2

Stage 2 comprises 127 cataclastic bands with the majority (109 bands) recorded in drill holes from Wide Lake (VR-56 and VR-57). Stage 2 forms an E-striking set of conjugate bands, moderately dipping N and S (Fig. 6). Deformation bands within Stages 2–6 exhibit both normal and reverse kinematics, attaining maxi-

mum displacements of 10 cm. Stage 2 is observed in all drill holes and field sites at Fox Lake and Wide Lake, albeit minor correlation with the Fox Lake surface bands.

#### 4.3.3 Stage 3

Stage 3 comprises 127 cataclastic bands, forming a conjugate set that dips moderately NW and SE. Although Stage 3 bands are found in all locations, the majority occur at Wide Lake with only nine observed bands in Fox Lake outcrop (Fig. 6).

#### 4.3.4 Stage 4

A total of 961 cataclastic bands are assigned to Stage 4 with the majority (873) documented in Fox Lake outcrop and another 49 in Fox Lake drill core (REA-181). Deformation bands assigned to Stage 4 exhibit Riedel shear geometric characteristics (Fig. 4). At Fox Lake these bands are predominantly NNW-trending and sub-vertical dipping, with a minor set striking ENE. At Wide Lake, Stage 4 sub-vertical bands strike NNW and E. (Fig. 6). Although bands assigned to Stage 4 are observed at all study locations, the dominant NNW to N orientation is best developed at Fox Lake. Stage 4 bands are defined by large quantities of data within these sets and best illustrated by rose diagrams in Figure. 6, an effective representation due their sub-vertical nature.

#### 4.3.5 Stage 5

Thirty-nine cataclastic bands are assigned to Stage 5 event which is represented in all three areas with 21 bands being recorded from the Wide Lake drill holes. These bands range between NW, E, and NE striking and dipping shallowly dipping to the N, NW, NE and S (Fig.

6). Northward dipping bands vary at Wide Lake and Fox Lake, which may be the result of localised stress rotation via faulting. Stage 5 is observed in all study locations, albeit minor correlation with the Fox Lake surface outcrops.

#### 4.3.6 Stage 6

A total of 45 bands are assigned to Stage 6. These bands form a conjugate set that is N-striking and shallow dips towards the E and W (Fig. 6). Stage 6 bands are observed in VR-56, VR-57, and the Fox Lake outcrops; however, it is absent in REA-181 (Fig. 6).

#### 4.3.7 Bedding parallel deformation bands

Fifty-nine bedding parallel deformation bands (BPDB) were recorded in REA-181 (Fox Lake). All BPDB were recorded in rock shallower than 384 m, from the drill hole measuring 788 m in length from surface to unconformity. Bedding parallel deformation bands were absent in the footwall and recorded in high quantities of the hanging-wall of VR-56 (Wide Lake) and VR-57 (Wide Lake); the drill fence – VR-56 (872 m hole length from surface to unconformity) and VR-57 (669 m hole length from surface to unconformity) – is situated 200 m spacing (Fig. 2).

#### 4.3.8 Chronology

Bedding parallel deformation bands are not included in the following palaeostress model because we did not observe enough cross-cutting relationships. Stage 1 was the first set of deformation bands to form because it is cross cut by Stages 2, 3, and 5 (Table 4). Stage 2 formed next because it cross-cuts Stage 1 and is crosscut by Stage 4 and 6 (Table 4). Stage 3 formed next because

it crosscuts Stage 1 and is crosscut by Stage 6 (Table 4). Stage 4 formed next because it crosscuts Stage 2 (Table 4). Stage 5 formed next because it crosscuts Stage 1 (Table 4). Stage 6 formed last, owing to the fact that these deformation bands cross-cut Stage 2 and Stage 3 (Table 4).

#### 4.4 Dufferin Fault splay model

The Dufferin Fault trends NE-SW, parallel to the ironically narrow, Wide Lake (Fig. 2). Drill holes VR-56 and VR-57 form a drill fence, conceptually planned to intercept the Dufferin Fault at different depths in order to understand the fault in three dimensions (Fig. 7). Deformation bands from VR-56 and VR-57 and belonging to Stages 1–6 are plotted in Figure 7, using the ground surface as the datum. Multiple deformation band zones of highly partitioned strain were observed in the sandstone core, inferred as Dufferin Fault splays (Fig. 7). These zones are associated with thick clusters, up to 4.5 m thick, consisting of hundreds of individual tightly packed (e.g. spaced every 3–5 mm), anastomosing cataclastic bands (Fig. 8). Grain crushing and grain fracture are observed within the tightly packed inter-deformation band zone at the microscopic scale, where cataclasis and grain fracture is not limited to discrete deformation bands; rather, cataclasis is pervasive throughout the tightly packed interband zones as well (Fig. 8). Microscopic discrete fractures appear along pre-existing deformation band planes in small individual segments up to 5 mm in length (Fig. 8). In VR-57, these deformation band zones appear at 50 m, 100 m, 140 m, 290 m, 230 m, 300 m, 340 m, 400 m, 460 m, 500 m, 530 m, 590 m, 600 m, and 640 m depth (Fig. 7). In VR-56, deformation band zones appear at 30 m, 90 m, 140 m, 190 m, 270 m, 380 m, 520 m, and 650

m depth (Fig. 7).

It is worth noting that drill hole REA-181 is completely void of Stage 6 structures (Table 2). Whereas, Fox Lake outcrops are completely void of Stage 1 structures and partially void of Stage 2 and 5 structures (Table 3). At Wide Lake, VR-57 deformation bands were all observed in the hanging wall of the Dufferin Fault. Whereas, VR-56 bands were mainly observed within the hanging wall, while a small portion were observed within the Dufferin Fault footwall at Wide Lake (Fig. 7).

#### 4.6 Deformation band cements

Deformation bands at Fox Lake are cemented with silica and dravite. Silica is observed in all Stages of our palaeostress model. Dravite cemented bands conform specifically to Stage 4 of our palaeostress model. However, dravite veins were observed to conform specifically to Stage 1, Stage 2, and Stage 3. Deformation bands at Fox Lake and Wide Lake are variably coloured within the central core, exhibiting colour transitions between the deformation band and host rock (Fig. 9). Sample WL 57-13b exhibits dark pink hematite-stained quartz cement within the central core, while the outer core exhibits pale pink hematite-stained quartz (Fig. 9c). On the edge of this particular bands transition zone, bright white quartz cement grades into a dull white quartz cement in the adjacent undeformed wall-rock. The gradient transitions into purple hematite-stain quartz cement in the undeformed host rock on the opposing side of this deformation band (Fig. 9c). Based on these observations, hematite concentrations within the quartz cement is inferred to be higher within the centre of the deformation band, lessening to-

ward the deformation band edges.

To understand the cement chemistry in a single deformation band, we sampled cement that formed within a fractured grain within the deformation band as standard pure cement from drill hole WL-57 (Fig. 9d). Catholuminescence images indicate slight alteration in gray scale, within the fractured quartz grain cement infill (Fig. 9e). Microprobe results indicate the pure cement chemistry sampled from within a fractured grain is enriched in aluminium, magnesium, calcium, iron, and potassium, with peak weight percentage around 0.18 WT% (Fig. 9a). Sample FLDL-2 from drill hole REA-181 was analysed in order to quantify the cement of a deformation band cluster (Fig. 9g). Results from this sample indicate variability in WT % of the aforementioned elements, jumping between 0.0 Wt% up to 0.2 Wt %, reaching a maximum of 0.7 Wt % (Fig. 9b).

## 5.0 Discussion: Faults within the Manitou Falls Group and their relationships to local uranium deposits

### 5.1 Structural evolution of the Manitou Falls Group

This study presents the palaeostress evolution of the Manitou Falls Group through the analysis of deformation bands. This study proposes an evolution from early stage Athabasca Basin crustal thinning, intermediate stage transition to transpression, and finally late stage crustal shortening.

The geometric relationships of Stage 1 through Stage 3 (i.e. conjugate sets) indicates that they formed under tectonic extension with variable principal stress orientations associated with crustal thinning (Fig. 6). Stages 1–3  $\sigma_H$  orientation variations evolved from NW-SE during

Stage 1 to E-W during Stage 2 and finally NE-SW during Stage 3 (Fig. 6). This interpretation indicates a uniform counter-clockwise rotation of  $\sigma_H$  from NW-SE to E-W to NE-SW in Stages 1–3. These variations may reflect the tectonic plate scale interactions. For example, the breakup of the supercontinent Nuna and the emplacement of the Mackenzie Dike Swarm.

At Fox Lake, the absence of Stage 1 and partial presence of Stage 2 deformation bands in outcrops may imply the local faults were not active during Stage 1 (Fig. 6). However, representative data collection may have been hampered by the flat glacially polished outcrops at Fox Lake that means flat or very shallow dipping deformation bands would be difficult to confirm true a dip inclinations.

A provisional constraint on the timing of Stage 3 is proposed based on a comparable structure orientation; the NE-SW striking normal fault structures associated with the Dominique-Peter uranium deposit. The Dominique-Peter deposit located near the Carswell Structure (Fig. 1) is structurally controlled by a series of NE-SW striking normal-lithic faults (Baudemont and Fedorowich, 1996). Uranium mineralisation gave U-Pb discordant ages, which range from 1330 to 850 Ma (Baudemont and Fedorowich, 1996). However, the age of deformation was obtained from fault zone sericite within the D orebody, which gave a K-Ar isochron of 1293  $\pm$  36 Ma (Clauer et al., 1985). This implies NW-SE extension at 1.3 Ga. A provisional correlation of these two events is based on the similar strike and dip of structures and stress state they were subject to, thereby adding temporal constraint to our palaeostress model (Fig. 6). Ramaekers and Eccles (2004) suggest that basin subsidence

continued from 1.82–1.65 Ga as a result of crustal loading, which is likely – although lacking evidence – contemporaneous with Stage 1 (Fig. 6).

Riedel shear zones induce localised stress rotation by simple shear, thereby making it difficult to interpret the regional stress state (e.g. Davis et al., 2000; Mandl, 1988). However in this case, we interpret the stress rotation caused by Riedel shear at Fox Lake to be negligible because we have inferred  $\sigma_H$  from Andersonian strike-slip faulting. The geometry and orientation of Stage 4 deformation bands indicates they formed under a strike-slip tectonic setting (Fig. 6). The geometry and orientation of Stage 5 and Stage 6 deformation bands indicate they formed under a compressional tectonic setting (Fig. 6). These relationships reflect the transition from crustal thinning to crustal shortening.

Observed fractures paralleling deformation bands are interpreted as later strain features, which utilized pre-existing rheological anisotropy of the Manitou Falls Group.

### *5.2 Deformation band link to basement fault geometry – Riedel Vs Anderson*

A fundamental component of mineral exploration in sedimentary basins is understanding subsurface geology and fault systems. Riedel shear geometries have been proposed for basement structures underlying the Athabasca Basin (e.g. Card et al., 2007). Card et al. (2007) noted that the Grease River Shear Zone is synthetic to the Black Lake – Legs Lake Shear Zone, and the geometric relationships infer the Grease River Shear Zone may be a Riedel shear zone (Fig. 1). Riedel shear geometries have also been proposed for sandstone fault systems in a number of unpublished industry stud-

ies, such as Eagle Point, Cigar Lake, Key Lake, and Arrow Lake.

High concentrations of deformation bands conforming to Riedel shear geometry demonstrate the orientation of the underlying basement geometry, including the Fox Lake Fault and Dufferin Fault (Fig. 2). Riedel shear zones are inferred from Stage 4 deformation bands, observed in outcrop and bore holes REA-181 at Fox Lake and VR-56–VR-57 at Wide Lake. Three individual sets of Riedel shear zones show a strong correlation to a NW-trending (dextral), N-trending (sinistral), and ENE-trending (sinistral) principal shear zones at Fox Lake (Fig. 6). At Wide Lake, two individual sets of Riedel shear zones show a strong correlation to N-trending (dextral) and NW-trending (sinistral) principal shear zones (Fig. 6). Under Andersonian faulting, it may be inferred that  $\sigma_H$  was oriented NNW-SSE or WNW-ESE at the time of faulting, at Fox Lake (Fig. 6). Two individual sets of Riedel shear zones show a strong correlation to N-trending and NW-trending principal shear zones at Wide Lake (Fig. 6). Under Andersonian faulting, it may be inferred that  $\sigma_H$  was oriented NNW-SSE at the time of faulting, at Wide Lake (Fig. 6). We thereby demonstrate that at the time the conjugate fault system formed (i.e. Stage 4),  $\sigma_H$  was oriented between ENE-WNW and NNW-SSE (Fig. 6).

Our fault interpretations are based on spatial relationships between thick clusters (up to 9 cm) of deformation bands, Riedel shear geometric patterns, and the Fox Lake uranium deposit (Fig. 2). The Fox Lake uranium deposit trends ENE-WSW, following the trend of the Fox Lake Fault (Fig. 2). Located 280 m SW of Grid Map B, a high concentration of Riedel shears indicate a WNW-ESE principal

shear zone (Fig. 4b & 5c), Fault A (Fig. 2). We provide two fault models at Grid Map B, where a large 9 cm thick cluster was observed trending NW-SE. Andersonian geometry implies the underlying basement fault to be parallel to the cluster, illustrated by Fault B; however, Riedel geometry indicates a NNW-SSE striking principal shear zone illustrated by Fault B' (Fig 3). We provide two fault models at Grid Map C, where a large 9 cm thick cluster was observed trending NW-SE (Fig. 5b). Andersonian geometry infers the underlying basement fault is parallel to the cluster, as illustrated by Fault C'. However, the Riedel geometry observed nearby including Grid Map C indicates a NNW-SSE striking principal shear zone, as illustrated by Fault C (Fig. 2).

Faults are important controls on economic uranium mineralisation in the Athabasca Basin (e.g. Baudemont and Fedorowich, 1996; Baudemont and Pacquet, 1999; Reid et al., 2014). Faults are typically sites of crustal weakness while active faulting commonly induce fluctuations or cycling of fluid pressure along the structural zone. Faults can provide highly permeable fluid pathways, particularly along their damage zones or may be low permeability zones along the fault core zone.

Riedel shear-related deformation bands are well-known to compartmentalise highly porous sandstones (Davis et al., 2000). Factors demonstrated to control the petrophysical properties of a deformation band include cluster cumulative thickness and the extent and pervasiveness of host rock grain comminution (Fossen and Bale, 2007). Rapid variations in thickness and connectivity along a single deformation band make them incapable of arresting fluid flow (Rotevatn et al., 2013). However, deformation

bands may retard fluid flow in certain directions reorienting bulk fluid flow as a consequence of permeability anisotropy (e.g. Farrell et al., 2014; Fossen and Bale, 2007). Therefore, cluster zones with the high cumulative thicknesses (large clusters observed in Grid Maps B and D) are expected to have the negative influence on fluid flow (Fig. 3). We infer that Riedel geometry enhanced compartmentalisation in the sandstones surrounding the Fox Lake Fault (*sensu* Davis et al., 2000). We infer that compartmentalisation and permeability anisotropy may therefore promote fluids approaching a fault zone to flow via path of least resistance, either around or over the highest concentration deformation bands. Therefore, the uranium deposit may be shielded by a high density of shear bands. In other words, deformation bands may act as reinforcement or barriers in the structural permeability of the sandstone surrounding the uranium deposit. The deformation bands observed in this study may have acted to enhance the emplacement and longevity of the Fox Lake uranium deposit.

### *5.3 Structural permeability of sandstone faults at Fox Lake and Wide Lake*

It is postulated that the Fox Lake deposit formed during Stage 4 event of the paleostress model (Fig. 10). In an unpublished exploration study, one segment along the NE pod of the Fox Lake uranium deposit provides evidence of a possible fault splay resulting in a small positive structure (i.e. transpression). We suggest the structure to have been a negative structure (transtension) at the time of uranium deposition (Stage 4). It is proposed that the Fox Lake Fault is partitioned into three parallel segments at the Fox Lake deposit; these segments are connected via two fault jogs, thereby

creating a rhombic fault geometry (Figure 10). These fault jogs are inferred to have parallel orientation as Fault A or Fault B. This is interpreted from deformation bands observed in Fox Lake outcrop (Fig. 4 and Fig. 2). This type of fault geometry is likely to produce transtension to a region undergoing compression, during Stage 4 and Stage 6 of our palaeostress model dependent on the orientation of  $\sigma_H$  (Fig. 10). For example, E-W  $\sigma_H$  orientation invokes Andersonian strike-slip faulting and NW-SE  $\sigma_H$  invokes Riedel strike-slip faulting; both producing favourable tensile conditions for transtensional strain accommodation considering fault jog rhomb geometry (Fig. 10). Our palaeostress model implies the Athabasca Basin was subject to approximately NW-SE and E-W  $\sigma_H$  orientations during Stages 4 and 6, respectively (Fig. 6). Thus, Stage 4 and Stage 6 likely supported opening of dilational jogs at the Fox Lake uranium deposit location. These fault jog zones have a lower ambient fluid pressure than the surrounding host rock. This type of pressure gradient drives fluids – uranium bearing fluids in this case – towards the ambient zone.

This model offers a structural control to uranium mineralisation at Fox Lake and implies pressure gradient is an important factor in driving fluid flow into areas of dilation (Fig. 10). Fox Lake uranium deposit mineralisation exhibit massive textures (Rogers et al., 2017). Massive textured mineralisation fits our mineral model for Fox Lake because dilational fault jogs form by transtension rather than transpression (Fig. 10). Transtensional strain accommodation creates a negative void space, conducive for massive textured mineralisation within the dilational fault jog. This type of fault analysis may be used as an analogue for uranium exploration under thick sequenc-

es of cover.

Sandstone faults form as a three-stage process outlined by Aydin and Johnson (1978), through the evolution of singular deformation bands into clusters, which then rupture to create a slip surface. The largest clusters of cataclastic bands observed at Fox Lake were fractured and represent slip surfaces (Fig. 5b). Figure 8 demonstrates that these clusters are full of small fractures and may represent preferential conduits for fluid flow through what are otherwise heavily silicified Athabasca Group sequences, an impediment to fluid flow (e.g. Ramaekers and Eccles, 2004). The formation of drusy quartz on fractured clusters (i.e. slip surfaces) may be inferred as simple pressure dissolution processes due to grain-grain impingement in the sandstone. This results in silica enriched fluids collecting in porosity spaces, localized (mm- to cm to m scale) migration of these fluids towards extensional fractures (Mode 1 fractures in particular). Therefore, active fracturing resulted in syntaxial quartz precipitation in open fractures. Weak to moderately desilification occurred within the fractures, which supports the notion that fractures are sites for fluid migration and precipitated quartz, due to fluctuating pressure, which caused fluid silica oversaturation.

Formation of dravite cemented dilation bands is constrained to Stage 4, implies dravite fluid alteration occurred during Stage 4 of our palaeostress model (Fig. 6). The formation of dravite veins adjacent to pre-existing cataclastic bands in Stages 1–3, infers hydraulic fracturing via crack propagation, supporting our interpretation that the dravite fluid event is contemporaneous with Stage 4 of our model.

Deformation bands observed at Fox Lake outcrops are sparse in some areas and highly concentrated in others (Fig. 2). This indicates that strain is distributed unequally in the Fox Lake outcrops and may be reflecting localised strain partitioning. In drill holes VR-056 and VR-057, we observed extensive grain fracturing and cataclasis within densely populated deformation band zones. This was also seen for most interband grain-grain boundaries, demonstrating high strain partitioning in these zones (*sensu* Shipton et al., 2005). Seven deformation band zones were observed evenly spaced throughout the drill hole, appearing every ~50 m (Fig. 7a). This may reflect a function of inherent sedimentary characteristics, such as grain size, sorting, primary porosity, etc. The uppermost formation, the Dunlop-Clampitt Formation exhibits a well sorted, medium to fine grain size. The lower Collins and Read formations exhibit moderately sorted medium to large grain size. However, depth does not seem to be a factor in strain partitioning (Fig. 7).

At Fox Lake and Wide Lake, silica cement is characterised by opaque purple, pink, and white coloured deformation bands (e.g. Fig. 9a). We suggest the change in colour represents a gradation of hematite intensities and reflect a temporal balance of fluid chemistry. Microprobe results indicate geochemical signatures of deformation band cement (pure silica cement) contain elevated concentrations of aluminium, magnesium, calcium, potassium, and iron, with the highest concentration in the middle of the healed quartz grain (Fig. 9a). These results demonstrate over the course of the deformation band cementation period, aluminium, magnesium, calcium, potassium, and iron concentrations increased by syntaxial sealing. These results also indicate that

geochemical signatures of deformation band clusters (comminuted matrix and cement) fluctuate between high and low concentrations of aluminium, magnesium, calcium, potassium, and iron, peaking in the centre of the cluster (Fig. 9b). We propose two models to account for cement instability within deformation bands, in terms of enrichment or rather depletion of aluminium, magnesium, calcium, potassium, and iron: 1) micro-fractures at deformation band edges increase permeability, enhancing fluid flow parallel to the deformation band, resulting in demineralisation of enriched cement; or 2) micro-fractures within deformation bands enhance band permeability, resulting in heavy fluid flow through the deformation band and cement precipitation.

## 6.0 Conclusions

- A total of 1713 deformation bands are documented within the Manitou Falls Group at Fox Lake (i.e. DDH REA-181, outcrop) and Wide Lake (DDH VR-56, VR-57). Four grid maps were constructed at Fox Lake, which highlight areas with high concentrations of deformation bands. The largest deformation band clusters observed reach thicknesses in excess of 9 cm and were oriented NW-SE.
- A palaeostress model is presented for the Manitou Falls Group of the Athabasca Basin. That includes six stages. Stage 1: NE-SW extension; Stage 2: N-S extension; Stage 3: NW-SE extension; Stage 4: NW-SE transtension; Stage 5: N-S compression; Stage 6: E-W compression.
- Uranium mineralisation at Fox Lake is provisionally proposed to be related to transtensional strain

accommodation, which occurred during Stage 4 and Stage 6 of the palaeostress model. Structural evidence implies transtensional stress driven fluid flow gradients into low pressure sites and likely enhanced the concentration of uranium-bearing fluid to the Fox Lake uranium deposit.

- Deformation band zones reflecting high intensity strain demonstrates strain partitioning is not influenced by sedimentary characteristics of the Manitou Falls Group sandstones. Individual splays reactivated with the evolving stress regime.
- Dravite fluid alteration proximal to the Fox Lake uranium deposit is synchronous with Stage 4 of our palaeostress model.

### Acknowledgements

We thank the Geological Survey of Saskatchewan for their help with fieldwork logistics and financial support. The Government of Saskatchewan, Ministry of the Economy (ECON) research grant. Cameco Inc. was very generous to accommodate us on their research camp at Wide Lake. We also thank Colin Card, Derek Johnson, Arin Kitchen, Joshua Mukakwami, Aaron Brown, and countless others for their helpful discussions and field work assistance.

### References

- Ahlgren, S. G., 2001, The nucleation and evolution of Riedel shear zones as deformation bands in porous sandstone: *Journal of Structural Geology*, v. 23, no. 8, p. 1203-1214.
- Alexandre, P., Kyser, K., Jiricka, D., and Witt, G., 2012, Formation and Evolution of the Centennial Unconformity-Related Uranium Deposit in the South-Central Athabasca Basin, Canada: *Economic Geology*, v. 107, no. 3, p. 385-400.
- Alikarami, R., and Torabi, A., 2015, Micro-texture and petrophysical properties of dilation and compaction shear bands in sand: *Geomechanics for Energy and the Environment*, v. 3, p. 1-10.
- Allmendinger, R. W., Cardozo, N., and Fisher, D. M., 2012, *Structural geology algorithms: vectors and tensors*, New York, Cambridge University Press.
- Anderson, E. M., 1951, *The dynamics of faulting and dyke formation with applications to Britain*, Hafner Pub. Co.
- Annesley, I. R., Madore, C., and Portella, P., 2005, Geology and thermotectonic evolution of the western margin of the Trans-Hudson Orogen: evidence from the eastern sub-Athabasca basement, Saskatchewan: *Canadian Journal of Earth Sciences*, v. 42, no. 4, p. 573-597.
- Annesley, I. R., Madore, C., Shi, R., and Krogh, T. E., 1997, U-Pb geochronology of thermotectonic events in the Wollaston Lake area, Wollaston Domain: A summary of 1994-1996 results: *Summary of investigations*, p. 97-94.
- Ansdell, K. M., 2005, Tectonic evolution of the Manitoba-Saskatchewan segment of the Paleoproterozoic Trans-Hudson Orogen, Canada: *Canadian Journal of Earth Sciences*, v. 42, no. 4, p. 741-759.
- Antonellini, M., and Aydin, A., 1994, Effect of

- faulting on fluid flow in porous sandstones: petrophysical properties: AAPG bulletin, v. 78, no. 3, p. 355-377.
- Antonellini, M. A., Aydin, A., and Pollard, D. D., 1994, Microstructure of deformation bands in porous sandstones at Arches National Park, Utah: *Journal of Structural Geology*, v. 16, no. 7, p. 941-959.
- Ashton, K., Boivin, D., and Heggie, G., 2001, Geology of the southern Black Bay belt, west of Uranium City, Rae province: Summary of investigations, v. 2, p. 2001-2004.2002.
- Ashton, K., Hartlaub, R., Bethune, K., Heaman, L., Rayner, N., and Niebergall, G., 2013, New depositional age constraints for the Murmac Bay group of the southern Rae craton, Canada: *Precambrian Research*, v. 232, p. 70-88.
- Aydin, A., 1978, Small faults formed as deformation bands in sandstone: *Pure and Applied Geophysics*, v. 116, no. 4-5, p. 913-930.
- Aydin, A., Borja, R. I., and Eichhubl, P., 2006, Geological and mathematical framework for failure modes in granular rock: *Journal of Structural Geology*, v. 28, no. 1, p. 83-98.
- Aydin, A., and Johnson, A., 1978, Development of faults as zones of deformation bands and as slip surfaces in sandstone: *Pure and Applied Geophysics*, v. 116, no. 4-5, p. 931-942.
- Aydin, A., and Johnson, A. M., 1983, Analysis of faulting in porous sandstones: *Journal of Structural Geology*, v. 5, no. 1, p. 19-31.
- Ballas, G., Fossen, H., and Soliva, R., 2015, Factors controlling permeability of cataclastic deformation bands and faults in porous sandstone reservoirs: *Journal of Structural Geology*, v. 76, p. 1-21.
- Baudemont, D., and Fedorowich, J., 1996, Structural control of uranium mineralization at the Dominique-Peter Deposit, Saskatchewan, Canada: *Economic Geology*, v. 91, no. 5, p. 855-874.
- Baudemont, D., and Pacquet, A., 1999, The Sue D and E uranium deposits, northern Saskatchewan: Evidence for structurally controlled fluid circulation in the Athabasca Basin.
- Bickford, M., Collerson, K., Lewry, J., Van Schmus, W., and Chiarenzelli, J., 1990, Proterozoic collisional tectonism in the Trans-Hudson orogen, Saskatchewan: *Geology*, v. 18, no. 1, p. 14-18.
- Bosman, S. A., and Ramaekers, P., 2015, Athabasca Group+ Martin Group= Athabasca Supergroup? Athabasca Basin multi-parameter drill log compilation and interpretation, with updated geological map: Summary of Investigations, v. 2, p. 2015-2014.2012.
- Card, C., Pana, D., Portella, P., Thomas, D., Annesley, I., Jefferson, C., and Delaney, G., 2007, Basement rocks to the Athabasca Basin, Saskatchewan and Alberta: *BULLETIN-GEOLOGICAL SURVEY OF CANADA*, v. 588, p. 69.
- Card, C. D., 2016, A coming together: The juxtaposition of the Rae and Hearne cratons along the Virgin River shear zone (Snowbird tectonic zone), Saskatchewan, Canada, and the implications for proto-Laurentia: *Faculty of Graduate Studies and Research, University of Regina*.
- Card, C. D., Bethune, K. M., Rayner, N., and Creaser, R. A., 2018, Characterising the southern part of the Hearne Province: A forgotten part of Canada's shield revisited: *Precambrian Research*, v. 307, p. 51-65.
- Clauer, N., Ey, F., and Gauthier-Lafaye, F., 1985, K-Ar dating of different rock types from the Cluff Lake uranium ore deposits (Saskatchewan, Canada): The Carswell structure uranium deposits, Saskatchewan. Edited by R. Lainé, D. Alonso, and M. Svab. *Geological Association of Canada, Special Paper*, v. 29, p. 47-53.
- Corrigan, D., 2012, Paleoproterozoic crustal evolution and tectonic processes: Insights

- from the Lithoprobe program in the Trans-Hudson Orogen, Canada: Tectonic Styles in Canada: The LITHOPROBE Perspective, p. 237-284.
- Cox, S., Knackstedt, M., and Braun, J., 2001, Principles of structural control on permeability and fluid flow in hydrothermal systems, Structural controls on ore genesis, Volume 14, Society of Economic Geologists Littleton, CO, p. 1-24.
- Creaser, R., and Stasiuk, L., 2007, Depositional age of the Douglas Formation, northern Saskatchewan, determined by Re-Os geochronology: BULLETIN-GEOLOGICAL SURVEY OF CANADA, v. 588, p. 341.
- Davis, G. H., Bump, A. P., García, P. E., and Ahlgren, S. G., 2000, Conjugate Riedel deformation band shear zones: Journal of Structural Geology, v. 22, no. 2, p. 169-190.
- Debenham, N., King, R. C., and Holford, S. P., 2018, The influence of a reverse-reactivated normal fault on natural fracture geometries and relative chronologies at Castle Cove, Otway Basin: Journal of Structural Geology, v. 112, p. 112-130.
- DeDecker, J., 2019, Alteration and Mineral Paragenesis of the McArthur River and Fox Lake Uranium Deposits, Athabasca Basin: A New Model for the Formation of Unconformity-related Uranium Deposits: Colorado School of Mines. Arthur Lakes Library.
- Du Bernard, X., Eichhubl, P., and Aydin, A., 2002, Dilation bands: A new form of localized failure in granular media: Geophysical Research Letters, v. 29, no. 24, p. 2176-2180.
- Exner, U., Kaiser, J., and Gier, S., 2013, Deformation bands evolving from dilation to cementation bands in a hydrocarbon reservoir (Vienna Basin, Austria): Marine and Petroleum Geology, v. 43, p. 504-515.
- Fairburn, B., 1998, The Willunga Embayment - a stratigraphic revision: Mineral Resources of South Australia, v. 11, p. 35-41.
- Farrell, N. J. C., Healy, D., and Taylor, C. W., 2014, Anisotropy of permeability in faulted porous sandstones: Journal of Structural Geology, v. 63, p. 50-67.
- Fossen, H., and Bale, A., 2007, Deformation bands and their influence on fluid flow: AAPG Bulletin, v. 91, no. 12, p. 1685-1700.
- Fossen, H., Schultz, R. A., Shipton, Z. K., and Mair, K., 2007, Deformation bands in sandstone: a review: Journal of the Geological Society of London, v. 164, no. 4, p. 755-769.
- Fossen, H., Schultz, R. A., and Torabi, A., 2011, Conditions and implications for compaction band formation in the Navajo Sandstone, Utah: Journal of Structural Geology, v. 33, no. 10, p. 1477-1490.
- Hiatt, E., and Kyser, T., 2007, Sequence stratigraphy, hydrostratigraphy, and mineralizing fluid flow in the Proterozoic Manitou Falls Formation, eastern Athabasca Basin, Saskatchewan: BULLETIN-GEOLOGICAL SURVEY OF CANADA, v. 588, p. 489.
- Hoeve, J., and Sibbald, T. I., 1978, On the genesis of Rabbit Lake and other unconformity-type uranium deposits in northern Saskatchewan, Canada: Economic Geology, v. 73, no. 8, p. 1450-1473.
- Hoeve, J., Sibbald, T. I., Ramaekers, P., and Lewry, J. F., 1980, Athabasca basin unconformity-type uranium deposits A special class of sandstone-type deposits, International Atomic Energy Agency (IAEA), IAEA.
- Hoffman, P. F., 1988, United plates of America, the birth of a craton: Early Proterozoic assembly and growth of Laurentia: Annual Review of Earth and Planetary Sciences, v. 16, no. 1, p. 543-603.
- Jefferson, C., Thomas, D., Gandhi, S., Ramaekers, P., Delaney, G., Brisbin, D., Cutts, C., Portella, P., and Olson, R., 2007, Unconformity-associated uranium deposits of

- the Athabasca Basin, Saskatchewan and Alberta: *Bulletin-Geological Survey of Canada*, v. 588, p. 23.
- Li, Z., Bethune, K. M., Chi, G., Bosman, S. A., and Card, C. D., 2015, Topographic features of the sub-Athabasca Group unconformity surface in the southeastern Athabasca Basin and their relationship to uranium ore deposits: *Canadian Journal of Earth Sciences*, v. 52, no. 10, p. 903-920.
- Li, Z., Chi, G., Bethune, K. M., David, T., and Zaluski, G., 2017, Structural Controls on Fluid Flow During Compressional Reactivation of Basement Faults: Insights from Numerical Modeling for the Formation of Unconformity-Related Uranium Deposits in the Athabasca Basin, Canada: *Economic Geology*, v. 112, no. 2, p. 451-466.
- Lubiniecki, D. C., White, S. R. S., King, R. C., Holford, S. P., Bunch, M. A., and Hill, S., 2019, Structural evolution of carbonate-hosted cataclastic bands adjacent to a major neotectonic fault, Sellicks Beach, south Australia: *Journal of Structural Geology*, v. 126, p. 11-24.
- Mandl, G., 1988, *Mechanics of Tectonic Faulting*, *Dev. Struct. Geol.*, vol. X, edited by HJ Zwart, Elsevier, New York.
- Micklethwaite, S., Sheldon, H. A., and Baker, T., 2010, Active fault and shear processes and their implications for mineral deposit formation and discovery: *Journal of Structural Geology*, v. 32, no. 2, p. 151-165.
- Pagel, M., 1975, *Cadre Géologique des gisements d'uranium dans la structure Carswell (Saskatchewan-Canada)–«Etude des phases fluides»*. Unpub: PhD thesis, Université de Nancy 1.
- Potts, G. J., and Reddy, S. M., 2000, Application of younging tables to the construction of relative deformation histories—1: fracture systems: *Journal of Structural Geology*, v. 22, no. 10, p. 1473-1490.
- Pysklywec, R., and Mitrovica, J., 2000, Mantle flow mechanisms of epeirogeny and their possible role in the evolution of the Western Canada Sedimentary Basin: *Canadian Journal of Earth Sciences*, v. 37, no. 11, p. 1535-1548.
- Rainbird, R., Stern, R., Rayner, N., and Jefferson, C., 2007, Age, provenance, and regional correlation of the Athabasca Group, Saskatchewan and Alberta, constrained by igneous and detrital zircon geochronology: *Bulletin-Geological Survey of Canada*, v. 588, p. 193.
- Ramaekers, P., and Eccles, D., 2004, Development, stratigraphy and summary diagenetic history of the Athabasca Basin, early Proterozoic of Alberta and its relation to uranium potential, Alberta Energy and Utilities Board. Alberta Geological Survey.
- Ramaekers, P., Jefferson, C., Yeo, G., Collier, B., Long, D., Drever, G., McHardy, S., Jiricka, D., Cutts, C., and Wheatley, K., 2007, Revised geological map and stratigraphy of the Athabasca Group, Saskatchewan and Alberta: *Bulletin-Geological Survey of Canada*, v. 588, p. 155.
- Reid, K. D., Ansdell, K., Jiricka, D., Witt, G., and Card, C., 2014, Regional Setting, Geology, and Paragenesis of the Centennial Unconformity-Related Uranium Deposit, Athabasca Basin, Saskatchewan, Canada: *Economic Geology*, v. 109, no. 3, p. 539-566.
- Rogers, S., Bridge, N., O'Dowd, C., Yang, H., Aubin, A., and Yackulic, A., 2017, Geological framework of the Fox Lake uranium deposit, Athabasca Basin, Canada, Open House: Saskatoon, Saskatchewan, Saskatchewan Geological Survey.
- Rotevatn, A., Sandve, T. H., Keilegavlen, E., Kolyukhin, D., and Fossen, H., 2013, Deformation bands and their impact on fluid flow in sandstone reservoirs: the role of natural thickness variations: *Geofluids*, v. 13, no. 3, p. 359-371.
- Shipton, Z., Evans, J., and Thompson, L., 2005, The geometry and thickness of deformation-band fault core and its influence

on sealing characteristics of deformation-band fault zones.

- Tondi, E., Rustichelli, A., Cilona, A., Balsamo, F., Storti, F., Napoli, G., Agosta, F., Renda, P., and Giorgioni, M., 2016, Hydraulic properties of fault zones in porous carbonates, examples from central and southern Italy: *Italian Journal of Geosciences*, v. 135, no. 1, p. 68-79.
- Wong, T.-f., and Baud, P., 2012, The brittle-ductile transition in porous rock: A review: *Journal of Structural Geology*, v. 44, p. 25-53.
- Yeo, G., Delaney, G., and Jefferson, C., 2007, The Wollaston Supergroup, stratigraphy and metallogeny of a Paleoproterozoic Wilson cycle in the Trans-Hudson orogen, Saskatchewan: *BULLETIN-GEOLOGICAL SURVEY OF CANADA*, v. 588, p. 89.
- Zhu, W., Baud, P., and Wong, T.-f., 2010, Micro-mechanics of cataclastic pore collapse in limestone: *Journal of Geophysical Research: Solid Earth*, v. 115.

# CHAPTER 6

# Statement of Authorship

Title of Paper	Cataclastic-dilation deformation bands: A new type of cataclastic deformation band in the Athabasca Basin, Canada.		
Publication Status	<input type="checkbox"/> Published	<input type="checkbox"/> Accepted for Publication	<input checked="" type="checkbox"/> Unpublished and Unsubmitted work written in manuscript style
Publication Details	<input type="checkbox"/> Submitted for Publication		

## Principal Author

Name of Principal Author (Candidate)	Drew Lubiniecki		
Contribution to the Paper	Completed fieldwork, collected and interpreted data, collected and analysed samples, wrote and prepared manuscript, acted as corresponding author.		
Overall percentage (%)	75%		
Certification:	This paper reports on original research I conducted during the period of my Higher Degree by Research candidature and is not subject to any obligations or contractual agreements with a third party that would constrain its inclusion in this thesis. I am the primary author of this paper.		
Signature		Date	<b>24/9/2019</b>

## Co-Author Contributions

By signing the Statement of Authorship, each author certifies that:

- i. the candidate's stated contribution to the publication is accurate (as detailed above);
- ii. permission is granted for the candidate to include the publication in the thesis; and
- iii. the sum of all co-author contributions is equal to 100% less the candidate's stated contribution.

Name of Co-Author	Rosalind King		
Contribution to the Paper	Supervised fieldwork, aided in collection of data and samples, helped with data interpretation and manuscript revision.		
Signature		Date	<b>18/9/2019</b>

Name of Co-Author	Simon Holford		
Contribution to the Paper	Supervised fieldwork, aided in collection of data and samples, helped with data interpretation and manuscript revision.		
Signature		Date	18/9/19

Name of Co-Author	Mark Bunch		
Contribution to the Paper	Supervised fieldwork, aided in collection of data and samples, helped with data interpretation and manuscript revision.		
Signature		Date	<b>18/9/2019</b>

Name of Co-Author	Dave Thomas		
Contribution to the Paper	Industry correspondent, aided in fieldwork and overall concept of module.		
Signature		Date	<i>July 30, 2019</i>

Name of Co-Author	Gary Delaney		
Contribution to the Paper	Financial support, government correspondent, and overall concept of thesis.		
Signature		Date	<i>July 29/19</i>

Please cut and paste additional co-author panels here as required.

---

## Cataclastic-dilation deformation bands: A new type of cataclastic deformation band in the Athabasca Basin, Canada.

---

### Abstract

Deformation bands are the most common strain feature found in porous granular sedimentary rocks of the rigid upper crust. Strain-hardened cataclastic bands are undoubtedly the most commonly documented deformation band formation mechanism. Despite nearly 50 years of research, reactivation of strain-hardened deformation band (not including slip-surfaces) has not been considered plausible, until now. We present the first documented case study challenging this paradigm, filling the knowledge gap that divides the mechanical evolution and reactivation of cataclastic bands. Dissolution bands, cataclastic bands, dilational cataclastic bands, and fractures were identified in outcrop and drill cores of sandstones from the Proterozoic Manitou Falls Group of the Athabasca Basin, in the vicinity of the Fox Lake and Centennial unconformity associated uranium deposits. Microstructural evidence from optical and electron microscopy has revealed that cataclastic bands were reactivated via dilation, inferred to happen under fault-induced hydrostatic conditions associated with faulting. We suggest that hydraulic fault suction pumped dravite fluid, associated with uranium mineralisation in the Athabasca Basin, into newly developed cataclastic bands. Resulting fluid overpressure positively dilated the pre-existing cataclastic bands prior to cataclastic band cementation and formed the newly discovered dilational cataclastic bands presented here. This work challenges our current understanding of cataclastic deformation bands and enhances our understanding of the mechanics of C10 Fault at Fox Lake.

**Keywords:** Athabasca Basin; Structural Evolution; Centennial Uranium Deposit; Fox Lake Uranium Deposit; Manitou Falls Formation; Deformation Band.

---

### 1. Introduction

Deformation bands are discrete zones of localized strain that form as a result of compaction or dilation through sediment loading and high deviatoric stress in porous granular sedimentary rocks, such as sandstone (Fossen et al., 2007). Strain may be accommodated by the following mechanical processes: grain boundary sliding (disaggregation band), grain crushing (cataclastic band), phyllosilicate alignment (phyllosilicate band), cementation (cemented band), and dissolution (dissolution band) (Fossen et al., 2007). These mechanisms facilitate pore space collapse (compaction band) or pore space enlargement (dilation band) to accommodate either kinematic simple shear strain (e.g. shear-enhanced dila-

tion band), or pure volumetric strain (pure compaction band) (Aydin et al., 2006). Cataclastic bands, the first type of deformation band to be recognised (Aydin, 1978), have been well studied due to their ubiquitous mechanical nature, characterised by grain size reduction via fracture and comminution (e.g. Cashman and Cashman, 2000; Fossen et al., 2007; Philit et al., 2018). However, nearly four decades after Aydin (1978) described the first cataclastic band, our understanding of dilation and dissolution bands remains poor. Dilation bands have been predicted theoretically (e.g. Bésuelle, 2001b) and produced in lab experiments (e.g. Bésuelle, 2001a). However, they are not commonly recognized in the field (e.g. Alikarami and Torabi, 2015; Antonellini et al., 1994; Du Bernard et al., 2002; Exner

et al., 2013; Lommatzsch et al., 2015). Lack of recognition has resulted in a poor overall understanding of the mechanical behaviours underpinning dilation band formation (e.g. Schultz and Siddharthan, 2005). Dissolution bands also have a poor field record, mainly observed in carbonate-hosted deformation bands at grain boundaries (e.g. Aydin et al., 2010; Gaviglio et al., 2009; Kaminskaite et al., 2019; Tondi, 2007; Tondi et al., 2016) and far less commonly observed in siliciclastic sandstone (e.g. Torabi, 2008; Torabi and Fossen, 2009; Torabi et al., 2008).

Aydin (1978) noted the well-accepted sequential evolution of deformation bands, which progresses from individual bands to zones of deformation bands and finally to slip surfaces. Zones of compaction bands are often associated with reduced permeability, resulting in altered fluid flow direction and compartmentalisation in aquifers and reservoirs (e.g. Antonellini and Aydin, 1994; Ballas et al., 2015; Fossen and Bale, 2007; Lubiniecki et al., 2019; Tondi et al., 2016). However, deformation bands may also kinematically dilate, forming as a dilation band. Dilation bands enhance porosity and permeability, resulting in fluid conduits relative to background host rocks (e.g. Exner et al., 2013; Fossen et al., 2007). Structurally controlled mineral deposits are intrinsically linked to faults as conduits for fluid (e.g. Li et al., 2017; Sibson, 1981, 1994). Despite deformation bands fluid flow enhancing and retarding properties, their role in structurally controlled mineral deposits is understudied.

In most cases the formation of deformation bands is a result of the strain hardening process (Rudnicki and Rice, 1975). Cataclasis development enhances friction at grain contacts and invokes strain hardening (Fossen et al., 2007).

Strain hardening strengthens the cataclastic band, until strain accommodation reaches yield strength, making continual strain accommodation – energetically conservative – favourable in the adjacent host rock (Rudnicki and Rice, 1975). For strain to continue, new deformation bands will initiate in the adjacent host rock rather than continue in a single band, thus forming clusters (Aydin and Johnson, 1978; Philit et al., 2018). These newly formed bands are stronger than the surrounding host rock; however, their strength is a product of friction and lithostatic and deviatoric stress (Rudnicki and Rice, 1975).

The linear stress-strain relationships of strain hardening underpins the geomechanics behind our current understanding that governs the formation of cataclastic bands. The strain hardening paradigm relies on strength produced by continual stress to drive grain-boundary friction (Mair et al., 2000). Without continual stress, friction decreases and strength is lost. Sibson (1981) and Sibson et al. (1988) argue strike-slip faulting may induce high hydrostatic pressures and cause localised dilatant fractures; this is caused by fault-induced hydraulic pumping, which effectively reduces the internal friction of the rock. Thus, we suggest fault-induced hydraulic pumping may provide a mechanism to reduce the internal friction in sandstones of the Manitou Falls Group (Bosman and Ramaekers, 2015, equalize the lithostatic and deviatoric stress conditions, and effectively reduce strain hardening and cataclastic band strength. Considering this well accepted phenomena (i.e. strain hardening), fault-induced hydraulic pumping may provide mechanism for reactivation of cataclastic bands via dilation under continual lithostatic stress conditions.

This study was undertaken to improve understanding of the structural regime that formed deformation bands in Manitou Falls Group, associated with the unconformity related uranium deposits of the Dufferin Fault at Wide Lake and C-10 fault zone at Fox Lake. A second objective of this work was to enhance understanding of the progressive evolution of deformation bands as fluid conduits near the uranium deposits. In support of this study, structural data was collected from deformation bands in sandstone in oriented core from three drill holes, as well outcrops near the Centennial and Fox Lake uranium deposits. A broad spectrum of samples of different deformation bands were examined and analysed using optical and scanning electron microscopy (SEM). As such, this study undertakes rigorous investigation of deformation

bands in the Manitou Falls Group to better understand the role of fault mechanics in the Athabasca Basin. For the first time, we present a conceptual model of the dilational reactivation of cataclastic bands and argue they enhance fluid flow and structural permeability surrounding the Fox Lake uranium deposit, northern Saskatchewan, Canada.

## 2. Geological history of the Athabasca Basin

The crystalline basement underlying the Athabasca Basin comprises rocks of the Rae and Hearne provinces (Fig. 1). The two entities are heavily partitioned by numerous complicated fault arrays, including the prominent Snowbird Tectonic Zone (Card et al., 2007), which separates them. The Snowbird Tectonic Zone is a 5 km wide shear zone, defined

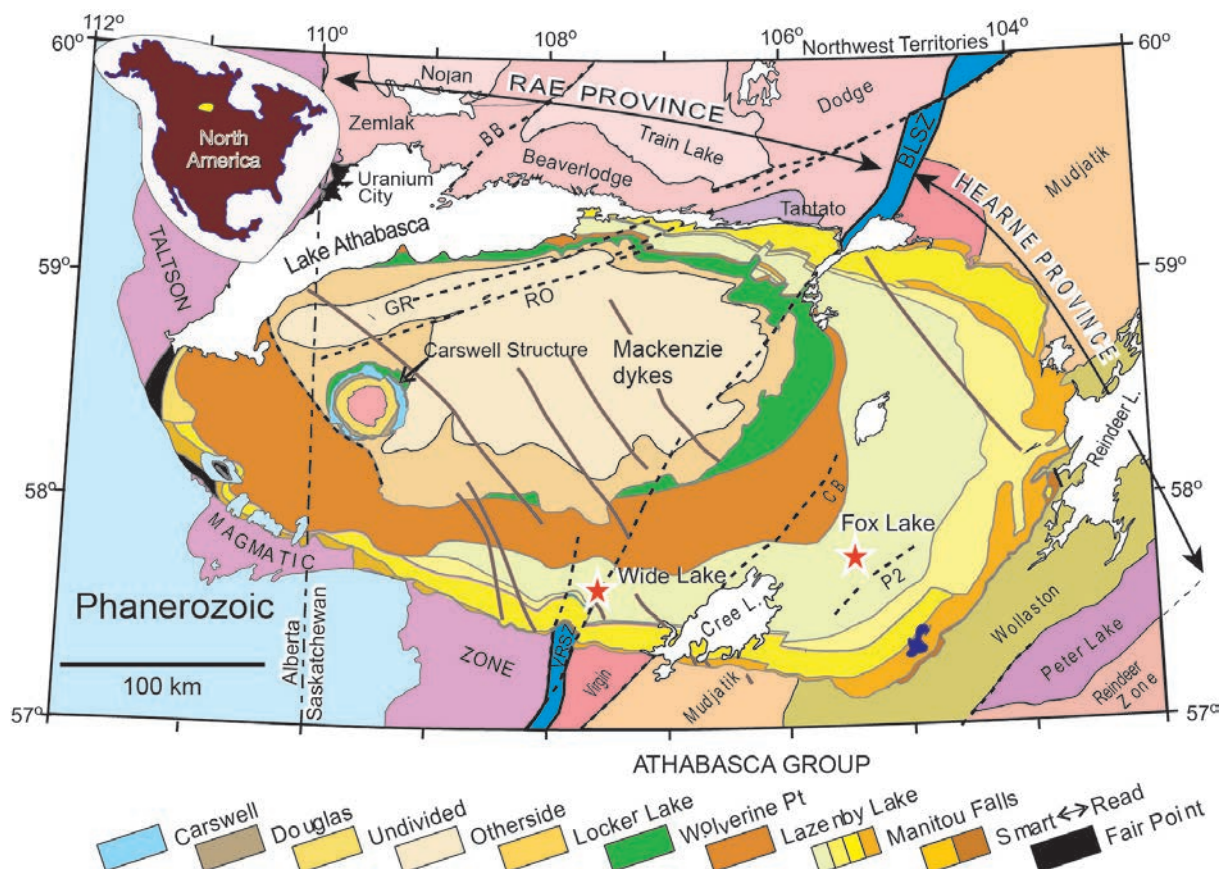


**Figure 1.** Geological map of the Athabasca Basin modified after Reid et al. 2014. Map key formations are listed from youngest to oldest (left to right).

as the Virgin River Shear Zone (VRSZ) in the southern portion of the Athabasca Basin and Black Lake Shear Zone (BLSZ) in the northern part of the basin (Fig. 1). The Rae Province is dominated by orthogneisses and accreted to the Hearn and Slave Cratons during the 2.0–1.9 Ga Taltson and Thelon orogenies (Card, 2016; Hoffman, 1988). Metasedimentary rocks are common in the Rae Province, north of the Athabasca Basin (e.g. Ashton et al., 2013) but are insignificant to the south (Card et al., 2014). The Hearne Province is dominated by Archean orthogneisses (e.g. Card et al., 2018) except near the eastern part of the Athabasca Basin, where high-grade siliciclastic metasedimentary rocks of the Wollaston Supergroup locally mantle Archean inliers (e.g. Yeo et al., 2007).

The formation of the intracratonic Athabasca Basin of northern Saskatchewan and north-eastern Alberta is related to isostatic flexural sag, as a result of top crustal loading, in response to the rapid uplift near the end of the Trans Hudson Orogeny at 1.75 Ga (Hiatt and Kyser, 2007). The Athabasca Basin contains strata deposited in the Palaeoproterozoic Jackfish Basin and Cree Basin, and the Mesoproterozoic Cree Basin and Mirror Basin (Bosman and Ramaekers, 2015). The study areas are located within the Basin formations are temporarily constrained; for example, the age of the Wolverine Point Formation is constrained to 1644 +/- 13 Ma using zircon in tuff clasts (Rainbird et al., 2007), and the Douglas Formation was dated using Re-Os, constrained to 1541 +/- 13 Ma (Creaser and Stasiuk, 2007). Deep weathering and intense erosion of the crystalline basement prior to deposition indicates the Cree Basin is younger than 1.75–1.78 Ga, which is the youngest retrograde metamorphic age of basement (Annesley et al., 1997).

The Cree and Mirror Basins formed between 1.80–1.50 Ga, constrained by Rb-Os and U-Pb methods (Ramaekers et al., 2007).

Palaeocurrent data indicating westerly flow infers that the Trans Hudson Orogeny provided the main source of sediment for the Manitou Falls Group (Rainbird et al., 2007; Ramaekers et al., 2007). The basin strata largely consist of the Athabasca Supergroup fluvial quartz arenites, listed in imbricate order from youngest to oldest in Figure 1. Extensive basin-wide unconformities marcate the stratigraphic extent of each basin (Ramaekers et al., 2007). The Manitou Falls Group is located within the Cree Basin, an overall fining upward succession of interbedded quartz-pebble conglomerate and quartz arenite. The Clampitt Formation and Dunlop Formation are stratigraphic equivalents, deposited in different deposystems (Fox Lake-Dunlop and Dufferin Lake approaches the Clampitt Formation boundary); they mark the beginning of a rapid increase in clay intraclasts, indicating rapid and sustained increase in accommodation space; however, this may also reflect changes in climate e.g. increased seasonality and aridity (Ramaekers et al., 2007). Pagel (1975) suggested this spike in accommodation space led to the deep burial of the Manitou Falls Group. Hoeve and Sibbald (1978) inferred a geothermal gradient of 35°, interpreted to have been buried to an approximate depth of 4800 m during peak diagenesis. Basin-wide isopach maps indicate these deposits are analogues in size to modern 150 km wide Kosi megafans in the southern Himalayas (Ramaekers et al., 2007).

This study focusses on two areas of the Athabasca Basin: the Fox Lake area and the Wide Lake area. The Fox Lake area

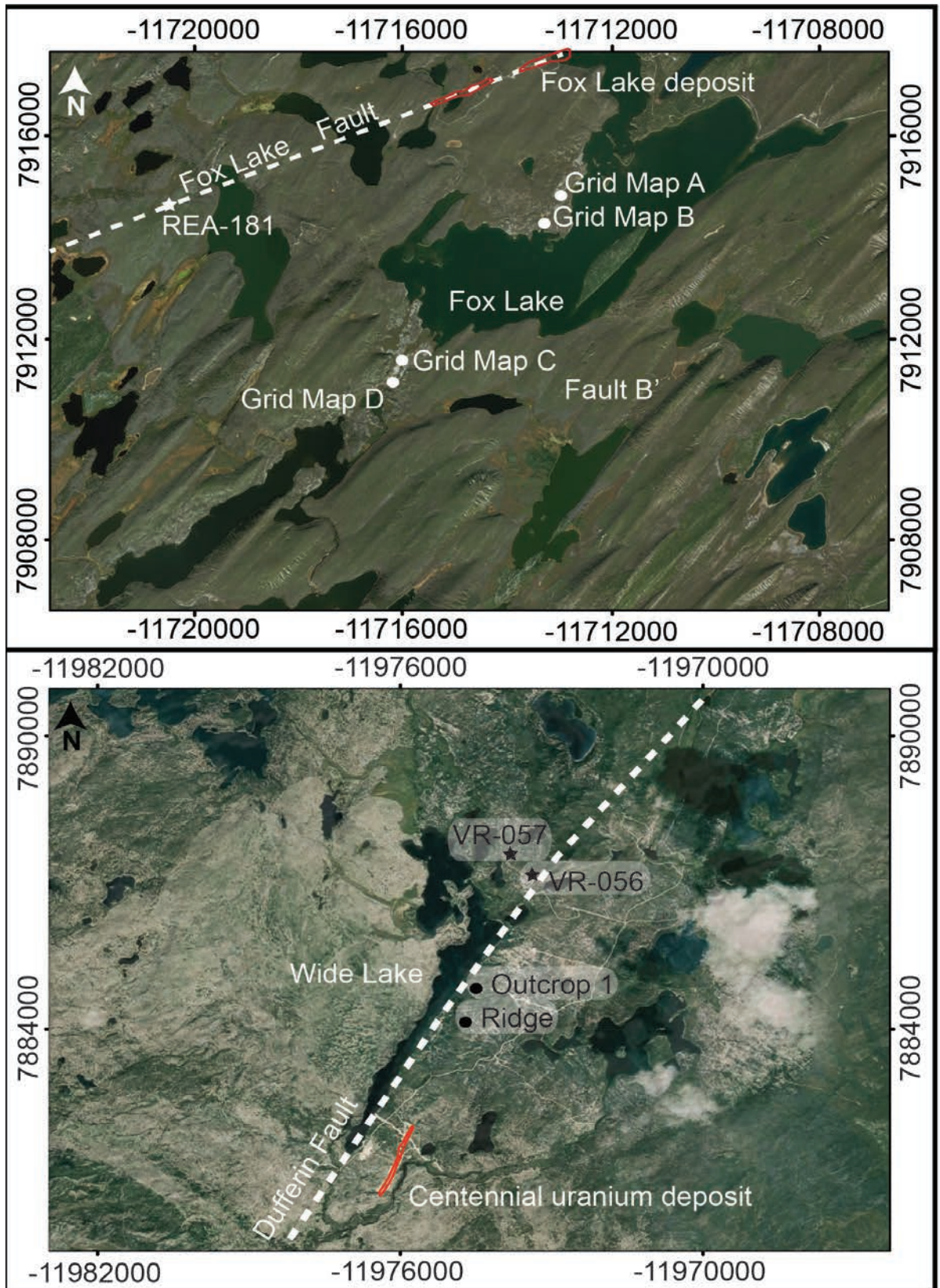


**Figure 2.** Satellite maps of the Fox Lake and Wide Lake regions. Red outlines define uranium mineralisation occurrences.

lies above over seven hundred metres of Manitou Falls Group quartz arenite. The graphitic basement fault array is rooted in rocks of the Hearne Province. The Fox Lake uranium deposit was discovered in 2015, spatially related to the graphitic fault system C10 Fault Zone and the basal unconformity of the Athabasca Basin (DeDecker, 2019; Rogers et al., 2017). The deposit displays a partitioned NE-SW trend at Fox Lake (Fig. 2). The Wide Lake, which hosts the Centennial uranium deposit area overlies the Snowbird Tectonic Zone in the southern Athabasca Basin that lies under 850 m to 900 m of Manitou Falls Group quartz arenites. Basement rocks entrained in the Snowbird Tectonic Zone are highly strained rocks of the Rae Province, including a relatively low-grade metasedimentary rock assemblage named the Virgin schist group (e.g., Card, 2016). The Dufferin Fault represents a reactivation of the northeast-trending Snowbird Tectonic Zone and has experienced over 200 m of northwest over southeast vertical displacement after deposition of the Manitou Falls Group (Card et al., 2007). The Centennial uranium deposit is located at Wide Lake, situated 300–400 m east of the Dufferin Fault (Fig. 2). A network of diabase dikes and sills intrude the main uranium mineralisation (Alexandre et al., 2012). Main uranium mineralisation formed between 1.27–1.59 Ga, coinciding with emplacement of the diabase dikes at 1270 Ma and has since been partially mobilised at ca. 380 Ma (Alexandre et al., 2012).

### 1. Methods

This study uses a structural dataset comprising 1713 deformation bands collected from drill core and outcrops of the Manitou Falls Group quartz arenite from Wide Lake (Fig. 2a) and Fox Lake (Fig. 2b) to

develop understanding of the histories of the Dufferin Fault and Fox Lake Fault. Three drill holes VR-56 (Wide Lake), VR-57 (Wide Lake), and REA-181 (Fox Lake) were logged, measured, and sampled, and outcrop at Fox Lake were measured and sampled (Table 1). Thirty-four thin sections were prepared for transmitted light microscopy. Samples were digitized, analysed using a petrographic microscope, then described in terms of their petrographic characteristics.

In northern Saskatchewan, the landscape is covered by glacial features and deposits such as glacial till and drumlins, made obvious by the linear NE-SW trending features observed in satellite imagery (Fig. 2). Bright areas on satellite imagery indicating high solar albedo were assumed to be areas of outcropping sandstones. At Fox Lake, three such areas were identified and are named Area 1, Area 2, and Area 3 in Fig. 2. Deformation bands were noted in both sparse and dense populations in these three areas and were mapped by a grid system in areas showing highest abundance (proximal to or within large clusters; Fig. 3). These grid maps were constructed from data collected in the field, individually mapped in 1x1 m blocks, then stitched together and digitized in digital image drafting software. Supplementing the outcrop data, structural measurements were also collected from drill hole (REA-181) located 4 kilometres west of Fox Lake, along the ENE-trending Fox Lake fault which hosts the Fox Lake uranium deposit (Fig. 2a).

### 2. Microstructural analysis of Fox Lake and Wide Lake deformation bands

The deformation bands observed in this study were classified following Aydin et

al. (2006) conforming to the basis of: a) orientation relative to bedding; b) geometry; c) presence or absence of observable shear relationships; and d) deformation mechanism. We have identified: three distinct types of deformation kinematics within the Manitou Falls Group; i) pure compaction band (PCB), ii) shear-enhanced compaction band (SECB), and iii) shear-enhanced dilation band (SEDB). Four distinct types of formation mechanism are inferred; i) dissolution band, ii) cataclastic band, iii) dilation band, and iv) fracture.

#### 4.1 Dissolution bands

Dissolution bands are made up of a singular silica-enriched 1 mm wide tabular zone with observable primary porosity reduction, commonly appearing as multiples of two to four parallel bands (Fig. 4a). Dissolution bands are observed to be bedding-parallel in all field locations. Dissolution bands appear in hand sample as thin (<1 mm) planar bands with no obvious indication of grain size reduction, under a hand lens at x10 magnification and higher content of siliceous cement relative to surrounding host rock (Fig. 4a). However, under a petrographic microscope at x10 magnification, most background sandstone grains exhibit a silica overprint that is rarely observed within the dissolution bands. Microscopic investigations reveal dissolution band granular alteration is primarily expressed by crenulated and sutured grain-grain boundaries, making the grains appear intergrown within the dissolution bands (Fig. 5a). Undulose extinction observed within many intraband grains is spotty and appearing polycrystalline, whereas extinction observed in the host rock grains appears to be normal and monocrystalline (Fig. 5a). Thus, the spotty extinction delineates the localisa-

tion of strain and highlights the boundaries of the dissolution band. Bands reach maximum widths of 2 mm and exhibit localised band thickening and thinning when observed under a petrographic microscope (x10 magnification; Fig. 5a). Shear displacement was not observed. Dissolution bands are partitioned by zones of undeformed host rock, making the bands discontinuous along strike; this characteristic was only observed in thin section (Fig. 5a).

#### 4.2 Cataclastic bands

Cataclastic deformation bands are characterized in hand samples by grain size reduction and an amorphous siliceous cement (Fig. 4b). These bands appear to have both planar and anastomosing geometries, which formed islands of undeformed host rock (Fig. 3c). Commonly, deformation bands are connected by a deformation band eye, defined as a zone where two parallel deformation bands meet and join, analogous to a fault step over zone (Fig. 3b). In outcrop, dip-sense was difficult to determine due to the glacially polished outcrop surfaces; however, within core, both normal and reverse offsets of bedding and other deformation bands were observed. Dextral and sinistral offsets were recorded in outcrop with up to 10 cm in displacement. Individual bands range from 0.5–4.0 mm in thickness (Fig. 3). Large cluster zones have been traced out for up to 50 m before being lost under the glacial till cover sequence. The widest cluster of cataclastic bands observed at Fox Lake were in excess of 9 cm wide (Fig. 3a). Cumulate thicknesses of up to 10 cm are noted in cluster zones and are metre scale in length, with a discontinuous, *en echelon* overstepping geometry (Fig. 3a).

Further investigation with petrographic

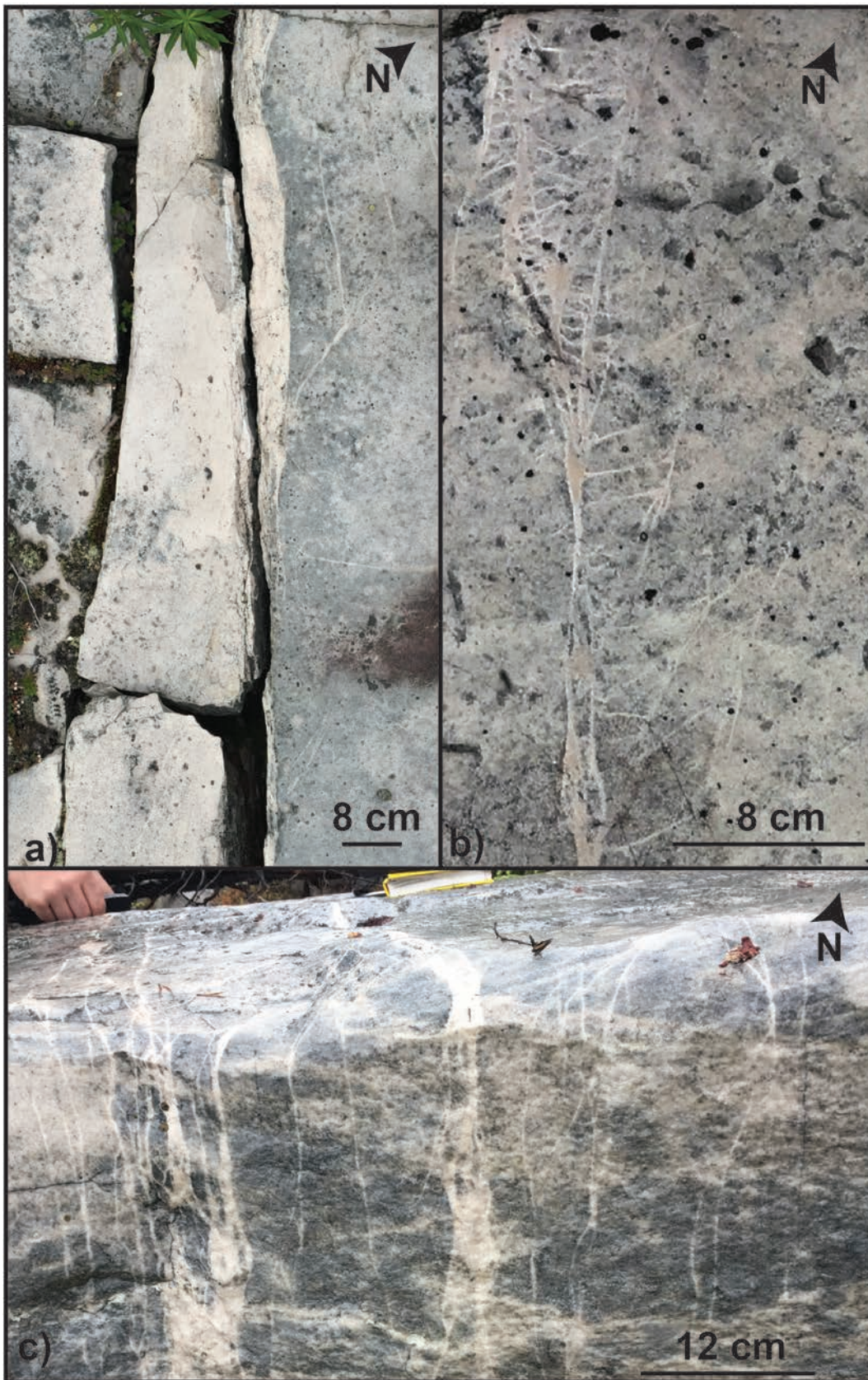


**Figure 3.** Photographs of cataclastic bands from the Manitou Falls Formation at Fox Lake: **a)** deformation band cluster and slip surface; **b)** plan view of a Riedel Shear Zone; **c)** face view of a Riedel Shear Zone.

microscope and SEM indicates distinct grain size reduction are associated with grain scale fractures and brecciation, indicative of crushing and milling (Fig. 5b). These cataclastic bands are made up of a central core zone defined by high-intensity cataclasis, surrounded by two outer zones defined by low-intensity cataclasis (Fig. 5b). The central core zone is comprised of silt–clay-sized grains of crushed quartz matrix, which hosts medium-sized spalled grains. The outer zones are thin (~0.5 mm) and comprised of fractured, yet minimally crushed grains. An interband transition zone is observed between parallel or oblique cataclastic bands in cluster zones, similar to other documented cases reported in carbonate systems (e.g. Antonellini et al., 2014; Rotevatn et al., 2016). Interband transition zones consist of low intensity cataclasis, defined by fractured and minimally crushed grains between two cataclastic bands (Fig. 5b). Thicker bands (>2 mm) tend to be more heterogeneous and have large undeformed or fractured grains hosted within the crushed matrix. However, thinner bands (<2 mm) exhibit a higher degree of comminution and homogeneity within their matrix. Pore space reduction is not obvious, although siliceous overprint is observed at most grain boundaries within host and cataclastic band (Fig. 5). Cataclastic bands form oblique to bedding and are noted forming in Stages 1–6 of palaeostress model (Fig. 6).

#### 4.3 Dilative cataclastic bands

Dilative cataclastic bands appear in hand sample as crushed quartz and non-crushed quartz grains floating within a non-siliceous cement matrix (Fig. 4c and Fig. 5d). Dilative cataclastic bands range in thickness from 1–7 mm, observed forming with white clay infill and dravite.

Voids were observed both in hand sample and thin section coinciding with small jogs in deformation band (Fig. 4d). Rafts of undeformed host rock are observed at an intersection junction between two adjoining bands (Fig. 5e). It should be noted that fractured grains are not confined to the dilation band, rather fairly pervasive throughout the entire sample; however, cataclasis is concentrated within the band (Fig. 5e). Dravite cemented dilative cataclastic bands only appear in deformation bands conforming to Stage 4 of our palaeostress model (Fig. 6).

Closer examination under a x10 magnification petrographic microscope reveals dilation bands with no apparent grain size reduction in hand sample reveals a fine grained mineral (i.e. clay or dravite) bounding fractured quartz grains (Fig. 5e). Other dilation bands exhibit a central core zone comprised of quartz grains that have been reduced in size (e.g. undeformed grain (0.5mm), comminuted grain (<0.1mm)) (Fig. 5d). These grains are hosted within a fine-grained cement matrix (i.e. dilation zone), surrounded by two outer cataclastic zones defined by remnant tightly packed fractured and crushed grains from an earlier cataclastic event (Fig. 5d). Matrix cement is composed mainly of greenish blue dravite while less commonly, drusy quartz is observed at Wide Lake and Fox Lake. Dravite is fine-grained and has been observed filling pore space in the undeformed host rock (Fig. 5d). The fine grained quartz and dravite matrix is then cross-cut by a secondary dravite texture, which is larger in grain size, fibrous, and growing radially from sharp cross-cut boundaries with the fine-grained dravite (Fig. 5d). The sharp boundary is laterally equivalent with a cusp and carrie texture, which extends out to create a sharp boundary with undeformed sandstone

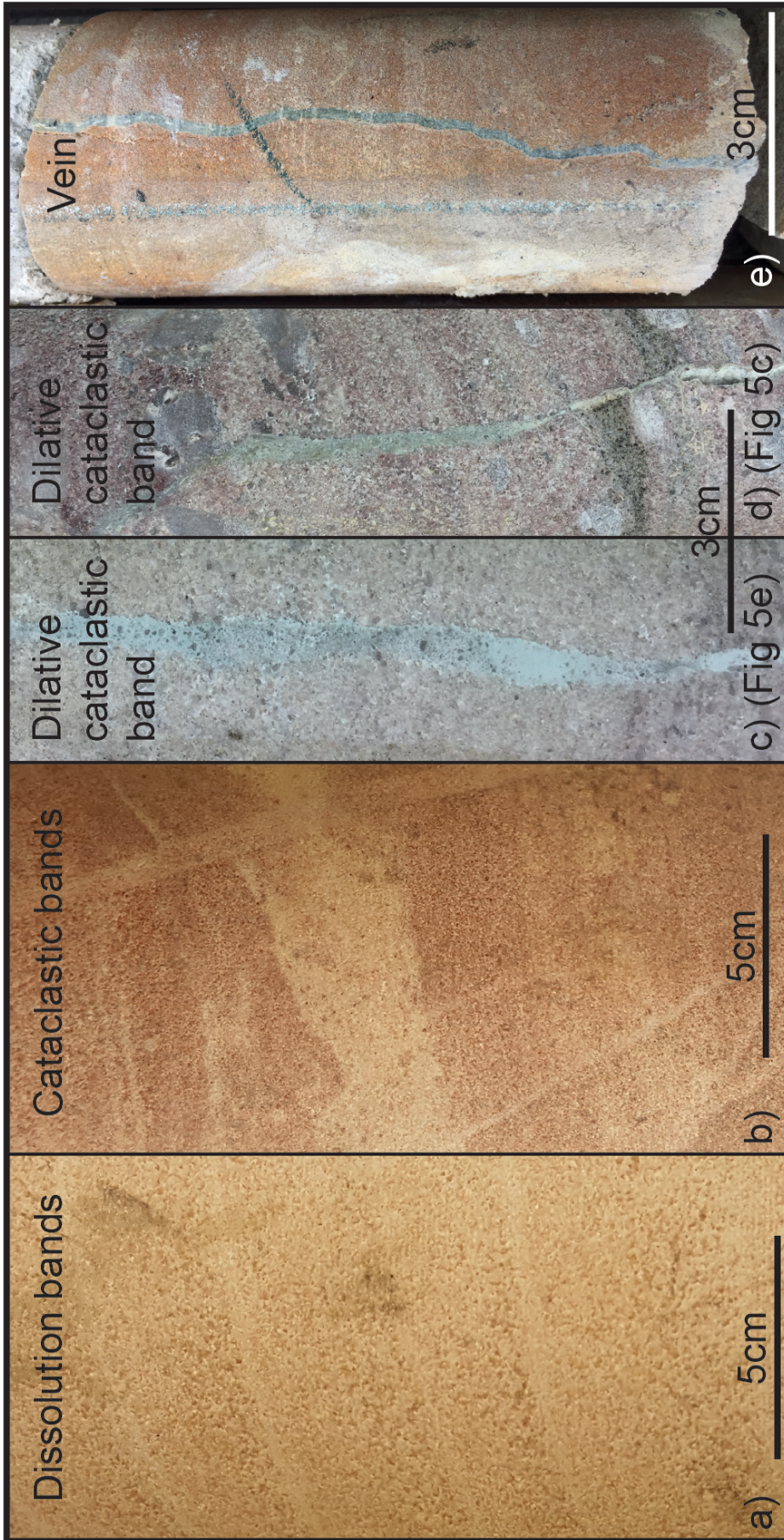


**Figure 4.** Photographs of hand sample of deformation bands observed within the Manitou Falls Group at Fox Lake and Wide Lake: **a)** dissolutions bands; **b)** cataclastic bands; **c)** dilative cataclastic band; **d)** dilative-cataclastic band and; **e)** vein.

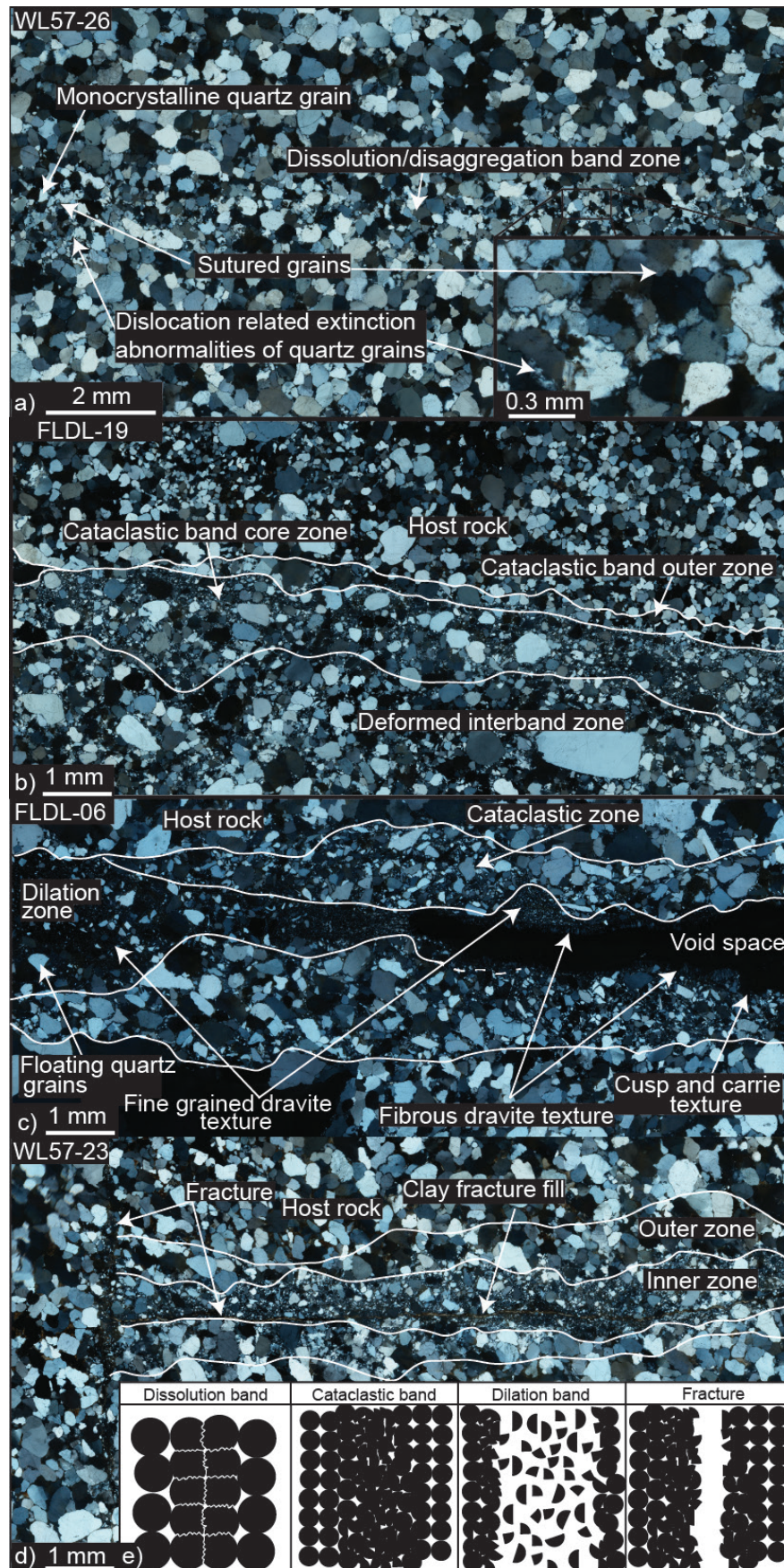


**Figure 5.** Micrographs and schematic diagrams of deformation bands observed within the Manitou Falls Formation: **a)** dissolution band; **b)** cataclastic band; **c)** dilative cataclastic band; **d)** cataclastic band and parallel fracture.

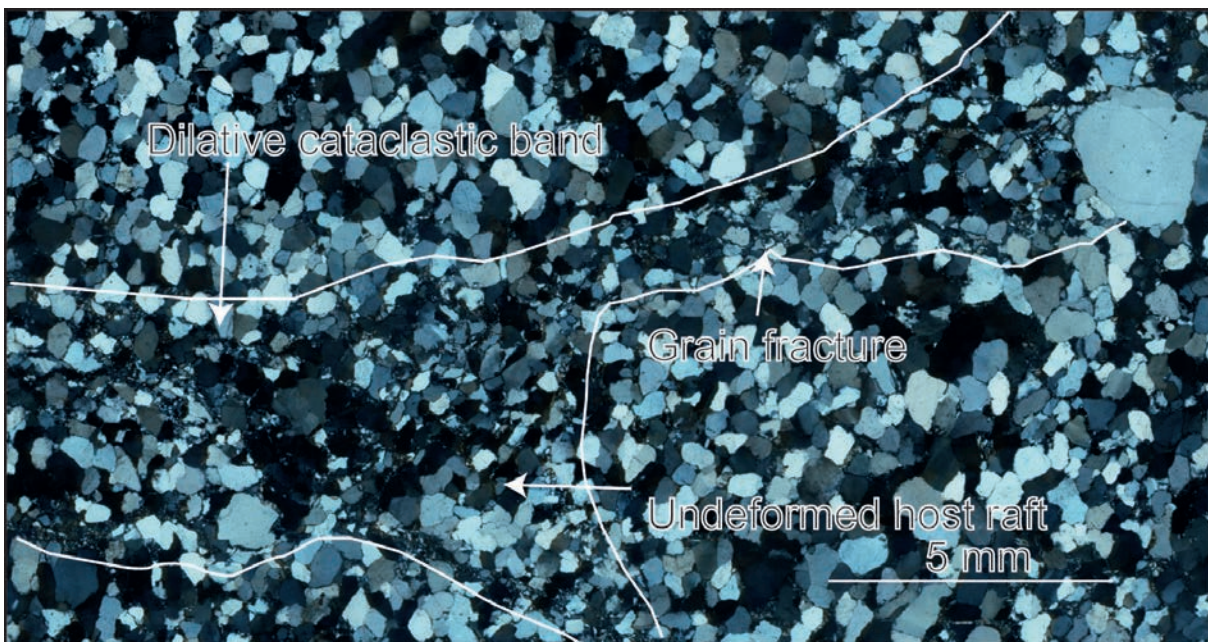


**Figure 5e.** Micrograph of a dilative cataclastic band, highlighting grain fractures and undeformed host rafts within the band.

(Fig. 5d).

#### 4.4 Fractured bands

Cataclastic band clusters observed within drill hole VR-56 exhibit overprint by fracture failure, commonly parallel to individual cataclastic bands (Fig. 4e). Fractures observed at depth appear to be fractured parallel and along the margin of pre-existing deformation band structures (Fig. 4e). In cataclastic bands, fractures are contained to the inner core zone and may migrate from the central inner core zone to the edge of the inner and outer core zone (Fig. 5d). However, not all fractures observed formed parallel to pre-existing deformation bands (Fig. 5d). We observed drusy quartz, white clay, and dravite forming as vein filled fractures on the surfaces of fractured deformation bands. One polished slip surface, steep-dipping and NNW-striking, contained a striation with a pitch of  $18^{\circ}$ S, indicating Mode II fracture. Many deformation bands and clusters were fractured with drusy quartz growth along the fractured wall rock contacts. One Mode III fracture

was observed striking NNW-SSE, which crosscuts and pinches out into a rippled surface at Fox Lake. Fractured bands with dravite cement are constrained to Stages 1–3 of our palaeostress model; whereas fractures cemented with silica are observed within all stages of our palaeostress model (Fig. 6)

### 5. Discussion: Growth and temporal evolution of Manitou Falls Group deformation bands

Here, we interpret the temporal evolution of dissolution bands, cataclastic bands, dilation bands, and fractures observed within the Manitou Falls Group at Fox Lake and Wide Lake.

#### 5.1. Pure compaction bands: dissolution bands

We define the bedding parallel deformation bands observed at Fox Lake and Wide Lake as PCBs, based on lack of shear displacement. These bands are ubiquitously characterised and associated with the formation mechanism disso-

lution. The formation of these bands may include grain boundary sliding, which would enhance the interlocking grain-grain relationships prior to dissolution. In the study areas, PCB formation appears to be localised to the hanging walls of the Fox Lake Fault at Fox Lake and Dufferin Fault at Wide Lake. However, it should be noted that all drill holes are collared in the hanging wall.

Dissolution band formation may be explained by the relationship between PCBs, clay, and high temperatures. Dissolution is a geochemical process that usually requires deep and hot formation conditions to make quartz dissolution favourable. Quartz dissolution accelerates at temperatures exceeding 90°C, usually at depths greater than 3 km (Walderhaug, 1996); however, dissolution bands commonly form at shallower depths (Fossen et al., 2007). Aluminium and potassium bearing clays reduce the stress and temperatures required to dissolve quartz, theoretically calculated to be at pressures less than 10 bars (Bjorkum, 1996). Ramaekers et al. (2007) duly noted clay-rich sediments in the Manitou Falls Group, which may provide ideal chemical conditions to enhance shallow quartz dissolution in the Manitou Falls Group.

The breakup of the supercontinent Nuna resulted in crustal thinning of the Athabasca region ca. 1.55 Ga (Ramaekers et al., 2017). Chi et al. (2018) suggested the geothermal gradient was much higher at this time and envisaged the Athabasca Basin was never very thick (<3 km), rather influenced by an anomalous crustal geothermal gradient. A high geothermal gradient would enhance quartz dissolution. We suggest compaction of the Manitou Falls Group induced grain boundary sliding and the formation of disaggregation bands. Increased strain

from grain boundary sliding combined with an anomalously high geothermal gradient likely enhanced discrete quartz dissolution as PCBs. Quartz dissolution may have also been enhanced by clay-rich strata (i.e. clay intraclasts). These clay rich beds may account for the formation of clusters of dissolution bands. Thus, the formation of dissolution bands within the Manitou Falls Group supports the notion of a high geothermal gradient suggested by Chi et al. (2018).

### *5.2 Shear-enhanced compaction bands: cataclasis-dilation-fracture*

The majority of deformation bands observed at Fox Lake and Wide Lake are oriented obliquely to bedding and are classified as SECB, based on their relationship to Riedel and Anderson geometry, consistent with shear offsets of bedding planes and deformation bands (Fig. 3). These bands are characterised primarily by mechanical comminution; however, dilation bands and fractures have also been recognised at Fox Lake within REA 181, forming parallel to pre-existing cataclastic bands (Fig. 5d). Cross cutting relationships infer cataclastic bands formed first in sequence, prior to dilative cataclastic bands (Fig. 5c). Fractures formed last along pre-existing zones of weakness (i.e. cataclastic and dilative bands) via crack propagation (Fig. 5d) (*sensu* Fossen et al., 2007). Based on observations presented earlier, we suggest the following model accounts for the temporal evolution of these three modes of deformation, resulting in the dilative reactivation of a strain hardened cataclastic band.

A cataclastic deformation band is a localized zone of strain, mechanically induced by grain crushing and pore space collapse, strengthened by the strain hardening process (Aydin, 1978). Strain

hardening increases the yield strength of cataclastic bands relative to the adjacent undeformed host rock. Thus, stress must increase in order to continue increasing strain within the deformation band (Fossen et al., 2007). However, by definition the strain hardened cataclastic band only attains its strength under continual stress (Mair et al., 2000). Cementation usually occurs post-cataclasis, owing to the fact that cataclasis produces fresh and highly reactive grain surfaces, which react with formation fluids and precipitate cement if formation fluid can permeate through the cataclastic band (Fossen et al., 2007).

Thus, the timely precipitation of cement will enhance chemical and physical robustness of the cataclastic band.

In contrast, dilation bands are noted to enhance fluid flow and cementation, resulting in cement-locking of the dilation band (Exner et al., 2013). Dilation bands accommodate porosity enhancement and usually develop in poorly consolidated porous rocks, where lithostatic pressure is low (Du Bernard et al., 2002). Despite this documented occurrence, we propose dilation bands can also form as a result of enhanced pore pressure, similar to an

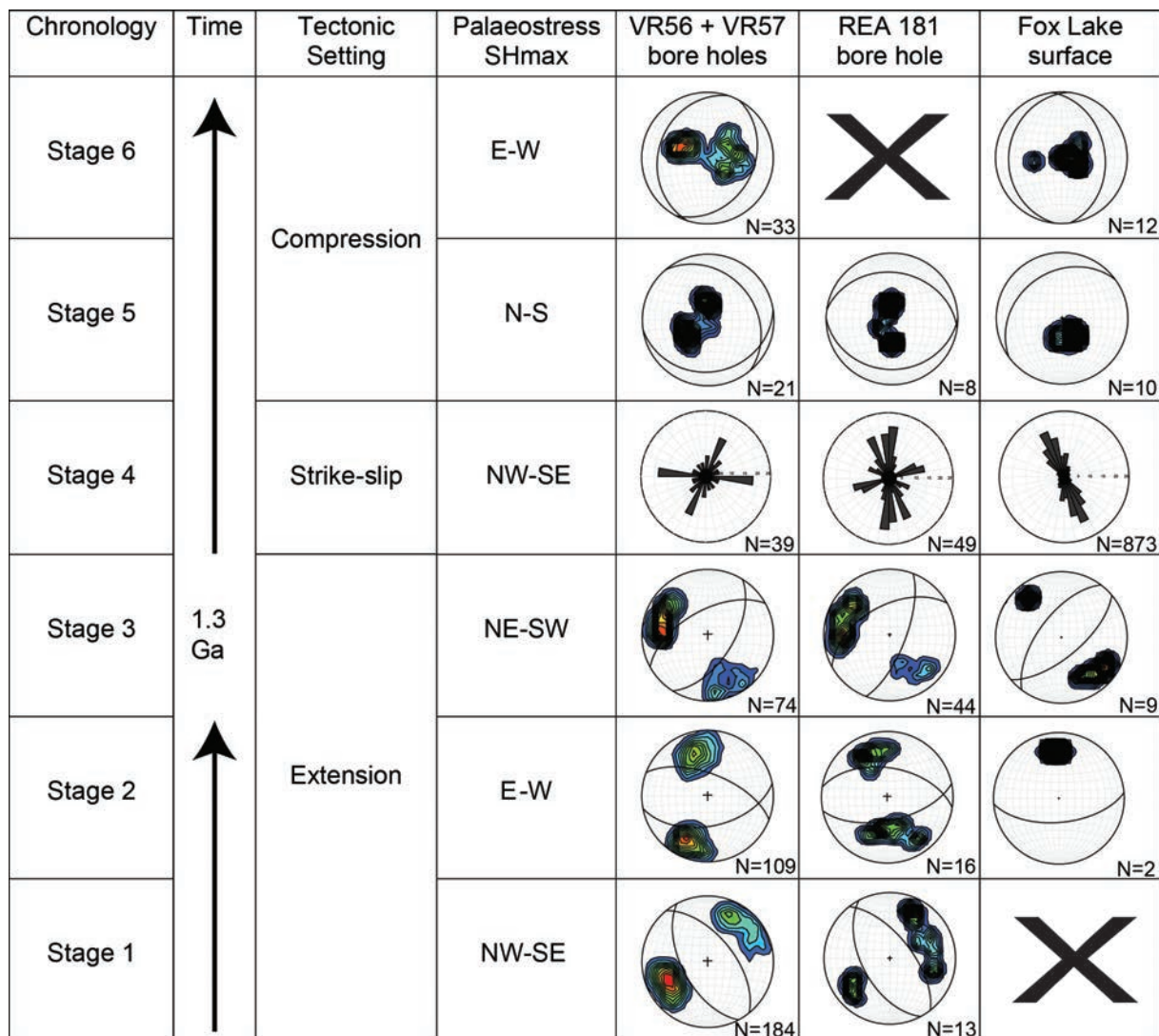


**Figure 6.** Stereonet diagrams illustrating the palaeostress evolution of basement faults underlying the Manitou Falls Group, Athabasca Basin.

extensional fracture. Thus, we pose the question, what is the difference between a dilation band and fracture? Like any other type of deformation band, the availability of granular rock porosity is essential to initiate the localised interactions between pore space morphology and grain-boundary sliding. Dilation band form by grain-boundary sliding and dilation of pore space in high primary porosity rocks (e.g. unaltered sandstone). However, we suggest dilation bands may lose fluid pore pressure resulting in dilation band collapse (Fig. 4c and Fig. 5e). In contrast, fractures form in low primary porosity rocks (e.g. silicified sandstone) and form via crack propagation (Fig. 4e and Fig. 5d). Therefore, the deformation bands observed in this study must have formed prior to silicification.

Pore fluids reduce the normal stress acting upon a rock, thereby reducing the principal stresses; e.g. the influx of fluid shifts the Mohr Circle left, which represents the stress regime along the normal stress axis towards the shear stress axis into the tensile regime (Fig. 7). For this to occur, geothermal fluid must be forced into a low permeable and possibly confined system or thermodynamically charged to introduce the overpressure. The silicified Athabasca sandstone matches this geological setting. Fluid overpressures can cause fault failure and enhanced fluid flow along fault zones (Sibson, 1981). Fluid inclusion assemblages imply several uranium deposits in the Athabasca Basin are associated with fluid boiling (Chi et al., 2014). Chi et al. (2018) suggests low pressure fluid boiling can be explained by suction pump models, which involves extensional fractures and induced suction of fluids across a fault jog. We suggest the Fox Lake Fault, which is a strike-slip structure, may have supported episodic transtensional

strain accommodation within the Fox Lake uranium deposit. In one segment along the northeast pod of the Fox Lake uranium deposit there is evidence of a possible fault splay resulting in a small positive structure (i.e. transpression) (Rogers et al., 2017). We suggest the presence of the flower structure infers the presence of a fault jog spatial related to the Fox Lake uranium deposit. The presence of a fault jog may imply the Fox Lake Fault evolved from a negative structure (i.e. transtension) at the time of uranium deposition to the positive structure observed by Rogers et al. (2017), with the evolving stress regime. Therefore, a fault suction pump mechanism supports our hypothesis of localised fluid overpressure, which accommodated tensile strain and the formation of dilational-cataclastic band in the Fox Lake region.

It is generally well accepted that deformation bands do not reactivate once formed, because their strain hardening property requires higher stress magnitudes to continue accommodating higher strain rates (Fossen et al., 2007). Rather, continual strain may be achieved by forming a new deformation band or fracture adjacent to the existing band due to a pre-existing weakness (i.e. micro-fractures), created by the formation of the initial band (Fossen et al., 2007). In contrary, our model for dilative cataclastic bands deviates from this hypothesis because it implies deformation bands can reactivate under high fluid pressure conditions. This model implies the Fox Lake Fault experienced fluid overpressures during Stage 4 of our palaeostress model and resulted in influx of dravite-rich fluid at Fox Lake (Fig. 6). We invoke fault step-over geometry, localised transtension, and fault suction pump in the region to explain the fluid overpressure. The temporal and spatial relationship between dravite and

uranium mineralisation in the Athabasca Basin may be able to provide a temporal constraint for our palaeostress model, as dravite is found to be contemporaneous with uranium mineralising fluids in other Athabasca Basin uranium deposits (e.g. Mercadier et al., 2012). However, the timing of dravite in some deposits clearly predates the uranium event, and dravite rich structures exist in the basin completely void of uranium enrichment (e.g. Jefferson et al., 2007).

Stage 4 of our palaeostress model resulted in strike-slip failure of the interpreted basement faults at Fox Lake (Fig. 6). Basement fault reactivation resulted in the formation of cataclastic bands within the overlying sandstone, which conform to Riedel geometry (Fig. 3). Most stage 4 deformation bands are purely cataclastic. We suggest the dravite fluid alteration event at Fox Lake only existed during Stage 4 of our model, considering dilation-cataclastic bands observed only relate to Stage 4, while dravite filled fractures were observed relative to Stages 1–3 (Fig. 5). Dravite mineralisation in dilation bands implies dravite-rich fluid was channelled along the fault, infiltrating fault strain structures (i.e. deformation bands). Influx of dravite fluid likely enhanced pore pressure around the vicinity of the Fox Lake Fault (Fig. 2). We suggest enhanced pore pressure drove the Mohr's Circle into the tensile regime, which caused tensile stress within the sandstone effected by the fluid overpressure (Fig 7). At the time of formation, newly developed Stage 4 strike-slip cataclastic bands represent potential weaknesses in the formation because they have not yet had time for cement to precipitate and strengthen the deformation band. Newly formed deformation bands strength is linearly linked to the stresses acting upon the rock. Theoretically, if the normal

stress was to be eliminated, the incipient cataclastic would crumble because the friction holding the cataclastic band particles together would no longer exist. Thus, incipient cataclastic bands represent points of weakness if the normal stress is reduced. We suggest tensile strain accommodated in pre-existing rock weaknesses (i.e. newly developed Stage 4 cataclastic bands), considering cataclastic bands only retain their strength under continual stress. Fluids propagated along pre-existing cataclastic bands caused individual crushed grains to dilate (Fig. 5c). This in turn caused the formation of a new dilational deformation band along a pre-existing cataclastic deformation band. Thus, these newly dilated structures may act as fluid conduits.

Dilation bands with fractured grains have been documented (e.g. Exner et al., 2013); however, they are associated with breaking of the grain-bonding cement, rather than transitioning from a cataclasis mechanism to kinematic dilation, documented here (Fig. 5c). As previously determined, cataclastic bands formed prior to dilative cataclastic bands on the basis of their cross-cutting relationships

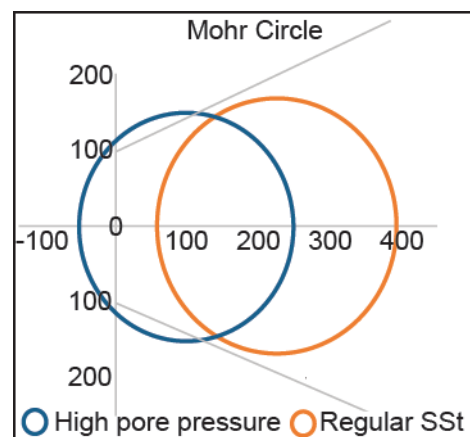


**Figure 7.** Mohr Diagram illustrating enhanced formation pore pressure, driving the failure envelope into the tensile regime.

(Fig. 5c)). However, dilation must have promptly succeeded cataclasis, possibly contemporaneously, otherwise the freshly exposed quartz grains that resulted from cataclasis and grain boundary sliding would have promoted timely cement precipitation, thus strengthening the band. If this was the case, a fracture would have formed rather than dilation of individual grains observed in Figure. 5c. While we have observed cataclastic grains dilated and floating within a dravite matrix; we make the interpretation that dilation occurred promptly following cataclasis in Stage 4 of the palaeostress model (Fig. 6). Cataclastic band would have fractured via crack propagation if dravite fluid dilation occurred too long after cataclasis because the grains would have been 'cement-locked', resulting in fracture, rather than individual cataclastic grains dilating (Fig. 5e). We observed this exact process with dravite veins conforming to Stages 1–3 (i.e. fracture via crack propagation) (Fig. 4e). We only observed the dilational texture in Stage 4, which supports our interpretation that the influx of dravite rich-fluid is temporally related to Stage 4 (Fig. 6). Therefore, dravite fluid influx at Stage 4 caused pre-existing Stages 1–3 bands to fracture and newly formed Stage 4 cataclastic bands to dilate.

## 6.0 Conclusions

- Cataclastic bands, dissolution bands, dilative cataclastic bands, and slip surfaces are present within the Manitou Falls Group in the Athabasca Basin.
- High geothermal temperatures and clay intraclasts may have enhanced quartz dissolution, resulting in the formation of bedding parallel dissolution bands at Fox Lake and Wide Lake.
- Dilative cataclastic bands are a new type of deformation band observed in the Athabasca Basin, correlated with the Fox Lake uranium deposit. Dilative cataclastic bands form as a result as a result of fluid overpressure, using newly formed cataclastic bands as fluid pathways, causing the pore space to be created within the band rather than fracture via crack propagation. These bands form promptly following cataclasis prior to band cementation.
- Riedel shear faults induced hydraulic suction of the C10 Fault, responsible for enhanced hydrostatic pressure of the sandstone fault rock. Increased hydrostatic pressure forced kinematic dilation and reactivation of newly formed cataclastic bands.

## References

- Alexandre, P., Kyser, K., Jiricka, D., and Witt, G., 2012, Formation and Evolution of the Centennial Unconformity-Related Uranium Deposit in the South-Central Athabasca Basin, Canada: *Economic Geology*, v. 107, no. 3, p. 385-400.
- Alikarami, R., and Torabi, A., 2015, Micro-texture and petrophysical properties of dilation and compaction shear bands in sand: *Geomechanics for Energy and the Environment*, v. 3, p. 1-10.
- Annesley, I. R., Madore, C., Shi, R., and Krogh, T. E., 1997, U–Pb geochronology of thermotectonic events in the Wollaston Lake area, Wollaston Domain: A summary of 1994–1996 results: Summary of investigations, p. 97-94.
- Antonellini, M., and Aydin, A., 1994, Effect of faulting on fluid flow in porous sandstones: petrophysical properties: *AAPG bulletin*, v. 78, no. 3, p. 355-377.
- Antonellini, M., Petracchini, L., Billi, A., and Scrocca, D., 2014, First reported occurrence of deformation bands in a platform limestone, the Jurassic Calcare Massiccio Fm., northern Apennines, Italy: *Tectonophysics*, v. 628, p. 85-104.
- Antonellini, M. A., Aydin, A., and Pollard, D. D., 1994, Microstructure of deformation bands in porous sandstones at Arches National Park, Utah: *Journal of Structural Geology*, v. 16, no. 7, p. 941-959.
- Ashton, K., Hartlaub, R., Bethune, K., Heaman, L., Rayner, N., and Niebergall, G., 2013, New depositional age constraints for the Murmac Bay group of the southern Rae craton, Canada: *Precambrian Research*, v. 232, p. 70-88.
- Aydin, A., 1978, Small faults formed as deformation bands in sandstone: *Pure and Applied Geophysics*, v. 116, no. 4-5, p. 913-930.
- Aydin, A., Antonellini, M., Tondi, E., and Agosta, F., 2010, Deformation along the leading edge of the Maiella thrust sheet in central Italy: *Journal of Structural Geology*, v. 32, no. 9, p. 1291-1304.
- Aydin, A., Borja, R. I., and Eichhubl, P., 2006, Geological and mathematical framework for failure modes in granular rock: *Journal of Structural Geology*, v. 28, no. 1, p. 83-98.
- Aydin, A., and Johnson, A., 1978, Development of faults as zones of deformation bands and as slip surfaces in sandstone: *Pure and Applied Geophysics*, v. 116, no. 4-5, p. 931-942.
- Ballas, G., Fossen, H., and Soliva, R., 2015, Factors controlling permeability of cataclastic deformation bands and faults in porous sandstone reservoirs: *Journal of Structural Geology*, v. 76, p. 1-21.
- Bésuelle, P., 2001a, Compacting and dilating shear bands in porous rock: Theoretical and experimental conditions: *Journal of Geophysical Research*, v. 106, no. B7, p. 13435-13442.
- Bésuelle, P., 2001b, Evolution of strain localisation with stress in a sandstone: brittle and semi-brittle regimes: *Physics and Chemistry of the Earth, Part A: Solid Earth and Geodesy*, v. 26, no. 1-2, p. 101-106.
- Bjorkum, P. A., 1996, How important is pressure in causing dissolution of quartz in sandstones?: *Journal of Sedimentary Research*, v. 66, no. 1, p. 147-154.
- Bosman, S. A., and Ramaekers, P., 2015, Athabasca Group+ Martin Group= Athabasca Supergroup? Athabasca Basin multi-parameter drill log compilation and interpretation, with updated geological map: *Summary of Investigations*, v. 2, p. 2015-2014.2012.
- Card, C., Pana, D., Portella, P., Thomas, D., Annesley, I., Jefferson, C., and Delaney, G., 2007, Basement rocks to the Athabasca Basin, Saskatchewan and Alberta: *BULLETIN-GEOLOGICAL SURVEY OF CANADA*, v. 588, p. 69.

- Card, C. D., 2016, A coming together: The juxtaposition of the Rae and Hearne cratons along the Virgin River shear zone (Snowbird tectonic zone), Saskatchewan, Canada, and the implications for proto-Laurentia: Faculty of Graduate Studies and Research, University of Regina.
- Card, C. D., Bethune, K. M., Rayner, N., and Creaser, R. A., 2018, Characterising the southern part of the Hearne Province: A forgotten part of Canada's shield revisited: *Precambrian Research*, v. 307, p. 51-65.
- Cashman, S., and Cashman, K., 2000, Cataclasis and deformation-band formation in unconsolidated marine terrace sand, Humboldt County, California: *Geology*, v. 28, no. 2, p. 111-114.
- Chi, G., Li, Z., and Bethune, K., 2014, Numerical modeling of hydrocarbon generation in the Douglas Formation of the Athabasca basin (Canada) and implications for unconformity-related uranium mineralization: *Journal of Geochemical Exploration*, v. 144, p. 37-48.
- Chi, G., Li, Z., Chu, H., Bethune, K. M., Quirt, D. H., Ledru, P., Normand, C., Card, C., Bosman, S., Davis, W. J., and Potter, E. G., 2018, A SHALLOW-BURIAL MINERALIZATION MODEL FOR THE UNCONFORMITY-RELATED URANIUM DEPOSITS IN THE ATHABASCA BASIN: *Economic Geology*, v. 113, no. 5, p. 1209-1217.
- Creaser, R., and Stasiuk, L., 2007, Depositional age of the Douglas Formation, northern Saskatchewan, determined by Re-Os geochronology: *BULLETIN-GEOLOGICAL SURVEY OF CANADA*, v. 588, p. 341.
- DeDecker, J., 2019, Alteration and Mineral Paragenesis of the McArthur River and Fox Lake Uranium Deposits, Athabasca Basin: A New Model for the Formation of Unconformity-related Uranium Deposits: Colorado School of Mines. Arthur Lakes Library.
- Du Bernard, X., Eichhubl, P., and Aydin, A., 2002, Dilation bands: A new form of localized failure in granular media: *Geophysical Research Letters*, v. 29, no. 24, p. 2176-2180.
- Exner, U., Kaiser, J., and Gier, S., 2013, Deformation bands evolving from dilation to cementation bands in a hydrocarbon reservoir (Vienna Basin, Austria): *Marine and Petroleum Geology*, v. 43, p. 504-515.
- Fossen, H., and Bale, A., 2007, Deformation bands and their influence on fluid flow: *AAPG Bulletin*, v. 91, no. 12, p. 1685-1700.
- Fossen, H., Schultz, R. A., Shipton, Z. K., and Mair, K., 2007, Deformation bands in sandstone: a review: *Journal of the Geological Society of London*, v. 164, no. 4, p. 755-769.
- Gaviglio, P., Bekri, S., Vandycke, S., Adler, P., Schroeder, C., Bergerat, F., Darquennes, A., and Coulon, M., 2009, Faulting and deformation in chalk: *Journal of structural geology*, v. 31, no. 2, p. 194-207.
- Hiatt, E., and Kyser, T., 2007, Sequence stratigraphy, hydrostratigraphy, and mineralizing fluid flow in the Proterozoic Manitou Falls Formation, eastern Athabasca Basin, Saskatchewan: *BULLETIN-GEOLOGICAL SURVEY OF CANADA*, v. 588, p. 489.
- Hoeve, J., and Sibbald, T. I., 1978, On the genesis of Rabbit Lake and other unconformity-type uranium deposits in northern Saskatchewan, Canada: *Economic Geology*, v. 73, no. 8, p. 1450-1473.
- Hoffman, P. F., 1988, United plates of America, the birth of a craton: Early Proterozoic assembly and growth of Laurentia: *Annual Review of Earth and Planetary Sciences*, v. 16, no. 1, p. 543-603.
- Jefferson, C., Thomas, D., Gandhi, S., Ramaekers, P., Delaney, G., Brisbin, D., Cutts, C., Portella, P., and Olson, R., 2007, Unconformity-associated uranium deposits of the Athabasca Basin, Saskatchewan and Alberta: *Bulletin-Geological Survey of*

- Canada, v. 588, p. 23.
- Kaminskaite, I., Fisher, Q. J., and Michie, E. A. H., 2019, Microstructure and petrophysical properties of deformation bands in high porosity carbonates: *Journal of Structural Geology*, v. 119, p. 61-80.
- Li, Z., Chi, G., Bethune, K. M., David, T., and Zaluski, G., 2017, Structural Controls on Fluid Flow During Compressional Reactivation of Basement Faults: Insights from Numerical Modeling for the Formation of Unconformity-Related Uranium Deposits in the Athabasca Basin, Canada: *Economic Geology*, v. 112, no. 2, p. 451-466.
- Lommatzsch, M., Exner, U., Gier, S., and Grasmann, B., 2015, Dilatant shear band formation and diagenesis in calcareous, arkosic sandstones, Vienna Basin (Austria): *Marine and petroleum geology*, v. 62, p. 144-160.
- Lubiniecki, D. C., White, S. R. S., King, R. C., Holford, S. P., Bunch, M. A., and Hill, S., 2019, Structural evolution of carbonate-hosted cataclastic bands adjacent to a major neotectonic fault, Sellicks Beach, south Australia: *Journal of Structural Geology*, v. 126, p. 11-24.
- Mair, K., Main, I., and Elphick, S., 2000, Sequential growth of deformation bands in the laboratory: *Journal of Structural Geology*, v. 22, no. 1, p. 25-42.
- Mercadier, J., Richard, A., and Cathelineau, M., 2012, Boron-and magnesium-rich marine brines at the origin of giant unconformity-related uranium deposits:  $\delta^{11}\text{B}$  evidence from Mg-tourmalines: *Geology*, v. 40, no. 3, p. 231-234.
- Pagel, M., 1975, Cadre Géologique des gisements d'uranium dans la structure Carswell (Saskatchewan-Canada)-«Etude des phases fluides». Unpub: PhD thesis, Université de Nancy 1.
- Philit, S., Soliva, R., Castilla, R., Ballas, G., and Taillefer, A., 2018, Clusters of cataclastic deformation bands in porous sandstones: *Journal of Structural Geology*, v. 114, p. 235-250.
- Rainbird, R., Stern, R., Rayner, N., and Jefferson, C., 2007, Age, provenance, and regional correlation of the Athabasca Group, Saskatchewan and Alberta, constrained by igneous and detrital zircon geochronology: *Bulletin-Geological Survey of Canada*, v. 588, p. 193.
- Ramaekers, P., Jefferson, C., Yeo, G., Collier, B., Long, D., Drever, G., McHardy, S., Jiricka, D., Cutts, C., and Wheatley, K., 2007, Revised geological map and stratigraphy of the Athabasca Group, Saskatchewan and Alberta: *Bulletin-Geological Survey of Canada*, v. 588, p. 155.
- Ramaekers, P., McElroy, R., and Catuneanu, O., 2017, Mid-Proterozoic continental extension as a control on Athabasca region uranium emplacement, Saskatchewan and Alberta, Canada, *Society for Geology Applied to Mineral Deposits, SGA Biennial Conference*, Volume 2: Quebec City, p. 759-762.
- Rogers, S., Bridge, N., O'Dowd, C., Yang, H., Aubin, A., and Yackulic, A., 2017, Geological framework of the Fox Lake uranium deposit, Athabasca Basin, Canada, *Open House: Saskatoon, Saskatchewan, Saskatchewan Geological Survey*.
- Rotevatn, A., Thorsheim, E., Bastesen, E., Fossmark, H. S. S., Torabi, A., and Sælen, G., 2016, Sequential growth of deformation bands in carbonate grainstones in the hangingwall of an active growth fault: Implications for deformation mechanisms in different tectonic regimes: *Journal of Structural Geology*, v. 90, p. 27-47.
- Rudnicki, J. W., and Rice, J., 1975, Conditions for the localization of deformation in pressure-sensitive dilatant materials: *Journal of the Mechanics and Physics of Solids*, v. 23, no. 6, p. 371-394.
- Schultz, R. A., and Siddharthan, R., 2005, A general framework for the occurrence and faulting of deformation bands in porous granular rocks: *Tectonophysics*, v. 411,

- no. 1, p. 1-18.
- Sibson, R. H., 1981, Fluid flow accompanying faulting: field evidence and models: Earthquake prediction: an international review, v. 4, p. 593-603.
- , 1994, Crustal stress, faulting and fluid flow: Geological Society, London, Special Publications, v. 78, no. 1, p. 69-84.
- Sibson, R. H., Robert, F., and Poulsen, K. H., 1988, High-angle reverse faults, fluid-pressure cycling, and mesothermal gold-quartz deposits: *Geology*, v. 16, no. 6, p. 551-555.
- Tondi, E., 2007, Nucleation, development and petrophysical properties of faults in carbonate grainstones: Evidence from the San Vito Lo Capo peninsula (Sicily, Italy): *Journal of Structural Geology*, v. 29, no. 4, p. 614-628.
- Tondi, E., Rustichelli, A., Cilona, A., Balsamo, F., Storti, F., Napoli, G., Agosta, F., Renda, P., and Giorgioni, M., 2016, Hydraulic properties of fault zones in porous carbonates, examples from central and southern Italy: *Italian Journal of Geosciences*, v. 135, no. 1, p. 68-79.
- Torabi, A., 2008, Deformation bands in porous sandstones, their microstructure and petrophysical properties.
- Torabi, A., and Fossen, H., 2009, Spatial variation of microstructure and petrophysical properties along deformation bands in reservoir sandstones: *Aapg Bulletin*, v. 93, no. 7, p. 919-938.
- Torabi, A., Fossen, H., and Alaei, B., 2008, Application of spatial correlation functions in permeability estimation of deformation bands in porous rocks: *Journal of Geophysical Research: Solid Earth*, v. 113, no. B8.
- Walderhaug, O., 1996, Kinetic modeling of quartz cementation and porosity loss in deeply buried sandstone reservoirs: *AAPG bulletin*, v. 80, no. 5, p. 731-745.
- Yeo, G., Delaney, G., and Jefferson, C., 2007, The Wollaston Supergroup, stratigraphy and metallogeny of a Paleoproterozoic Wilson cycle in the Trans-Hudson orogen, Saskatchewan: *BULLETIN-GEOLOGICAL SURVEY OF CANADA*, v. 588, p. 89.

# CHAPTER 7

This project builds on our current understanding of the structural evolution of deformation bands and explores their applicability as a tool for predicting the guidance and precipitation of fluids and mineral deposits over geological timescales in sedimentary basins. In particular this project has involved:

1. Detailed investigation of the structure and geomechanics of deformation bands and fractures within the Bridgewater Formation, Hallet Cove Sandstone, Port Willunga Formation, Eyre Formation, Parabarana Sandstone, and Heatherdale Shale in South Australia, and the Manitou Falls Formation in Saskatchewan, to better understand the evolution of regional stress over geological time and the structural evolution of local faults and their influence on formation fluid flow.
2. Combination of analytical techniques and conceptual models to define the localised geomechanics and petrophysical characteristics of the observed deformation bands, in order to better understand their role in structurally controlled uranium mineralisation.
3. Comparing our results with other case studies and building knowledge that underpins our understanding of fault-induced deformation bands.

This project was supported through an international collaboration between the Saskatchewan Geological Survey and the Geological Survey of South Australia and was designed to bridge knowledge gaps concerning the impact of structural geology on subsurface resources in South Australia and Saskatchewan. In

particular, the goal was to improve understanding of mineral prospectivity, and thus enhance the growth and efficiency of minerals exploration and development in each state. These goals have been accomplished through: i) detailed structural mapping of sedimentary basin fault zones and associated brittle deformation features (e.g. deformation bands); ii) establishing new workflows for modelling palaeostress evolution and structurally controlled mineralisation; iii) broadening the approach to standardise carbonate-hosted cataclastic band nomenclature (for applications elsewhere).

### *Chapter 2*

This chapter uses data collected from the Bridgewater Formation, Hallet Cove Sandstone, Port Willunga Formation, Eyre Formation, Parabarana Sandstone, and Heatherdale Shale to elucidate the Cenozoic structural evolution of the Mt Lofty Ranges and Flinders Ranges. We have produced a palaeostress model of the Mt Lofty Ranges and Flinders Ranges using deformation bands as indicators of discrete changes in the regional palaeostress regime. We have identified 737 deformation bands and 397 fractures from five field sites that indicate a five stage palaeostress evolution of the Mt Lofty Ranges and Flinders Ranges:

Stage 5: (late Pleistocene–Holocene) E–W compression related to denudation;

Stage 4: (Pliocene–middle Pleistocene) NW–SE compression followed by a clockwise rotation of  $\sigma_H$  to E–W related to denudation;

Stage 3: (Late Miocene) N–S compression related to formation of the Southern Alps;

Stage 2: (middle Eocene–middle Miocene): N–S extension related to opening

of the Southern Ocean;

Stage 1: NW–SE extension (early Palaeocene–early Eocene) related to opening of the Tasman Sea.

Our palaeostress model enhances our comprehension of the dynamic palaeostress evolution of southeastern Australia, underpinning our understanding of hydrocarbon accumulations and economic mineral deposits in the region. Structural analysis of brittle deformation features like fractures and deformation bands provide specific neotectonic indicators that enable the identification of discrete changes in the regional stress regime. This work validates our interpretations of the relationship between the regional stress regime and subsequent development of deformation features such as deformation bands and fractures documented in the Port Willunga Formation (Chapter 3) and supports model development for mineral deposit genesis in the Eyre Formation (Chapter 4).

### *Chapter 3*

This chapter focuses on the structural evolution of deformation bands associated with the structural evolution of the Willunga Fault in South Australia, specifically examining deformation styles and mechanisms within the Oligocene–late Miocene Port Willunga Formation carbonate grainstone. This analysis involved developing a series of detailed structural grid and face maps of deformed sections of the Port Willunga Formation for structural analysis. Structural analysis included mapping and description of 221 shear-enhanced compaction bands mapped at Sellicks Beach and Port Willunga, defining four individual structural sets: 1) bedding parallel; 2) E-W striking; 3) striking between E-W and N-S; 4) N-S striking. Deformation bands observed

within the Port Willunga Formation are interpreted to be as a result of progressive reactivation of the Willunga Fault, which is a product of neotectonic intra-Australian Plate strain accommodation within the Mount Lofty Ranges. Observed deformation band geometric relationships demonstrate that regional stress conditions evolved from extension to compression in the late Miocene; this model supports the hypothesis that the Willunga Fault experienced inversion from the late Miocene to present-day, resulting in near-vertical surface expression of the Willunga Fault. Demonstrated spatial and quantitative relationships of these deformation bands may indicate potential locations of splays associated with the Willunga Fault.

Petrographic microscopic analysis of the deformation bands within the Port Willunga Formation demonstrates a hierarchy of pore space and grain-size reduction, indicating two mechanically different cataclasis intensities at Sellicks Beach. The differential mechanical behaviour of these two deformation styles demands a new classification scheme for cataclastic deformation bands in carbonate host rocks. A uniform classification already used for siliciclastic deformation bands and fault rocks was adopted and modified to include strain intensity as part of a new, more coherent classification scheme. Cataclasis is the primary controlling mechanism behind the development of deformation bands in the Port Willunga Formation; however, disaggregation, pressure solution, and cementation formation mechanisms are identified as secondary controlling factors.

### *Chapter 4*

This chapter focuses on deformation bands with the Eyre Formation, an Eocene kaolinized sandstone that hosts the

Four Mile uranium deposit adjacent to the Paralana Fault. We have documented 286 deformation bands within the Eyre Formation at the Dead Tree section; they occur in four sets of shear-enhanced dilation and compaction bands. The dilation bands demonstrate a distinct microstructural evolution involving at least two phases of cementation and fracture via crack propagation.

I make the interpretation that a transtensional fault jog between the Paralana Fault and Four Mile Fault is responsible for the formation of dilation bands and fractures observed at the Dead Tree section. Conceptual models that follow indicate at least two phases of transtension are responsible for the dilation bands observed at the Dead Tree section.

Handheld permeameter and computed tomography results indicate that the dilation bands may have enhanced the effective permeability of the Eyre Peninsula between the Mount Painter Inlier and the Frome Embayment, potentially acting as conduits for meteoric fluid transportation from the uranium source to sink (deposit). Enhanced fluid flow promotes mineral leaching from the radiogenic Mount Painter Inlier. This inference is supported by the unequivocal spatial relationships of observed palaeoredox roll fronts rich in uranium and thorium and dilation bands. This work underpins our understanding of the structural relationships that form this type of sedimentary-hosted mineral resource and may be used for exploration of other deposits not yet known in the region.

#### *Chapter 5*

This chapter focuses on the structural evolution of the Manitou Falls Formation, a Mesoproterozoic quartz arenite host to the Fox Lake and Centennial uranium de-

posits. The Fox Fault and Dufferin Fault damage zones are defined as observed Riedel Shear Zones and Andersonian Fault Zones. 1713 deformation bands and fractures were recorded and documented from surface outcrops and three drill holes at Fox Lake and Dufferin Lake. From this data, we produced four grid maps at Fox Lake and a vertical cross section of the Dufferin Fault at Wide Lake. Grid maps were focused around the thickest observed cataclastic band clusters, measuring up to 9 cm wide. The vertical profile of the Dufferin Fault indicates seven localised zones of high intensity strain, demonstrating sequential phases of reactivation with the progressive evolution of the palaeostress regime. Our structural analysis demonstrates the Manitou Falls Formation experienced six stages of palaeostress evolution, progressing from extension, transpression, and finally compression, which are likely related to major tectonic events like supercontinent breakup (Columbia), regional volcanism (Mackenzie dyke swarm), and supercontinent formation (Rhodina).

#### *Chapter 6*

Chapter 6 focuses on the microstructural evolution of Manitou Falls Formation deformation bands and fractures. These structures are categorized as having formed due to four mechanically distinct processes, namely by dissolution (dissolution bands), cataclasis (cataclastic bands), shear-enhanced dilation (dilation-cataclastic bands), and fracturing. We present evidence for the reactivation of deformation bands previously thought not to be reactivatable. Petrographic microscopy and scanning electron microscopic analysis indicates mechanical reactivation of cataclastic bands by enhanced pore pressure. Volumetric dilation is responsible for enhancing deformation

band permeability and resulted in the formation of localised fluid conduits for alteration-related dravite fluids to permeate the rocks surrounding the Fox Lake uranium deposit. I suggest that the timing of this event occurred following the incipient formation of the cataclastic bands, prior to cataclastic band cementation. This work enhances our knowledge of the structural evolution of the Athabasca Basin, which can be used to enhance our understanding of the structural history of known uranium deposits and delineate localised zones of transtension for future exploration.

*Linking deformation bands and sedimentary-hosted mineral deposits*

The main take away message put forward by this thesis concludes uranium-bearing fluid flow – which resulted in uranium mineralisation in Saskatchewan and South Australian study areas – is intrinsically linked to the formation of dilational deformation bands, transtensional fault geometry, and specific corresponding palaeostress. These outlined factors are shown here to be important controls governing enhanced permeability between

*Implications for understanding the structural evolution of deformation bands and structural history of their host sedimentary basins*

The overall contributions and implications of the case studies (Chapters 2–5) in this project have been:

1. The identification and detailed structural analysis of deformation bands in the St. Vincent Basin, Lake Eyre Basin, and Athabasca Basin, linked to regional faulting histories and palaeostress records.
2. To present a new workflow for understanding palaeostress evolution in brittle sedimentary rocks, temporally constrained by stratigraphy. This method proves deformation bands are excellent indicators of discrete changes in both local and regional stress regimes.
3. The identification of a new type of deformation band that forms as a result of reactivation (dilation) of a pre-existing cataclastic band.
4. The development of a new classification scheme for carbonate-hosted cataclastic deformation bands, building on classification schemes already used for fault rocks and siliciclastic deformation bands.

---

# Supplementary Data

---

# Appendix A

### Key

All structural measurements were recorded manually as dip/dip direction

Bedding : Bedding  
DB : Undifferentiated deformation band  
DIL : Dilation band  
DIS : Dissolution band  
CAT : Cataclastic band  
C-P : Cataclastic-protocataclastic band  
P : Protocataclastic band  
C : Crush micro-breccia  
F : Fracture

Formation Location	GPS Map	Structure width (mm)	Structure type	Reading
Port Willunga	Zone 54H 267731E 6086250S	3-8	C	76/025
Formation Sellicks Beach	Face Map 1	8-10	C	79/029
		1-3	C	50/024
		6-10	C	53/025
		2-1	C	66/031
		3-6	C	38/082
		1-3	C	47/130
		5-8	C	45/170
		1-3	C	40/200
		4	C	38/018
		4	C	50/016
		4-5	C	29/020
		3-4	C	00/018
		2	C	07/012
		2-4	C	13/012
		2	C	10/016
		1	C	05/005
		1	C	46/060
		1-2	C	38/149
		3-5	C	59/023
		3-5	C	64/044
1-4	C	43/066		
2-5	C	66/229		
1-2	C	52/005		
1	C	36/015		
2-3	C	37/015		
2-3	C-P	40/349		
1	P	81/219		
1	P	75/015		
2-4	P	71/340		
4-8	P	57/023		
1	P	63/030		
1	P	52/035		
2-3	P	75/098		
1-2	P	55/124		
1-2	P	52/205		

		2-5	P	36/029
		2	P	28/030
		2-4	P	25/034
		3-4	P	58/021
		2	P	19/349
		2	P	40/020
		2	P	20/349
		2-3	C-P	55/030
		2-5	C-P	58/029
		2-3	C-P	65/043
		2-4	C-P	60/079
		1-2	C-P	69/034
		2-4	C-P	34/025
		2-4	C-P	40/029
		3-4	C-P	34/022
		2-3	C-P	50/031
		1-3	C-P	45/035
		1-3	C-P	64/041
		1-2	C-P	73/045
Port	Zone 54H	1-2	C	80/350
Willunga	267787E			
	6086367S	2-5	C	73/025
Formation	Face Map 2	2-5	C	88/023
Sellicks				
Beach		3	C	81/002
		1-2	C	63/030
		1-3	C	58/059
		1-2	C	55/062
		2-3	C	63/054
		1-2	C	62/055
		1	C	50/129
		1	C	68/053
		1-2	C	40/068
		1	C	70/224
		2-4	C	12/340
		5	C	09/342
		5	C	00/010
		5	C	11/192
		2-5	C	08/330
		5	C	07/356

		2	C	68/064
		2-6	C	86/001
		2-5	C	60/000
		2-4	DB	15/195
		2-4	P	69/013
		2-4	P	71/350
		2-4	P	87/019
		2-3	P	78/221
		2-3	P	82/004
		2-3	P	73/029
		1	P	66/037
		1	P	60/055
		1-2	P	90/160
		1	P	90/001
		2	P	07/352
		2-4	P	11/180
		2	P	10/196
		2	P	10/198
		2	P	08/198
		1-3	C-P	69/075
		1-2	C-P	78/013
		1-3	C-P	38/070
Port	Zone 54H	2-4	C	84/232
Willunga	267866E			
	6086490S	2-6	C	87/054
Formation	Face Map 3	2	C	66/231
Sellicks		2	C	78/251
Beach		4	C	12/192
		4	C	10/194
		5	C	16/202
		4	C	30/179
		8	C	10/140
		6	C	10/143
		2	C	50/008
		2-3	C	68/038
		4	C	40/072
		2-4	C	62/236
		2	P	90/012
		2-8	P	75/044

		1-3	P	68/045
		1-5	P	90/266
		1-2	P	72/340
		4-15	P	82/054
		2-4	P	82/000
		2	P	80/251
		2-5	P	85/275
		2	P	88/240
		1	P	44/010
		1	P	62/024
		40-110	P	48/035
		1	P	44/084
		2	P	30/094
		1	P	64/204
		1	P	80/224
		2	P	12/198
		2	P	08/133
		2-3	C-P	42/038
		1	C-P	36/080
		1-2	C-P	70/058
		2-3	C-P	71/068
		1-2	C-P	74/144
		3-6	C-P	60/072
		2-5	C-P	80/256
		2-5	C-P	36/350
		2	DB	30/154
			DB	14/202
		3	DB	16/145
		4	DB	14/142
			DB	07/013
			DB	07/139
		5-10	DB	08/140
Port	Zone 54H	3-6	C	70/218
Willunga	267787E			
	6086367S	2	C	88/223
Formation	Face Map 4		C	80/190
Sellicks		1-2	C	80/165
Beach		2-6	C	15/011
		1-3	C	18/288

		1-3	P	74/254
		1-3	P	79/233
		1-2	P	61/245
		3	P	83/020
		1	P	69/350
		1-3	P	90/240
		1	P	66/040
		1	P	88/214
		<1	P	72/060
		1	P	38/080
		1	P	79/074
		1-2	P	39/087
		1	P	70/095
		1-3	P	49/129
		2-3	P	41/138
		1-3	P	40/143
		2	P	35/211
		1	P	53/345
		1-3	P	26/069
		4-5	P	16/129
		4-5	P	16/129
		3	P	22/130
		3	P	22/130
		3-8	P	15/140
		2-4	P	19/130
		1-10	C-P	90/234
		1-2	C-P	30/093
		1-2	C-P	67/187
		1-2	C-P	63/203
		2	C-P	82/245
		2	C-P	78/074
		2-3	C-P	53/357
		1-2	C-P	58/010
			DB	90/250
			DB	85/031
		100	DB	10/154
			DB	10/154
		2-8	DB	10/154
		4	DB	20/138
Port	Zone 54H	1-2	C	72/228

Willunga	267731E	1-2	C	65/064
	6086250S			
Formation	Face Map 5	5-10	C	40/060
Sellicks		3-5	C	39/129
Beach		3-4	C	20/064
		2-3	C	36/143
		3	C	20/094
		1-2	C	21/140
		2-3	C	70/015
		1-2	C	80/222
		2-3	C	60/072
		3-5	C	68/078
		2-3	C	27/080
		2-3	C	36/145
		2-3	C	17/195
		1-2	C	54/258
		1-2	C	72/228
		4-6	C	18/313
		1-2	P	63/225
		1-2	P	55/218
		1	P	85/060
		1	P	70/014
		1	P	65/020
		2-4	P	62/026
		2	P	81/053
		1	P	60/049
		2-3	P	35/029
		2-3	P	39/037
		1	P	66/060
		2-3	P	27/040
		2-3	P	66/084
		2	P	69/090
		2-3	P	21/070
		2	P	47/095
		1-2	P	45/098
		7-10	P	18/086
		1-2	P	18/044
		2-3	P	24/280
		2-3	P	120/25

		2-3	P	108/22
		2-3	P	110/20
		2	P	144/26
		2	P	109/27
		2-4	P	128/22
		2	P	51/015
		2	P	45/020
		2-4	P	57/018
		10	P	16/155
		5-10	P	20/127
		5-10	P	16/133
		1	C-P	80/019
		15-20	C-P	40/060
		2-3-8	C-P	18/142
		1-3	C-P	24/344
		1-2	C-P	55/218
		1-2	C-P	63/225
		1-2	C-P	66/353
			DB	24/107
Port Willunga	Zone 54H 268946E 6095000S	1-2	P	45/094
Formation	Face Map 6	1	P	65/066
Port Willunga		1	P	47/227
		1	P	74/086
		1	P	38/059
		1	P	49/066
		1	P	41/045
		2	P	54/044
Port Willunga	Zone 54H 268968E 6095025S		DB	68/180
Formation	Face Map 7	1	P	68/197
Port Willunga		1	P	71/234
		2	P	54/065
		2	P	68/222
Bridgewater	Zone 53H 678240E 6095649S	2	C	80/100
Formation			P	
Stenhouse Bay			P	80/300
		3	P	80/300

		2-4	C	60/145
			P	82/300
			DB	80/090
			F	78/249
		4	P	79/350
			DB	80/320
			DB	80/240
			P	80/280
			F	70/230
		5-10	P	88/250
		5-10	P	79/042
		5-10	DB	85/320
		5-10	P	85/080
		5-10	DB	82/052
			Bedding	41/074
			Bedding	32/342
Bridgewater Formation	Zone 53H 679197E 6097032S	15	DB	90/182
Marion Bay		10	DB	90/150
		10	DB	90/250
		35	DB	90/218
			DB	90/254
		10	DB	90/148
		2	DB	90/270
		12	DB	90/230
		10	DB	90/373
		4	DB	90/290
		5	DB	90/180
		2	DB	90/239
			DB	90/250
		2	DB	68/310
			DB	90/264
		1	DB	90/215
			DB	90/320
			DB	65/050
		2	DB	90/208
		3	DB	90/203
		3	DB	90/203
		4	DB	30/136
		4	DB	30/136

		4	DB	30/136
		4	DB	30/136
		5	DB	40/356
		4	DB	28/358
		4	DB	28/358
		4	DB	28/358
			DB	38/050
		5	DB	90/184
		6	DB	05/215
		10	DB	90/242
		10	DB	90/242
		10	DB	90/250
		10	DB	90/250
		10	DB	90/316
		5	DB	90/238
		5	DB	90/238
Hallet Cove	Zone 53H	4	DB	30/260
Sandstone	762583E	4	DB	32/146
	6152609S			
Port Vincent			DB	30/160
North of stairs		2	DB	21/142
		2	DB	30/120
		7	DB	76/242
		4	DB	28/090
		3	DB	30/140
		5	DB	60/338
		3	DB	30/140
		1	DB	35/180
		2	DB	45/146
		2	DB	50/170
		3	DB	58/135
		2	DB	24/238
			DB	38/283
		2	DB	26/270
		4	DB	25/184
		3	DB	28/274
		5	DB	35/170
		2	DB	50/170
		2	DB	28/286
		2	DB	38/110

		2	DB	30/180
		2	DB	30/120
		2	DB	34/166
		5	DB	60/190
		3	DB	20/249
		1	DB	35/210
		2	DB	36/240
		3	DB	36/090
			DB	30/259
		2	DB	10/269
		3	DB	20/262
		2	DB	24/169
		3	DB	38/158
		4	DB	30/260
			DB	20/240
		3	DB	32/250
		4	DB	32/154
		4	DB	28/256
		4	DB	34/090
		2	DB	30/180
		5	DB	32/270
		5	DB	32/270
		9	DB	26/274
		3	DB	26/180
		5	DB	40/265
		2	DB	30/058
		2	DB	28/286
		2	DB	24/264
		1	DB	30/145
		9	DB	26/274
		4	DB	30/330
Hallet Cove	Zone 53H	5	DB	38/094
Sandstone	762585E			
	6152468S	2	DB	34/110
South of stairs			Bedding	34/206
		4-5	Bedding	12/258
		2-3	DB	21/088
		2-3	DB	28/020
		5-10	DB	28/025

		5-10	DB	38/060
		2-3	DB	18/105
			Bedding	23/322
Eyre Formation	Zone 54J 355296E 6665123S	2	DIL	02/301
Dead tree section	Face Map 1	6	DIL	10/107
		1	DIL	10/302
		10	DIL	12/109
		1	DIL	12/124
		3	DIL	12/125
		1	DIL	14/072
		10	DIL	14/130
		9	DIL	17/342
		4	DIL	18/098
		1	DIL	18/119
		4	DIL	18/138
		4	DIL	18/142
		1	DIL	19/076
		1	DIL	19/102
		2	DIL	19/330
		4	DIL	20/039
		30	DIL	20/104
		5	DIL	20/114
			DIL	20/310
		20	DIL	20/350
		2	DIL	21/058
			DIL	22/024
			DIL	22/024
		10	DIL	22/064
		20	DIL	22/084
		20	DIL	22/086
			DIL	22/109
		10	DIL	22/125
		1	DIL	23/278
		10	DIL	23/306
		1	DIL	24/038
		2	DIL	24/052
		1	DIL	24/096
		4	DIL	24/106

---

2	DIL	24/108
5	DIL	24/118
5	DIL	24/118
5	DIL	24/118
1	DIL	24/119
1	DIL	24/119
5	DIL	24/120
	DIL	25/093
20	DIL	27/110
1	DIL	28/014
2	DIL	28/025
	DIL	28/082
2	DIL	28/090
1	DIL	28/092
5	DIL	28/111
2	DIL	28/114
4	DIL	28/120
	DIL	28/136
2	DIL	28/078
2	DIL	29/070
9	DIL	29/082
2	DIL	29/119
4	DIL	30/100
6	DIL	30/104
	DIL	30/112
2	DIL	30/122
2	DIL	30/306
10	DIL	31/098
1	DIL	31/142
10	DIL	31/250
2	DIL	32/040
1	DIL	32/078
4	DIL	32/108
	DIL	32/120
2	DIL	32/232
10	DIL	32/239
10	DIL	32/239
2	DIL	32/317
10	DIL	33/134
20	DIL	33/142

---

---

1	DIL	33/146
	DIL	34/072
10	DIL	34/081
1	DIL	34/112
10	DIL	35/134
	DIL	35/320
2	DIL	36/060
6	DIL	36/072
1	DIL	36/082
1	DIL	36/102
5	DIL	36/116
4	DIL	36/138
2	DIL	36/150
2	DIL	36/270
2	DIL	37/220
20	DIL	37/314
1	DIL	38/001
	DIL	38/002
4	DIL	38/078
16	DIL	38/084
1	DIL	38/087
3	DIL	38/099
1	DIL	38/100
	DIL	38/120
3	DIL	38/138
1	DIL	38/275
5	DIL	38/322
1	DIL	39/135
10	DIL	40/090
2	DIL	40/096
2	DIL	40/106
4	DIL	40/107
1	DIL	42/058
4	DIL-F	42/062
1	DIL	42/088
2	DIL	42/090
	DIL	42/092
10	DIL	42/102
10	DIL	42/102
10	DIL	42/102

---

---

	DIL	42/105
5	DIL	42/106
	DIL	42/163
2	DIL	42/280
2	DIL	42/298
	DIL	42/327
	DIL	43/008
1	DIL	44/110
	DIL	44/110
1	DIL	44/116
2	DIL	44/308
50	DIL	45/059
4	DIL	45/098
4	DIL	45/104
2	DIL	46/063
4	DIL	47/050
2	DIL	47/296
1	DIL	48/060
1	DIL	48/083
2	DIL	48/104
2	DIL	48/108
2	DIL	48/123
	DIL	48/264
	DIL	48/288
1	DIL	49/004
2	DIL	49/049
5	DIL	49/080
2	DIL	49/128
1	DIL	50/038
	DIL	50/050
2	DIL	50/096
4	DIL	50/099
2	DIL	50/127
2	DIL	50/359
	DIL	51/286
5	DIL	51/321
1	DIL	51/340
6	DIL	52/074
2	DIL	52/092
	DIL	52/190

---

---

	DIL	52/278
4	DIL	52/308
5	DIL	52/314
2	DIL	53/130
	DIL	54/080
1	DIL	54/090
2	DIL	54/118
2	DIL	54/128
1	DIL	54/270
2	DIL	54/317
1	DIL	55/120
	DIL	56/096
2	DIL	56/190
	DIL	56/341
4	DIL	58/083
2	DB	58/103
4	DIL	58/320
2	DIL	59/118
	DIL	59/322
2	DIL	59/330
2	DIL	60/089
1	DIL	60/124
	DIL	60/147
2	DIL	60/196
	DIL	61/144
	DIL	61/159
2	DIL	61/210
	DIL	61/311
1	DIL	62/097
	DIL	62/146
1	DIL	62/276
	DIL	63/030
4	DIL	64/212
5	DIL	64/320
	DIL	66/308
	DIL	68/000
2	DIL	68/079
	DIL	68/279
	DIL	68/300
2	DIL	69/330

---

---

1	DIL	70/034
1	DIL	70/059
2	DIL	70/103
1	DIL	70/300
1	DIL	71/050
	DIL	71/228
2	DIL	71/248
2	DIL-F	72/116
	DIL	73/305
	DIL	74/032
	DIL	74/052
	DIL	74/138
	DIL	74/190
1	DIL	75/176
1	DIL	75/176
2	DIL	76/216
	DIL	76/314
10	DIL	77/310
	DIL	78/170
1	DIL	78/188
	DIL	79/126
2	DIL	79/239
2	DIL	80/099
	DIL	81/179
	DIL	81/204
2	DIL	82/020
2	DIL	82/023
	DIL	82/041
2	DIL	82/050
2	DIL	82/154
	DIL	82/166
8	DIL	82/288
	DIL	84/016
	DIL	85/020
	DIL	86/186
	DIL	90/025
3	DIL	90/049
	DIL	90/050
	DIL	90/056
	DIL	90/060

---

		1	DIL	90/079
			DIL	90/083
		1	DIL	90/166
Parabarana	Zone 54J	3	CAT	59/130
Sandstone	375312E 6681354S	3	CAT	39/174
Moolawatana		1	CAT	53/079
		1	CAT	56/073
		3	CAT	68/120
		3	CAT	55/081
		2	CAT	45/249
		3	CAT	46/101
		2	CAT	75/133
		2	CAT	59/129
		2	CAT	50/108
		5	CAT	80/173
		2	CAT	40/182
		1	CAT	57/087
		1	CAT	78/177
		1	CAT	53/076
		1	CAT	58/087
		1	CAT	81/176
		1	CAT	82/178
		1	CAT	89/173
			CAT	58/183
		4	CAT	18/065
		6	CAT	68/201
		5	CAT	77/254
		2	CAT	50/082
		5	CAT	69/311
		10	CAT	50/346
		1	CAT	46/185
		2	CAT	75/335
		1	CAT	56/094
		1	CAT	56/094
		1	CAT	43/098
		1	CAT	56/203
		5	CAT	81/354
		8	CAT	39/091
			CAT	25/201

---

1	CAT	41/234
2	CAT	53/095
5	CAT	76/354
1	CAT	41/161
1	CAT	44/194
	CAT	64/350
	CAT	67/144
1	CAT	73/100
3	CAT	65/172
5	CAT	50/349
1	CAT	62/172
2	CAT	79/185
2	CAT	79/185
2	CAT	86/358
4	CAT	52/346
1	CAT	53/164
	CAT	21/308
3	CAT	79/348
1	CAT	63/120
3	CAT	58/347
2	CAT	49/194
1	CAT	41/016
1	CAT	39/169
1	CAT	54/357
1	CAT	28/212
1	CAT	25/175
1	CAT	22/283
2	CAT	50/193
2	CAT	70/001
2	CAT	67/093
2	CAT	57/169
	CAT	52/001
5	CAT	86/000
1	CAT	17/170
	CAT	58/350
1	CAT	48/171
1	CAT	39/047
	CAT	56/180
1	CAT	25/204
1	CAT	44/331

---

			CAT	90/183
		2	CAT	33/043
		1	CAT	23/176
		5	CAT	79/172
		1	CAT	63/074
		2	CAT	85/155
		1	CAT	61/073
		1	CAT	28/034
		1	CAT	65/200
		2	CAT	58/094
		2	CAT	56/103
		2	CAT	50/077
		1	CAT	84/340
		1	CAT	61/097
		5	CAT	61/094
		1	CAT	58/091
		1	CAT	60/093
		4	CAT	62/091
		1	CAT	64/101
Heatherdale	Zone 54H		F	30/275
Shale	267426E		F	25/276
	6084997S			
Sellicks			F	78/084
Beach			F	78/040
			F	22/290
			F	37/294
			F	80/237
			F	26/275
			F	44/256
			F	55/232
			F	60/233
			F	68/256
			F	28/254
			F	82/246
			F	78/248
			F	09/007
			F	82/195
			F	23/254
			F	35/250

F	34/250
F	27/286
F	50/220
F	13/346
F	60/064
F	66/256
F	43/083
F	50/002
F	33/176
F	28/231
F	26/275
F	72/242
F	28/285
F	07/190
F	80/194
F	23/214
F	83/215
F	70/180
F	50/068
F	49/063
F	33/229
F	20/260
F	20/057
F	06/084
F	60/237
F	32/270
F	20/112
F	43/282
F	17/248
F	48/050
F	45/283
F	42/280
F	39/277
F	30/175
F	43/281
F	34/177
F	40/280
F	45/210
F	70/080
F	26/270

F	60/037
F	40/051
F	41/280
F	46/189
F	25/291
F	10/114
F	42/255
F	60/047
F	40/255
F	24/276
F	20/230
F	17/234
F	23/274
F	47/238
F	70/060
F	35/065
F	47/248
F	20/290
F	39/270
F	75/040
F	40/172
F	56/223
F	27/259
F	78/074
F	12/152
F	40/042
F	38/040
F	45/250
F	20/265
F	05/111
F	26/278
F	80/233
F	80/075
F	45/176
F	37/249
F	11/151
F	34/326
F	80/240
F	64/140
F	77/084

F	64/052
F	30/250
F	55/087
F	05/360
F	70/258
F	78/138
F	30/262
F	72/055
F	40/306
F	80/188
F	10/152
F	40/247
F	44/176
F	29/260
F	25/263
F	60/055
F	58/050
F	68/082
F	20/300
F	30/276
F	28/242
F	72/083
F	82/041
F	63/069
F	30/256
F	38/266
F	10/005
F	46/247
F	42/200
F	34/028
F	64/219
F	88/238
F	71/044
F	69/266
F	20/130
F	45/212
F	17/302
F	05/323
F	80/070
F	85/214

F	64/055
F	16/213
F	06/086
F	25/156
F	25/126
F	11/236
F	12/085
F	07/334
F	05/126
F	76/082
F	74/076
F	61/215
F	70/241
F	22/278
F	82/062
F	25/154
F	41/065
F	10/038
F	04/146
F	68/238
F	22/232
F	41/250
F	21/228
F	80/037
F	82/151
F	40/227
F	30/240
F	68/047
F	75/072
F	21/097
F	41/065
F	15/356
F	79/071
F	85/229
F	72/074
F	10/030
F	34/233
F	82/076
F	73/073
F	20/315

F	78/076
F	03/140
F	16/180
F	34/240
F	12/044
F	08/034
F	18/055
F	80/052
F	51/224
F	20/110
F	31/238
F	10/062
F	18/252
F	02/067
F	74/066
F	18/237
F	22/210
F	79/064
F	48/080
F	29/290
F	75/072
F	68/068
F	18/260
F	83/089
F	25/290
F	62/072
F	82/069
F	84/062
F	64/076
F	16/214
F	78/079
F	39/335
F	18/126
F	66/038
F	73/054
F	77/016
F	18/344
F	58/217
F	50/084
F	39/218

F	40/054
F	30/200
F	44/245
F	41/156
F	08/124
F	41/253
F	85/240
F	59/234
F	37/222
F	78/072
F	10/186
F	37/175
F	42/137
F	25/244
F	24/056
F	38/266
F	60/047
F	10/271
F	53/266
F	52/108
F	60/174
F	29/235
F	26/056
F	78/041
F	23/268
F	27/233
F	37/232
F	12/250
F	20/207
F	20/098
F	12/070
F	64/022
F	60/056
F	18/237
F	82/051
F	37/066
F	80/224
F	30/120
F	12/120
F	50/051

F	69/070
F	25/240
F	30/221
F	21/255
F	25/240
F	30/172
F	25/240
F	30/172
F	66/077
F	65/702
F	68/070
F	67/062
F	69/080
F	60/226
F	90/160
F	26/230
F	28/222
F	16/300
F	24/042
F	40/035
F	90/051
F	89/050
F	82/234
F	33/202
F	90/220
F	82/029
F	25/208
F	73/150
F	30/270
F	24/332
F	46/064
F	50/248
F	54/330
F	70/151
F	72/156
F	68/008
F	01/102
F	35/360
F	78/222
F	72/037

---

F	55/228
F	74/122
F	78/108
F	43/050
F	87/212
F	89/252
F	37/154
F	28/060
F	57/120
F	74/244
F	70/047
F	54/134
F	62/227
F	65/230
F	68/230
F	70/206
F	60/120
F	50/132
F	56/129
F	40/139
F	13/199
F	34/144
F	60/138
F	53/136
F	67/229
F	54/032
F	53/021
F	57/049
F	10/219
F	70/063
F	45/128
F	52/326
F	52/122
F	24/154
F	25/153
F	24/150
F	26/150
F	30/203
F	75/157
F	66/215

---

F	22/240
F	50/169
F	50/128
F	26/154
F	89/259
F	31/159
F	47/114
F	36/146
F	70/039
F	73/041
F	25/150
F	82/224
F	30/169
F	53/070
F	11/290
F	87/232
F	83/192
F	23/156
F	34/145
F	50/120
F	80/224
F	49/126
F	89/230
F	25/151
F	72/040
F	49/169
F	76/142
F	70/150
F	48/070
F	25/154
F	30/158
F	23/152
F	49/120
F	48/121
F	49/120
F	85/054
F	48/119
F	50/122
F	82/210
F	34/294

F	50/070
F	52/121
F	48/123
F	65/112
F	36/116
F	62/114
F	87/310
F	63/325
F	55/349
F	22/294
F	24/150
F	75/126
F	87/055
F	70/040
F	80/210
F	23/150
F	20/150
F	23/150
F	88/261
F	33/145
F	49/120
F	72/012
F	44/300
F	13/204
F	68/210
F	24/295
F	55/121
F	49/150
F	48/146
F	90/010
F	76/170
F	73/180
F	44/101
F	86/160
F	62/214
F	70/213
F	55/142
F	59/132
F	90/237
F	90/238

			F	90/232
			F	90/223
			F	70/192
			F	58/334
			F	28/201
			F	72/255
			F	83/166
			F	20/280
			F	65/075
			F	75/170
			F	62/030
			F	50/036
			F	32/056
			F	62/019
			F	41/142
			F	33/112
			F	62/030
			F	70/036
			F	65/034
Manitou Falls	483949E			
	6397933N	5	CAT	90/065
Formation	483994E			
	6398059N	2	CAT	90/104
Fox Lake	483994E			
	6398059N	2	CAT	90/120
Surface	484141E			
	6397687N	30	CAT	90/236
	484141E			
	6397687N	1	CAT	90/276
	484230E			
	6397731N	21	CAT	90/228
	484244E			
	6397697N	1	CAT	90/226
	484244E			
	6397697N	1	CAT	90/242
	484244E			
	6397697N	1	CAT	90/204
	484244E			
	6397697N	1	CAT	90/230
	484244E			
	6397697N	1	CAT	90/236
	484244E			
	6397697N	1	CAT	90/261

484247E 6397745N	20	CAT	22/290
484247E 6397745N	4-15	CAT	90/090
484247E 6397745N		CAT	88/014
484247E 6397745N		CAT	90/065
484250E 6397704N	1	CAT	90/186
484250E 6397704N	1	CAT	90/206
484250E 6397704N	1	CAT	90/236
484250E 6397704N	1	CAT	90/239
484252E 6397674N	11	CAT	90/200
484252E 6397674N	1-6	CAT	90/233
484252E 6397674N	15	CAT	90/212
484252E 6397674N	1	CAT	90/230
484252E 6397674N	2	CAT	90/246
484252E 6397674N	3	CAT	90/226
484252E 6397674N	3	CAT	90/248
484252E 6397674N	3	CAT	90/254
484255E 6397702N	3	CAT	90/189
484329E 6397709N	1	CAT	90/192
484329E 6397709N	1	CAT	90/206
484329E 6397709N	1	CAT	90/226
485152E 6398836N		CAT	88/188
485152E 6398836N		CAT	80/070
485169E 6398854N	5	CAT	88/238

485176E 6398847N	5	CAT	74/104
485176E 6398847N	5	CAT	78/254
485176E 6398847N	5	CAT	72/050
485187E 6398828N	2	CAT	90/226
485187E 6398828N	2	CAT	90/244
485191E 6398848N	15-20	CAT	70/075
485191E 6398848N	10	CAT	78/130
485198E 6398881N	12	CAT	72/228
485198E 6398881N	20	CAT	82/225
485198E 6398881N	6	CAT	88/229
485199E 6398841N	2	CAT	82/254
485199E 6398841N	2	CAT	60/287
485199E 6398841N	2	CAT	74/074
485199E 6398841N	3	CAT	69/105
485199E 6398841N	3	CAT	80/230
485199E 6398841N	3	CAT	81/044
485199E 6398841N	5	CAT	84/247
485199E 6398841N	5	CAT	80/045
485202E 6398817N	5	CAT	90/206
485218E 6398796N	1	CAT	80/226
485218E 6398796N	1	CAT	80/250
485218E 6398796N	5	CAT	80/250
485233E 6398846N	3	CAT	82/270

485237E 6398993N	1	CAT	90/227
485237E 6398993N	1	CAT	90/231
485237E 6398993N	1	CAT	90/238
485237E 6398993N	1	CAT	90/250
485237E 6398993N	1	CAT	90/254
485237E 6398993N	1	CAT	90/256
485237E 6398993N	1	CAT	90/258
485237E 6398993N	1	CAT	90/268
485237E 6398993N	1	CAT	90/269
485244E 6398965N	1	CAT	90/238
485244E 6398965N	1	CAT	90/256
485244E 6398965N	1	CAT	90/260
485244E 6398995N	1-2	CAT	340/82 18/320
485244E 6398995N	1	CAT	80/276
485244E 6398995N	2	CAT	79/065
485244E 6398995N	2	CAT	90/260
485244E 6398995N	2	CAT	90/260
485244E 6398995N	2	CAT	80/052
485244E 6398995N	2	CAT	80/084
485244E 6398995N	2-3	CAT	74/230
485244E 6398995N	2-3	CAT	74/230
485244E 6398995N	3	CAT	74/280

485244E 6398995N	4	CAT	86/082
485244E 6398995N	5	CAT	90/280
485245E 6398991N	1	CAT	74/211
485245E 6398991N	1	CAT	90/214
485245E 6398991N	1	CAT	90/215
485245E 6398991N	1	CAT	90/226
485247E 6398836N	5-8	CAT	80/090
485247E 6398836N	2-3	CAT	80/289
485247E 6398836N	2-5	CAT	86/068
485250E 6399025N	6	CAT	90/261
485255E 6399022N	1	CAT	90/225
485255E 6399022N	3	CAT	90/240
485260E 6399006N	2	CAT	90/237
485264E 6398975N	5	CAT	90/260
485266E 6398999N	2	CAT	90/253
485266E 6398999N	4	CAT	90/256
485266E 6398999N	4	CAT	90/265
485269E 6399011N	1	CAT	90/237
485269E 6399011N	1	CAT	90/240
485271E 6399019N	3	CAT	90/240
485271E 6399019N	1	CAT	90/134
485271E 6399019N	1	CAT	90/140
485272E 6398994N	4	CAT	90/248

485286E 6399027N	1	CAT	90/224
485286E 6399027N	3	CAT	90/248
485291E 6398923N	5	CAT	90/270
485291E 6398923N	5	CAT	85/082
485342E 6399059N	2	CAT	90/040
485342E 6399059N	2	CAT	90/076
485342E 6399059N	1-5	CAT	80/056
485342E 6399059N	2-10	CAT	84/096
485342E 6399059N	2-10	CAT	86/058
485342E 6399059N	4-10	CAT	88/068
485342E 6399059N	5-13	CAT	86/037
485342E 6399059N	5-20	CAT	89/053
485342E 6399059N	8-60	CAT	80/096
485342E 6399059N	1	CAT	89/073
485342E 6399059N	1	CAT	89/090
485342E 6399059N	1	CAT	80/091
485342E 6399059N	1	CAT	85/037
485342E 6399059N	2	CAT	88/120
485384E 6399430N	2	CAT	90/104
485384E 6399430N	2	CAT	65/113
485384E 6399430N	3-4	CAT	84/066
485384E 6399430N	2	CAT	90/268
485393E 6399490N	2	CAT	78/048

485452E 6399502N	2	CAT	90/056
485452E 6399502N	2	CAT	90/089
485505E 6398939N	1	CAT	90/097
485505E 6398939N	1	CAT	90/100
485505E 6398939N	1	CAT	90/114
485505E 6398939N	1	CAT	90/227
485505E 6398939N	1	CAT	90/243
485505E 6398939N	1	CAT	90/287
485505E 6398939N	1	CAT	90/094
485505E 6398939N	1	CAT	90/200
485505E 6398939N	1	CAT	90/242
485505E 6398939N	1	CAT	90/267
485505E 6398939N	1	CAT	90/208
485505E 6398939N	1	CAT	90/210
485505E 6398939N	1	CAT	90/210
486098E 6400482N	1	CAT	90/227
486098E 6400482N	1	CAT	90/241
486098E 6400482N	1	CAT	90/245
486098E 6400482N	1	CAT	90/247
486098E 6400482N	1	CAT	90/249
486399E 6400438N	10	CAT	78/285
486399E 6400438N	20	CAT	90/088
486399E 6400438N	3	CAT	81/246

486399E 6400438N	2-10	CAT	90/109
486399E 6400438N		CAT	90/110
486399E 6400438N		CAT	90/130
486400E 6400418N		CAT	90/024
486400E 6400418N		CAT	90/242
486400E 6400418N		CAT	90/297
486400E 6400418N		CAT	90/304
486401E 6400481N	1-5	CAT	85/093
486401E 6400481N	1-5	CAT	90/090
486402E 6400459N	1	CAT	80/290
486402E 6400459N	1	CAT	62/085
486402E 6400459N	3	CAT	84/100
486417E 6400428N	1-6	CAT	72/270
486441E 6400493N	1-2	CAT	84/090
486475E 6400477N	1	CAT	86/100
486475E 6400477N	2	CAT	90/112
486475E 6400477N	2-3	CAT	88/094
486475E 6400477N	5	CAT	88/100
486475E 6400477N		CAT	84/109
486487E 6400500N	2	CAT	80/278
486487E 6400500N	4	CAT	80/280
486487E 6400500N	4	CAT	80/284
486487E 6400500N	6	CAT	72/292

486616E 6400467N	1	CAT	90/253
486616E 6400467N	1	CAT	90/266
486648E 6400478N	3	CAT	79/305
486648E 6400478N	4	CAT	82/269
486648E 6400478N		CAT	90/250
486715E 6400747N	4	CAT	90/231
486715E 6400747N	1	CAT	90/231
486715E 6400747N	1	CAT	90/278
486715E 6400747N	1	CAT	90/282
486715E 6400747N	1	CAT	90/284
486764E 6400613N	4	CAT	90/125
486764E 6400613N	14	CAT	90/084
486764E 6400613N	8-10	CAT	90/070
486764E 6400613N	1-2	CAT	90/172
486768E 6400734N	25	CAT	90/054
486777E 6400626N	3	CAT	90/181
486777E 6400626N	4	CAT	90/240
486787E 6400644N	3	CAT	90/271
486787E 6400644N	3	CAT	90/295
486787E 6400644N	4	CAT	90/276
486787E 6400644N	1	CAT	90/131
486787E 6400644N	1	CAT	90/143
486883E 6400927N		CAT	85/238

486883E 6400927N	1	CAT	65/299
486883E 6400927N	1	CAT	70/076
486903E 6400956N	10-50	CAT	80/240
486903E 6400956N	1	CAT	68/253
486903E 6400956N	1	CAT	78/258
486903E 6400956N	1	CAT	74/261
486911E 6400916N	1	CAT	90/238
486911E 6400916N	1	CAT	90/254
486911E 6400916N	1	CAT	90/273
486911E 6400916N	1	CAT	84/276
486911E 6400916N	1	CAT	90/299
486911E 6400916N	1	CAT	90/304
486911E 6400916N	2	CAT	84/232
486952E 6400851N	12	CAT	80/242
486952E 6400851N	15	CAT	82/245
486952E 6400851N	3	CAT	78/254
486952E 6400851N	3	CAT	76/289
486952E 6400851N	1-3	CAT	84/250
486952E 6400851N	3	CAT	69/242
486952E 6400851N	4	CAT	78/224
486952E 6400851N	1-2	CAT	89/246
486952E 6400851N	2	CAT	82/254
486952E 6400851N	2-6	CAT	87/242

486952E 6400851N	2-6	CAT	81/256
486952E 6400851N	2-8	CAT	87/247
486952E 6400851N	5	CAT	69/242
486952E 6400851N	9	CAT	87/242
486957E 6400841N		CAT	82/205
486957E 6400841N		CAT	82/206
486957E 6400841N		CAT	76/215
486957E 6400841N		CAT	80/218
486957E 6400841N		CAT	88/220
486957E 6400841N		CAT	88/220
486957E 6400841N		CAT	88/224
486957E 6400841N		CAT	85/244
486957E 6400841N		CAT	90/254
486957E 6400841N		CAT	90/256
486957E 6400841N		CAT	90/262
486957E 6400841N		CAT	70/270
486958E 6400864N		CAT	80/257
486958E 6400864N		CAT	63/250
486958E 6400864N		CAT	81/262
486958E 6400864N		CAT	82/270
486958E 6400864N		CAT	80/270
486958E 6400864N		CAT	80/046
486958E 6400864N		CAT	88/098

486958E 6400864N		CAT	75/259
486958E 6400864N		CAT	78/262
486958E 6400864N		CAT	78/038
486958E 6400864N		CAT	90/062
486958E 6400864N		CAT	84/090
486958E 6400864N		CAT	78/220
486958E 6400864N		CAT	80/032
486963E 6400831N	1	CAT	84/176
486963E 6400831N	1	CAT	78/232
486963E 6400831N	1	CAT	84/295
486963E 6400831N	1	CAT	78/296
486963E 6400831N	1	CAT	84/229
486963E 6400831N	1	CAT	78/230
486963E 6400831N	1	CAT	84/230
486963E 6400831N	1	CAT	78/232
486963E 6400831N	1	CAT	84/233
486963E 6400831N	1	CAT	78/235
486969E 6400876N	1	CAT	64/096
486969E 6400876N	1	CAT	85/255
486969E 6400876N	1	CAT	76/035
486969E 6400876N	1	CAT	79/049
486969E 6400876N	1	CAT	82/050
486974E 6401059N	1-3	CAT	15/240

487045E 6401050N	1-5	CAT	62/310
487045E 6401050N	1-2	CAT	78/248
487123E 6401054N	1-4	CAT	08/284
487126E 6011065N	1-2	CAT	88/294
487137E 6401108N	3-5	CAT	74/296
487137E 6401108N	1	CAT	90/300
487137E 6401108N	1	CAT	86/153
487137E 6401108N	1-3	CAT	85/305
487137E 6401108N	2	CAT	84/321
487137E 6401108N	2-3	CAT	86/336
487137E 6401108N		CAT	89/290
487137E 6401108N		CAT	90/301
487137E 6401108N		CAT	90/330
Grid 1	1	CAT	90/221
Grid 1	1	CAT	90/234
Grid 1	1	CAT	90/268
Grid 1	1	CAT	90/269
Grid 1	5	CAT	90/220
Grid 1	6	CAT	90/218
Grid 1	100	CAT	80/288
Grid 1	2	CAT	76/095
Grid 1	2	CAT	90/99
Grid 1	2	CAT	82/256
Grid 1	2-5	CAT	86/226
Grid 1		CAT	90/291
Grid 1		CAT	90/050
Grid 1		CAT	90/072
Grid 1		CAT	25/300
Grid 1		CAT	20/294
Grid 1	2-8	CAT	80/060

Grid 1	2-9	CAT	78/232
Grid 1	6	CAT	74/276
Grid 1	6-16	CAT	78/286
Grid 1	8	CAT	78/276
Grid 1	9	CAT	90/059
Grid 1		CAT	86/230
Grid 1		CAT	88/254
Grid 1		CAT	90/090
Grid 1	10	CAT	85/230
Grid 1	1c	CAT	90/270
Grid 1	2-5	CAT	88/099
Grid 1	2-5	CAT	84/240
Grid 1	3-10	CAT	90/107
Grid 1	5	CAT	90/241
Grid 1	5	CAT	74/248
Grid 1	50	CAT	70/234
Grid 1	8	CAT	80/270
Grid 1		CAT	82/254
Grid 1		CAT	90/080
Grid 1		CAT	90/090
Grid 1	1	CAT	90/092
Grid 1	1	CAT	90/224
Grid 1	1	CAT	84/226
Grid 1	12	CAT	90/252
Grid 1	2	CAT	90/101
Grid 1	2	CAT	90/222
Grid 1	2	CAT	85/226
Grid 1	2	CAT	90/238
Grid 1	2	CAT	32/334
Grid 1	2	CAT	90/025
Grid 1	3	CAT	90/242
Grid 1	3	CAT	90/258
Grid 1	3	CAT	90/268
Grid 1	5	CAT	90/244
Grid 1	5	CAT	90/254
Grid 1		CAT	90/226
Grid 1		CAT	73/250
Grid 1		CAT	90/090
Grid 1	2	CAT	90/070
Grid 1		CAT	81/280

Grid 1		CAT	76/346
Grid 1	1	CAT	90/096
Grid 1	1	CAT	90/118
Grid 1	1	CAT	90/210
Grid 1	1	CAT	90/240
Grid 1	1	CAT	90/067
Grid 1	1	CAT	90/085
Grid 1	1	CAT	90/090
Grid 1	12	CAT	90/224
Grid 1	1-2	CAT	90/113
Grid 1	1-2	CAT	80/090
Grid 1	1-3	CAT	90/094
Grid 1	2	CAT	90/093
Grid 1	2	CAT	76/098
Grid 1	2	CAT	76/098
Grid 1	2	CAT	90/231
Grid 1	2	CAT	90/246
Grid 1	2	CAT	75/280
Grid 1	2	CAT	75/050
Grid 1	2	CAT	76/060
Grid 1	2	CAT	82/072
Grid 1	2-10	CAT	80/245
Grid 1	2-15	CAT	80/090
Grid 1	2-3	CAT	90/049
Grid 1	2-6	CAT	76/253
Grid 1	2-6	CAT	72/088
Grid 1	3	CAT	79/094
Grid 1	3	CAT	70/230
Grid 1	3	CAT	84/245
Grid 1	3	CAT	75/057
Grid 1	3	CAT	80/066
Grid 1	3	CAT	76/074
Grid 1	3-12	CAT	82/064
Grid 1	3-5	CAT	80/072
Grid 1	4	CAT	90/096
Grid 1	4	CAT	75/270
Grid 1	4	CAT	82/074
Grid 1	5	CAT	76/220
Grid 1	5	CAT	90/237
Grid 1	5	CAT	68/239

Grid 1	5-15	CAT	83/256
Grid 1	5-7	CAT	90/220
Grid 1	9	CAT	76/220
Grid 1	9	CAT	90/050
Grid 1	9	CAT	90/060
Grid 1		CAT	90/111
Grid 1		CAT	90/158
Grid 1		CAT	59/270
Grid 1		CAT	90/270
Grid 1		CAT	85/300
Grid 1		CAT	82/304
Grid 1		CAT	78/312
Grid 1		CAT	90/079
Grid 1	1	CAT	90/118
Grid 1	1	CAT	90/118
Grid 1	2	CAT	90/108
Grid 1	2	CAT	90/040
Grid 1	2	CAT	80/054
Grid 1	2	CAT	84/060
Grid 1	2	CAT	90/080
Grid 1	2	CAT	90/080
Grid 1	2-3	CAT	85/105
Grid 1	2-3	CAT	80/090
Grid 1	3	CAT	78/088
Grid 1	4	CAT	90/228
Grid 1	5-6	CAT	64/230
Grid 1		CAT	88/294
Grid 1		CAT	90/107
Grid 1		CAT	90/110
Grid 1		CAT	90/128
Grid 1		CAT	68/210
Grid 1		CAT	74/220
Grid 1		CAT	78/226
Grid 1		CAT	80/240
Grid 1		CAT	86/260
Grid 1		CAT	80/302
Grid 1		CAT	80/050
Grid 1		CAT	90/054
Grid 1		CAT	90/059
Grid 1		CAT	90/069

Grid 1	CAT	90/070
Grid 1	CAT	90/075
Grid 1	CAT	90/080
Grid 1	CAT	90/080
Grid 1	CAT	90/080
Grid 1	CAT	86/084
Grid 1	CAT	90/084
Grid 1	CAT	90/085
Grid 1	CAT	90/086
Grid 1	CAT	90/0256
Grid 1	F	90/094
Grid 1	F	90/098
Grid 1	F	80/122
Grid 1	F	90/170
Grid 1	F	90/172
Grid 1	F	60/180
Grid 1	F	85/192
Grid 1	F	90/222
Grid 1	F	90/229
Grid 1	F	62/230
Grid 1	F	90/230
Grid 1	F	90/232
Grid 1	F	90/234
Grid 1	F	75/240
Grid 1	F	90/242
Grid 1	F	90/242
Grid 1	F	65/245
Grid 1	F	84/246
Grid 1	F	60/250
Grid 1	F	75/250
Grid 1	F	90/250
Grid 1	F	80/259
Grid 1	F	70/260
Grid 1	F	90/286
Grid 1	F	62/287
Grid 1	F	72/287
Grid 1	F	90/290
Grid 1	F	72/294
Grid 1	F	90/298
Grid 1	F	90/300

Grid 1	F	90/310
Grid 1	F	56/323
Grid 1	F	90/324
Grid 1	F	90/328
Grid 1	F	90/330
Grid 1	F	56/336
Grid 1	F	90/336
Grid 1	F	82/350
Grid 1	F	90/350
Grid 1	F	90/351
Grid 1	F	90/352
Grid 1	F	90/002
Grid 1	F	90/006
Grid 1	F	90/006
Grid 1	F	90/007
Grid 1	F	90/009
Grid 1	F	90/011
Grid 1	F	90/013
Grid 1	F	90/014
Grid 1	F	90/016
Grid 1	F	90/022
Grid 1	F	90/024
Grid 1	F	90/026
Grid 1	F	80/045
Grid 1	F	90/045
Grid 1	F	90/047
Grid 1	F	90/050
Grid 1	F	90/052
Grid 1	F	90/052
Grid 1	F	90/058
Grid 1	F	90/058
Grid 1	F	90/059
Grid 1	F	90/060
Grid 1	F	90/060
Grid 1	F	90/066
Grid 1	F	90/066
Grid 1	F	90/069
Grid 1	F	90/070
Grid 1	F	90/072
Grid 1	F	88/075

Grid 1		F	76/079
Grid 1		F	90/080
Grid 1		F	90/090
Grid 1		F	85/090
Grid 1		CAT	72/287
Grid 1		CAT	90/020
Grid 1		CAT	90/050
Grid 1	1	CAT	90/200
Grid 1		CAT	90/111
Grid 1		CAT	90/060
Grid 2	1-4	CAT	90/227
Grid 2	1-4	CAT	90/252
Grid 2	15	CAT	90/227
Grid 2	10	CAT	90/227
Grid 2	10	CAT	00/180
Grid 2	1-5	CAT	26/320
Grid 2		CAT	30/326
Grid 2	2	CAT	20/290
Grid 2		CAT	20/254
Grid 2		CAT	20/290
Grid 2	90	CAT	90/054
Grid 2	90	CAT	80/237
Grid 2	10	CAT	78/240
Grid 2	20	CAT	90/250
Grid 2	5-10	CAT	80/287
Grid 2	5-10	CAT	90/059
Grid 2	1	CAT	90/163
Grid 2	1	CAT	90/223
Grid 2	1	CAT	90/230
Grid 2	1	CAT	90/233
Grid 2	1	CAT	90/248
Grid 2	1	CAT	90/252
Grid 2	1	CAT	90/257
Grid 2	1	CAT	90/261
Grid 2	10	CAT	15/321
Grid 2	2	CAT	90/100
Grid 2	2	CAT	90/152
Grid 2	2	CAT	90/215
Grid 2	2	CAT	90/222
Grid 2	2	CAT	90/228

Grid 2	2	CAT	90/240
Grid 2	2	CAT	90/259
Grid 2	2	CAT	90/264
Grid 2	2	CAT	90/269
Grid 2	2	CAT	90/271
Grid 2	2	CAT	29/322
Grid 2	2	CAT	20/020
Grid 2	2	CAT	90/070
Grid 2	2	CAT	90/078
Grid 2	2-3	CAT	90/260
Grid 2	3	CAT	90/152
Grid 2	3	CAT	90/232
Grid 2	3	CAT	90/246
Grid 2	3	CAT	90/271
Grid 2	3	CAT	30/347
Grid 2	3	CAT	90/054
Grid 2	4	CAT	90/225
Grid 2	4	CAT	90/226
Grid 2	5	CAT	90/229
Grid 2		CAT	30/014
Grid 2		CAT	65/090
Grid 2	1	CAT	90/232
Grid 2	1	CAT	90/240
Grid 2	10-20	CAT	78/239
Grid 2	2	CAT	90/205
Grid 2	2	CAT	90/220
Grid 2	2	CAT	90/221
Grid 2	2	CAT	90/238
Grid 2	2	CAT	78/240
Grid 2	2	CAT	80/242
Grid 2	2	CAT	90/249
Grid 2	2	CAT	90/249
Grid 2	2	CAT	90/054
Grid 2	2	CAT	82/070
Grid 2	2	CAT	82/077
Grid 2	2	CAT	80/080
Grid 2	2-3	CAT	78/224
Grid 2	2-4	CAT	70/070
Grid 2	2-6	CAT	81/094
Grid 2	20-60	CAT	81/094

Grid 2	3	CAT	74/258
Grid 2	3	CAT	70/040
Grid 2	3	CAT	83/062
Grid 2	3-6	CAT	80/050
Grid 2	4	CAT	24/320
Grid 2	5-6	CAT	90/240
Grid 2	7	CAT	90/094
Grid 2	7	CAT	90/252
Grid 2		CAT	82/251
Grid 2	2	CAT	60/060
Grid 2	2-3	CAT	78/080
Grid 2	4	CAT	62/098
Grid 2	4	CAT	71/076
Grid 2	4	CAT	68/090
Grid 2	5	CAT	72/110
Grid 2		CAT	30/230
Grid 2	2	F	82/238
Grid 2		F	90/153
Grid 2		F	90/159
Grid 2		F	78/195
Grid 2		F	80/222
Grid 2		F	90/229
Grid 2		F	90/230
Grid 2		F	80/230
Grid 2		F	80/240
Grid 2		F	84/249
Grid 2		F	80/255
Grid 2		F	70/256
Grid 2		F	90/260
Grid 2		F	90/260
Grid 2		F	82/263
Grid 2		F	90/272
Grid 2		F	90/294
Grid 2		F	90/054
Grid 2		F	90/070
Grid 2	1	CAT	90/163
Grid 2	2	CAT	90/138
Grid 2	2	CAT	90/143
Grid 2	2	CAT	90/146
Grid 2	2	CAT	90/153

---

Grid 2	2	CAT	90/154
Grid 2	2	CAT	90/163
Grid 2	2	CAT	90/167
Grid 2	2	CAT	90/168
Grid 2	2	CAT	90/169
Grid 2	2	CAT	90/179
Grid 2	3	CAT	90/170
Grid 2	4	CAT	90/127
Grid 3	1	CAT	90/241
Grid 3	2	CAT	90/227
Grid 3	3	CAT	90/276
Grid 3	4	CAT	90/246
Grid 3	5	CAT	90/137
Grid 3	16	CAT	90/248
Grid 3	2-5	CAT	78/048
Grid 3	3	CAT	80/113
Grid 3	5	CAT	80/296
Grid 3	1-5	CAT	80/070
Grid 3	2	CAT	90/122
Grid 3		CAT	82/070
Grid 3	20	CAT	86/276
Grid 3	4-13	CAT	82/116
Grid 3	5-10	CAT	86/114
Grid 3	5-12	CAT	78/270
Grid 3	6	CAT	90/082
Grid 3	10-15	CAT	90/072
Grid 3	20	CAT	90/084
Grid 3	3-8	CAT	79/116
Grid 3	5	CAT	90/090
Grid 3	5-15	CAT	82/076
Grid 3	1	CAT	90/230
Grid 3	1	CAT	90/244
Grid 3	1	CAT	90/247
Grid 3	1	CAT	90/248
Grid 3	1	CAT	90/248
Grid 3	1	CAT	90/251
Grid 3	1	CAT	90/255
Grid 3	1	CAT	90/258
Grid 3	1	CAT	90/269
Grid 3	1	CAT	90/270

---

---

Grid 3	1	CAT	90/282
Grid 3	2	CAT	90/236
Grid 3	2	CAT	90/249
Grid 3	2	CAT	90/290
Grid 3	2	CAT	90/309
Grid 3	2	CAT	76/360
Grid 3	2	CAT	80/018
Grid 3	3	CAT	90/242
Grid 3	3	CAT	90/250
Grid 3	5	CAT	90/245
Grid 3	5	CAT	90/282
Grid 3		CAT	90/235
Grid 3		CAT	90/247
Grid 3		CAT	90/248
Grid 3		CAT	90/256
Grid 3		CAT	90/262
Grid 3		CAT	90/270
Grid 3		CAT	90/275
Grid 3		CAT	90/283
Grid 3		CAT	90/289
Grid 3	1	CAT	78/131
Grid 3	1	CAT	90/305
Grid 3	1	CAT	82/006
Grid 3	1	CAT	77/045
Grid 3	1	CAT	88/060
Grid 3	1	CAT	80/076
Grid 3	1	CAT	80/089
Grid 3	1-2	CAT	90/124
Grid 3	1-2	CAT	78/313
Grid 3	1-2	CAT	88/070
Grid 3	1-2	CAT	82/072
Grid 3	1-4	CAT	80/106
Grid 3	2	CAT	75/116
Grid 3	2	CAT	81/141
Grid 3	2	CAT	79/291
Grid 3	2	CAT	88/312
Grid 3	2	CAT	88/312
Grid 3	2	CAT	80/050
Grid 3	2	CAT	89/075
Grid 3	2	CAT	88/076

---

Grid 3	2	CAT	80/078
Grid 3	2-3	CAT	86/050
Grid 3	2-3	CAT	90/090
Grid 3	2-4	CAT	86/061
Grid 3	2-5	CAT	85/124
Grid 3	2-5	CAT	85/072
Grid 3	3	CAT	86/296
Grid 3	4	CAT	90/255
Grid 3	9	CAT	90/254
Grid 3		CAT	90/257
Grid 3		CAT	90/259
Grid 3		CAT	90/259
Grid 3		CAT	90/268
Grid 3		CAT	90/269
Grid 3		CAT	90/047
Grid 3		CAT	90/058
Grid 3		CAT	90/088
Grid 3	1	CAT	87/092
Grid 3	1	CAT	90/106
Grid 3	1	CAT	90/115
Grid 3	1	CAT	90/118
Grid 3	1	CAT	70/140
Grid 3	1	CAT	78/320
Grid 3	1	CAT	99/090
Grid 3	2	CAT	90/118
Grid 3	2	CAT	90/082
Grid 3	2	CAT	90/090
Grid 3	2-3	CAT	62/140
Grid 3	2-3	CAT	78/074
Grid 3	2-4	CAT	85/059
Grid 3	3-5	CAT	83/283
Grid 3		CAT	90/071
Grid 3	10-20	F	90/076
Grid 3		F	90/096
Grid 3		F	90/137
Grid 3		F	90/139
Grid 3		F	80/144
Grid 3		F	90/153
Grid 3		F	90/153
Grid 3		F	90/159

Grid 3	F	90/163
Grid 3	F	90/170
Grid 3	F	62/172
Grid 3	F	90/174
Grid 3	F	90/180
Grid 3	F	01/180
Grid 3	F	90/181
Grid 3	F	90/183
Grid 3	F	90/190
Grid 3	F	90/200
Grid 3	F	90/204
Grid 3	F	83/208
Grid 3	F	90/225
Grid 3	F	90/226
Grid 3	F	90/228
Grid 3	F	90/229
Grid 3	F	90/235
Grid 3	F	90/237
Grid 3	F	85/240
Grid 3	F	90/240
Grid 3	F	90/241
Grid 3	F	90/243
Grid 3	F	90/244
Grid 3	F	90/248
Grid 3	F	90/249
Grid 3	F	90/252
Grid 3	F	90/252
Grid 3	F	90/253
Grid 3	F	90/253
Grid 3	F	76/256
Grid 3	F	90/256
Grid 3	F	90/257
Grid 3	F	90/258
Grid 3	F	90/261
Grid 3	F	90/265
Grid 3	F	72/302
Grid 3	F	80/311
Grid 3	F	90/315
Grid 3	F	90/318
Grid 3	F	80/325

Grid 3		F	86/333
Grid 3		F	72/359
Grid 3		F	90/360
Grid 3		F	80/008
Grid 3		F	75/010
Grid 3		F	80/011
Grid 3		F	90/054
Grid 3		F	78/070
Grid 3		F	90/076
Grid 3		F	90/080
Grid 3		F	90/080
Grid 3		F	90/080
Grid 3		F	90/080
Grid 3		F	90/090
Grid 3		F	90/090
Grid 3	1	CAT	90/121
Grid 3	1	CAT	90/239
Grid 3	1	CAT	90/205
Grid 3	1	CAT	90/206
Grid 3	1	CAT	90/207
Grid 3	1	CAT	90/208
Grid 3	1	CAT	90/211
Grid 3	1	CAT	90/213
Grid 3	1	CAT	90/214
Grid 3	1	CAT	90/215
Grid 3	1	CAT	90/215
Grid 3	1	CAT	90/222
Grid 3		CAT	90/119
Grid 3		CAT	90/154
Grid 3		CAT	90/300
Grid 3		CAT	90/303
Grid 3		CAT	90/305
Grid 3		CAT	90/318
Grid 3		CAT	90/210
Grid 3		CAT	90/212
Grid 3		CAT	90/216
Grid 3		CAT	90/219
Grid 3		CAT	90/228
Grid 3		CAT	90/251
Grid 3		CAT	90/265

Grid 3		CAT	90/272
Grid 4	10	CAT	70/287
Grid 4	6-7	CAT	79/308
Grid 4	1	CAT	90/328
Grid 4	15-90	CAT	90/070
Grid 4	2-5	CAT	90/246
Grid 4	40	CAT	82/247
Grid 4	40	CAT	90/270
Grid 4	5	CAT	76/300
Grid 4	90	CAT	82/262
Grid 4	2	CAT	90/120
Grid 4	2	CAT	90/274
Grid 4	3	CAT	90/290
Grid 4	6	CAT	90/241
Grid 4	8	CAT	90/285
Grid 4		CAT	90/233
Grid 4		CAT	90/241
Grid 4		CAT	90/251
Grid 4		CAT	90/259
Grid 4		CAT	90/264
Grid 4	10	CAT	68/320
Grid 4	1-2	CAT	90/279
Grid 4	2	CAT	90/091
Grid 4	2	CAT	79/239
Grid 4	2	CAT	80/260
Grid 4	2	CAT	80/270
Grid 4	2	CAT	80/299
Grid 4	2	CAT	86/041
Grid 4	2	CAT	90/082
Grid 4	2-5	CAT	72/308
Grid 4	4	CAT	80/304
Grid 4	4-10	CAT	80/290
Grid 4	5	CAT	86/131
Grid 4	5	CAT	86/131
Grid 4	5	CAT	80/254
Grid 4	5	CAT	78/312
Grid 4	5-17	CAT	85/241
Grid 4		CAT	78/236
Grid 4	2-5	CAT	88/254
Grid 4	2-5	CAT	80/271

	Grid 4	2-5	CAT	90/305
	Grid 4	5-7	CAT	90/022
	Grid 4		F	90/155
	Grid 4		F	90/159
	Grid 4		F	90/160
	Grid 4		F	90/166
	Grid 4		F	90/176
	Grid 4		F	90/187
	Grid 4		F	90/190
	Grid 4		F	82/190
	Grid 4		F	85/210
	Grid 4		F	70/220
	Grid 4		F	90/229
	Grid 4		F	90/230
	Grid 4		F	90/231
	Grid 4		F	90/232
	Grid 4		F	90/236
	Grid 4		F	90/237
	Grid 4		F	80/240
	Grid 4		F	74/240
	Grid 4		F	90/240
	Grid 4		F	90/246
	Grid 4		F	90/251
	Grid 4		F	90/331
	Grid 4		F	78/352
	Grid 4		F	90/354
	Grid 4		F	90/004
	Grid 4		F	90/038
	Grid 4		F	90/040
	Grid 4		F	90/054
	Grid 4		F	84/068
	Grid 4		F	90/072
	Grid 4		F	88/080
	Grid 4		CAT	90/222
	Grid 4		CAT	90/231
Manitou Falls Formation	Zone 13N 482928E 6400703N	1	F	68/204
		1	CAT	60/183
Fox Lake	REA 181	1	F	61/284
		2	F	63/166

---

2	CAT	68/310
1	CAT	75/268
2	CAT	88/266
2	CAT	88/246
1	CAT	50/085
1	CAT	79/184
1	CAT	78/196
1	CAT	63/330
	CAT	46/018
1	CAT	53/135
1	CAT	39/330
	CAT	58/058
1	CAT	81/161
1	CAT	82/221
1	CAT	52/288
1	CAT	55/134
1	DIS	62/123
1	DIS	59/128
8	DIS	19/179
4	DIS	22/181
2	DIS	19/154
1	DIS	38/149
1	DIS	62/204
1	DIS	71/138
2	DIS	00/000
1	DIS	82/208
1	DIS	00/000
1	DIS	53/216
1	DIS	00/000
1	DIS	81/207
4	DIS	69/62
2	DIS	64/109
1	DIS	73/115
1	DIS	64/52
1	DIS	82/146
2	DIS	58/109
1	DIS	62/117
1	DIS	50/128
1	DIS	58/98
1	DIS	64/131

---

1	F	68/208
	F	59/242
	F	50/90
	F	70/270
	F	54/94
	F	56/120
	F	51/100
	F	68/098
	F	62/145
	F	55/260
	F	68/110
	F	60/090
	F	54/096
	F	62/088
	F	64/082
	F	52/128
	F	70/282
	DIS	60/080
	DIS	60/080
	F	84/160
	F	80/164
	F	48/060
	F	72/151
	F	72/151
	F	39/009
	F	39/009
	F	56/152
	F	56/152
	F	69/154
	F	69/154
	D	62/091
	F	87/071
	F	48/349
	F	75/109
4	CAT	19/076
	F	66/042
	F	79/281
1	F	71/092
	DIL	76/079
	FLT	79/063

	F	78/262
1	DIS	82/233
1	CAT	86/237
	DIL	78/292
	DIL	72/279
10	CAT	90/115
3	CAT	19/036
	DIS	08/149
	DIL	33/344
	F	65/320
	DIL	70/089
	F	88/038
	F	74/108
1	CAT	86/241
1	CAT	40/240
	CAT	87/276
	CAT	87/275
	CAT	87/274
	CAT	87/273
1	CAT	70/357
1	CAT	51/170
4	CAT	69/308
1	DIS	69/268
4	CAT	89/268
4	CAT	88/108
1	DIL	81/068
4	CAT	78/061
1	F	87/027
1	CAT	86/304
2	CAT	54/310
2	CAT	64/132
1	CAT	90/219
4	CAT	82/348
3	DIL	68/074
4	CAT	53/029
2	CAT	70/127
5	DIL	81/278
1	DIL	83/089
1	CAT	81/078
1	CAT	89/057

		2	CAT	42/125
		4	CAT	78/170
Manitou Falls	Zone 13N	1	CAT	56/023
Formation	347148E			
	6389073N	2	CAT	59/013
Wide Lake	VR-56	1	DIS	73/308
		1	DIS	57/112
		2	DIS	75/207
		2	DIS	42/061
		2	DIS	76/239
		1	DIS	77/353
		1	DIS	56/324
		3	CAT	66/206
		2	CAT	49/208
		1	CAT	44/224
		1	DIS	74/003
		1	CAT	48/048
		1.5	DIS	72/212
		1	DIS	47/205
		1	DIS	53/170
		2	CAT	73/001
		2	CAT	67/043
		3	CAT	42/102
		2	DIS	47/067
		2	CAT	43/180
		8	CAT	52/105
		2	CAT	35/133
		2	CAT	28/324
		1	CAT	59/053
		3	CAT	64/083
		2	CAT	47/183
		5	CAT	58/170
		3	CAT	66/207
		1	CAT	64/225
		2	CAT	54/195
		3	CAT	48/131
		3	CAT	66/073
		2	DIS	60/153
		4	DIS	70/026
		1	CAT	78/261

---

2	CAT	75/096
2	DIS	70/031
3	DIS	84/327
3	DIS	84/327
1	CAT	65/353
2	CAT	12/290
2	CAT	62/160
3	CAT	56/035
2	DIS	70/051
2	DIS	61/179
2	DIS	55/083
3	CAT	53/099
3	DIS	69/013
2	DIS	26/163
2	DIS	25/140
2	CAT	63/053
2	CAT	57/122
1	DIS	03/325
2	DIS	77/356
4	CAT	59/118
2	DIS	58/167
2	F	75/018
2	F	83/004
3-5	F	46/064
2	CAT	33/098
4	CAT	45/041
2	DIS	64/186
2	CAT	58/106
5	CAT	53/054
1	CAT	27/303
1-2	DIS	53/090
2-3	DIS	50/075
1-2	DIS	54/053
2-3	DIS	81/237
2-3	DIS	50/076
1-2	DIS	48/104
2	DIS	51/031
2	CAT	62/169
	F	48/127
	F	68/131

---

	F	79/028
	F	44/153
1	DIS	90/261
	DIS	56/198
3-4	DIS	51/166
2	DIS	66/206
2	DIS	68/062
	DIS	51/166
1	CAT	51/086
1	CAT	51/086
1	CAT	47/040
2	DIS	73/235
3	DIS	66/072
2	CAT	58/099
2	CAT	63/208
2	CAT	46/019
2	CAT	56/007
	CAT	30/168
	DIS	71/048
1	DIS	44/151
	DIS	70/084
2-3	CAT	62/067
2	CAT	49/212
2	CAT	74/230
3	CAT	59/190
1-8	DB	33/137
18	CAT	43/148
1	CAT	48/066
2	DIS	84/012
	DB	61/199
1	F	17/114
1	DIS	56/222
	DIS	58/014
	DIS	29/265
2-3	DIS	59/210
2-3	DIS	60/194
2-3	CAT	62/041
3-4	CAT	62/358
3-4	CAT	77/037
3-4	CAT	73/229

2-3	CAT	42/020
2-4	CAT	65/033
2	CAT	65/033
2	CAT	75/218
3	DIS	40/004
4	DB	77/328
	DIS	54/057
	DIS	40/137
2	DIS	88/255
3	DIS	60/080
2	DB	86/154
2	DB	86/154
	DIS	60/080
	F	87/119
3	DIS	30/172
1	F	43/064
	F	42/070
4	DIS	48/255
	DB	29/165
	DB	47/183
	DB	60/032
2-3	DB	40/081
3	DIS	71/350
2	F	50/272
2	F	44/048
2	F	33/060
2	F	17/108
2	F	22/185
1-2	F	58/063
2	F	54/057
2-5	F	61/048
3	DIS	67/322
1-2	DIS	45/054
2-5	DIS	38/150
3	CAT	47/044
5	DIS	70/240
1	F	51/025
2	F	71/031
1	CAT	45/085
4	CAT	49/162

		1	CAT	59/214
		2	DIS	75/220
		15-50	CAT	56/065
		2	CAT	32/127
			CAT	28/244
		3	CAT	56/227
		3	CAT	60/246
		1	CAT	44/331
		1	CAT	42/294
		2	CAT	71/202
		2	CAT	47/047
		2	CAT	14/166
Manitou Falls	Zone 13N	1	CAT	50/278
Formation	346964E	1	DIS	88/295
	6389157N	2	Bedding	39/258
Wide Lake	VR-57	1	DIS	88/126
		1	DB	69/204
		7	CAT	62/064
		1	CAT	42/063
		2-4	CAT	71/075
		1	DIS	41/345
		2	CAT	75/323
		2	CAT	54/135
		10	CAT	56/075
		2	CAT	65/144
		3	CAT	63/131
		2	CAT	34/137
		1	CAT	62/162
		1	DIS	56/108
		1	CAT	69/257
		2	CAT	20/187
			F	80/178
			DB	31/086
		1	DIS	32/123
		2	DIS	43/007
		2	DIS	52/119
		2	DIS	56/156
		3	DIS	52/053
		1	DIS	41/103

---

2	DIS	43/039
2	DIS	41/068
2	DIS	41/074
1	CAT	52/052
	DIS	61/096
2	DB	61/107
	DIS	49/357
4	DIS	79/275
	DIS	61/096
	DB	76/075
	DB	82/344
	DB	82/344
	DB	62/011
5	DIS	56/069
2	CAT	86/181
2	CAT	82/304
2	CAT	75/024
	DB	66/075
3	DIS	74/256
1	DB	51/097
3	DIS	63/102
	DIS	88/206
	DIS	88/206
1	DIS	73/106
2	CAT	67/122
2	DIS	51/058
1	CAT	64/001
2	CAT	44/034
2	CAT	52/119
2	CAT	56/097
2	CAT	46/097
2-3	CAT	61/064
2	CAT	46/068
1	CAT	76/067
	DB	11/071
3	CAT	27/304
2	CAT	31/102
1-2	CAT	60/084
3	DIS	46/078
2	DIS	31/077

---

1	DIS	46/078
3	DIS	22/301
3	DIS	62/195
9	DB	13/188
3	CAT	54/034
3-10	CAT	72/193
2-5	CAT	54/034
2	CAT	54/034
2	CAT	67/121
2	DIS	42/054
1	DIS	86/114
1	CAT	74/177
2	DB	74/177
2	DB	63/052
1	CAT	77/236
	DB	51/072
	DB	72/167
2	DIS	67/063
3	DIS	77/069
2	CAT	56/083
2	DIS	56/083
1	DIS	87/165
1	DIS	87/165
2	DIS	61/090
2	DIS	85/206
2	DIS	85/206
2	DB	53/051
	F	44/038
	F	49/254
2	DIS	47/061
5	CAT	71/228
	F	90/005
2	DB	10/338
2-3	CAT	48/241
2	CAT	70/158
1	CAT	65/001
	F	57/020
2	CAT	84/319
2	CAT	84/319
2	CAT	58/063

---

3	CAT	71/011
3	CAT	66/075
2	CAT	56/044
1	CAT	74/338
2	CAT	54/076
1	DIS	38/045
2	CAT	60/139
2	CAT	82/314
2	CAT	82/314
3	CAT	74/353
1	DIS	75/000
1	CAT	76/351
	CAT	75/184
1	DIS	50/070
1	CAT	83/215
1	CAT	83/215
2	CAT	74/250
1	CAT	64/068
3	CAT	68/041
2	CAT	53/347
2	CAT	34/340
1	DIS	72/232
2	CAT	79/030
2	CAT	63/014
1	CAT	64/058
2	CAT	78/228
2	CAT	62/030
2	CAT	48/042
1	DIS	74/055
1	DIS	70/292
2	CAT	74/298
2	CAT	49/079
6	CAT	64/056
2	CAT	72/030
2	CAT	48/147
2	CAT	56/029
2	CAT	54/037

---

---

3	CAT	39/020
2	CAT	54/146
1	CAT	55/070
2	CAT	59/038
5	CAT	69/052
5	CAT	73/024
3	CAT	59/062
2	CAT	53/045
1	DIS	79/325
1	DIS	29/111
3	CAT	68/108
2	CAT	67/039
2	CAT	52/017
2	CAT	61/209
2	CAT	69/002
2	CAT	23/047
2	CAT	38/065
2	CAT	27/053
2	CAT	30/060
5	CAT	77/185
2	CAT	39/032
1	CAT	47/018
1.5	CAT	55/029
2	CAT	65/126
3	CAT	63/039
2	CAT	65/016
3	CAT	42/044
3	CAT	70/036
2	CAT	59/046
2	CAT	65/058
3	CAT	62/114
4	CAT	55/038
4	CAT	55/061
3	CAT	55/078
4	CAT	41/067
2	CAT	62/027
3	CAT	52/049
3	CAT	59/030
3	CAT	59/023
2	CAT	73/013

---

---

2	CAT	17/225
3	CAT	77/029
3	CAT	72/044
5	CAT	81/009
2	CAT	68/009
3	CAT	70/044
1	DIS	80/017
2	CAT	66/039
2	CAT	62/038
	CAT	65/028
2	CAT	55/078
1	DIS	68/084
1	DIS	56/116
1	CAT	66/138
3	DB	78/183
2	DIS	53/094
6	DIS	75/235
3	DIS	75/204
2	DIS	55/157
3	DIS	44/079
5	CAT	59/114
4	CAT	42/174
3	CAT	84/285
5	DIS	36/261
2	CAT	49/206
3	DIS	57/161
3	CAT	71/039
2	CAT	80/256
1	DIS	49/215
1	DIS	55/072
3	CAT	71/091
2	CAT	55/137
2	DIS	69/201
2	CAT	65/014
2	CAT	56/086
2	CAT	56/086
2	CAT	70/253
5	CAT	61/070
3	CAT	31/054
8	CAT	82/273

---

---

3	CAT	56/057
1	CAT	48/139
1	CAT	45/116
2	CAT	44/107
1	CAT	38/121
1	DIS	72/292
1	CAT	82/310
1	CAT	82/310
1	CAT	68/130
1	CAT	64/122
2	CAT	77/254
4	CAT	46/154
2	CAT	64/239
2	CAT	71/082
2	CAT	70/072
2	CAT	65/163
2	CAT	85/331
2	CAT	85/331
3	CAT	62/149
3	CAT	40/156
1	CAT	39/153
1	CAT	49/166
2	CAT	60/193
3	CAT	42/190
1	CAT	25/221
2	CAT	24/143
2	CAT	59/217
3	CAT	43/170
2	CAT	55/173
2	DB	54/213
3	DB	61/217
1	CAT	49/194
	DB	37/267
	DB	40/198
2	CAT	63/241
1	DIS	56/244
1	DIS	72/279
1	CAT	62/222
1	DIS	54/265
2	CAT	60/200

---

---

1	DIS	64/114
5	DB	68/218
7	DB	63/243
9	DB	55/247
5	DB	48/237
0	DB	73/223
0	DIS	63/240
5	CAT	87/069
1	DIS	39/216
2	CAT	88/007
1	DIS	70/165
1	DIS	63/172
2	DIS	53/012
4	DIS	55/034
3	CAT	55/246
3	CAT	55/317
2	DIS	60/079
6	CAT	67/089
6	CAT	67/089
25	CAT	45/082
15	CAT	53/087
15	CAT	53/087
3	CAT	30/066
2	CAT	23/177
2	CAT	12/191
3	CAT	28/047
1	DIS	66/196
4	F	57/092
4	F	55/090
2	DIS	57/065
2	DIS	52/061
2	CAT	65/021
3	CAT	60/117
2	CAT	47/68
1.5	CAT	48/189
2	CAT	74/182
2	DIS	50/143
2	CAT	62/189
3.5	CAT	30/234

---

# Appendix B

Sample	Description	GPS location
WILLUN- GA-1 Thin section: 7H	Port Willunga Formation. Sample of bioclastic carbonate grainstone host rock. This rock is moderate to poorly sorted, rounded to subrounded fragmented bioclasts (bryozoans, brachiopods, bivalves, and echinoids), clasts size ranges from 0.1–1.0 mm.	Zone 54H  267755E 6086307S
WILLUN- GA-2 Thin section: 8H	Port Willunga Formation. Sample of bioclastic carbonate grainstone host rock. This rock is moderate to poorly sorted, rounded to sub-rounded fragmented bioclasts (bryozoans, brachiopods, bivalves, and echinoids), clasts size ranges from 0.1–1.0 mm.	Zone 54H  267916E 6086685S
WILLUN- GA-3 Thin section: 1G	Port Willunga Formation. Sample of crush microbreccia. This band is characterised by clast fracturing and minor compaction causing interlocking fossil clasts. Band width ranges from 3.5–4.5 mm.	Zone 54H  267730E 6086240S
WILLUN- GA-4 Thin section: 2G	Port Willunga Formation. Sample of crush microbreccia. This band is characterised by clast fracturing and minor compaction causing interlocking fossil clasts. Band width ranges from 3.5–4.5 mm.	Zone 54H  267916E 6086685S
WILLUN- GA-5 Thin section: 5S	Port Willunga Formation. Sample of a protocataclastic band with calcite cement, characterised by heavy comminution, high compaction, and lack of interlocking clasts, predominantly 2 mm width.	Zone 54H  267918E 6086685S
WILLUN- GA-6 Thin section: 6S	Port Willunga Formation. Sample of a protocataclastic band with calcite cement, characterised by heavy comminution, high compaction, and lack of interlocking clasts, predominantly 2 mm width.	Zone 54H  267935E 6086792S
WILLUN- GA-7 Thin section: 3B	Port Willunga Formation. Sample of a protocataclastic band with iron-hydroxide cement, characterised by heavy comminution, high compaction, and lack of interlocking clasts, predominantly 2 mm width.	Zone 54H  267914E 6086604S
WILLUN- GA-8 Thin section: 4B	Port Willunga Formation. Sample of a protocataclastic band with iron-hydroxide cement, characterised by heavy comminution, high compaction, and lack of interlocking clasts, predominantly 2 mm width.	Zone 54H  267946E 6086792S
HALLET- COVE-1	Hallet Cove Sandstone. Sample of crush microbreccia. This band is characterised by clast fracturing and minor compaction causing interlocking fossil clasts. Band width ranges from 3.5–4.5 mm.	Zone 53H  762584E 6152467S
HALLET- COVE-2	Hallet Cove Sandstone. Sample of crush microbreccia. This band is characterised by clast fracturing and minor compaction causing interlocking fossil clasts. Band width ranges from 3.5–4.5 mm.	Zone 53H  762584E 6152467S
EYRE-1a & 1b	Eyre Formation. Grab sample of silica cemented dilation band cross-cutting a palaeoredox roll front collected as a drop sample from the Dead Tree section. Band width ranges from 2–4 mm.	Zone 54J  355296E 6665123S

EYRE-3	Eyre Formation. Grab sample of host kaolinized sandstone, coarse to fine-grained, rounded–subrounded spherical grains, minor iron-hydroxide stain.	Zone 54J 355296E 6665123S
EYRE-4	Eyre Formation. Grab sample of host kaolinized sandstone, coarse to fine-grained, rounded–subrounded spherical grains, minor iron-hydroxide stain.	Zone 54J 355296E 6665123S
EYRE-5	Eyre Formation. Grab sample of host kaolinized sandstone, coarse to fine-grained, rounded–subrounded spherical grains, minor iron-hydroxide stain. Interfingering fine grained sand with coarse grained sand.	Zone 54J 355296E 6665123S
EYRE-8	Eyre Formation. Grab sample of host kaolinized sandstone, coarse to fine-grained, rounded–subrounded spherical grain. Coarse grained sand bleached and fine grained sand is iron-hydroxide stained.	Zone 54J 355296E 6665123S
EYRE-10	Eyre Formation. Grab sample of host kaolinized sandstone, coarse to fine-grained, rounded–subrounded spherical grains, minor iron-hydroxide stain (redox roll front).	Zone 54J 355296E 6665123S
EYRE-11	Eyre Formation. Grab sample of cemented dilation band, exhibiting pinch out.	Zone 54J 355296E 6665123S
EYRE-13	Eyre Formation. Grab sample of host kaolinized sandstone, coarse to fine-grained, rounded–subrounded spherical grains, minor iron-hydroxide stain (redox roll front).	Zone 54J 355296E 6665123S
EYRE-15	Eyre Formation. Grab sample of cataclastic band within kaolinized sandstone, coarse to fine-grained, rounded–subrounded spherical grains.	Zone 54J 355296E 6665123S
FLDL-1	Manitou Falls Formation. White quartz arenite, medium grained, well-rounded, well-sorted, spherical grains, grain size reduction (grain-crushing).	Zone 13N 486957E 6400841N
FLDL-2	Manitou Falls Formation. White quartz arenite, medium grained, well-rounded, well-sorted, spherical grains, grain size reduction (grain-crushing), slip surface and cluster >5 cm wide.	Grid 3
FLDL-3	Manitou Falls Formation. Grab sample taken from rubble near road next to grid. White quartz arenite, medium grained, well-rounded, well-sorted, spherical grains, grain size reduction (grain-crushing), cluster 3.5 cm wide.	Grid 3
FLDL-6 Depth: 681.6m	Manitou Falls Formation. White quartz arenite, medium grained, well-rounded, well-sorted, spherical grains, grain size reduction (grain-crushing), dravite vein 2-3 mm wide adjacent to cataclastic band 2 mm wide, 1 cm normal dip-slip displacement.	Zone 13N 482928E 6400703N

FLDL-9 Depth: 535.5m	Manitou Falls Formation. White quartz arenite with hematite stain, medium to coarse grained, well-rounded, well-sorted, spherical grains, grain size reduction (grain-crushing), cataclastic band 1 mm wide.	Zone 13N 482928E 6400703N
FLDL-10 Depth: 471.2m	Manitou Falls Formation. White quartz arenite with limonite stain, medium to coarse grained, well-rounded, well-sorted, spherical grains, grain size reduction (grain-crushing), 4 x 1 mm wide cataclastic bands.	Zone 13N 482928E 6400703N
FLDL-16 Depth: 141.9m	Manitou Falls Formation. White quartz arenite with hematite stain, medium to coarse grained, well-rounded, well-sorted, spherical grains, grain size reduction (grain-crushing), multiple cataclastic bands, 1 mm wide with slip surfaces, white clay infill.	Zone 13N 482928E 6400703N
FLDL-18 Depth: 86.5m	Manitou Falls Formation. White quartz arenite with hematite stain, medium to coarse grained, well-rounded, well-sorted, spherical grains, ~7 bedding parallel dissolution bands-1 mm wide each.	Zone 13N 482928E 6400703N
FLDL-19 Depth: 85.3m	Manitou Falls Formation. White quartz arenite with hematite stain, medium to coarse grained, well-rounded, well-sorted, spherical grains, grain size reduction (grain-crushing), cataclastic bands, 1 mm wide each with slip surfaces, white clay infill.	Zone 13N 482928E 6400703N
FLDL-21 Depth: 631.6m	Manitou Falls Formation. White quartz arenite, medium grained, well-rounded, well-sorted, spherical grains, grain size reduction (grain-crushing), dravite vein 2-3 mm wide adjacent to remnant cataclastic band.	Zone 13N 482928E 6400703N
FLDL-22 Depth: 111.4m	Manitou Falls Formation. White quartz arenite with hematite stain, medium to coarse grained, well-rounded, well-sorted, spherical grains, grain size reduction (grain-crushing), multiple cataclastic bands, 1 mm wide with slip surfaces.	Zone 13N 482928E 6400703N
WL56-2 Depth: 813.3m	Manitou Falls Formation. White quartz arenite with hematite stain, medium to coarse grained, well-rounded, well-sorted, spherical grains, grain size reduction (grain-crushing), cataclastic band, 3 mm wide.	Zone 13N 347148E 6389073N
WL56-6 Depth: 720.0m	Manitou Falls Formation. White quartz arenite with hematite stain, medium- to coarse grained, well-rounded, well-sorted, spherical grains, grain size reduction (grain-crushing), fault zone through silicified zone, dravite cement replacement.	Zone 13N 347148E 6389073N
WL56-7 Depth: 716.4m	Manitou Falls Formation. White quartz arenite, medium- to coarse grained, well-rounded, well-sorted, spherical grains, grain size reduction (grain-crushing), cataclastic band, 1 mm wide.	Zone 13N 347148E 6389073N
WL56-8 Depth: 704.8m	Manitou Falls Formation. White quartz arenite, medium to coarse grained, well-rounded, well-sorted, spherical grains, grain size reduction (grain-crushing), cataclastic band, 3 mm wide, slip surface, 9 mm reverse dip-slip displacement	Zone 13N 347148E 6389073N
WL56-9 Depth: 704.2m	Manitou Falls Formation. White quartz arenite with hematite stain, medium to coarse grained, well-rounded, well-sorted, spherical grains, grain size reduction (grain-crushing), cataclastic band, 3-5 mm wide.	Zone 13N 347148E 6389073N

WL56-12 Depth: 561.8m	Manitou Falls Formation. White quartz arenite with hematite stain, medium to coarse grained, well-rounded, well-sorted, spherical grains, grain size reduction (grain-crushing), cataclastic band, 3-4 mm wide.	Zone 13N 347148E 6389073N
WL56-20 Depth: 59.5m	Manitou Falls Formation. White quartz arenite with limonite stain, medium to coarse grained, well-rounded, well-sorted, spherical grains, grain size reduction (grain-crushing), cataclastic band, 1 mm wide, slip surface.	Zone 13N 347148E 6389073N
WL57-2 Depth: 51.4m	Manitou Falls Formation. White quartz arenite, medium to coarse grained, well-rounded, well-sorted, spherical grains, bedding parallel dissolution bands (1-2mm wide) crosscut by cataclastic band (1-2 mm wide).	Zone 13N 346964E 6389157N
WL57-3 Depth: 71.8m	Manitou Falls Formation. White quartz arenite with limonite stain, medium to coarse grained, well-rounded, well-sorted, spherical grains, grain size reduction (grain-crushing), cataclastic band, 4 mm normal dip-slip displacement.	Zone 13N 346964E 6389157N
WL57-5 Depth: 116.7m	Manitou Falls Formation. White quartz arenite with hematite stain, medium to coarse grained, well-rounded, well-sorted, spherical grains, grain size reduction (grain-crushing), cataclastic band, 7 mm reverse dip-slip displacement.	Zone 13N 346964E 6389157N
WL57-7 Depth: 137.4m	Manitou Falls Formation. White quartz arenite with hematite stain, medium to coarse grained, well-rounded, well-sorted, spherical grains, grain size reduction (grain-crushing), cataclastic band, 3 mm.	Zone 13N 346964E 6389157N
WL57-9	Manitou Falls Formation. White quartz arenite, medium to coarse grained, well-rounded, well-sorted, spherical grains, grain size reduction (grain-crushing), anastomosing cataclastic band zone, 1 mm each, slip surface.	Zone 13N 346964E 6389157N
WL57-11 Depth: 231.9m	Manitou Falls Formation. White quartz arenite, medium to coarse grained, well-rounded, well-sorted, spherical grains, grain size reduction (grain-crushing), 3-4 anastomosing cataclastic bands, 1 mm each, slip surface, white clay infill.	Zone 13N 346964E 6389157N
WL57-13 Depth: 247.5m	Manitou Falls Formation. White quartz arenite with hematite stain, medium to coarse grained, well-rounded, well-sorted, spherical grains, grain size reduction (grain-crushing), cluster of bands up to 10mm wide, and band stained with red-pink-purple hematite.	Zone 13N 346964E 6389157N
WL57-18 Depth: 420.0m	Manitou Falls Formation. White quartz arenite with hematite stain, medium to coarse grained, well-rounded, well-sorted, spherical grains, grain size reduction (grain-crushing), 4-5 parallel cataclastic bands, 1 mm each.	Zone 13N 346964E 6389157N
WL57-19 Depth: 489.1m	Manitou Falls Formation. White quartz arenite with purple hematite stain, medium to coarse grained, well-rounded, well-sorted, spherical grains, grain size reduction (grain-crushing), pink hematite stained cluster >8 mm wide.	Zone 13N 346964E 6389157N
WL57-20 Depth: 527.3m	Manitou Falls Formation. White quartz arenite with purple hematite stain, medium to coarse grained, well-rounded, well-sorted, spherical grains, grain size reduction (grain-crushing), purple hematite stained cluster 5 mm wide.	Zone 13N 346964E 6389157N

WL57-22 Depth: 629.9m	Manitou Falls Formation. White quartz arenite with purple hematite stain, coarse to very coarse grained, well-rounded, well-sorted, spherical grains, grain size reduction (grain-crushing), 1 mm wide cataclastic bands abutting another 1 mm wide cataclastic band.	Zone 13N 346964E 6389157N
WL57-23 Depth: 636.6m	Manitou Falls Formation. White quartz arenite with purple hematite stain, medium to coarse grained, well-rounded, well-sorted, spherical grains, grain size reduction (grain-crushing), 1 mm wide cataclastic band slip-surface crosscutting a 1 mm wide cataclastic band slip-surface.	Zone 13N 346964E 6389157N
WL57-26 Depth: 231.6m	Manitou Falls Formation. White quartz arenite with pink hematite stain, medium to coarse grained, well-rounded, well-sorted, spherical grains, grain size reduction (grain-crushing), 2 mm wide cataclastic band.	Zone 13N 346964E 6389157N
WL57-28 Depth: 294.9m	Manitou Falls Formation. White quartz arenite with purple hematite stain, medium to coarse grained, well-rounded, well-sorted, spherical grains, grain size reduction (grain-crushing), 2-1 mm wide purple hematite stained cataclastic bands.	Zone 13N 346964E 6389157N
WLRIDGE-1	Manitou Falls Formation. Grab sample. White quartz arenite, medium grained, well-rounded, well-sorted, spherical grains, grain size reduction (grain-crushing), 16 mm wide cataclastic band cluster.	Zone 13N 346392E 6387322N
WLRIDGE-4	Manitou Falls Formation. Grab sample. White quartz arenite, medium grained, well-rounded, well-sorted, spherical grains, grain size reduction (grain-crushing), >11 mm wide cataclastic band cluster with slip surface.	Zone 13N 346470E 6387773N

# Appendix C

Analysis number	Location	Formation	Type	Permeability (nm)
1	Sellicks Beach	Port Willunga Formation	Host rock	3100
2	Sellicks Beach	Port Willunga Formation	Host rock	915.8
3	Sellicks Beach	Port Willunga Formation	Host rock	3800
4	Sellicks Beach	Port Willunga Formation	Host rock	2800
5	Sellicks Beach	Port Willunga Formation	Host rock	4900
6	Sellicks Beach	Port Willunga Formation	Host rock	4200
7	Sellicks Beach	Port Willunga Formation	Host rock	2500
8	Sellicks Beach	Port Willunga Formation	Host rock	2800
9	Sellicks Beach	Port Willunga Formation	Host rock	5500
10	Sellicks Beach	Port Willunga Formation	Host rock	4000
11	Sellicks Beach	Port Willunga Formation	Crush microbreccia	2800
12	Sellicks Beach	Port Willunga Formation	Crush microbreccia	3400
13	Sellicks Beach	Port Willunga Formation	Crush microbreccia	2000
14	Sellicks Beach	Port Willunga Formation	Crush microbreccia	3200
15	Sellicks Beach	Port Willunga Formation	Crush microbreccia	2100
16	Sellicks Beach	Port Willunga Formation	Crush microbreccia	2400
17	Sellicks Beach	Port Willunga Formation	Crush microbreccia	3500
18	Sellicks Beach	Port Willunga Formation	Crush microbreccia	1800
19	Sellicks Beach	Port Willunga Formation	Protocataclastic	1000
20	Sellicks Beach	Port Willunga Formation	Protocataclastic	247
21	Sellicks Beach	Port Willunga Formation	Protocataclastic	766
22	Sellicks Beach	Port Willunga Formation	Protocataclastic	615.3
23	Sellicks Beach	Port Willunga Formation	Protocataclastic	1045.4
24	Sellicks Beach	Port Willunga Formation	Protocataclastic	1200
25	Sellicks Beach	Port Willunga Formation	Protocataclastic	1300
26	Sellicks Beach	Port Willunga Formation	Protocataclastic	443.8
27	Sellicks Beach	Port Willunga Formation	Protocataclastic	138.3
28	Sellicks Beach	Port Willunga Formation	Protocataclastic	1100
29	Sellicks Beach	Port Willunga Formation	Protocataclastic	1500
30	Sellicks Beach	Port Willunga Formation	Protocataclastic	422.7
31	Sellicks Beach	Port Willunga Formation	Protocataclastic	1600
32	Sellicks Beach	Port Willunga Formation	Protocataclastic	2000
33	Sellicks Beach	Port Willunga Formation	Protocataclastic	477.8
34	Sellicks Beach	Port Willunga Formation	Protocataclastic	738.2
35	Sellicks Beach	Port Willunga Formation	Protocataclastic	3200
36	Sellicks Beach	Port Willunga Formation	Protocataclastic	727.4
37	Sellicks Beach	Port Willunga Formation	Protocataclastic	264.6
38	Sellicks Beach	Port Willunga Formation	Protocataclastic	2600
39	Sellicks Beach	Port Willunga Formation	Protocataclastic	2700
40	Sellicks Beach	Port Willunga Formation	Protocataclastic	652.7

41	Sellicks Beach	Port Willunga Formation	Protocataclastic	129.3
42	Sellicks Beach	Port Willunga Formation	Protocataclastic	1400
43	Sellicks Beach	Port Willunga Formation	Protocataclastic	419.1
44	Sellicks Beach	Port Willunga Formation	Protocataclastic	377.7
45	Sellicks Beach	Port Willunga Formation	Protocataclastic	604.5
46	Sellicks Beach	Port Willunga Formation	Protocataclastic	2600
47	Sellicks Beach	Port Willunga Formation	Protocataclastic	329.9
48	Sellicks Beach	Port Willunga Formation	Protocataclastic	658
49	Sellicks Beach	Port Willunga Formation	Protocataclastic	915.8
50	Dead Tree section	Eyre Formation	Host rock (limonite)	123.9
51	Dead Tree section	Eyre Formation	Host (fine sand)	638.7
52	Dead Tree section	Eyre Formation	Host (Coarse sand)	2040
53	Dead Tree section	Eyre Formation	Dilation band	1300
54	Dead Tree section	Eyre Formation	Dilation band	1400
55	Dead Tree section	Eyre Formation	Dilation band	2400
56	Dead Tree section	Eyre Formation	Dilation band	3400
57	Dead Tree section	Eyre Formation	Dilation band	3500
58	Dead Tree section	Eyre Formation	Dilation band	3500
59	Dead Tree section	Eyre Formation	Dilation band	4100
60	Dead Tree section	Eyre Formation	Dilation band	5100
61	Dead Tree section	Eyre Formation	Dilation band	8100
62	Dead Tree section	Eyre Formation	Dilation band	8300
63	Dead Tree section	Eyre Formation	Dilation band	11600
64	Dead Tree section	Eyre Formation	Dilation band	13900

---

# Appendix D

---

Loaded dataset: J:\Drew\DL1\bmp\VOI(3)\dl1\_\_rec\_voi1\_

<<<<< Begin of task (25a30d61-24b8-4bc2-8aeb-6b975f5a3f7a) >>>>>

CT Analyser Version: 1.16.4.1

Task file: J:\Drew\shrink wrap and subtract out pores task list 241016.ctt

Dataset name	J:\Drew\DL1\bmp\VOI(3)\dl1__rec_voi1_0112.bmp		
--------------	---	--	--

File postfix length	4		
---------------------	---	--	--

File type	BMP		
-----------	-----	--	--

Image size (W/H)	1344	769	
------------------	------	-----	--

Total number of images	832		
------------------------	-----	--	--

Total Z-position range	112	943	
------------------------	-----	-----	--

Number of images inside VOI	832		
-----------------------------	-----	--	--

Z-position range of VOI	112	943	
-------------------------	-----	-----	--

Z spacing	1		
-----------	---	--	--

Pixel size (um)	17.00131		
-----------------	----------	--	--

-----  
[ 05/10/17 14:15:45 ] Thresholding

Mode	Global		
------	--------	--	--

Lower grey threshold	31		
----------------------	----	--	--

Upper grey threshold	255		
----------------------	-----	--	--

[ 05/10/17 14:15:47 ] Thresholding done

-----  
[ 05/10/17 14:15:47 ] Despeckle

Type: Remove white speckles (3D space)

Volume : less than 25 voxels

Apply to: Image

14057 speckles removed

[ 05/10/17 14:15:54 ] Despeckle done

-----  
[ 05/10/17 14:25:04 ] ROI shrink-wrap

Mode : Shrink-wrap (2D space)

Stretch over holes with a diameter in 100 pixels

-----  
[ 05/10/17 14:25:04 ] Bitwise operations

<Image> = <Region of Interest> NAND <Image>  
 [ 05/10/17 14:25:05 ] Bitwise operations done

-----  
 [ 05/10/17 14:25:05 ] 3D analysis

Date and time            10.05.2017 14:25  
 Operator identity        skyscan3  
 Computer name           DC86000BC2A1B  
 Computation time        0:01:24  
 Dataset                 dl1\_\_rec\_voi1\_  
 Location                J:\Drew\DL1\bmp\VOI(3)\

#### MORPHOMETRY RESULTS

-----

Description	Abbreviation	Value	Unit
Number of layers		832	
Lower vertical position		1.90415	mm
Upper vertical position		16.03223	mm
Pixel size		17.00131	um
Lower grey threshold		31	
Upper grey threshold		255	
Total VOI volume	TV	1235.51	mm <sup>3</sup>
Object volume	Obj.V	195.3435	mm <sup>3</sup>
Percent object volume	Obj.V/TV	15.81076	%
Total VOI surface	TS	1091.05	mm <sup>2</sup>
Object surface	Obj.S	7501.067	mm <sup>2</sup>
Intersection surface	i.S	154.028	mm <sup>2</sup>
Object surface / volume ratio	Obj.S/Obj.V	38.39936	1/mm
Object surface density	Obj.S/TV	6.07123	1/mm
Surface convexity index	SCv.I	13.67635	1/mm
Centroid (x)	Crd.X	9.07642	mm
Centroid (y)	Crd.Y	6.84855	mm
Centroid (z)	Crd.Z	8.53867	mm
Moment of inertia (x)	MMI(x)	4253.957	mm <sup>5</sup>
Moment of inertia (y)	MMI(y)	6557.447	mm <sup>5</sup>
Moment of inertia (z)	MMI(z)	6109.97	mm <sup>5</sup>
Polar moment of inertia	MMI(polar)	8460.687	mm <sup>5</sup>

Radius of gyration (x)	Gr.R(x)	4.61935	mm
Radius of gyration (y)	Gr.R(y)	5.73525	mm
Radius of gyration (z)	Gr.R(z)	5.5361	mm
Polar radius of gyration	Gr.R(polar)	6.51459	mm
Product of inertia (xy)	Pr.In(xy)	221.0688	mm <sup>5</sup>
Product of inertia (xz)	Pr.In(xz)	-1694.18	mm <sup>5</sup>
Product of inertia (yz)	Pr.In(yz)	124.7453	mm <sup>5</sup>
Total orientation (theta)	T.Or(theta)	59.50602	°
Total orientation (phi)	T.Or(phi)	182.5505	°
Number of objects	Obj.N	189618	
Number of closed pores	Po.N(cl)	437	
Volume of closed pores	Po.V(cl)	0.112	mm <sup>3</sup>
Surface of closed pores	Po.S(cl)	13.99274	mm <sup>2</sup>
Closed porosity (percent)	Po(cl)	0.0573	%
Volume of open pore space	Po.V(op)	1040.055	mm <sup>3</sup>
Open porosity (percent)	Po(op)	84.18018	%
Total volume of pore space	Po.V(tot)	1040.167	mm <sup>3</sup>
Total porosity (percent)	Po(tot)	84.18924	%
Euler number	Eu.N	63624	
Connectivity	Conn	126431	
Connectivity density	Conn.Dn	102.331	1/mm <sup>3</sup>

<<<<< End of task (25a30d61-24b8-4bc2-8aeb-6b975f5a3f7a) >>>>>

<<<<< Begin of task (75f219c7-d6ef-42c1-854e-5ed0bffa1885) >>>>>

CT Analyser Version: 1.16.4.1

Task file: J:\Drew\shrink wrap and subtract out pores task list 241016.ctt

Dataset name	J:\Drew\DL1\bmp\VOI(3)\dl1__rec_voi1_0112.bmp		
File postfix length	4		
File type	BMP		
Image size (W/H)	1344	769	
Total number of images	832		
Total Z-position range	112	943	

Number of images inside VOI	832		
Z-position range of VOI	112	943	
Z spacing	1		
Pixel size (um)	17.00131		

-----  
 [ 05/12/17 13:48:18 ] Thresholding

Mode	Global		
Lower grey threshold	31		
Upper grey threshold	255		

[ 05/12/17 13:49:41 ] Thresholding done

-----  
 [ 05/12/17 13:49:42 ] Despeckle

Type: Remove white speckles (3D space)

Volume : less than 25 voxels

Apply to: Image

114750 speckles removed

[ 05/12/17 13:49:55 ] Despeckle done

-----  
 [ 05/12/17 13:56:43 ] ROI shrink-wrap

Mode : Shrink-wrap (2D space)

Stretch over holes with a diameter in 100 pixels

-----  
 [ 05/12/17 13:56:43 ] Bitwise operations

<Image> = <Region of Interest> NAND <Image>

[ 05/12/17 13:56:44 ] Bitwise operations done

-----  
 [ 05/12/17 13:56:44 ] 3D analysis

Date and time	12.05.2017 13:56
Operator identity	skyscan3
Computer name	DC86000BC2A1B
Computation time	0:01:16
Dataset	dl1__rec_voi1_
Location	J:\Drew\DL1\bmp\VOI(3)\

## MORPHOMETRY RESULTS

Description	Abbreviation	Value	Unit
Number of layers		832	
Lower vertical position		1.90415	mm
Upper vertical position		16.03223	mm
Pixel size		17.00131	um
Lower grey threshold		31	
Upper grey threshold		255	
Total VOI volume	TV	1200.635	mm <sup>3</sup>
Object volume	Obj.V	1006.76	mm <sup>3</sup>
Percent object volume	Obj.V/TV	83.85235	%
Total VOI surface	TS	1465.359	mm <sup>2</sup>
Object surface	Obj.S	8044.748	mm <sup>2</sup>
Intersection surface	i.S	1103.097	mm <sup>2</sup>
Object surface / volume ratio	Obj.S/Obj.V	7.99073	1/mm
Object surface density	Obj.S/TV	6.70041	1/mm
Surface convexity index	SCv.I	-35.238	1/mm
Centroid (x)	Crd.X	8.72868	mm
Centroid (y)	Crd.Y	6.39821	mm
Centroid (z)	Crd.Z	9.10659	mm
Moment of inertia (x)	MMI(x)	20973.47	mm <sup>5</sup>
Moment of inertia (y)	MMI(y)	30248.38	mm <sup>5</sup>
Moment of inertia (z)	MMI(z)	27072.34	mm <sup>5</sup>
Polar moment of inertia	MMI(polar)	39147.09	mm <sup>5</sup>
Radius of gyration (x)	Gr.R(x)	4.57019	mm
Radius of gyration (y)	Gr.R(y)	5.48845	mm
Radius of gyration (z)	Gr.R(z)	5.19232	mm
Polar radius of gyration	Gr.R(polar)	6.24379	mm
Product of inertia (xy)	Pr.In(xy)	1813.983	mm <sup>5</sup>
Product of inertia (xz)	Pr.In(xz)	-7215.25	mm <sup>5</sup>
Product of inertia (yz)	Pr.In(yz)	-1034.41	mm <sup>5</sup>
Total orientation (theta)	T.Or(theta)	56.92005	°
Total orientation (phi)	T.Or(phi)	189.8672	°
Number of objects	Obj.N	3343	
Number of closed pores	Po.N(cl)	19643	
Volume of closed pores	Po.V(cl)	20.09762	mm <sup>3</sup>
Surface of closed pores	Po.S(cl)	1381.899	mm <sup>2</sup>

---

Closed porosity (percent)	Po(cl)	1.9572 %
Volume of open pore space	Po.V(op)	173.7767 mm <sup>3</sup>
<b>Open porosity (percent)</b>	<b>Po(op)</b>	<b>14.47373 %</b>
Total volume of pore space	Po.V(tot)	193.8743 mm <sup>3</sup>
<b>Total porosity (percent)</b>	<b>Po(tot)</b>	<b>16.14765 %</b>
Euler number	Eu.N	-34855
Connectivity	Conn	57841
Connectivity density	Conn.Dn	48.17535 1/mm <sup>3</sup>

<<<<< End of task (75f219c7-d6ef-42c1-854e-5ed0bffa1885) >>>>>

|

# Appendix E

<b>SAM- PLE</b>	<b>LINE</b>	<b>Al WT%</b>	<b>Mg WT%</b>	<b>Ca WT%</b>	<b>K WT%</b>	<b>Fe WT%</b>	<b>Mn WT%</b>
FLDL2 Area 1	109	0.018788	0.000555	0.004179	0.001609	0.013082	0
FLDL2 Area 1	110	6.55533	0.991835	0.480721	0.29563	0.385455	0.004846
FLDL2 Area 1	111	0.181559	0.048394	0.153107	0.014268	0.082689	0
FLDL2 Area 1	112	0.2369	0.094959	0.284246	0.037634	0.115003	0.00434
FLDL2 Area 1	113	1.66152	0.261002	0.084991	0.177435	0.120061	0.004979
FLDL2 Area 1	114	0.028531	0.001854	0.002609	0.002495	0.003067	0
FLDL2 Area 1	115	0.041507	0.000634	0.00366	0.001279	0.002106	0
FLDL 2 Spot 1 test 2	116	0.004126	0.000279	0.003569	0.007251	0.004652	0
FLDL 2 Spot 1 test 2	117	0.030584	0.000823	0.004259	0.005778	0	0.000097
FLDL 2 Spot 1 test 2	118	0.166873	0.002863	0.006024	0.021572	0	0
FLDL 2 Spot 1 test 2	119	0.046763	0.000788	0.008761	0.006043	0.000252	0
FLDL 2 Spot 1 test 1	120	0.024012	0	0.001828	0.003891	0.000663	0
FLDL 2 Spot 1 test 1	121	0.007146	0.000791	0.004735	0.004965	0.004538	0.000189
FLDL 2 Spot 1 test 1	122	0.068474	0.050451	0.083468	0.037597	0.076196	0.004042
FLDL 2 Spot 1 test 1	123	0.154822	0.112791	0.177597	0.047167	0.183094	0.005244
FLDL 2 Spot 1 test 1	124	0.008877	0.002688	0.006397	0.003451	0.01009	0.000039
FLDL 2 Spot 1 test 1	125	0.028337	0	0.000381	0.003444	0.005253	0

FLDL 2 Spot 1 test 1	126	0.030305	0.000903	0.000626	0.003639	0.004377	0.005139
WL57- 13b transect	283	0.033898	0.008582	0.005963	0.008567	0.015117	0
WL57- 13b transect	284	0.059679	0.012344	0.007424	0.020035	0.022183	0.002849
WL57- 13b transect	285	0.064531	0.021003	0.009056	0.013518	0.038247	0.000242
WL57- 13b transect	286	3.75974	1.16038	0.057624	0.028917	0.687511	0.002786
WL57- 13b transect	287	0.004909	0.00133	0.002009	0.000687	0.004931	0
WL57- 13b transect	288	0.005716	0.001058	0.00339	0.001949	0.007	0
WL57- 13b transect	289	1.91877	0.0531	0.004759	0.713004	0.141844	0.00346
WL57- 13b transect	290	0.003604	0.001144	0.002913	0.000973	0.00821	0
WL57- 13b transect	291	0.009914	0.002316	0.003438	0.004932	0.00888	0
WL57- 13b transect	292	0.008854	0.001459	0.003402	0.002617	0.007292	0.002301
WL57- 13b transect	293	0.14612	0.053204	0.015273	0.032455	0.049245	0.001273
WL57- 13b transect	294	0.180159	0.077116	0.037428	0.048588	0.1308	0.002565
WL57- 13b transect	295	0.097625	0.03403	0.023499	0.030757	0.10262	0
WL57- 13b transect	296	0.246874	0.100173	0.048934	0.081614	0.235498	0
WL57- 13b transect	297	1.32191	0.121146	0.069996	0.652676	0.148441	0.003151

WL57-13b transect	298	0.101111	0.029521	0.009191	0.024214	0.028497	0.002959
WL57-13b transect	299	0.117495	0.035641	0.010059	0.032016	0.036768	0
WL57-13b transect	300	0.168895	0.031244	0.010417	0.068708	0.039516	0.002077
WL57-13b transect	301	0.252136	0.086747	0.047882	0.117567	0.164739	0
WL57-13b transect	302	0.073673	0.016122	0.009443	0.026924	0.044021	0
WL57-13b transect	303	0.0369	0.005952	0.006099	0.016943	0.009411	0
WL57-13b transect	304	0.196706	0.048281	0.033097	0.061481	0.085802	0
WL57-13b transect	305	0.006606	0.002373	0.004611	0.003083	0.008231	0
WL57-13b transect	306	0.11118	0.028138	0.025577	0.036853	0.047035	0.001249
WL57-13b transect	307	0.209754	0.067223	0.061215	0.071197	0.100479	0.002339
WL57-13b transect	308	0.270104	0.091023	0.047535	0.097202	0.168252	0.000323
WL57-13b transect	309	0.065721	0.014	0.018706	0.023608	0.037593	0.002979
WL57-13b transect	310	0.042262	0.016078	0.007237	0.00975	0.014779	0
WL57-13b transect	311	0.036827	0.008838	0.01662	0.011148	0.01626	0
WL57-13b transect	312	0.122247	0.043907	0.022543	0.034419	0.072675	0.000502
WL57-13b transect	313	0.153789	0.049231	0.033287	0.065014	0.153028	0

WL57-13b transect	314	0.08391	0.033797	0.009886	0.017381	0.048115	0.001698
WL57-13b transect	315	0.018792	0.001574	0.00328	0.003804	0.007489	0.000713
WL57-13b transect	316	0.042435	0.005341	0.006599	0.010785	0.017662	0.00307
WL57-13b transect	317	0.121993	0.017045	0.011783	0.017528	0.04164	0
WL57-13b transect	318	0.081236	0.02437	0.051154	0.018924	0.015079	0
WL57-13b transect	319	0.733977	0.191943	0.472258	0.32844	0.270945	0.004919
WL57-13b transect	320	0.170285	0.106623	2.4717	0.044125	0.13231	0.002994
WL57-13b transect	321	0.130659	0.032317	0.013795	0.042669	0.047146	0
WL57-13b transect	322	0.325362	0.124535	0.078653	0.102117	0.115132	0.001864
WL57-13b transect	323	0.251858	0.127913	0.096215	0.068819	0.216487	0.004059
WL57-13b transect	324	0.022653	0.008547	0.172972	0.008717	0.029073	0.003337
WL57-13b transect	325	0.261059	0.118462	0.117775	0.05012	0.21065	0.003785
WL57-13b transect	326	0.012537	0.004382	0.018872	0.004803	0.012641	0.003637
WL57-13b transect	327	0.385051	0.115406	0.099156	0.072227	0.139861	0.000256
WL57-13b transect	328	0.24429	0.052116	0.018597	0.10351	0.071196	0
WL57-13b transect	329	9.3061	0.067332	0.021213	0.064848	0.066124	0

WL57-13b transect	330	0.049778	0.016268	0.019614	0.010447	0.054007	0
WL57-13b transect	331	0.065023	0.024392	0.030647	0.016276	0.089153	0
WL57-13b transect	332	0.295319	0.163029	0.132273	0.069855	0.389238	0.009766
WL57-13b transect	333	0.210514	0.07531	0.026046	0.066903	0.097854	0
WL57-13b transect	334	0.042248	0.027149	0.017343	0.01354	0.052683	0
WL57-13b transect	335	0.516731	0.246078	0.170769	0.149731	0.458622	0.010129
WL57-13b transect	336	0.324403	0.086992	0.057992	0.182432	0.135198	0.002001
WL57-13b transect	337	0.147535	0.047018	0.038729	0.055754	0.070883	0.000533
WL57-13b transect	338	0.21285	0.111531	0.081827	0.049014	0.264035	0.004149
WL57-13b transect	339	0.129787	0.065766	0.045739	0.037166	0.119741	0.001236
WL57-13b transect	340	0.041792	0.010835	0.009627	0.015318	0.017198	0
WL57-13b transect	341	0.24907	0.109322	0.068277	0.069703	0.166089	0.001985
WL57-13b transect	342	0.054402	0.018979	0.009739	0.012272	0.037282	0.000007
WL57-13b transect	343	0.247355	0.025839	0.046027	0.076032	0.257454	0.002709
WL57-13b transect	344	0.00727	0.001459	0.0025	0.00261	0.005935	0.004337
WL57-13b transect	345	0.157397	0.080115	0.049406	0.050168	0.1273	0.000962

WL57-13b transect	346	0.405113	0.05579	0.015662	0.207539	0.071041	0.001134
WL57-13b transect	347	0.125345	0.063007	0.048275	0.047266	0.163751	0.003036
WL57-13b transect	348	0.056765	0.028445	0.021784	0.027637	0.077133	0.003114
WL57-13b transect	349	0.105084	0.031661	0.011016	0.030745	0.038241	0
WL57-13b transect	350	0.048773	0.005589	0.008919	0.011263	0.018202	0.000173
WL57-13b transect	351	0.115638	0.056205	0.036178	0.028439	0.093171	0.001069